TURBULENCE AND ENERGETIC ION PRODUCTION IN THE PLUME OF THE PARTIALLY MAGNETIZED HOLLOW CATHODE

Margaret Mary Mooney, Ph.D.

Western Michigan University, 2025

Hall effect thrusters (HETs) are the most widely used electric propulsion (EP) device for in-space satellite propulsion. EP devices provide high efficiencies for extended mission lifetimes and low thrust for precision maneuvers. The hollow cathode is a critical HET component and undergoes extensive lifetime testing in addition to the lifetime testing of the full HET. Significant density gradients, non-Maxwellian electron behavior, and magnetic fields sufficiently strong enough to magnetize electrons in hollow cathode plumes create favorable conditions for the formation of plasma instabilities, which have an impact on cathode lifetime. Cathode qualification testing is typically conducted independently and includes a downstream cylindrical anode and a magnetic field simulator that mimics the HET environment. It is critical to operate lone cathode experiments in environments that best match the conditions the cathode experiences in the full thruster to accurately model cathode lifetime. However, it remains unclear which cathode operational variables significantly influence the dynamic and turbulent profile in the cathode plume to best replicate the thruster profile. This work shows an investigation of key variables in standalone cathode testing, including variations in magnetic field, background pressure, induced current oscillations on the anode, and cathode mass flow rate, to evaluate how independent cathode operation compares to thruster operation. High-speed diagnostics were employed to investigate the downstream plasma of the independent cathode. Fluctuations in the ion density were used to spatially map the wave energy divided into two regimes: a low-frequency band (100 Hz – 250 kHz), encompassing large-scale

oscillations such as cathode breathing mode and azimuthal ion drifts; and a high-frequency band (250 kHz – 14 MHz), capturing small-scale turbulences in the plume (e.g., ion acoustic turbulence and lower hybrid drift modes). It was shown that the onset of the azimuthal ion drift varies with respect of magnetic field strength for argon, krypton, and xenon, and is dominant in the frequency spectra at HET magnetic field strengths.

Regions of heightened high-frequency wave energy were identified, including along the steep density gradient in the cathode plasma region, near the cathode exit plane away from the centerline, and near the anode entrance downstream. The wave energy along the cathode density gradient was primarily influenced by changes in mass flow rates, and relatively unaffected by changes in background pressure. In contrast, the regions near the cathode exit plane (off-centerline) and near the anode entrance were significantly affected by background pressure, mass flow rates, and induced cathode oscillations. Lowering the flow rate of independent cathode operation can enhance local turbulence for a closer match to the HET profile, while global changes to the neutral pressure by adjusting the number of cryogenic pumps might not be sufficient in replicating the dynamic and turbulent environment to the HET.

TURBULENCE AND ENERGETIC ION PRODUCTION IN THE PARTIALLY MAGNETIZED HOLLOW CATHODE

by

Margaret Mary Mooney

A dissertation submitted to the Graduate College
in partial fulfillment of the requirements
for the degree of Doctor of Philosophy
Mechanical Engineering
Western Michigan University
April 2025

Doctoral Committee

Kristina Lemmer, Ph.D., chair
William Liou, Ph.D.
Robert Lobbia, Ph.D.
Michael McDonald, Ph.D.

ACKNOWLEDGMENTS

First, I must thank my advisor, Professor Kristina Lemmer, for her mentorship in my past 8 years at WMU. My journey into EP began as an undergrad at WMU and working with Professor Lemmer in ALPE is the single reason that kept me here for my graduate studies. I cannot thank you enough for all the guidance, kindness, and financial support you have provided me throughout my tenure in ALPE. You gave me a space in your lab and trusted me, and my capabilities, throughout my graduate studies. Most importantly, you believed in me as a scientist when I didn't believe in myself. I would not have made it through grad school if it weren't for your mentorship.

I took several courses with Dr. William Liou during my undergraduate and graduate career at WMU, including one of my favorite courses (for obvious reasons): Turbulence. Even though I might have selected an outside-the-box research project for his turbulence course, you were more than willing to meet with me to answer my silly questions and coach me through reading wild papers about black hole accretion disks. Thank you for all your mentorship in your courses and on my committee.

My first real foray into EP experimentation was as an NRIEP intern at the Naval Research Laboratory under Dr. Michael McDonald as a young undergrad. I knew almost nothing about vacuum chamber experimental work, let alone plasma physics, and Dr. McDonald spent hours guiding me through the complex art of plasma making. My internship collided with his summer vacation plans, and I will never forget calling him to teach me how to turn on a cathode while he stood in a sandbar in Lake Michigan. I never felt like a burden learning under Dr. McDonald, and he has remained a constant supportive force in my graduate career. Thank you for endlessly advocating for me and challenging me. You have shaped me into the engineer I am today.

I received several grants that supported me financially throughout my graduate career including the Georgeau fellowship early in the graduate studies and the NASA Space Technology Graduate Research Opportunities (NSTGRO) fellowship, under grant number 80NSSC20K1179, throughout my Ph.D. While the NSTGRO supported me financially, it also gave me the invaluable experience of the visiting technologist experiences, most of which I spent at the NASA Jet Propulsion Laboratory. Most importantly, the NSTGRO placed me under the tutelage of Dr. Robert Lobbia. You went way above and beyond as my NASA mentor for the duration of my NSTGRO. I cannot thank you enough for all the time and effort you put into mentoring me in high-speed diagnostics, plasmas, and in professional development. I barely understood what time-resolved meant at the beginning of my Ph.D., and now I feel confident designing complex experiments and building tiny, tiny probes. You were invaluable at every step of the way.

I am grateful to have experienced such a positive lab experience in ALPE. From the moment I joined, the senior lab members welcomed me in. Ken "living the dream" Domingue is by far the most positive person you will ever meet. Thank you for making my start in ALPE fun and teaching me that black coffee IS the superior way to drink coffee. Matt Baird was always showing off his cool plasmas in the chamber I would come to nearly live in for four years. Our shared love for cats and plasmas made learning under you an absolute blast. Tom Kerber started his research journey at the same time as me and we even defended three weeks apart (I win!). Thank you, Tom, for being a great lab-mate and an even better friend. From driving across the country chasing balloons to lamenting about writing our dissertations simultaneously, you have been such a stable part of my life, and I am sad to see this chapter close. But, hey, we're both dead now! For those lab-mates who have joined since – Austen Thomas, Nate Allwine, David Sirbescu-Stanley, Grace Klang, Logan Alvesteffer, Ayla Adams – thanks for listening to my random plasma physics rambles and joining me for tacos at Condados. Nate – thank you, especially, for all the coffee runs and lunch runs that made the 13 hour research days

manageable. Good luck to you all in ALPE! I look forward to seeing your name up on the WMU flag! I want to especially thank Hannah Watts, who was far more than an ALPE lab-mate. We were friends before COVID, but once we were secluded indoors, our friendship really grew. As COVID buddies, we watched Molecular Gas Dynamics lectures, watched rocket launches, and bonded over crafting and video games. Our to-this-day weekly stitching/spilling-of-the-tea calls keep me sane. You have been such a supportive friend throughout this journey, and I wouldn't trade our friendship for anything. Thank you from the bottom of my heart-of-hearts.

I must thank my family for supporting this crazy graduate studies career I chose. Thank you, Dad, for always being available for my anxiety-filled calls – as long as they are before 9pm – and calming me down enough to get through whatever nonsense I was worrying about. Thank you to my Mom, whom I think of all the time while I've been writing by keeping her quilts close. Thank you to my siblings – Rachael and Andrew – for maybe not understanding my work but understanding me. Thank you, Jen, for making me feel like one of your own and welcoming me and the rest of the (very loud) Mooney family into your life.

Finally, I want to thank my family. Scott, the animals (Pavel, Simba, and Reginald), and our little baby girl on the way. Scott, thank you for always making sure I and the animals are fed and watered, especially in these last few months as I write well into the night. I would be living off ramen and Gatorade if it weren't for you. I could not have asked for a better life-long partner. Thank you for spending time on long road trips across the country so I could make pretty plasma in LA. I will cherish those memories forever.

This Ph.D. is shared amongst those who carried the burden of shaping this book.

Margaret Mary Mooney, 2025

TABLE OF CONTENTS

Table of Contents – Continued

Table of Contents – Continued

LIST OF TABLES

List of Tables - Continued

LIST OF FIGURES

List of Figures – Continued

List of Figures – Continued

CHAPTER 1

Introduction

"Exploration is in our nature. We began as wanderers, and we are wanderers still. We have lingered long enough on the shores of the cosmic ocean. We are ready at last to set sail for the stars."

Carl Segan, Cosmos

1.1 Human Occupation of Space

For over two decades, the International Space Station (ISS) has maintained uninterrupted human occupation in space, which has enabled groundbreaking research in various fields, including biology, chemistry, material science, and human physiology. Building upon this heritage, the next generation space station comes in the form of the NASA Gateway program [1], [2]. This outpost will live in a Near Rectilinear Halo Orbit (NRHO) around the moon, supporting further research in microgravity environments and allowing easy access to the lunar surface. A key feature of the Gateway is the power and propulsion element (PPE), which will provide orbital corrections and changes to the spacecraft's trajectory.

NASA has selected high-power electric propulsion (EP) devices to drive the PPE. The appeal of EP devices lies in their high fuel efficiency, often an order of magnitude greater than traditional chemical propulsive systems, which establishes EP systems as a pivotal technology for human exploration and long-term habitation in space. Among the

many EP device options, Hall effect thrusters (HETs) and gridded ion engines (GIEs) stand out with significant flight heritage and high Technology Readiness Levels (TRLs), a NASA metric signifying the maturity of a technology. A GIE was the first EP device to demonstrate deep space exploration onboard the Deep Space 1 mission launched in 1998 which visited the asteroid 9660 Braille and the comet Borrelly [3]. Following the success of Deep Space 1, the Dawn spacecraft was launched in 2007 led by NASA JPL which visited the asteroid Vesta and the dwarf planet Ceres [4]. In recent years, HETs have become the preferred EP device due to their higher thrust-to-power ratio, relative simplicity, and ease of scalability when compared with GIEs. Government and private industries are significantly investing in HET technology for various applications, from deep space missions like NASA Psyche, which will travel to the asteroid belt to investigate metal planetary cores [5], to near-Earth orbits, such as SpaceX's Starlink constellations, which aims to provide reliable global internet coverage [6]. Further, since 2022, the Federal Communications Commission (FCC) has mandated a five-year deorbiting timeframe for any new satellite launched, in part due to the proliferation of constellation networks [7]. In this context, the high efficiency of EP devices makes them highly desirable for satellites as they allow for greater allocation of spacecraft mass to mission payloads rather than to the propulsion system.

The Gateway PPE is a 60 kW array of HETs. Three 12-kW HETs developed by NASA and four BHT-6000 6-kW HETs developed by Busek combined make up the Advanced Electric Propulsion System (AEPS). The 12-kW thrusters were developed by NASA initially as the Hall Effect Rocket with Magnetic Shielding (HERMeS). The thrusters of the AEPS are required to operate for a minimum of 15 years [8]. As such, long-term reliability is a necessity, as on-orbit servicing will be costly and complex. Extensive qualification testing is required to ensure the thrusters meet this standard of reliability. However, the extended mission times make full-range life testing of these thrusters impractical. Conducting lifetime testing of long mission times lasting several

years is not only time-consuming but also demands exclusive use of vacuum chambers, dedicated personnel, and significant costs in terms of propellant and power to operate the thruster for these extended periods. Models can bridge the gap between timely qualification tests and understanding the thruster's long-term performance and erosion characteristics. However, achieving a high-fidelity model that accurately captures the complex instabilities and long-term erosion characteristics has been an ongoing challenge. Significant improvements in HET technology, such as magnetic shielding, which will be discussed in Chapter 2, have extended the lifetime of these devices. Yet, the enhanced energetic ion production due to plasma turbulence leading to erosion on thruster faces is still debated in the literature [9], [10], [11], [12], [13], [14], [15], [16], [17], [18], [19].

1.2 Research Objectives

The hollow cathode is a critical HET component and undergoes extensive lifetime testing in addition to the lifetime testing of the full HET. Significant density gradients, non-Maxwellian electron behavior, and magnetic fields sufficiently strong enough to magnetize electrons in hollow cathode plumes create favorable conditions for the formation of plasma instabilities, which have an impact on cathode lifetime [11], [12], [20], [21], [22], [23], [24], [25], [26]. Cathode qualification testing is typically conducted independently and encompasses a downstream cylindrical anode and a magnetic field simulator that mimics the HET environment [10], [27]. In this configuration, the lone cathode is operated at a fixed DC discharge current; however, in the HET, the discharge current can oscillate with magnitudes on the order of the full DC current. It is necessary to operate lone cathode experiments in environments that best match the conditions the cathode experiences in the full thruster. It remains unclear which variables, such as a closely matched magnetic field topography, similar background pressure, or induced oscillations, need to be consistent between lone cathode experiments and HET testing such that the cathode plume turbulence within a lone cathode best matches the HET operation. In this context, this work aims to define the turbulent wave growth in the independently operated hollow

cathode plume and how this space is comparable to the full thruster geometry. This work consisted of operating flight-like hollow cathodes independently while adjusting external parameters such as background pressure, anode configuration, magnetic field strength, and induced oscillations on the anode. Specifically, this research contributed the following to the field:

1. **Onset of large-scale oscillations in the partially magnetized cathode plume.** This effort utilized the HERMeS hollow cathode and a magnetic field simulator that closely matches the thruster magnetic field topography to investigate the onset of the rotational modes in the cathode plume as a function of increasing magnetic field strength.
2. **Spatial instability mapping of the turbulent and dynamic behavior of the HERMeS cathode operated independently of the HET.** A comprehensive spatial investigation of the waves in the cathode plume was performed. This dissertation investigated the high-frequency turbulence and the large-scale ion oscillations near the cathode exit. Variations in the independent cathode operation included:
    a. Induced anode oscillations to mimic the AC characteristics of the HERMeS HET discharge.
    b. Adjustment of the testing facility pressure during operation using additional cryogenic vacuum pumps.
    c. Mass flow rate to the cathode.
    d. Adjusted magnetic field strength.

    To investigate this wave space, this dissertation utilized the following diagnostics:
    a. High-speed monitoring of cathode components, such as floating keeper voltage, discharge voltage, and discharge current.
    b. An axially injected wave probe consisting of high-speed ion saturation probes utilizing the fixed-separation pair method to capture spatial wave dispersions.

c. Optical emission spectroscopy to get estimated electron temperatures.

This work was performed with the HERMeS cathode, a magnetic field simulator that generates a magnetic field topography similar to the HERMeS thruster, and downstream cylindrical anode at the NASA Jet Propulsion Laboratory (JPL). These data are directly compared to the near-cathode high-speed testing of the HERMeS thruster.

3. **Cathode performance and instabilities on alternative noble gas propellants with HET-like magnetic fields.** This effort utilized the LaB_6 cathode developed for the H6 thruster.
    a. The H6 thruster was developed through a collaboration between the Air Force Research Laboratory, NASA Jet Propulsion Laboratory (JPL), and the University of Michigan (UM) [4], [10], [28], [29], [30].

1.3 Organization

This dissertation explores the range of instabilities measured in the cathode plume while operated inside the HET environment. **Chapter 2** discusses the background of EP devices and HET operation. The chapter also provides the necessary background in plasma physics to describe electron and ion trajectories and waves in plasmas. This chapter also outlines the history of cathode-driven instabilities as reported in the literature on independent cathode configurations and full thruster experiments. **Chapter 3** discusses the experimental methods used in this work to investigate these instabilities including the probe designs and configurations. **Chapter 4** presents the initial proof of concept for these experimental methods and introduces the large-scale azimuthal wave characteristics. **Chapter 5** discusses the wave energy growth and propagation during independent cathode operation, examining the effects of induced oscillations to the DC cathode discharge and the impact of varying background pressure on downstream turbulence. This chapter also offers a comparison of the cathode plume when operated in the HET environment verses independently using the oscillations measured on full thruster and independent cathode

surfaces and downstream plume measurements to investigate the downstream turbulence. **Chapter 6** explores how varying the neutral species influences the independent cathode configuration's plasma wave behavior, particularly the large-scale oscillations induced by the HET magnetic field. The waves in the ion population are presented and paired with optical emission spectroscopy measurements. Finally, **Chapter 7** provides a comprehensive summary with final remarks and potential areas of further research.

CHAPTER 2

Background

"Learn all there is to learn and then choose your own path."

George Frederic Handel

2.1 Overview of Electric Propulsion Systems

Since the launch of the Soviet satellite Sputnik in 1957, the number of satellites sent into space has grown exponentially, with a 2300% increase between 2011 and 2020 alone [31]. Presently, 10,345 functional satellites are in orbit as of August 2024 [32]. EP device for spacecraft attitude control began with the Russian Zond-2 satellite, which used pulsed plasma thrusters (PPTs). Since then, EP devices has been prolific onboard satellites for station keeping, drag compensation, and orbital corrections, with GIEs, HETs, and arcjets as the primary technologies used [4]. While governmental space agencies primarily performed the initial development of HETs, as the TRL of HETs increased, they have become more attractive for commercial development. Today, companies such as Busek Inc., SpaceX, Orbion Space Technology Inc., and Exoterra Resources have demonstrated power capabilities of HETs from 100 W to 20 kW [33], [34], [35], [36]. In fact, two-thirds of the satellites in orbit as of August 2024 belong to SpaceX's Starlink constellation, each of which utilizes HETs for station keeping, orbital maneuvering, and deorbiting [32]. This significant growth underscores SEP as the future of space travel as it allows more spacecraft mass to be allocated to useful payloads for the spacecraft.

Chemical propulsion systems utilize a chemical reaction in a controlled explosion to generate thrust. Dual-propellant chemical rocket propulsion can be fundamentally described as the mixing of two reactive substances to generate an explosive reaction, which is directed to and accelerated through a nozzle. Meanwhile, single-propellant chemical propulsion systems use a propellant, such as hydrazine, with a catalytic bed to generate the explosion. The efficiency of the chemical propulsion process is entirely dependent upon the energy stored within the bonds of the propellant. Alternatively, EP devices decouples the generation of thrust from chemical reactions. Jahn defines EP as "The acceleration of gases for propulsion by electrical heating and/or by electric and magnetic body forces [37]." The nature in which the applied electrical or magnetic power inputs energy into the propellant defines the type of EP thruster. Generally, EP devices can be divided into three categories depending on the mode of acceleration:

1. **Electrothermal**. The propellant is heated electrically and thermally accelerated through a nozzle. Common versions of these thrusters include the resistojet, the arcjet, and RF heating.
2. **Electrostatic**. Ions or non-neutral atoms/molecules are accelerated through the direct application of electrostatic fields (Coulombic forces). Common versions of these devices include the gridded ion engine (GIE), the Hall effect thruster (HET), and the electrospray thruster.
3. **Electromagnetic**. Acceleration is achieved through internal and external magnetic and electric fields with driving currents in the stream. Examples of these devices include the pulsed plasma thruster and the magnetoplasmadynamic thruster.

2.1.1 The Case for Electric Propulsion

The fundamental advantage of EP devices begins with the rocket equation first derived by the Russian scientist Konstantin Tsiolkovsky in 1903. This simple derivation begins with the mathematical expression of Newton's second law of motion in the frame of spacecraft thrust:

$$T = m_{sc}\frac{\mathrm{d}v}{\mathrm{d}t} \tag{2.1}$$

Where T is the spacecraft thrust, m_{sc} is the spacecraft mass, and dv/dt is the incremental change in velocity of the spacecraft with respect to time. Newton's law of equal and opposite reaction shows that the thrust of the spacecraft can also be described as

$$T = -\frac{d}{dt}(m_p v_{ex}) = -v_{ex}\frac{\mathrm{d}m_p}{\mathrm{d}t} \tag{2.2}$$

where dm_p/dt is the propellant mass flow rate and v_{ex} is the exit velocity of the propellant. The propellant mass onboard the spacecraft is a function of time as the thruster depletes it, but the exit velocity of the propellant remains relatively constant. Since the total spacecraft mass also changes at the rate of the propellant flow rate, eq. (2.2) and eq. (2.1) can be combined to result in

$$m_{sc}\frac{dv}{dt} = -v_{ex}\frac{dm_{sc}}{dt} \quad . \tag{2.3}$$

Simplifying, eq. (2.3) becomes

$$dv = -v_{ex}\frac{dm_{sc}}{m_{sc}}. \tag{2.4}$$

By integrating the left hand side of eq. (2.4) from the spacecraft initial velocity, v_i, to its final velocity, v_f, and the right hand side from its initial mass, m_i, to its final mass, m_f, the result is:

$$v_1 - v_2 = \Delta v = v_{ex}\, ln\left(\frac{m_i}{m_f}\right) \tag{2.5}$$

where m_f is the spacecraft dry mass, or the mass that arrives at the destination, which includes all payloads onboard the spacecraft including rovers, scientific hardware, astronauts, etc., and Δv is the total change in velocity of the spacecraft that is needed to reach its destination. Rearranging (2.5), we arrive at the rocket equation:

$$\frac{m_f}{m_i} = \frac{m_f}{m_p + m_f} = exp\left(-\frac{\Delta v}{v_{ex}}\right) \tag{2.6}$$

where the ratio m_f/m_i is commonly referred to as the payload fraction and m_p is the mass of the propellant. Δv is an important metric for mission planning and can essentially be

considered as the currency for space travel. For example, a transfer from Earth's surface to orbit is a Δv of about 12 km/s and an orbital transfer from Earth's orbit to an orbit around Jupiter and back is a Δv of about 64 km/s [37]. In order to maximize the payload fraction for a fixed Δv mission, the propellant exhaust velocity must be maximized.

Specific impulse is another critical mission metric used for space travel planning. It is quantified by the total impulse over the propellant consumption of the spacecraft, and it is often used as a proxy for propulsive efficiency. Combing the definition of specific impulse with equation (2.2), we have:

$$I_{sp} = \frac{T}{\dot{m}_p g} = \frac{v_{ex}\dot{m}_p}{\dot{m}_p g} = \frac{v_{ex}}{g} \tag{2.7}$$

where g is the gravitational constant. The resultant unit of I_{sp} is seconds, which provides an indication of how effectively the thruster uses the propellant to generate thrust. Since chemical propulsion systems are limited by the energy stored within the bonds of the propellant, the maximum exhaust velocities achievable are around 5 km/s, or an I_{sp} of 500 s [38]. As such, chemical propulsion systems are not well suited for deep space travel (large Δv missions) or extended orbital habitation since a large fraction of the spacecraft mass would need to be dedicated to the propellant.

Alternatively, the ions generated in EP thrusters can provide significantly high exhaust velocities. These accelerated ions are governed by the conservation of energy equation, which for electrostatic EP devices is defined as:

$$\frac{1}{2} M_i v_{ex}^2 = q\,\Phi \tag{2.8}$$

where Φ is the applied voltage to the EP system, q is the charge of an electron, and M_i is the ion particle mass. EP systems can theoretically achieve exhaust velocities up to 100 km/s, with most HETs operating around 10-40 km/s [38], [39]. Even low powered EP systems can produce significant exhaust velocities. For example, let's consider the Western Hall Thruster (WHT-44) developed at Western Michigan University. The WHT-44

nominally operates at a xenon discharge voltage of 170 V, which will produce ion velocities of approximately 15 km/s, for an I_{sp} of about 1,500 s [40].

The raison d'être of EP thrusters is their high propellant utilization; however, the price for this benefit is the power required to operate them. The input power of an EP thruster can be expressed as:

$$P_{in} = \frac{T_{SEP} v_{ex}}{2\eta_e} \tag{2.9}$$

where T_{SEP} is the thrust and η_e is the thruster efficiency. For example, the WHT-44 operated at 170 V with a discharge of 1.4 A (240 W) and an estimated efficiency of 50% would result in a thrust of 12 mN. In contrast, the SpaceX Merlin engines use RP-1 and LOX to generate 845 kN of thrust, per engine, with exit velocities around 3.5 km/s ($I_{sp} \cong$ 350 s). The Falcon Heavy houses 27 Merlin engines in its first stage for a cumulative thrust of 22,819 kN [41]. For an HET with an overall efficiency of 50% and ion exhaust velocities of 20 km/s to match the thrust of a single Merlin engine, the HET would need to be supplied with an electrical power input of 17 GW, or 456 GW to match the Falcon Heavy. For reference, the entirety of New York City uses 10 GW on a hot summer day with American levels of air conditioning [42].

Rocket science is often exaggerated in its complexity; the fundamental principles, as defined above, are relatively straightforward. The difficulty in EP-powered space exploration lies in rocket engineering, plasma physics, and the design of complex thrusters. The following sections will explore some of those challenges.

2.1.2 Necessary Plasma Physics for the Electric Propulsion Engineer

To fully appreciate the beauty of the EP thrusters, one must first understand the plasma physics that drive them. Plasma is generated when a gas is given enough energy to strip one or more electrons from its atoms. This process yields an ionized gas containing a mixture of free electrons and ions. To be considered a plasma, the ionized mixture must satisfy three fundamental criteria, as defined below.

The first plasma criterion is that the ionized gas must be quasi-neutral (i.e. $n_i \cong n_e$). This assumption of quasineutrality is valid when the characteristic length scale of the plasma far exceeds the Debye length, $l_p >> \lambda_D$, where the Debye length is defined as the length in which charges are shielded [43]. Mathematically, this is represented as

$$\lambda_D = \sqrt{\frac{\epsilon_0 T_e}{q n_e}} \ll l_p \tag{2.10}$$

where ϵ_0 is the permittivity of free space, T_e is the electron temperature in eV, and q is the charge of an electron in Coulombs. The second plasma criterion is that the plasma behaves collectively. For this to be true, the number of particles within a Debye sphere, N_D, must be large:

$$N_D = n^{4/3} \pi \lambda_D^3 \gg 1 \tag{2.11}$$

where n is the plasma species density. The third plasma criterion is that the frequency of collisions between ions and electrons with neutrals must be low. This collision frequency is described as

$$\nu = n \sigma \langle v \rangle \tag{2.12}$$

where σ is the cross section of the collision and $\langle v \rangle$ is the average velocity for all particles. The collective behavior of plasmas make them susceptible to manipulation by the magnetic and electric fields in EP devices. The following sections will dive into this collective nature of plasmas in greater detail.

2.1.2.1 Plasma Dynamics

Maxwell's equations and the Lorentz equation serve as the basis for describing particle motion in plasmas. If the ion and electron particle positions are known in the plasma, the electric and magnetic fields can be evaluated using Maxwell's equations:

$$\nabla \cdot \vec{B} = 0 \tag{2.13}$$

$$\nabla \times \vec{E} = -\frac{\partial \vec{B}}{\partial t} \tag{2.14}$$

$$\nabla \times \vec{B} = \mu_0 \left(\vec{j} + \epsilon_0 \frac{\partial \vec{E}}{\partial t} \right) \tag{2.15}$$

$$\nabla \cdot \vec{E} = \frac{\rho}{\epsilon_0} \tag{2.16}$$

where $\vec{B}$ and $\vec{E}$ are the magnetic and electric field vectors, respectively, μ_0 is the vacuum permeability constant, ρ is the charge density, and $\vec{j}$ is the current density. If the electric and magnetic fields are known, the Lorentz force equation can be used to determine the particle's trajectory. The Lorentz force equation is given by

$$F = m \frac{\mathrm{d}\vec{u}}{\mathrm{d}t} = q \left(\vec{E} + \vec{u} \times \vec{B} \right). \tag{2.17}$$

where q is the charge of an electron, m is the species mass, and $\vec{u}$ is the species velocity vector. In a simple plasma environment with no applied electric field and a constant magnetic field, the Lorentz force equation shows the circular motion of a particle about the field lines. The frequency of this motion is known as the cyclotron frequency, which is defined as

$$\omega_{i,e} = \frac{qB}{m_{i,e}} \tag{2.18}$$

where B is the magnetic field strength and the subscripts i and e denote the ion and electron populations, respectively. The radius of the particle's circular motion about a magnetic field line, known as the Larmor radius, is derived from the centripetal motion of the particle. The Larmor radius is mathematically defined as

$$r_{L_{i,e}} = \frac{m_{i,e} u_{\perp,\,(i,e)}}{qB} = \frac{u_{\perp,(i,e)}}{\omega_{i,e}} \tag{2.19}$$

where $u_\perp$ is the perpendicular velocity of the charged particle with respect to the magnetic field. In a plasma with a Maxwellian electron velocity distribution, the electron Larmor radius can simplify to

$$r_{L,e} = \frac{1}{B} \sqrt{\frac{8}{\pi} \frac{m_e}{q} T_{eV}} \, . \tag{2.20}$$

However, the perpendicular velocity for the ions can vary widely. At the exit plane of the HET, the ion velocity is the exhaust velocity. The Larmor radius in this region is then described as

$$r_{L,i} = \frac{1}{B}\sqrt{\frac{2m_i}{q}\,V_b}\ . \tag{2.21}$$

Depending on the forces acting on the plasma, the Lorentz force and Maxwell's equations can describe different forms of particle drifts. For instance, the motion of a charged particle in constant electric and magnetic fields results in the $E\ X\ B$ drift, given by

$$\vec{u}_{E\times B} = \frac{\vec{E}\times\vec{B}}{B^2}\ . \tag{2.22}$$

There are many other forms of particle drifts in plasmas that can occur depending on the nature of the applied forces on the plasma. Refer to [43], [44] for detailed derivations of the various particle drifts.

2.1.2.2 Collisions in Solar Electric Propulsion Devices

The electron, ion, and neutral populations in plasmas of EP devices experience various forms of collisions, including Coulombic collisions, electron-neutral collisions, ion-neutral collisions, and charge exchange collisions (CEX). Coulombic collisions, commonly referred to as classical collisions, are perfectly elastic collisions between the ion and electron populations. For example, the frequency of an elastic collision where electrons impact the ions can be expressed as

$$\nu_{ei} \approx 2.9\times10^{-12}\,\frac{n_e \ln(\lambda)}{T_e^{3/2}} \tag{2.23}$$

where n_e is the electron number density and $\ln(\lambda)$ is the Coulomb logarithm, which is often approximated as 10 for laboratory plasmas [44]. The electron-electron Coulombic collision frequency, ν_{ee}, occurs at generally the same rate as ν_{ei}. Other elastic collisions, such as ion-electron, ν_{ei}, and ion-ion, ν_{ii}, also exist in the plasmas in EP devices, though they occur over longer time scales when compared to electron-ion collisions due to the

relatively large mass of the ions. The collision frequency relationship for classical collisions is described as

$$\nu_{ie} \ll \nu_{ii} \ll \nu_{ei} \sim \nu_{ee}. \tag{2.24}$$

Inelastic collisions between electrons and neutrals can lead to the ionization or excitation of neutral particles. The collision frequency of electrons impacting a neutral particle is described as

$$\nu_{\mathrm{en}} = 6.6\times10^{-19}\left[\frac{\frac{T_e}{4}\text{-}0.1}{1+\left(\frac{T_e}{4}\right)^{1.6}}\right] n_n \sqrt{\frac{8\,T_e}{\pi m_e}}\ . \tag{2.25}$$

where n_n is the neutral density in the partially ionized plasma. Electrons colliding with ions or neutrals lead to an increase of plasma resistivity defined as

$$\eta = \frac{\mathrm{m_e}(\nu_{\mathrm{ei}}+\nu_{\mathrm{en}})}{q^2 n_e}\ . \tag{2.26}$$

The rise in the resistivity leads to increased ohmic heating of the plasma as a result of heat dissipation from the energy transferred during the collisions between electrons and ions and/or neutrals. This can lead to efficiency losses in HETs and exacerbate various instabilities as the temperature difference between the ion and electron populations grow.

Charge exchange collisions (CEX) occurs when a fast-moving ion impacts a neutral particle, and an electron is exchanged. The result is a high-energy neutral and a slow moving ion shown as

$$\mathrm{Xe^+ + Xe^0 \rightarrow Xe^0 + Xe^+}. \tag{2.27}$$

In the HET plume, the newly generated ion travels at a fraction of the speed of beam ions and may not be parallel to the thruster axis. As such, an increased rate of CEX in the HET plume can result in thruster efficiency losses [45]. However, in the hollow cathode, CEX ions aid in the heating of the cathode surface and reduce the velocity of the ions impacting the emitter surface. These mechanism is explored in depth in section 2.3.

2.1.2.3 Waves in Plasmas

The propagation of oscillations in a plasma is often described by a sinusoidal behavior. For example, a sinusoidal oscillation in the density can be described as

$$n = \overline{n} \exp\left(i\left(\vec{k}\cdot\vec{r} - \omega t\right)\right) \tag{2.28}$$

where $\overline{n}$ is the average density, $\vec{k}$ is the wave vector, $\vec{r}$ is the direction of the unit vector, and ω is the frequency of the oscillation. Manipulation and linearization of the Lorentz force equation (eq. (2.17)) and Maxwell's equations (eq. (2.13)-(2.16)) result in the dispersion relation for various oscillations, which depend on the forces acting on the plasma. The dispersion relation mathematically describes the relationship between the frequency of the wave and the wavevector [46]. Let's consider a simple condition in which all plasma criteria are met, there is no applied magnetic field, there is no thermal motion of the particles, the plasma is initially at rest, and there exists only election motion in the $\hat{x}$ direction. The Lorentz equations gives

$$m n_e \left[\frac{\partial \vec{u}_e}{\partial t} + (\vec{u}_e \cdot \nabla)\vec{u}_e\right] = -q n_e \vec{E}. \tag{2.29}$$

The continuity equation, which dictates the conservation of particle number within the plasma, can be expressed as

$$\frac{\partial n_e}{\partial t} + \nabla \cdot (n_e \vec{u}_e) = 0. \tag{2.30}$$

The last equation needed is Poisson's equation (Maxwell's eq. (2.16)),

$$\nabla \cdot \vec{E} = \frac{\partial \vec{E}}{\partial x} = \frac{\rho}{\epsilon_0} = \frac{-q n_e}{\epsilon_0} \ . \tag{2.31}$$

By linearizing eq's (2.29), (2.30), and (2.31), we arrive at the following system of equations:

$$\begin{cases} m\left[\dfrac{\partial \vec{u}_{e,1}}{\partial t}\right] = -q\overrightarrow{E_1} \\ \dfrac{\partial n_{e,1}}{\partial t} + n_{e,0}\nabla\cdot\left(\vec{u}_{e,1}\right) = 0 \\ \epsilon_0 \dfrac{\partial \vec{E}}{\partial x} = -qn_{e,1} \end{cases} \tag{2.32}$$

where the subscript 0 indicates the equilibrium state and the subscript 1 indicates the perturbation. Introducing the sinusoidal treatment of perturbation as described in eq. (2.28), while noting the plasma criterion of quasineutrality ($n_e \approx n_i$), the system of equations in eq. (2.32) becomes

$$\begin{cases} -im\omega u_1 = -q\overrightarrow{E_1} \\ -i\omega \mathrm{n}_1 = -n_0 i k_x u_1 \\ i k_x \epsilon_0 E_1 = -qn_1 \end{cases} \tag{2.33}$$

where k_x is the wavevector in the $\hat{\mathrm{x}}$ direction. Solving this set of equations results in the dispersion relation for the wave:

$$\omega = \left[\frac{qn_0}{\epsilon_0 m}\right]^{1/2}. \tag{2.34}$$

This equation is also known as the fundamental plasma frequency, ω_p, where n_0 and m become $n_{e,\mathrm{i}}$ and $m_{e,i}$ for electrons and ions, respectively. The wavevector, $\vec{k}$, does not appear in eq. (2.34), meaning the plasma frequency is a global oscillation in the plasma describing the particle's oscillation about equilibrium. Waves that propagate due to additional external forces or time-varying fields that require the use of more of Maxwell's equations often leads to a direction of propagation. The system of equations may also become non-linear.

2.2 The Hall Effect Thruster

Figure 2.1 shows the four primary components of the HET: the magnetic coils, which instigate a radial magnetic field; the channel, which contains the discharge zone where the ionization and acceleration of ions occur; and the anode base plate and hollow cathode, which combined establish the axial electric field.

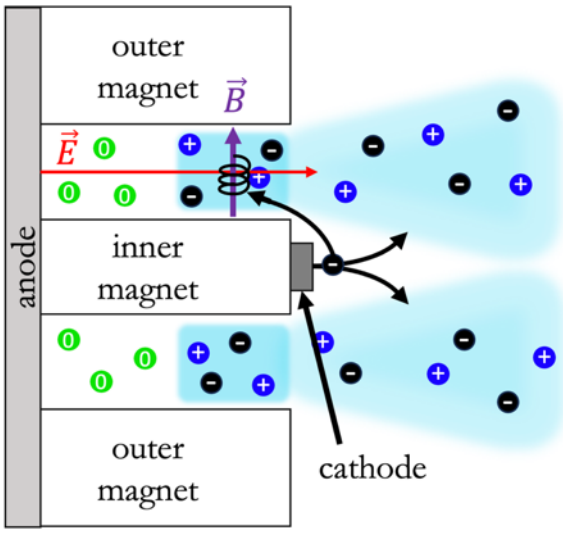

Figure 2.1: Cross section of Hall effect thruster with centrally mounted cathode.

Hollow cathodes in the HET perform two functions: ignition of the plasma generated in the channel and neutralization of the HET plume to prevent spacecraft charging. The electrons that neutralize the plume through recombination process couple to the beam. The location at which the electrons couple to the beam is called the "effective anode." The electrons generated by the cathode are primarily attracted to the positively charged anode upstream at the base of the channel. Along their path to the anode, they get trapped orbiting around the magnetic field lines within the channel of the thruster. The electric field generated between the anode and the cathode electrons and the radial magnetic field from the magnets establish an $\vec{E}X\vec{B}$ drift of electrons in the azimuthal direction. Since the electric and magnetic fields are perpendicular to each other, the $\vec{E}X\vec{B}$ drift equation (eq. (2.22)) becomes

$$u_{EXB} = \frac{E_z}{B_r} \tag{2.35}$$

where E_z is the axial electric field and B_r is the radial magnetic field. Integrating the particle drift over the acceleration region in the channel results in the Hall current,

$$I_H \approx n_e q w \frac{V_d}{B} \tag{2.36}$$

where w is the plasma width (generally the same as the channel width) and the electric field is approximated as the discharge voltage divided by the characteristic length of the acceleration region. Once the electrons have populated the channel, the propellant, commonly an inert gas such as xenon or krypton, is injected through the anode and diffuses down the length of the channel. Collisions between the neutral particles and the electrons begin an ionization cascade igniting the plasma. The axial electric field energizes the ions which are then ejected from the thruster at speeds typically greater than 10 km/s. Since the static electric field accelerates the ions in an HET, HETs are considered electrostatic devices despite the presence of the magnetic field. The ions in the downstream plume are neutralized by some of the electrons ejected from the cathode such that the downstream plume maintains quasineutrality.

While the hot electrons are circulating the channel confined by the magnetic field and colliding with neutrals to generate ions, some electrons are cooled through collisional processes and turbulent mechanisms and eventually fall to the anode surface. When only accounting for classical collisional processes, the perpendicular resistivity of an electron in a magnetic field, $\eta_\perp$, can be represented by

$$\eta_\perp = \frac{m_e(\nu_{ei}+\nu_{en})}{q^2 n_e}\left(1+\Omega^2\right). \tag{2.37}$$

where Ω is the Hall parameter. However, the measured current collected at the anode during experiments is higher than predicted through classical collisional processes. As such, fewer electrons than predicted are circulating the channel in the Hall current, reducing the thruster efficiency. This phenomenon is known as anomalous electron transport, and the understanding and modeling of this process remains a heavily researched topic [16], [20], [29], [47], [48], [49].

2.2.1 Advent of Magnetic Shielding Technology

In traditional HETs, erosion along the channel is the primary source of wear in the thruster. This is due to energetic ions bombarding the channel surfaces due to the shape

of the magnetic field lines. Magnetic shielding technology nearly eliminates this form of erosion in HETs [11], [12], [50], [51], [52]. In magnetically shielded HETs, the magnetic field line trajectories are modified to prevent the plasma from bombarding the channel. This technique leverages the isothermality and equipotentialization of force along magnetic field lines, which results in perpendicular electric fields directing ions away from the channel [53], [54]. This technique was originally applied to the H6 Hall thruster, with the shielded version entitled the H6MS and the original renamed the H6US [51], [54]. The H6MS was retrofitted from the H6 to be magnetically shielded, which resulted in complications such as saturation of the magnetic field. Following the success of the H6MS, the development of a higher-power magnetically shielded HET began with the HERMeS thruster. The AEPS program initially developed three Technology Demonstration Units (TDU-1,2, and 3) of the HERMeS thruster that have all undergone extensive testing since the initial development in 2013 [14], [15], [55], [56], [57], [58], [59].

While the main erosion mechanism is mitigated through magnetic shielding, new erosion patterns at longer time scales have been observed on the inner front pole cover, which protects the north pole of the HET, and the outer front pole, which protects the south pole of the HET [15], [16], [55]. The growth of this erosion rate is not yet fully understood. Some have suggested that CEX ions from the beam and energetic ions from turbulent plasma dynamics from the centrally mounted hollow cathode plume are the source of this erosion [60]. Further discussion on the generation of energetic ions from the cathode is discussed in section 2.3.4.

2.2.2 Historically Used Propellants

The ideal EP device propellant has a low first ionization energy (the energy require to remove an electron from the atom), is easily storable, and is non-corrosive to prevent damage to the spacecraft components and spacecraft surfaces. While higher mass propellants result in higher thrust, the I_{sp} of the thruster is inversely related to the ion mass. For an HET, this is demonstrated by substituting the exhaust velocity found in eq

(2.8) into the equation for I_{sp} (eq. (2.7)), while accounting for efficiency losses. The result is the specific impulse of an HET:

$$I_{sp} = \frac{\gamma \eta_{\mathrm{m}}}{g} \sqrt{\frac{2qV_b}{m_i}} \tag{2.38}$$

where γ is a correction factor to account for beam divergence and η_{m} is the thruster mass utilization efficiency defined as

$$\eta_{\mathrm{m}} = \frac{I_b}{q} \frac{M_i}{\dot{m}_p}. \tag{2.39}$$

Early forms of electric propulsion devices used mercury or cesium because of their relatively high atomic mass – 200.59 amu for mercury and 132.9 amu for cesium – and low first ionization energies – 10.44 eV for mercury and 3.99 eV for cesium. However, these propellants are corrosive which makes them difficult to store and can cause damage to the thruster and/or spacecraft [38]. For much of developmental history of HETs, xenon has been the primary choice of propellant because it is a non-reactive noble gas with a relatively low first ionization energy of 12.13 eV and relatively high atomic mass of 131 amu. While the properties of xenon align well with the advantages of EP devices, the cost of xenon has skyrocketed as it is often tied to the geopolitical climate due to where it is obtained. Xenon is sourced as a byproduct from steel production through a liquid cryogenic air separation in a process called fractional distillation. The majority of the world's infrastructure for xenon extraction is located at steel plants in Russia, Ukraine, and China. Steel manufacturing in China was reduced to diminish air pollution prior to the winter Olympics in 2022 and Russia's invasion of Ukraine in February of 2022 also significantly impacted many steel manufacturing plants in the region [61]. As a result, the price of xenon increased from \$20/L in 2020 to \$100/L in 2022 [62]. While prices have decreased to \$80/L in 2023, this volatility in cost suggests the sourcing of xenon is a significant complication for EP device design [63]. For reference, xenon was \$5/L in 2011 [64].

Recent efforts have been focused on operating HETs on alternative propellants. Among non-reactive noble gases, krypton and argon have been researched as propellant replacements [52], [62], [65], [66], [67], [68]. They have higher first ionization energies when compared to xenon – 14 eV for krypton and 15.76 eV for argon – and lower masses – 83.8 amu krypton and 39.9 amu for argon [69]. Further, since the channel length of HETs is dictated by the first ionization energy, HETs designed to operate on krypton and argon must be designed with longer and wider channels. The primary advantage of these propellants is the cost: \$0.80/L for krypton and <\$0.01/L for argon[63]. While krypton is sourced through the same process as xenon, and as a result, is tied to the global geopolitical climate, it is far more abundant in the atmosphere [62]. Argon is also obtained through fractional distillation but is even more abundant than krypton [70].

The more oscillatory behavior of HETs and hollow cathodes on alternative propellants remains an active area of research [23], [52], [62], [67], [71], [72]. HETs operated on argon have been known to be highly oscillatory, when compared to xenon or krypton [65]. Alternatively, HETs that use krypton show similar stability regimes and efficiencies to xenon, particularly at higher current density operations [62], [71]. Nonetheless, little data exist on the downstream high-speed plasma properties of HETs operated on these two alternative propellants.

2.3 The Hollow Cathode

Cathodes are a critical component for many EP thrusters as they provide the electrons to the plasma circuit. The earliest forms of cathodes used for EP devices was a tungsten filament [38], [73]. A current supplied to the filament raises the temperature of the material, the thermal energy of the electrons contained within the material increases, and electrons are released from the surface. This process is called thermionic emission, which can be mathematically described by the Richardson-Dushman equation:

$$J = DT^2 \exp\left(-\frac{q\phi_0}{k_B T}\right) \tag{2.40}$$

Where J is the emission current density, T is the temperature of the emission surface in Kelvin, D is an experimentally derived constant specific to the material, and ϕ_0 is the ideal work function in eV. The work function of the material is defined as the minimum amount of thermal work needed to extract an electron from the emission surface [38]. Materials with higher work functions require higher temperatures to begin the thermionic emission when compared to materials with lower work functions. Figure 2.2 shows the emission current density for the following common thermionic materials: tungsten impregnated with barium oxide (BaO-W), lanthanum hexaboride (LaB6), molybdenum (Mo), tantalum (Ta), and tungsten (W).

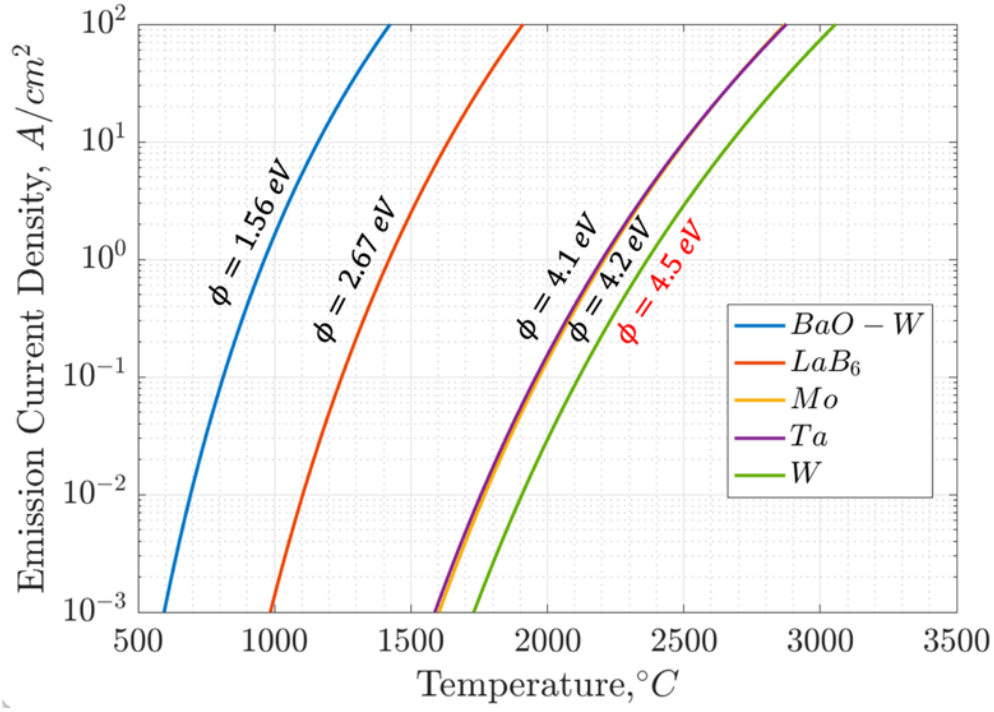

Figure 2.2: Emission current density verses temperature for various materials.

The rapid development in HETs and GIEs since the 1970s has resulted in higher current demands from the cathode. As such, tungsten emitters have become less desirable for the following reasons:

1) The high work function (~4.55 eV) requires high power demands from the spacecraft bus to heat the emitter surface. This is less power that can be allocated to the EP thruster itself reducing the overall efficiency of the EP system.
2) Tungsten is a brittle material, even at room temperature. The heat cycling the tungsten experiences during and after thruster operation can lead to the formation of crack structures eventually resulting in material failure [74].
3) Ion bombardment from the thruster plume causes evaporation of the tungsten from the emitter, limiting the lifetime to hundreds of hours.

The hollow cathode design solves many of the limitations of the tungsten filament. Figure 2.3 shows a cross-sectional view of the hollow cathode geometry. Generally, hollow cathodes are constructed of four elements: the cylindrical thermionic material, commonly referred to as the insert; the cathode tube, which retains the insert; a heating element, which raises the temperature of the emission surface; and a keeper electrode to extract the electron plasma from the cathode.

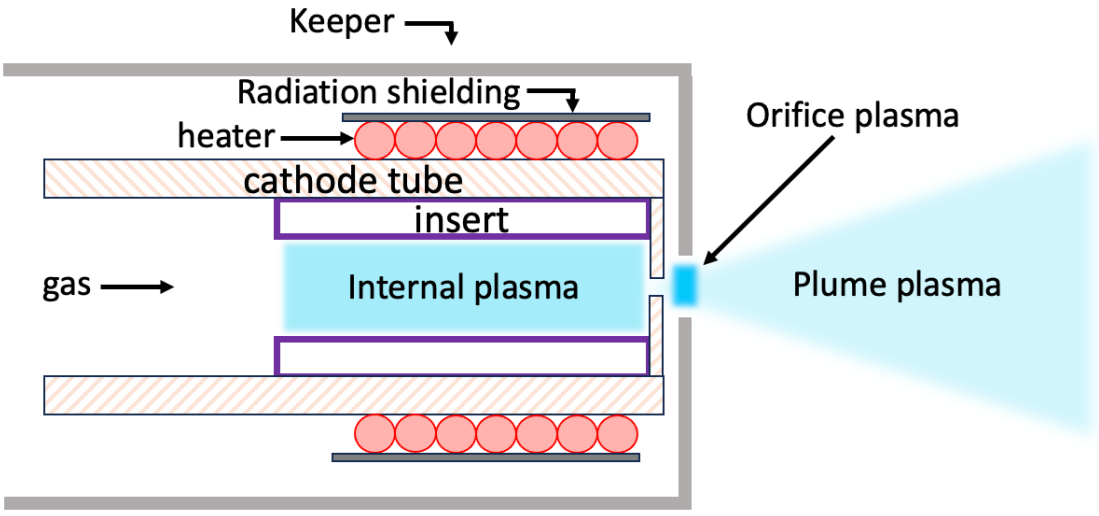

Figure 2.3: Cross section of the hollow cathode components.

As shown above in figure 2.3, the cathode plasma is often separated into three distinct regions:

Internal plasma: The plasma in this region is entirely contained within the tubular insert. The tubular geometry of the insert allows the emitted electrons to bounce around the inside of the tube increasing electron production through secondary electron emission, also known as the hollow cathode effect. This plasma is highly collisional with electron temperature typically less than 1 eV and small sheath voltages along the cathode surface. The low sheath voltages along the insert means the ions fall to the cathode surface at energies commonly less than 20 eV. Ion mobility to the insert surface is dictated by radial diffusion which is limited by the CEX in the insert plasma. The velocity of the ions to the insert surface is derived from the centerline density and the ambipolar diffusion coefficient resulting in:

$$u_r = \frac{2.4^2}{2R\sigma_{\mathrm{CEX}} n_0 v_{th,i}} \frac{e}{\mathrm{m_i}} (T_i + T_e) \tag{2.41}$$

where σ_{CEX} is the collisional cross section of the CEX and $v_{th,i}$ is the thermal velocity of the ions.

The cathode geometry can be manipulated to provide a self-heating emission surface by allowing the plasma within the region to maintain collisionality. Cathodes with small exit orifice diameters exhibit high pressures in the insert region, which increases the resistive heating from the current in the plasma. However, smaller orifice diameters often mean larger internal plasma gradients where the highest density is near the exit orifice. This can lead to non-uniform erosion along the insert [38], [75]. Alternatively, the plasma heating in cathodes with large orifice diameters results from larger sheath potential gradients near the insert. In this configuration, the insert is subjected to higher-energy ions impacting the insert surface as a result of the larger sheath potentials [38]. The high-energy neutrals from the CEX can also contribute to the heating of the insert surface.

Orifice plasma: This region acts as a bottleneck for the plasma resulting in the highest current density plasma contained within the orifice. This creates a particularly difficult engineering challenge as the high-current density can lead to erosion along the length of the orifice over time increasing the radius of the orifice. This can compromise the self-

heating mechanisms of the internal plasma. This degradation in the orifice can also reduce the lifetime of the cathode.

The current in this region can be calculated as:

$$I = n_e e u A_{or} \tag{2.42}$$

where u is the electron drift velocity and A_{or} is the cross-sectional area of the cathode orifice. Similar to the insert plasma, the plasma in this region is highly collisional, so the electron drift velocity can be approximated as the thermal speed of the electrons,

$$u_{th,e} = \sqrt{\frac{2k_B T_e}{m_e}} \tag{2.43}$$

where k_B is Boltzmann's constant.

Plume plasma: The downstream plume plasma transitions from a highly collisional, low temperature, Maxwellian plasma to a near-collisionless, diffuse plasma within a few cm. The plume plasma is often exposed to magnetic fields on the order of 100 G and above, depending on if it is operated within a GIE or an HET. The collisionless environment coupled with the external magnetic and electric fields in this region create favorable conditions for the formation of plasma instabilities and complex plasma dynamics. Section 2.3.4 discusses the instabilities measured in this region.

2.3.1 Common Insert Materials

The most commonly used insert materials in EP devices are BaO [56], [76] and LaB6 [21], [72], [77]. In BaO cathodes, the BaO is often combined with calcium oxide (CaO) and aluminum oxide (Al_2O_3), which is impregnated within a tungsten matrix. These cathodes provide some of the lowest work functions among cathode options, which can be as low as 1.56 eV. As the insert material is heated, the Ba and BaO contained within the matrix migrate to the surface of the emitter through complex chemical processes, which reduces the surface work function of the tungsten [78]. The impregnate resupplies the barium to the surface; however, over time, the impregnate can be depleted. The rate of depletion can also be nonuniform along the length of the emitter depending on the design of the

cathode [79]. Since BaO cathodes generate electrons through a chemical reaction, the surface of the material can also be poisoned when exposed to atmosphere, particularly while the emitter is warm. Contaminants, such as oxygen, water vapor, and other impurities in the air, can react with the barium layer on the cathode surface and effectively raise the work function of the material. Extensive conditioning consisting of heat cycling and a purge gas is often performed after initial installation inside the vacuum chamber before testing or when first operated in space to evacuate any contaminates embedded in the matrix. During this process, current is slowly applied to the heater enabling the evaporation of the contaminants within the emitter. The vacuum environment extracts the containments and a purge gas, typically the cathode propellant supplied at rate greater than the nominal flow rate, aids in the ejection of the impurities [80], [81].

Alternatively, LaB_6 cathodes are constructed by press sintering LaB_6 into rods which are then machined into a tube for the hollow cathode. The work function of LaB_6 is approximately 2.67 eV [82]. This is a higher work function when compared to BaO cathodes, but since there is no chemistry involved in the emission of the electrons, LaB_6 cathodes are not susceptible to the same poisoning effects. As such, conditioning of the cathode is not required prior to experimentation or operation in space. However, over extended use, the powdered LaB_6 material that is exposed to the plasma can erode limiting the life of the emitter [83]. Nonetheless, the lifetime of the LaB_6 emitters limited by LaB_6 sputtering is expected to exceed the lifetime of BaO depletion [38].

2.3.2 Ignition of Hollow Cathodes in Hall Effect Thrusters

Following any conditioning required of the insert, the cathode can be ignited. If the cathode is cold, the ignition process begins with heating the insert via the external heater. As the emission surface is heated, the electrons are emitted from the surface and a neutral species, typically a fraction of the thruster flow, is fed through the back to the cathode tube. A voltage is then applied between the cathode tube and the keeper electrode. High-energy electrons from the tail end of the Maxwellian distribution emitted from the insert

material collide with the injected neutrals generating the internal plasma. The cathode plasma then couples with an anode. The keeper electrode can be left on to aid in the extraction of the electrons or be left floating such that the keeper surface does not collect any current. In an HET, the cathode plasma couples with the upstream anode. When operated independent of the HET, the cathode plasma typically couples to a downstream anode. A review of independent cathode setups is given in Chapter 3.

The heating element is often a primary point of failure of the hollow cathode. As such, heaterless ignition of cathodes has been heavily researched in the past 20 years [84], [85], [86], [87], [88]. The plasma in a heaterless cathode is ignited through an arc discharge between the insert and the keeper electrode. According to Paschen's law, the breakdown voltage is minimized at a specific product of the distance between the cathode and keeper electrode and the propellant gas pressure [89]. The ignition process of heaterless cathodes typically involves a momentary burst of high-flow through the cathode tube while a potential is applied between the cathode and the keeper [90]. This ignition process can damage the surface of the cathode or keeper if ignition is attempted at low pressures or large separation distances between cathode and keeper [90]. Further, protective circuitry is often required to protect the power supplies from the arcing events [90]. Nonetheless, heaterless cathode ignition cycling has shown the cathodes can remain operational even after tens of thousands of ignitions [91]. This work uses exclusively heatered cathodes.

2.3.3 Configuration in the Hall Effect Thruster

Figure 2.4 shows the most common cathode configurations with the HET. For operation with the HET, the hollow cathode can be mounted external to the HET (figure 2.4(a)) or concentric with the magnets at the center of the thruster (figure 2.4(b)).

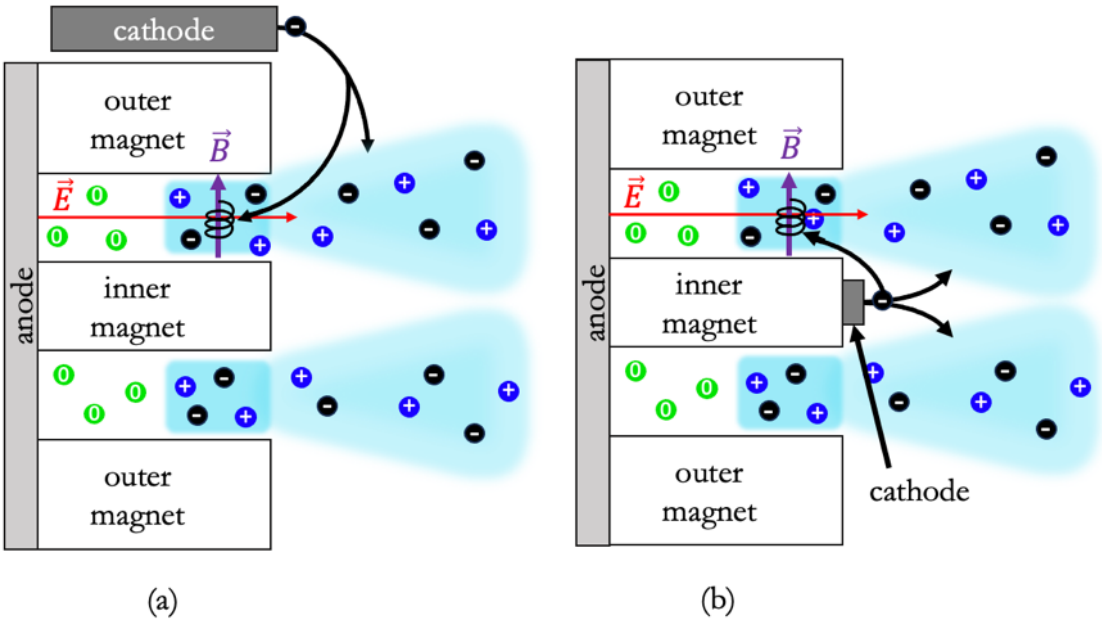

Figure 2.4: Cross section schematic of cathode orientations in the HET. (a) Centrally mounted cathode and (b) externally mounted cathode.

When mounted externally, the cathode discharge is placed within the magnetic field separatrix. This is the region where the magnetic field lines direct the electrons into the channel. The externally mounted design is beneficial because it allows for a secondary cathode to be installed for design redundancy; however, this configuration is also known to exhibit asymmetric exhaust plumes, which can lead to uneven wear on thruster components [92]. Additionally, externally mounted cathodes may contribute to increased beam divergence, where some of the ions ejected from the thruster do not travel parallel to the electric field. Poor beam divergence reduces the overall efficiency of the thruster as non-parallel ion flow results in reduced thrust [15,16]. Advancements in HET designs for higher power have congruently resulted in a growth in the size of the thruster. This provides more space inside the inner magnetic coil enabling the mounting of the cathode concentric to the thruster channel. The cathode discharge in centrally mounted configuration is along the thruster centerline. This orientation is known to produce a more symmetric plume and decrease thruster plume divergence [28]. Cathodes in this configuration are subjected to a magnetic mirror due to the shape of the magnetic field in

this location. The effect of this magnetic field topography is explored in the next section. Additionally, the steep density and potential gradients around the thruster centerline can result in large-scale oscillations in the cathode plasma. The formation of instabilities due to this configuration are explored in the next section.

2.3.4 Instabilities in Cathode Plumes

The downstream plume of the hollow cathode can be rich with plasma instabilities. These instabilities have the ability to generate energetic ions which can result in erosion of cathode and thruster faces. Erosion of thruster components has direct implications on the lifetime of the thruster; however, the current HET models do not accurately predict these erosion mechanisms, particularly in the region of the cathode plasma (on the inner front pole cover). This section explores the instabilities reported in literature that have been measured in cathode plumes both with and without an applied magnetic field.

2.3.4.1 Plume and Spot Modes

Hollow cathodes are known to operate under two distinctive modes: the stable spot mode and the oscillatory plume mode [59], [93]. Spot mode is visually characterized by a small region of high density plasma near the cathode orifice, referred to as a plasma ball, with large density gradients. Further, floating keeper voltages, discharge current oscillations, and downstream plasma properties (particularly the plasma potential) are small in spot mode. The transition into the unstable plume mode is marked by a luminous electron plume and oscillatory plasma behavior [29,30]. Figure 2.5 shows the visual evolution from spot to plume mode for the ALPE Heaterless Hollow Cathode (AHC-3.2) with overlayed light intensity contours [84]. A change in pixel intensity from the image can be approximated as corresponding changes in relative density [94]. In addition to the growth of the plasma plume, the color also shifts from light purple to light blue when the cathode shifted to plume mode. This shift in fluorescence reflects variations in the collision

dynamics, as the color emitted by the plasma is sensitive to the energy and frequency of particle interactions [95], [96], [97].

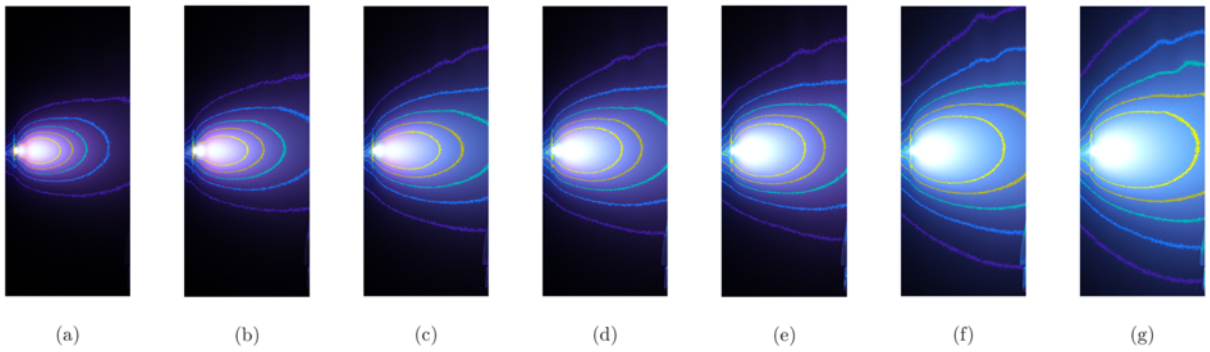

Figure 2.5: Photos with overlayed contour of the transition of spot to plume mode of the AHC-3.2 operated on xenon at (a) 0.4 A/sccm to (g) 1.6 A/sccm in 0.2 A/sccm increments. The cathode was operated at a constant 2.5 sccm with increasing discharge currents (1 A – 4 A). The camera settings are the same for all images.

For independent cathode tests operated in plume mode, the coupling voltage from cathode to anode is large, and the large-scale potential oscillations are on the order of or greater than the discharge voltage when compared to spot mode. The higher power required to maintain the discharge is unfavorable for the spacecraft. Further, the large potential between cathode and anode and the fluctuating plasma potential suggests plume mode can lead to the production of energetic ions. This is particularly true near the keeper face, which can lead to the erosion of keeper surfaces. As a result, this mode has often been defined by an increase in the magnitude of the floating keeper voltage oscillations [9]. For example, the NASA Solar Technology Application Readiness (NSTAR) GIE cathode entered plume mode when the keeper peak-to-peak voltage exceeded 5 V_{p2p}[59].

Literature suggests the onset of plume mode occurs when the ratio of the discharge current to cathode mass flow rate increases over some threshold value:

$$\frac{I_D}{\dot{m}} > \alpha \tag{2.44}$$

Where I_D is the discharge current and $\dot{m}$ is the mass flow rate to the cathode. Lower $I_D/\dot{m}$ ratios (as shown in figure 2.5 (a)), corresponds to a cathode operating in spot mode, while higher $I_D/\dot{m}$ ratios correlate with plume mode. Figure 2.6 shows the magnitude of

oscillations from signals measured on the cathode experiment including peak-to-peak keeper voltages, $V_{k,p2p}$, peak-to-peak anode currents, $I_{D,p2p}$, and peak-to-peak anode voltages, $V_{D,p2p}$, for various $I_D/\dot{m}$ ratios of the AHC-3.2. The magnitude of all oscillations exhibited a similar trend across the $I_D/\dot{m}$ ratios and the cathode entered into plume mode at the extremes. At high $I_D/\dot{m}$ ratios (greater than 1.5 A/sccm), the internal plasma was likely starved for neutrals and the large scale oscillations of plume mode manifested as large-scale oscillations on the keeper up to 12.5 V_{p2p}. At the very low $I_D/\dot{m}$ ratios, the magnitude of the peak-to-peak keeper voltage oscillations were high suggesting the cathode was in plume mode. At these ratios, the high propellant flow rate means the cathode surface was likely cooled sufficiently to where the internal plasma struggled to maintain ignition. Characterization of cathode lifetime often encompasses sweeping currents and mass flow rates to determine the $I_D/\dot{m}$ ratios at which the cathode operates stably.

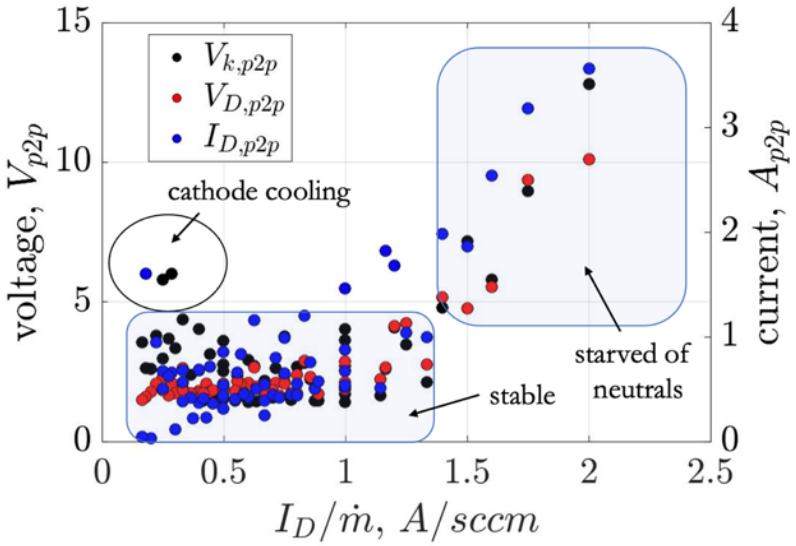

Figure 2.6: ALPE heaterless cathode peak-to-peak keeper and anode voltage and anode current measurements vs $I_D/\dot{m}$ ratio.

Fourier spectra of discharge current measured at the anode of cathodes operating in plume mode show narrow-band frequency peaks on the order of 10-100 kHz [59]. Literature suggests the spot-to-plume mode transition is likely related to predator prey

oscillations, commonly referred to the breathing mode in HETs [24], [30]. The frequency of ionization is defined by,

$$f_i = \frac{n_e \langle \sigma v_e \rangle}{n_i / n_0} \tag{2.45}$$

where $\langle \sigma v_e \rangle$ is the ionization rate coefficient, which is dependent on the neutral species [98]. The cyclical process of the ionization instability can be described as thus: when the neutral density is high, the ionization rate is high leading to a reduction in the neutral population. Once the neutral density is depleted, the plasma density then decreases and thus, the ionization rate decreases. This process repeats as the influx of neutrals begins the cycle again. The instability can be enhanced by the fluctuations observed in the electron temperature, which can drive the ionization oscillation unstable [24].

2.3.4.2 The Effect of Magnetic Fields on Cathode Plumes

As previously mentioned, the transition from spot-to-plume mode has largely been based on the NSTAR 5 V_{p2p} magnitude of keeper voltage oscillation criterion. However, utilizing floating keeper voltage oscillations to observe the plume mode transition in HETs has been extensively debated in literature [9], [24], [25], [99], [100]. This is largely because the environment for the cathode in GIEs differs significantly from HETs. In GIEs, cathodes are typically exposed to less than 100 G, meanwhile magnetic fields in HETs can exceed 300 G depending on the HET and the location of measurement. Additionally, GIE cathodes are operated at much lower flow rates and configured with smaller orifice diameters than HETs. This suggests that plume mode is less of a concern for HET cathodes as the $I_D/\dot{m}$ ratios are lower at higher flow rates [59]. As a result, interpreting voltage oscillations as indicators of plume mode transitions in HETs may not be as straightforward or universally applicable, leading to the ongoing debates about the validity and reliability of this approach. Downstream plume measurements of partially magnetized cathode plumes show significant oscillations in ion saturation and electron saturation currents as well as an increase in the measured energetic ion production all while the floating keeper voltage was less than 5 V_{p2p} [17], [25]. Centrally mounted

cathodes in HET magnetic fields have been referred to as operating in a unique mode coined as jet mode as the plasma is collimated along the field lines. Figure 2.7 shows the H6 cathode with an HET magnetic field operating in spot, plume, and jet modes.

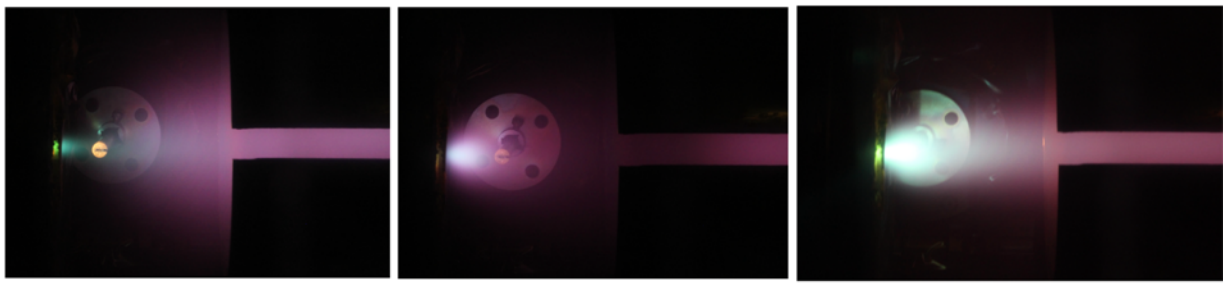

Figure 2.7: H6 Hollow cathode operating in (a) spot, (b) plume, and (c) jet mode with plasma collimation along the magnetic field lines.

Hall et. al. performed an analysis on the downstream ion population of the HERMeS cathode with a TDU-like magnetic field simulator. Retarding potential analyzer (RPA) measurements showed the growth of energetic ions in the radial direction well above the anode potential when the field strengths matched the thruster field strengths [17]. In addition to the RPA measurements, a clear visual change occurred in the cathode plume while in jet mode and an increase in the cathode orifice plate temperature was measured.

Frieman et al. noted a wear pattern with azimuthal characteristics observed on the inner front pole cover (IFPC), which protects the inner magnetic coil, during a long duration wear test of the HERMeS TDU-3 [55]. This erosion was a function of increased discharge voltage and increased magnetic field. These erosion patterns were not matched in Hall2De measurements, which suggest that ions are generated and further heated via some instability stemming from the cathode plume and/or the beam. Huang et al. performed plasma oscillation characterization tests on TDU-1 using high speed imaging and noted an azimuthal m=1 mode oscillation centralized at the cathode [58]. Mode number here represents the number of populations simultaneously present where a mode of m=1 notes a single population of ions travelling azimuthally in front of the IFPC. The

observed frequencies of this mode ranged from 50 kHz to 76 kHz with a slight increase in frequency as the magnetic field strength was increased. The oscillation did not appear to change with increasing background pressure; however, the frequency of the azimuthal mode decreased with increasing cathode flow fraction. The centralized high speed imaging suggests the mechanism for the erosion is likely linked to turbulence sourcing from the cathode plume.

In HETs plasmas, ions remain unmagnetized because of their relatively large masses and the high speeds at which they are travelling. However, we can evaluate the effect of the magnetic field on the electrons in the HET plasma by evaluating the Larmor radius and the Hall parameter. Electrons in the cathode plume can become magnetized when the electron Larmor radius (eq. (2.20)) is much less than the characteristic length,

$$r_{L,e}=\frac{1}{B}\sqrt{\frac{8}{\pi}\frac{m_e}{e}T_{eV}}=2.38\frac{\sqrt{T_{eV}}}{B}\ll L\ . \tag{2.46}$$

where L is the characteristic length. This length is specific to the region of interest for particle magnetization. For example, the characteristic length for an independent cathode setup could be the anode diameter. When the Larmor radius condition it met, the particle can make a full rotation about a magnetic field line before impacting the reference length (i.e. anode diameter, vacuum chamber diameter, etc.). Alternatively, the Hall parameter describes the number of orbits about magnetic field lines before a collision with another particle. When the particle's cyclotron frequency exceeds the collision frequency, the particle can complete an orbit about the magnetic field before encountering a collision. Mathematically, this condition for the electrons can be described as,

$$(\Omega_e)^2=\left[\frac{\omega_{c,e}}{\nu_e}\right]^2\gg 1 \tag{2.47}$$

where ω_{ce} is the electron cyclotron frequency as defined in eq. (2.18). The downstream cathode plume density generally varies between O(10^{20} m^{-3}) near the cathode exit and O(10^{14} m^{-3}) downstream near the exit plane of the anode, while the temperature can vary between 1 eV and 5 eV. Figure 2.8 shows the Larmor radius and Hall parameter

magnetization conditions for electrons. The maximum temperature in this plot was set at 20 eV to account for the possibility of warm electrons. The Hall parameter condition shows that in some regions of the cathode plasma, particularly in the denser regions, the magnetization condition is not met due to the high collisionality in these regions. However, outside of the highly dense regions, the electrons are strongly magnetized. Since ions remain unmagnetized, the cathode plume is commonly referred to as "partially magnetized".

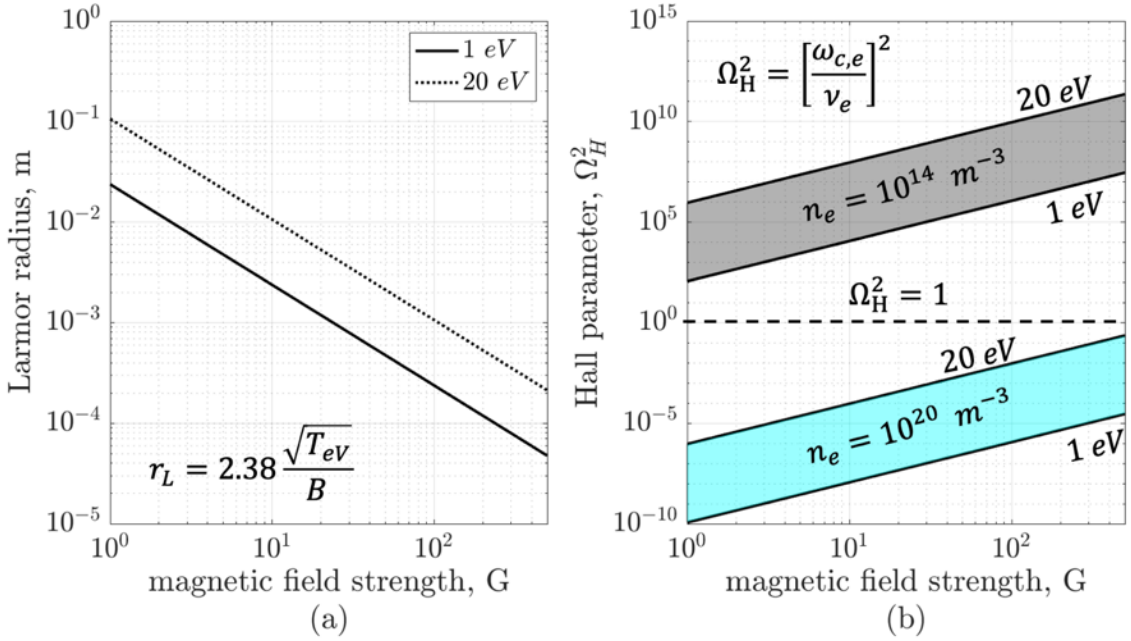

Figure 2.8: Larmor radius and Hall parameter for increasing magnetic field strengths. (a) Larmor radius for electron temperatures between 1 eV and 20 eV. (b) Hall parameter for densities between 10^{14} and 10^{20} m^{-3} with bounds for temperatures between 1 eV and 20 eV.

Figure 2.9 shows the approximate location of the peak magnetic field strength in the HET topography downstream of the cathode exit. In this orientation, the magnetic field lines generate a magnetic mirror. The electrons traveling on the field lines speed up as the magnetic field strength increases and are either lost (travel through the mirror) or reflected backwards (to the cathode exit).

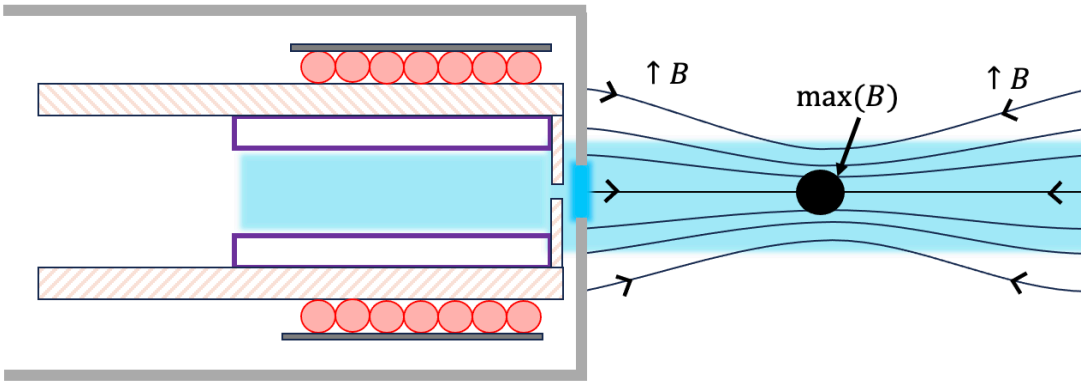

Figure 2.9: Schematic of a magnetic mirror downstream of the cathode exit. The downstream plasma is shown as it is in "jet" mode with a collimated beam from the magnetic field.

As electrons speed up along the field lines, the conservation of magnetic moment dictates that their perpendicular velocities must also increase. This is shown in the equation for the magnetic moment:

$$\mu_m = \frac{1}{2}\frac{m u_\perp^2}{B} \quad . \tag{2.48}$$

where $u_\perp$ is the perpendicular velocity of the electrons. Whether or not the electron is lost or reflected depends on the angle of the electron trajectory with respect to the maximum field strength location. Electrons that are lost must meet the condition:

$$\sin^2\theta \leq \frac{B_0}{B_m} \tag{2.49}$$

where θ is the pitch angle relative to centerline, B_0 is the initial magnetic field strength, and B_m is the maximum field strength in the mirror. Electrons with a pitch angle greater than the critical pitch angle are reflected. The reflected electrons resonate between the peak magnetic field downstream and the lower magnetic field strength near the cathode exit. This can lead to enhanced collisions in the region in which the electrons lose energy, cross the magnetic fields lines, and are then eventually lost through the mirror. The anisotropy in the electron velocity distribution can also cause a variety of instabilities discussed in the sections below.

2.3.4.3 The Azimuthal Wave

The m=1 structure has been measured on the HERMeS by Huang et al. [57] and previously on the H6MS by Jorns and Hofer [11]; however, the energy source of this instability is still unknown. Jorns et al. proposed an azimuthal anti-drift wave that is excited by applying the magnetic field, which could also generate anomalously energetic ions [101]. The large density gradient in the hollow cathode plume energizes the wave and allows the wave to propagate primarily azimuthally with a nearly negligible axial component parallel to the magnetic field lines. The assumptions for the anti-drift mode are that the electron collision frequency is between the ion and electron gyrofrequencies, $\Omega_\mathrm{i}<\nu_\mathrm{e}<\Omega_\mathrm{e}$, the electrons are much warmer than the ions, $T_e \gg T_i$, the frequency of the oscillation is between the ion and electron collision frequencies, $\nu_\mathrm{i}<\omega<\nu_\mathrm{e}$, and the phase velocity in the axial direction is much higher than the ion sound speed, $\omega/k_z \gg c_s$ [22], [24]. Armed with these assumptions, the real component of the dispersion relation is given by ref. [22],

$$\frac{\left(\frac{m}{R}\right) u_d + i\nu_\mathrm{pl}}{\omega - \left(\frac{m}{R}\right) v_{E\times B} - \left(\frac{m}{R}\right) u_{e,z} + \mathrm{i}\nu_\mathrm{pl}} = \frac{T_e}{m_i}\left[\frac{k}{\omega - \vec{k}\cdot\vec{u}_i}\right]^2 \tag{2.50}$$

where m is the azimuthal mode number, R is the radial component of the measurement, $u_{e,z}$ is the electron drift velocity in the axial direction, $\vec{u}_i$ is the ion drift velocity, ν_pl is a collisional term,

$$\nu_\mathrm{pl} = \frac{k_z^2 T_e}{m_e}\nu_{ei} \ , \tag{2.51}$$

and u_d is the diamagnetic drift defined as

$$u_d = \frac{T_e}{qB_0}\frac{\nabla n_e}{n_e} \tag{2.52}$$

where ∇n_e accounts for the fluctuating electron density. The helical nature of the anti-drift wave results in an anomalous collision term with both azimuthal and axial components:

$$\nu_{AN,\varphi}=\nu_e\left[\sum_{k_z,m}\left(\frac{n_{e(k_z,m)}}{n_e}\right)^2\left(\frac{m}{k_z r}\right)^2\left(1+\frac{k_z r u_{e(z)}}{m u_{e,\varphi}}\right)\right] \tag{2.53}$$

$$\nu_{AN,z}=\nu_e\left[\sum_{k_z,m}\left(\frac{n_{e(k_z,m)}}{n_e}\right)^2\left(1+\frac{m u_{e(\varphi)}}{k_z r u_{e(z)}}\right)\right] \tag{2.54}$$

Where $n_{e(k_z,m)}$ is the Fourier transform of the density, k_z is the axial wavenumber, and $u_{e(z)}$ and $u_{e(\varphi)}$ are the axial and azimuthal components of the electron drift velocity.

Alternatively, Becatti et al. argues the rotational mode measured in the partially magnetized cathode plume is due to a magnetohydrodynamic (MHD) kink instability [102]. The β parameter is a ratio of the plasma pressure to the magnetic pressure,

$$\beta=\frac{n_e k_b T_e}{B^2/2\mu_0} \tag{2.55}$$

where μ_0 is the permittivity of free space. HET plasmas are typically low-β plasmas, which means the kink instability that would form in this region is driven by the strong axial current provided by the cathode [19]. The low current cutoff for the ideal form of the MHD kink instability is around 100 A; however, Becatti et al. suggests a resistive MHD model utilizing the finite resistivity of the cathode plasma which can explain the propagation of the MHD modes at lower current. The dispersion relation of the MHD resistive model is complex and is explored in depth in ref [102]. Becatti et al suggests that it is possible both the MHD kink instability, and the anti-drift wave could both exist within the cathode plume, with the MHD kink instability dominating at higher discharge currents.

2.3.4.4 The Ion Acoustic Wave

Another energy source for the growth of energetic ions in the plume of the hollow cathode is suspected to be ion acoustic turbulence (IAT). IAT is an electrostatic wave which has been experimentally measured and theoretically shown to exist in the plume of a hollow cathode propagating primarily in the z-direction (axial) with no azimuthal modes

[22], [27], [30]. For IAT to exist in the plume, the wavelength must be much longer than the Debye length, the electron temperature must be much greater than the ion temperature, and the electron drift velocity must be much greater than the sound speed. IAT scales with the discharge current, but it can be masked by large-scale lower frequency modes when observed in the Fourier spectra space [103]. The real part of the dispersion relation for IAT can be expressed as,

$$\omega_r = \vec{k} c_s + \vec{u}_i \cdot \vec{k} = k_z(\vec{u}_i + c_s) \tag{2.56}$$

with simplification for purely axial propagation and where $c_s = \sqrt{qT_e/m_i}$ is the ion sound speed. The imaginary component of the dispersion relation gives the growth rate of IAT and is defined as:

$$\omega_i = \left(\frac{\pi}{8}\right)^{1/2} \vec{k} c_s \left[\left(\frac{\vec{k} \cdot (\vec{u}_e - \vec{u}_i) - k c_s}{k \nu_e}\right) - \left(\frac{T_e}{T_i}\right)^{\frac{3}{2}} e^{-\frac{T_e}{2T_i}}\right] - \frac{\nu_i}{2} \tag{2.57}$$

where ν_i is the total ion collision frequency ($\nu_i = \nu_{ie} + \nu_{in}$) [60]. The first term in eq. (2.57) shows that the growth of the ion acoustic wave is due to the strong drift velocities of electrons through collisionless processes. The second and third terms show that the wave loses energy through Landau damping and ion collisions, respectively. If the ions are not sufficiently cooled through Landau damping or ion collisions, the ion acoustic wave becomes turbulent. The large gradients in density and potential as a function of radial position with respect to centerline near the cathode exit aid in the generation of these instabilities in the region [20], [24]. The total wave energy density of IAT can be found by summing the wave energy over frequency space,

$$W_T = \frac{n_e}{T_e} \sum_{\omega_0}^{\omega_{p,i}} [q\phi(\omega)]^2 \tag{2.58}$$

where ω_0 is the lower cutoff frequency of IAT dictated by the ion-neutral collision frequency and $\omega_{p,i}$ is the ion plasma frequency.

The contribution to the anomalous collision frequency for IAT exists only in the axial direction and can be described as,

$$\nu_{\mathrm{AN,IAT}} = \frac{\alpha\omega_{\mathrm{pe}} W_{\mathrm{T}}}{n_e T_e} = \frac{\alpha\omega_{\mathrm{p,e}}}{T_e^2} \sum_{\omega_0}^{\omega_{\mathrm{p,i}}} [q\phi(\omega)]^2 \quad . \tag{2.59}$$

2.3.4.5 Lower-Hybrid Instability

Lower hybrid instabilities form perpendicular to the magnetic field and involve oscillations in both the electron and ion populations. This instability requires the magnetic field to be low enough as to not magnetized the ions, but high enough to magnetize the electrons. This partially magnetized condition is met in the cathode plume. The frequency of the instabilities are around the lower hybrid frequency defined as

$$\omega_{\mathrm{LH}} \approx \frac{1}{\sqrt{\frac{1}{\omega_{\mathrm{pi}}^2} + \frac{1}{\omega_{\mathrm{c,e}}\omega_{\mathrm{c,i}}}}} \quad . \tag{2.60}$$

The general dispersion relation is given in ref. [104]:

$$\frac{\omega^2}{\omega_{\mathrm{LH}}^2} = 1 + \frac{m_i}{m_e}\cos^2\theta + \left(3\frac{T_i}{T_e} + \frac{3}{4}\right)\frac{k^2 v_{\mathrm{th,e}}^2}{\omega_{\mathrm{c,e}}^2} \quad . \tag{2.61}$$

where θ is the angle between the magnetic field and the direction of wave propagation. The last term from the lower hybrid dispersion relation shows that the growth of the wave is through the warm electron drift. The lower hybrid waves can transfer energy from the electrons drifting along the magnetic field lines to heat the slow-moving ions. [19].

2.3.4.6 Summary of Cathode Instabilities

The previous section paints a picture of the instabilities that can form in the plume of the hollow cathode while operated in an HET-like magnetic field. Centrally mounted cathodes provide many benefits to the HET including reducing plume divergence and improving thruster symmetry; however, the region surrounding the cathode includes a magnetic mirror, strong axial currents, and steep potential and density gradients. This environment can create conditions that lead to complex plasma dynamics and turbulence leading to energetic ion production. Table 2.1 shows the summary of instabilities described in the

above sections. The work in this dissertation uses these frequency ranges as a guide for analysis of high speed probing of the downstream cathode plume.

Table 2.1: Frequency ranges of instabilities in cathode plumes.

Instability	**Frequency**	**Propagation Direction**
Breathing mode	O(10 kHz)	global
Azimuthal anti-drift wave/Resistive MHD modes	O(50 – 150 kHz)	azimuthal, radial
Ion Acoustic Turbulence	O($>\nu_{in} \cong$ 400 kHz)	axial
Lower hybrid	O($>\omega_{LH} \cong$ 3,000 kHz)	axial, radial

Figure 2.10 shows a sample Fourier spectra of the anode signal and a downstream high-speed probe from an independent cathode setup, featuring a downstream anode and a magnetic field simulator that creates a magnetic field topography similar to an HET. The frequency domains of the expected instabilities are outlined. In this instance, the cathode did not exhibit an ionization-like narrow band peak, the azimuthal m=1 mode was measured in the probe and the anode signal, and IAT was only measured in the downstream probe. Thus, downstream probing is necessary to capture the high-speed turbulence forming in the plume. Chapter 3 explores the diagnostic methods used to investigate these instabilities as well as the analysis techniques used throughout this work.

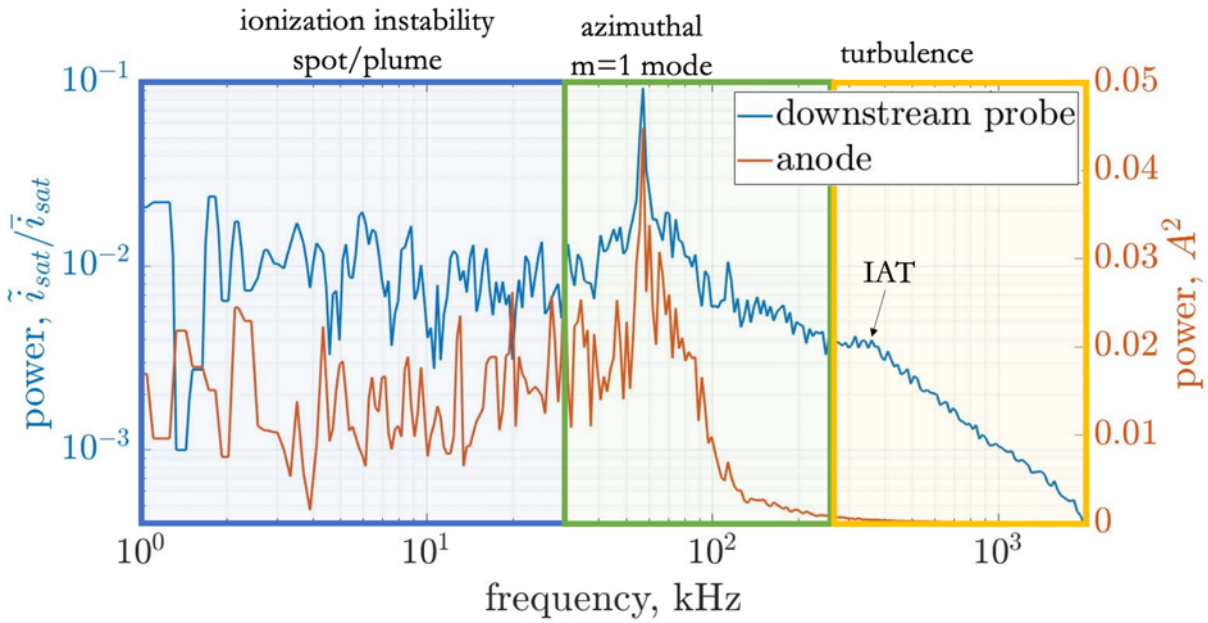

Figure 2.10: Fourier spectra of anode signal and downstream ion saturation probe from an independent cathode setup with a downstream anode and magnetic field simulator.

CHAPTER 3

Experimental Techniques

"To achieve great things, two things are needed; a plan and not quite enough time."

Leonard Bernstein

3.1 Introduction

This chapter establishes the experimental framework for this dissertation. It begins with a general overview of predictive models for Hall Effect Thrusters (HETs), emphasizing the need for experimental validation provided by this work. A review of the literature covering independent cathode setups, including anode configurations, background pressures, magnetic field simulations, and diagnostic techniques, follows. The chapter concludes with the theory behind the diagnostics, as well as descriptions of the vacuum chambers and cathodes used in the experiments.

3.2 Brief Overview of Predictive Models

Chapter 2 discussed the extensive flight heritage of HETs in Earth's orbit and how the maturation of HET technology has made them a prominent propulsion system for deep space exploration. These extended missions require longer lifetimes and may require a higher power output from the thruster. Full-term comprehensive lifetime testing of HETs at these timescales and powers is an expensive endeavor in terms of facility costs, propellant requirements, power to the thruster, vacuum facility time (particularly considering the LN2 costs for cryogenic cooling of cryogenic vacuum pumps), and

dedicated chamber and engineer time. Considerable efforts in the modeling of these thrusters aim to target these challenges by supplementing the experimental lifetime testing. However, there remain gaps in the knowledge that require closure, namely in the anomalous electron transport perpendicular to the magnetic field lines of an HET beyond the classic resistivity levels. High-fidelity particle-in-cell (PIC) models, which are entirely kinetic simulations, have identified small-scale turbulence as the contributor to enhanced electron transport [105], [106], [107]. Still, PIC models are computationally expensive, often taking days or longer to run on supercomputers [108].

Two dimensional (2D) fluid models are less computationally expensive, but the source of the anomalous transport is not inherently captured [107], [108], [109]. An estimation of the anomalous collision frequency is often introduced into the total collision term to calibrate the model. The total collision term becomes

$$\nu = \nu_{ei} + \nu_{en} + \nu_{a}. \tag{3.1}$$

where ν_a is the anomalous collision term. Various closure mechanisms have been used to approximate ν_a to better match the experimentally measured parameters [109], [110], [111]. Fluid models can investigate the effects of thruster operation on the plasma. For example, Dragnea et al. utilized the multifluid Hall2De code to examine the impact of using krypton as the propellant for HETs [112]. Through an analysis of the NASA 300M thruster in Hall2De, Dragnea predicted a higher specific impulse for the thruster when operated with krypton compared to xenon. While eq. (2.38) suggests krypton should theoretically outperform xenon in specific impulse, experiments have shown krypton exhibits a lower-than-predicted specific impulse likely due to reduced mass utilization efficiency [113]. Su experimentally showed that krypton exhibited higher specific impulse at higher thrust-to-power ratios [71]. Ref. [108] gives a comprehensive review of HET models.

Isolated cathode plume models have also been explored extensively in literature. Zero-dimensional (0D) models have been used to describe the internal plasma region by

averaging the plasma parameters along the length of the emitter. While the plasma density can vary along the length of the emitter due to the restricting cathode orifice, 0D models can be beneficial to characterize scaling laws [114]. One-dimensional (1D) models have also been used to describe the internal plasma, which has allowed for an analysis of the non-uniform plasma distribution. 1D models have allowed for the investigation into non-uniform barium depletion in BaO dispenser cathodes [75], [115]. 2D fluid models for hollow cathodes, such as OrCa2D [75], [79], and full PIC models [106] have been used to simulate the far more complex external plume with aims to elucidate the spot-to-plume mode transition or IAT propagation. Ref. [116] provides a detailed review of cathode-specific models.

While models are an indispensable tool for lifetime analysis, they still require verification through physical experimentation, especially when addressing the complex, small-scale turbulence that is challenging to capture in fluid models. This chapter will explore the experimental configurations and probing techniques used to investigate those instabilities in the cathode plume.

3.3 Independent Cathode Experimentation for Life Testing

Lifetime experiments on HETs are conducted to identify erosion mechanisms, assess overall thruster performance, and determine operational margins of stability. During the early stage of HET development, stability regime analyses are performed where the discharge current, discharge voltage, and magnetic field strength are all varied while the discharge current oscillations are measured. The HET is considered stabile in regions where the discharge oscillations are small. This is commonly referred to as IVB mapping and is similar to the $I_D/\dot{m}$ stability analysis performed with cathodes, as discussed in section 2.3.4.1. For example, the HERMeS thruster has undergone extensive life testing since its inception in 2013 [15], [55], [57], [58]. Now, at the end of the developmental campaign, the HERMeS thruster is used as a risk-reduction testbed for identifying any long-term life-limiting mechanisms [117].

A critical aspect of HET life testing is the independent component testing of the hollow cathode. This testing identifies and characterizes the long-term performance, erosion patterns, and stability regimes exhibited by the cathode independent of the thruster beam [118], [119], [120], [121], [122]. The orientation of the downstream anode, magnetic field topography, and power harnessing during these testing campaigns often depends on the intended use of the cathode. Despite the setups that have been used in literature, there is no universally accepted configuration for independent cathode testing to match the cathode operation in the thruster. This section explores independent cathode configurations, with a focus on those designed to mimic the conditions with the HET beam.

3.3.1 Anode Configurations

Lone cathode experiments often couple to a downstream anode. The configuration of the anode comes in a variety of flavors depending on the intention of the study. Figure 3.1 shows the most common anode configurations: planar (figure 3.1(a)), conical (figure 3.1(b)), and cylindrical (figure 3.1(c and d)). Planar anodes are the simplest configuration and have been used for independent cathode testing [72], [123] as well as cathode modeling [100], [106]. Potrivitu et al. showed that a LaB_6 cathode operated at 5 A with a planar anode transitioned to plume mode when the increasing anode-to-cathode distance reached 45 mm. Conversely, when the cathode was operated at 10 A in plume mode, increasing the planar anode-to-cathode distance increased the anode potential and the frequency of the plume-mode oscillation shifted to a lower frequency. Planar disk-like anodes increase the local neutral pressure, thereby increasing the ion-neutral collision frequency and damping oscillations in this region. Consequently, spot mode is favored in this configuration compared to the other anode geometries. The diverging section conical anode results in a lower local neutral pressure and the magnitude of the anode voltage more closely aligns with cathode operation in GIEs [124].

Cylindrical anodes are the most commonly used anode configuration to match cathode operation in the HET environment. Smaller cylindrical anodes are known to increase the local neutral pressure, damping the local oscillations. Alternatively, larger cylindrical anodes better match the neutral pressure near the cathode exit compared to smaller cylindrical anodes, but they require higher anode voltages to maintain the discharge [125]. Hall et al. found that cathode performance with smaller diameter cylindrical anodes is more sensitive to changes in anode-to-cathode separation distance, likely due to the dramatic change in neutral pressure with increasing cathode-to-anode separation distances [125]. This behavior is not replicated in the larger cylindrical anode configuration, where increasing the cathode-to-anode distance did not substantially change the local neutral pressure. Potrivitu et al. also demonstrated that the length of the cylindrical anode can influence cathode performance by changing the surface area available for electron collection [126].

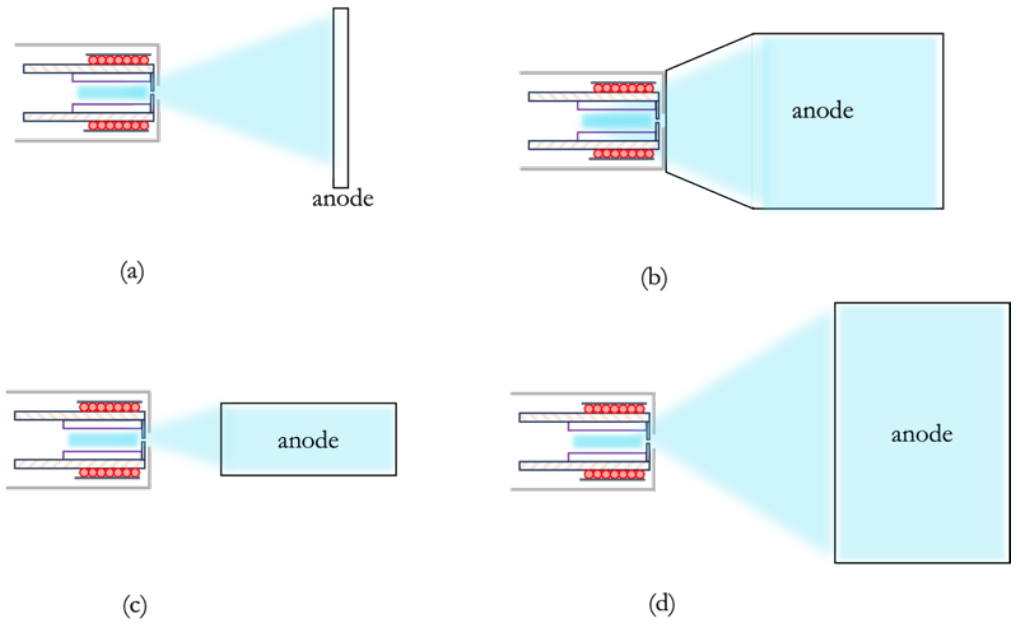

Figure 3.1: Anode configurations for lone cathode testing. (a) Planar anode, (b) cone (or conical) anode, (c) small-diameter cylindrical anode, and (c) large-diameter cylindrical anode.

3.3.2 Background Pressure

Background pressure effects on HETs are an ongoing area of research. Independent cathode experimentation often occurs in vacuum chambers with a vast difference in chamber pressures, typically between 1×10^{-5} Torr and 1×10^{-4} Torr; however, as mentioned in previous sections, heightened background pressure can dampen high-frequency waves, such as IAT. Background pressure studies on the HERMeS cathode revealed that higher background pressures led to increased discharge voltage, cathode orifice temperature, and centerline electron temperature while decreasing the magnitude of discharge current and voltage oscillations [127].

3.3.3 Magnetic Field Configuration

Section 2.3.4.2 discussed the magnetic field configuration near the cathode exit in an HET. To summarize, the topography at the cathode exit results in a magnetic mirror, and the field strength is large enough to strongly magnetize the electrons while ions remain unmagnetized. Various magnetic field simulator configurations have been used to mimic this environment on independent cathode setups. Figure 3.2 shows two field simulator configurations: a downstream solenoid often attached to the anode and an upstream simulator. The solenoid-anode assembly (figure 3.2(a)) is the most common and frequently incorporates water cooling along the anode due to the heat introduced by the solenoid coil [25], [91], [103]. The upstream magnetic field simulator (figure 3.2(b)) decouples the magnetic field simulator component with the anode, thus allowing for the adjustment of anode diameters and anode location [17], [125], [128], [129], [130]. Upstream magnetic field simulators that creates a magnetic field topography similar to HETs can be costly to produce compared to downstream solenoids due to the ferrous materials required to shape the magnetic field.

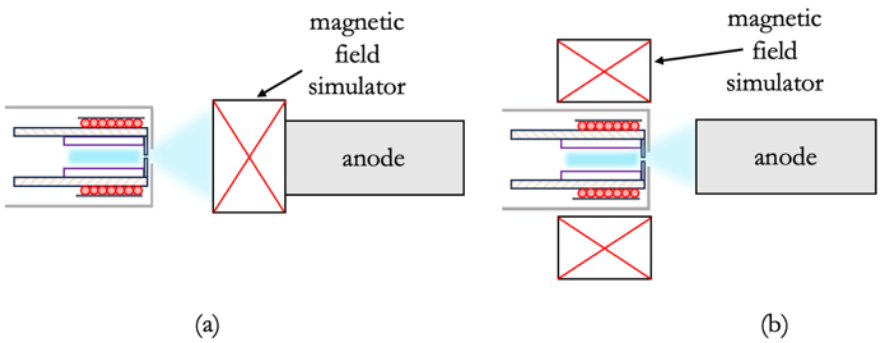

Figure 3.2: Magnetic field configuration for independent hollow cathode testing. (a) A solenoid and anode assembly and (b) an upstream magnetic field simulator.

3.3.4 Summary of Lone Cathode Experimentation

Literature has suggested that the anode configuration, background pressure, and magnetic field topography for independent hollow cathode testing can alter the macroscopic plasma properties, such as the transition to plume mode, and the microscopic plasma properties, such as turbulent wave growth as a function of neutral pressure. However, despite these efforts, accurately matching the downstream plume behavior between standalone cathode operation and full thruster experiments remains poorly understood. As such, independent cathode testing has been performed across various background pressures, discharge currents, and operational conditions. Table 3.1 highlights some of the independent cathode experiments with their associated currents and chamber pressures.

Table 3.1: Summary of hollow cathode experiments and the variety of background pressures.

Reference	Cathode current, A	Chamber pressure, Torr
Potrivitu et al. [72], [126]	2-14	1.5×10^{-5}
Hall et al. [125]	20	1.8×10^{-5}
Polk et al. [115]	4-15	$2.5\text{-}3.6\times10^{-5}$
Meng et al. [99]	3	9×10^{-5}
Lev et al. [86]	0.5-0.8	1×10^{-4}
Jorns et al. [21]	100	3.7×10^{-4}

While it is postulated that these variables play a significant role in matching operation in the HET environment, the refinement of these configurations on independent cathode testing is necessary. This work aims to observe similarities in the high-frequency turbulence and low-frequency dynamics in the downstream plume between independent cathode testing with a magnetic field simulator and full thruster testing using various invasive and non-invasive diagnostics techniques explored in the next section.

3.4 Diagnostic Methods

This section begins with an overview of diagnostics that have been used with hollow cathodes to measure different plasma parameters and/or addresses certain performance metrics. Following this, the fundamental theory of the diagnostics used in this work is provided.

3.4.1 Overview of Cathode Diagnostics

3.4.1.1 Performance Measurements

The most fundamental form of diagnostics on a cathode is the passive DC and AC measurements of cathode components. These include anode, keeper, heater, and magnetic coil currents and voltages.

The DC voltages and currents can be acquired from voltage dividers and in-line shunt resistors, respectively. High-speed voltages can be acquired using high-voltage probes on sense lines. High-speed current can be captured using a clamped current probe, which provides both the AC and DC component for bandwidths typically on the order of 500 kHz to 1 MHZ. Clamped current probes can drift due to thermal equilibration. Pearson coils can provide the AC component of the current at high bandwidths (up to 35 MHz) and do not exhibit the drifting behavior observed in clamped probes. These signals can be logged via data acquisition systems (DAQs). DAQ cards have limitations on input currents and voltages and have limitations on bandwidth. Oscilloscopes can also be used to provide higher bandwidth.

3.4.1.2 Invasive Probes

Thermocouples. Thermocouples are a baseline diagnostic tool used in all experiments with EP devices, as it can take hours for an EP device to reach thermal equilibrium. Thermal equilibration time and its impact on downstream plasma characteristics is an ongoing area of research. For instance, studies have demonstrated that the temperature of the HET channel can affect the neutral density, which has implications for HET performance [38].

Langmuir Probe (LP). LPs have been used as a plasma diagnostic tool since their inception by Mott-Smith and Langmuir [131]. Their simple construction and straightforward analysis methods make LPs a vital tool for understanding plasma environments. LPs can provide the following plasma parameters: ion and electron number densities, $n_{i,e}$; the plasma and floating potentials, $V_{f,p}$; and the electron temperature, T_e. LPs can be operated in various configurations to acquire a specific parameter. They can also be operated at high speeds to gather temporal resolution on the plasma parameters [132]. LPs are the primary diagnostic method used in this dissertation and the theory is discussed in section 3.4.2.

Emissive Probe. Emissive probes are also simple in construction, typically of a "hairpin" design [133]. They consist of routing a tungsten wire through ceramic so that a small portion is exposed to the plasm and a current is passed through the wire. As the probe heats up, it begins collecting electrons. Emissive probes can get hot enough to melt, and the probe material can break depending on the density of the plasma in which it is inserted ($T_{probe} \propto n_e$). Emissive probes provide a measure of V_p that is more accurate than the LP measurement.

Retarding Potential Analyzers (RPA). An RPA is an electrostatic tool that provides the ion energy distribution function at fixed locations. These devices use a series of biased grids and a collector plate for the ions. The first grid is left floating to minimize the probe perturbing the plasma environment. The second grid is held at a negative potential to repel electrons from the plume. The third grid, or the retarding grid, is swept from 0 V to a bias above the anode potential. The secondary electrons generated from the retarding grid are repelled with the third grid, which is held at a negative potential. Finally, the collector plate collects the ions and is routed to ground for slow speed RPA measurements or to an oscilloscope for high speed measurements.

3.4.1.3 Non-Invasive Probes

Non-invasive diagnostics are generally outside the scope of this thesis. Thus, only a brief overview of these diagnostics is provided here. Optical temperature measurements, including pyrometers and fiber optic cables, have provided information regarding cathode orifice temperature and insert temperature. Optical Emission Spectroscopy (OES) measures emission lines from the plasma, and the ratios of certain emission lines can be paired with collision-radiative models to determine electron temperature and density. Konopliv et al. recently performed high-speed OES measurements to capture the HET breathing mode [134]. Laser-induced fluorescence, LIF, is conducted by exciting specific ion transitions, and the fluorescence during de-excitation is measured. The result is the velocity of the ion population with high spatial and temporal resolution. LIF was the

diagnostic used to identify the energetic ion velocity trajectories near the IFPC of the HERMeS thruster discussed in Chapter 2 [13]. Finally, Thomson Scattering is a laser diagnostic that provides the electron density and velocity.

3.4.1.4 Summary

Table 3.2 provides a summary of the invasive and non-invasive probes used to investigate the hollow cathode plume. The references listed are experiments that used the diagnostic to analyze the cathode plasma specifically.

Table 3.2: Summary of Plasma Diagnostics with references of hollow cathode-focused experiments utilizing the diagnostic.

	Probe	Measurement	REF.
Invasive	Thermocouple	Temperature (max 4,200 ℃)	[17], [80], [87], [124], [125], [135], [136]
	LP	n_e, n_i, V_p, V_f, T_e	[9], [23], [84], [128], [137], [138], [139]
	Emissive	V_p	[135]
	RPA	IEDF	[17], [125]
Non-Invasive	Optical Temperature	Temperature	[88], [136], [140]
	OES	n_e, T_e	[96], [141], [142]
	LIF	u_i	[143], [144]
	Thomson Scattering	u_e, T_e	[145], [146]

3.4.2 Langmuir Probes

LPs are fundamentally an electrode placed inside a plasma and biased while the current is measured. The swept bias voltage, V_{bias}, and collected current, I, generate an I-V curve (figure 3.3), which is used to determine specific plasma parameters. The I-V curve can be separated into the following regions: the ion saturation region, where only ions are collected; the electron retarding region, where some electrons have sufficient energy to fall across the potential gradient to the probe; and the electron saturation region, where only

electrons are collected. These three regions are separated by the floating potential, V_f, where no net current is collected at the probe, and the plasma potential, V_p.

Despite their simplicity, it is necessary to take explicit care in the LP's design and construction to minimize the probe's perturbative effects on the plasma. Also, proper LP alignment and meticulous management of the data acquisition process are crucial for reducing measurement errors. This section will dive into the LP theory and design, discuss the data acquisition methods, and describe the LP configurations used in this work.

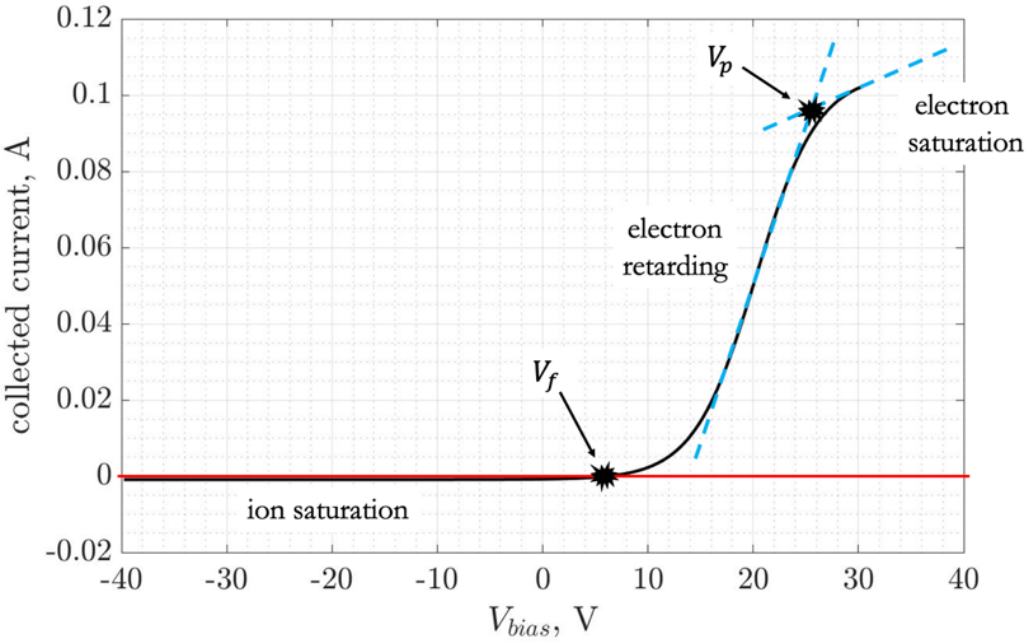

Figure 3.3: Sample *I-V* trace from a cylindrical LP showing the ion saturation, electron retarding, and electron saturation regions separated by the floating and plasma potentials.

3.4.2.1 Langmuir Probe Theory

For $V_{bias} < V_f$, only ions are collected at the probe surface and all electrons are repelled. The current density in this region can be defined as

$$j_i = \frac{I_{i,sat}}{A_s} = en_s u \tag{3.2}$$

where $I_{i,sat}$ is the ion saturation current, A_s is the area of the sheath around the probe, n_s is the density at the sheath, and u is the velocity of the ions entering the sheath. For cold ions ($T_i << T_e$), the ion velocity is the Bohm speed:

$$u_B = \sqrt{\frac{qT_e}{m_i}} \quad . \tag{3.3}$$

Using the Boltzmann relation and equating the sheath potential to the thermal energy of the ions at the sheath, the ion saturation current can be simplified to

$$I_{i,sat} = -\exp\left(-\frac{1}{2}\right) A_s q n_0 \sqrt{\frac{qT_e}{m_i}}. \tag{3.4}$$

The surface area of the sheath can be assumed to be the exposed probe area, A_P, when the sheath around the probe is thin ($A_s \cong A_P$). LPs can operate in three regimes: thin, transitional, and thick. The determination of sheath regime is dictated by the dimensions of the probe and the Debye length of the plasma (eq. (2.10)). For a cylindrical probe, the probe radius, r_p, is used as the referenced probe dimension. The sheath criterion is outlined in table 3.3.

Table 3.3: Sheath criteria for LPs in a low temperature plasma.

Sheath Size	Criterion
Thin	$r_p/\lambda_D > 50$
Transitional	$3 < r_p/\lambda_D > 50$
Thick, OML	$r_p/\lambda_D < 50$

To calculate λ_D at the probe location, the electron temperature and electron density must be known. These parameters are determined from investigating the electron retarding region. For $V_{bias} > V_f$, the electron current increases, exponentially for a Maxwellian plasma, until the plasma potential is reached. The electron current can be defined as:

$$I_e = I_{e,sat} \exp\left(\frac{V_{bias} - V_p}{T_e}\right) \tag{3.5}$$

where $I_{e,sat}$ is the electron saturation current:

$$I_{e,sat} = A_p q n_e \sqrt{\frac{qT_e}{2\pi m_e}} \quad . \tag{3.6}$$

By manipulating ion saturation current (eq. (3.4)) for the probe surface area (assuming thin sheath) and substituting that into eq. (3.6), we get the electron current saturation as a function of the ion saturation current:

$$I_{e,sat} = -\exp\left(\frac{1}{2}\right) I_{i,sat} \sqrt{\frac{m_i}{2\pi m_e}} \tag{3.7}$$

The electron temperature can be determined from the electron retarding region $\left(V_f < V_{bias} < V_p\right)$. By plotting the natural logarithm of the electron saturation current, $\ln(I_e)$, against V_{bias} between V_f and V_p. The least squared slope of this curve is the electron temperature:

$$T_e = \left(\frac{\mathrm{d}\ln(I_e)}{\mathrm{d}\,V_{bias}}\right)^{-1}. \tag{3.8}$$

An initial estimation of T_e can be performed by bounding the curve between V_f and V_p. This results in the potential difference between the plasma potential and the floating potential divided by the change in natural log of the difference in electron saturation current:

$$\begin{aligned} T_e &= \frac{V_p - V_f}{\ln\left(\sqrt{\frac{m_i}{2\pi m_e}}\right)} \\ &\approx \frac{V_p - V_f}{5.28}, \text{ Xe ions} \\ &\approx \frac{V_p - V_f}{5.05}, \text{ Kr ions} \\ &\approx \frac{V_p - V_f}{4.68}, \text{ Ar ions.} \end{aligned} \tag{3.9}$$

In practice, the plasma potential can be challenging to locate due to noisy data, probe orientation, probe construction, and/or the complex plasma environment the probe inhabits. Programmatically, this often means using eq. (3.8) with a small set of data points from the I-V curve beyond V_f. Armed with T_e, the electron and ion number densities can now be found by manipulating eq.(3.4) and (3.7):

$$n_e = \frac{I_{e,sat}}{q^{3/2} A_p} \sqrt{\frac{2\pi m_e}{T_e}} \tag{3.10}$$

$$n_i = -\frac{\exp\left(-\frac{1}{2}\right) I_{i,sat}}{q^{3/2} A_p} \sqrt{\frac{2\pi m_e}{T_e}} \tag{3.11}$$

3.4.2.2 Corrections Due to the EP Plasma Environment

The basis for LP theory is predicated upon the following conditions being met: $T_i/T_e \ll 1$, Maxwellian electrons, collisionless plasma, $dB/dt \approx 0$, nonmagnetized ($r_{L,e}/r_p \gg 1$), quasineturality, isotropic, and homogenous [147]. A large time-averaged error margin exists for LPs, summarized in table 3.4. Many EP plasmas violate the conditions for LP operation and consequently adds additional error in the measurement that requires correction.

Table 3.4: LP error ranges for various plasma parameters [148].

Parameter	Error (%)
n_e	3-30
n_i	10-50
T_e	2-11
V_p	12-20

There are many contributing factors in an EP plasma that might result in non-Maxwellian electrons [148], [149]. In the presence of strong magnetic fields, the electrons are heated along the field lines. These high-energy electrons push the distribution farther away from Maxwellian introducing significant error in the measurement. To observe this deviance, the Druyvesteyn method can be employed to provide the electron energy distribution function (EEDF) defined as:

$$f_e(\zeta) = \frac{2}{A_p q} \sqrt{\frac{2 m_e \zeta}{q}} \frac{d^2 I_{e,sat}}{d V_{bias}^2} \tag{3.12}$$

where $I_{e,sat}$ is the electron saturation current and ζ is the electron energy:

$$\zeta = q\left(V_p - V_{bias}\right) \tag{3.13}$$

In the case of the partially magnetized hollow cathode plume, the analysis of the *I-V* curve can largely remain unchanged as long as the electron Larmor radius ($r_L = m_e v_\perp / |q|B$) is much greater than the probe radius. Aligning the largest probe dimension perpendicular to magnetic field reduces distortion effects the magnetic field on the I-V curve [148], [150]. If the probe dimensions exceed the Larmor radius, an adjustment to the probe area must be made as $A_{p,eff} = A_p \cdot B/|B|$.

Finally, LPs are an invasive diagnostic tool. The plasma will be perturbed by the applied potential relative to the area of the probe, introducing error in the measurement. Monitoring the high-speed discharge current and voltage will determine if the probe is significantly perturbing the plasma. This can be performed by capturing the performance metrics at high speed simultaneously with the probe measurements, as mentioned in section 3.4.1.1. If the magnitude of anode current oscillations is affected by the injection of the probe, then the probe has sufficiently perturbed the plasma enough such that the probe measurement has become less reliable.

3.4.2.3 High-speed Dual Langmuir Probe

Rapidly sweeping V_{bias} resolves the temporal fluctuations in the plasma. The speed at which the probe is swept is limited by the plasma response time [132], [151]. Further, quickly sweeping the probe voltage induces capacitive effects due to the cable length. To mitigate these effects, a null probe of the same length as the active probe is placed near the LP and isolated, commonly with ceramic. The bias voltage is applied to both the null and active probe simultaneously, and the null current is subtracted from the active current during post processing. This technique is called the high speed dual Langmuir probe (HDLP). In this work, the HDLP probe is mounted to a high-speed motion stage for axial injections. Since the probe is also injected into the plasma at high-speed, the HDLP technique is used to capture time-average plasma parameters along the injection. This will be explained in depth in Chapter 5.

3.4.2.4 Langmuir Probe Sizing

LPs are ideally designed to operate in the thin sheath regime. Further, the data acquisition system for the LP must be able to resolve the small magnitude of ion saturation current and must also collect the electron saturation current without saturating the measurement equipment. The electron saturation current can be estimated from the magnitude of the ion saturation current as shown in eq. (3.7). Combining the constants, we get

$$\begin{aligned} I_{e,sat} &\approx -323\ I_{i,sat}, \text{ Xe ions} \\ I_{e,sat} &\approx -257\ I_{i,sat}, \text{ Kr ions} . \\ I_{e,sat} &\approx -178\ I_{i,sat}, \text{ Ar ions} \end{aligned} \tag{3.14}$$

LP sizing often initially relies upon plasma density and temperature estimations based on previous probe measurements or models (i.e., Hall2De or OrCad2D). Figure 3.4 shows an example density map of a 20-A class hollow cathode operated inside a magnetic field captured by an LP assuming thin sheath, highlighting the extremes in the high- and low- density regions. The large density gradients in hollow cathode plumes make it tricky to design a probe to function with a thin sheath across multiple density regimes.

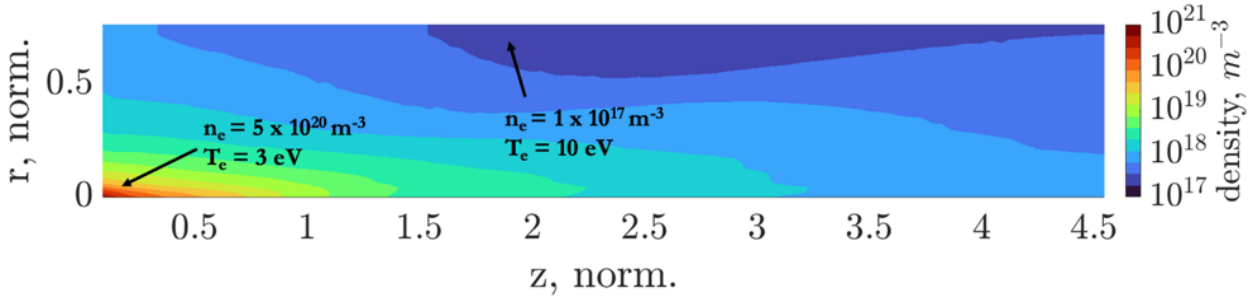

Figure 3.4: Sample density map for independent cathode setups with outlined expected maximum and minimum densities and temperature.

3.4.2.5 Wave Probe Configuration

The configuration of the traditional LP can be manipulated depending on the plasma environment to produce a single desired plasma property. Langmuir probes biased in the ion saturation regime while the high-speed ion saturation current is captured is a

common technique used to evaluate downstream plasma oscillations in EP thrusters [21], [24], [27], [94]. Fluctuations in the ion density are directly proportional to the ion saturation current, which allows for an estimation of potential oscillations as defined in ref. [21]:

$$\phi \approx \frac{T_e}{q}\frac{\tilde{n}_i}{\bar{n}_i} \approx \frac{T_e}{q}\frac{\tilde{i}_{sat}}{\bar{i}_{sat}} \tag{3.15}$$

The high-speed ion saturation current captured from two spatially fixed LPs held to a sufficiently negative bias can be used to determine the local wavevector from the ion frequency spectra of both probes using a cross-correlation technique outlined by Beall [152]:

$$\kappa_{r,z,\theta}(\omega) = \frac{1}{\Delta d}\tan^{-1}\frac{\mathrm{Im}\left(\mathrm{F}(i_{sat,1})\mathrm{F}^{*}(i_{sat,2})\right)}{\mathrm{Re}\left(\mathrm{F}(i_{sat,1})\mathrm{F}^{*}(i_{sat,2})\right)} \quad . \tag{3.16}$$

where $\kappa_{r,z,\theta}(\omega)$ is the wave vector, Δd is the separation distance of the ion saturation probes, $\mathrm{F}(i_{sat,1})$ is the Fourier spectra of one of the high-speed ion saturation probe current, and $\mathrm{F}^{*}(i_{sat,2})$ is the complex conjugate of the other high-speed ion saturation probe current. This form of LP is herein referred to as a wave probe. Due to the analysis method, the maximum wavenumber is limited by the probe separation distance such that $|k| < \pi/d$. The wave number and frequency spectrum can then be binned to produce a statistical histogram representing the wave dispersion, S(ω,k). The phase velocity can be determined from the statistical dispersion.

Wavelengths less than the diameter of the probe and waves with amplitudes less than the noise of the measurement device are difficult to resolve using the described method. In these instances, the wave propagation can spuriously appear as aliased or without any dispersion. This technique has been successfully employed to determine the propagation of plasma waves in the cathode and HET environment, particularly in capturing IAT propagation in cathode plumes [101], [153], [154], [155].

A Note Regarding Probe Separation Distance. The Beall analysis often requires the probes to be placed in non-ideal orientations. To capture longitudinal waves (i.e., IAT), the best orientation for the probe pair is such that the larger surface of the probe is perpendicular to the longitudinal axis. This results in the probe closest to the thruster exit capturing significant ram current from the high-speed ions exiting the device (where $I_{ram}=qn_iA\cdot U_\infty$). Further, depending on the size of the sheath around the probe, there could be spurious interactions between the two probe signals, such as sheath overlapping. A study showing the effects of the probe separation is included in Appendix A.1.

3.4.3 Optical Emission Spectroscopy

Optical Emission Spectroscopy (OES) is a non-invasive diagnostic technique used to measure the intensity of light emitted as a function of wavelength. Collisional radiative models (CRMs) describe the energy states in a plasma due to collisional processes. CRMs relate the intensity of emitted light to specific plasma parameters, namely electron temperature and density, by calculating the energy from collisional interactions between neutrals, ions, and electrons. Plasma ions primarily emit light in the visible spectrum, while neutrals mainly emit in the infrared (IR). A detailed derivation of the CRM for a xenon plasma is given in Karabadzhak et al. [95].

The CRM and specific line ratios from the OES spectra can provide electron temperature and density; however, a functional CRM is required to predict the line ratios related to the expected ion densities and electron temperatures. Work by Konopliv et al. provides the expected electron temperature as a function of I_{823}/I_{828}, where $I_{823,828}$ is the intensity of the neutral lines at wavelengths of 823 nm and 828 nm for xenon emission for specific electron number densities. Generally, the ratio of I_{823}/I_{828} is inversely related to electron temperature, and higher electron number densities correlate to higher temperatures.

Further, the line ratio I_{460}/I_{828} for xenon emission can be used to estimate the ionization fraction at the measurement location as this ratio has shown to be least dependent on other plasma parameters (i.e. electron temperature and density) [97]. 460 nm is an emission line for singly charged xenon. This work does not reference the CRM but instead uses the developed dependencies from the line ratios to plasma parameters to estimate temperature. Figure 3.5 gives a sample OES spectra trace for a hollow cathode operating on xenon with an applied magnetic field.

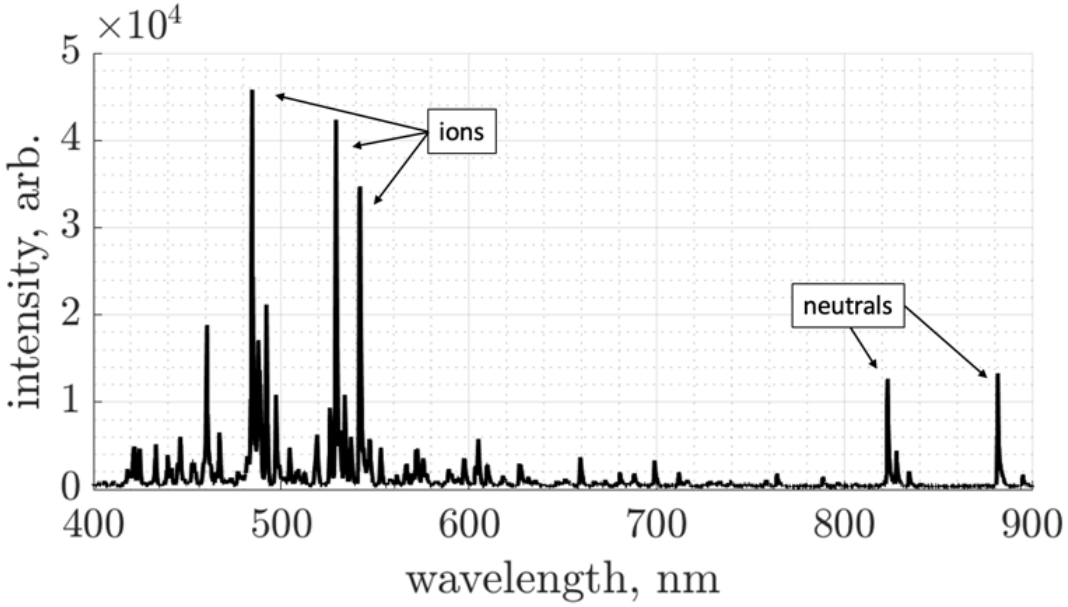

Figure 3.5: OES measurement from a partially magnetized hollow cathode plume operated on xenon.

3.5 Laboratory Equipment

This section provides an overview of the facilities used in this work including the capabilities of each chamber along with a general schematics of the power harnessing for the cathode in each chamber. Next, the hollow cathodes used in this work are described, excluding specific information regarding the anode configuration or magnetic field topography. Information regarding the anode and magnetic field topography will be

provided alongside the discussions on the specific experimental setups and probe orientations in subsequent chapters.

3.5.1 Facility Overview

This work was performed at the following facilities: the Aerospace Laboratory for Plasma Experiments (ALPE) at Western Michigan University (WMU) in Kalamazoo, Michigan, the NASA Jet Propulsion Laboratory (JPL) in Pasadena, California, the NASA Glenn Research Center (GRC) in Cleveland, Ohio, and the U.S. Naval Research Laboratory (NRL) in Washington, D.C. Each of the following sections focuses on one of these locations.

3.5.1.1 Cold plasma Experimental Research Station, Western Michigan University

Facility. Figure 3.6 shows the Cold plasma Experimental Research Station (CEReS) at WMU. CEReS is a 1-m-diameter by 1.5-m-long cylindrical vacuum chamber outfitted with two cryogenic pumps (a CTI-10 and CTI-250F) for a combined pumping capacity of 5,200 L/s-air. The base pressure of the chamber for this work was approximately mid-10^{-7} Torr. Chamber base and operational pressures were monitored using a BRAX Hornet cold cathode gauge and a Byard-Alpert glass hot cathode ionization gauge located behind the cathode exit plane. Pressure readings displayed throughout this dissertation for experiment performed in CEReS were corrected for each gas that was used (argon, krypton, and xenon). An Alicat scientific mass flow controller delivered gas to the cathode and was also calibrated for operation on each gas. The internal gas lines were isolated to ensure cathode isolation to ground.

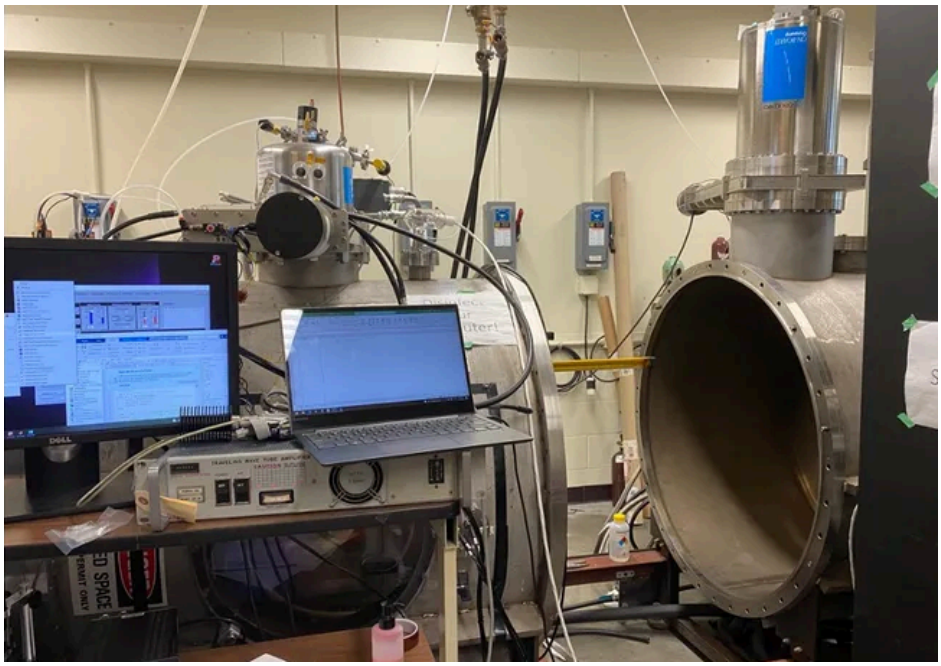

Figure 3.6: CEReS chamber at WMU ALPE.

Power Harnessing and Data Acquisition. Figure 3.7 shows the general schematic for power harnessing of cathode experiments in the CEReS vacuum chamber. The experiments performed in CEReS used the following power supplies: an EMS 60-40 (60-V, 40-A limit) for the anode; a lambda 600-5.5 (600-V, 5.5-A limit) for the keeper; and an EMS 30-20 (30-V, 20-A limit) for the heater. The negative terminals of these three power supplies were connected to the cathode common. When the cathode was grounded, this terminal was shorted to chamber ground. Otherwise, the cathode line was left floating. Additionally, an EMS 60-18 (60-V, 18-A limit) was used for the magnetic field simulator. A second EMS 60-18 was used when both HET coils were powered to control the magnetic field.

High-voltage measurements of the anode and keeper were captured using Micsig DP10013 differential probes. These provided selectable attenuation of 50X or 500X and offered a bandwidth of up to 100 MHz. A Pearson model 410 current monitor was used to measure AC anode current, with a sensitivity of 0.1 V/A and an accuracy of +1/-0%. The bandwidth range of the Pearson current probe spans from 120 Hz to 20 MHz. A

Vektrex VCS40 current sensor was used in line with the anode to provide the DC anode current.

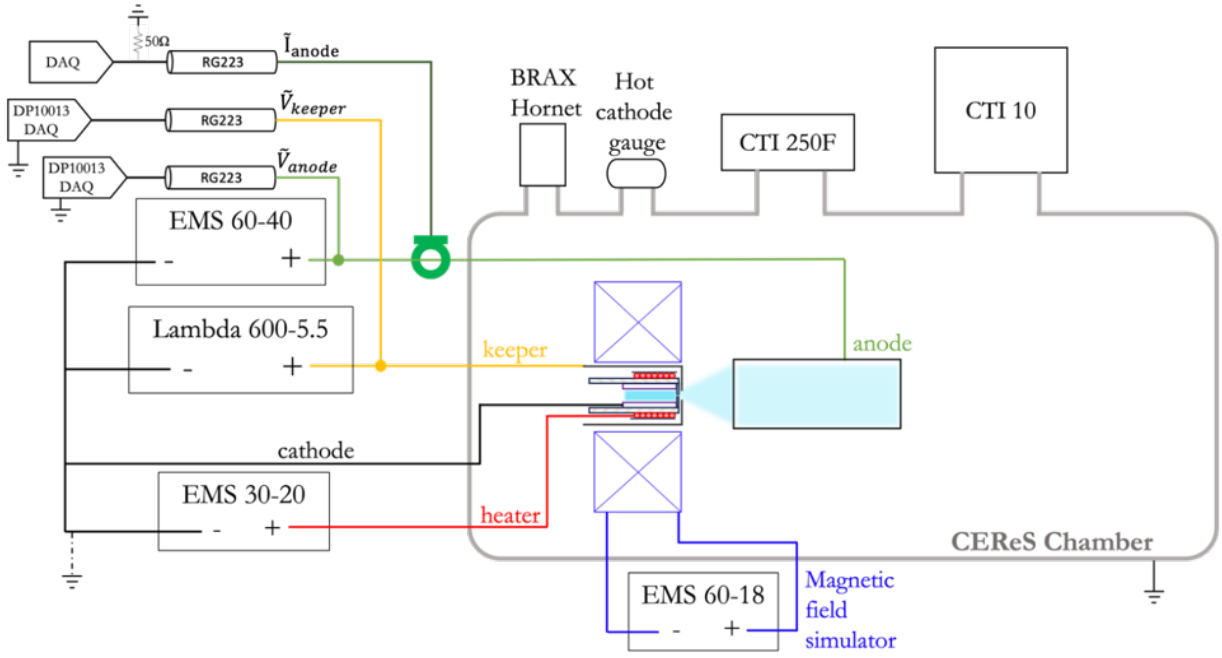

Figure 3.7: Power harnessing for the CEReS chamber at WMU.

A dedicated computer was used for high-speed data acquisition. Two 4-channel GaGe Oscar Express CompuScope CSE 4444 PCIe digitizers were installed into the computer tower and operated on the same clock to ensure simultaneous data acquisitions. Table 3.5 shows the specifications of each digitizer. LabVIEW communicated with the paired digitizers to collect and save high-speed data to the 8-TB hard drives. The computer was a custom-built tower with an Intel Core i9-10900K CPU a with a 3.70GHz clock speed.

Table 3.5: GaGe Oscar Express CompuScope CSE 4444 PCIe digitizer specifications.

Specification	CSE444
Maximum sample rate, per channel	50 MSa/s
Channel bandwidth	65 MHz
Number of channels	4
Vertical resolution	16-bit
Voltage ranges	±100 mV, ±200 mV, ±500 mV, ±1 V, ± 2V, ±10 V, ±20 V, and ±50 V.
DC accuracy	±0.5%
Memory	2 GSa (4 GB)

3.5.1.2 Vacuum Facility 1, NASA Glenn Research Center

Facility. Figure 5.4 shows the Vacuum Facility 1 (VF-1) facility at NASA GRC. VF-1 is a 1.5-m-diameter, 4.5-m-long cylindrical vacuum facility outfitted with with a 0.9-m-diameter cryogenic pump that provides base pressures in the low 10^{-7} Torr range. An ionization gauge mounted behind the hollow cathode exit plane monitored the chamber pressure. All background pressure readings presented in this dissertation from experiments in VF-1 are corrected for xenon.

Figure 3.8: VF-1 at NASA GRC.

Harnessing and Data Acquisition. Figure 3.9 shows the power harnessing of VF-1 at NASA GRC used for this dissertation work. A variety of TDK Lambda Genesys power supplies were used to power the hollow cathode. These supplies included a TDK-LG 80-125 (80-V, 125-A limit) for the anode; a TDK-LG 600-4 (600-V, 4-A limit) for the keeper; a TDK-LG 80-19 (80-V, 19-A limit) for the heater; and a TDK-LG 60-40 (60-V, 40-A limit) for the magnetic coils. The negative end of the power supply terminals were connected to cathode common. Cathode common was left floating for the duration of the work presented in this dissertation.

Tektronix high-voltage probes were used to monitor the keeper, anode, and heater voltages, while in-line resistors with Tektronix high-voltage probes were used to monitor anode current. The high-voltage probes were connected to a multiplexer DAQ. A Tektronix MSO58 oscilloscope was separately used for high-speed probe signals. The MSO58 scope was operated at a 3.125 GSa/s sample rate with 12-bit vertical resolution.

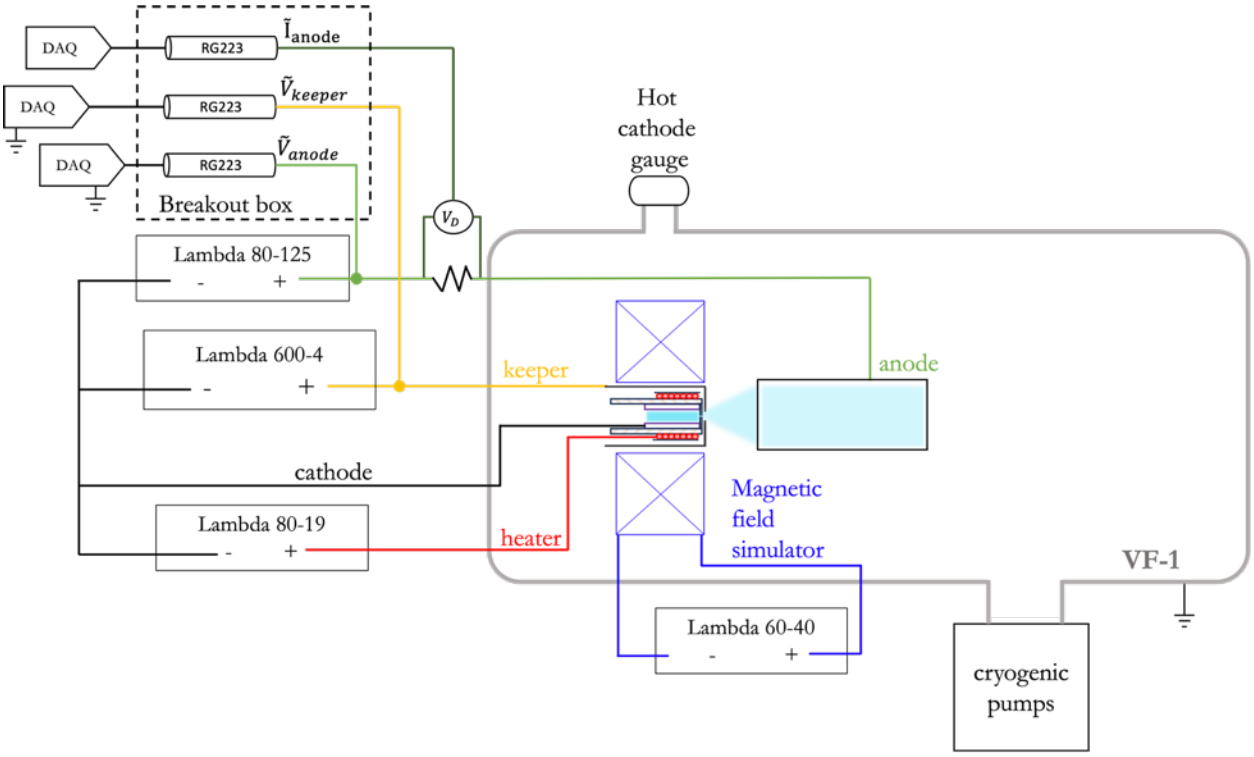

Figure 3.9: Power harnessing of VF-1 at NASA GRC.

3.5.1.3 Cathode Diagnostics Facility, NASA Jet Propulsion Laboratory.

Facility. The work performed at NASA JPL occurred in the cathode diagnostics vacuum facility (figure 3.10). The chamber is a 1-m-diameter and 2-m-long cylindrical vacuum facility. The chamber was outfitted with three cryogenic pumps: two 25-cm-diameter cryogenic tanks and an ALD 200 thumper with a 483-mm-diameter circular cryogenic surface with base pressures in the mid 10^{-7} Torr range. Pressure was monitored with a Granville Phillips Stabil ion gauge calibrated with xenon gas mounted to the chamber door behind the cathode.

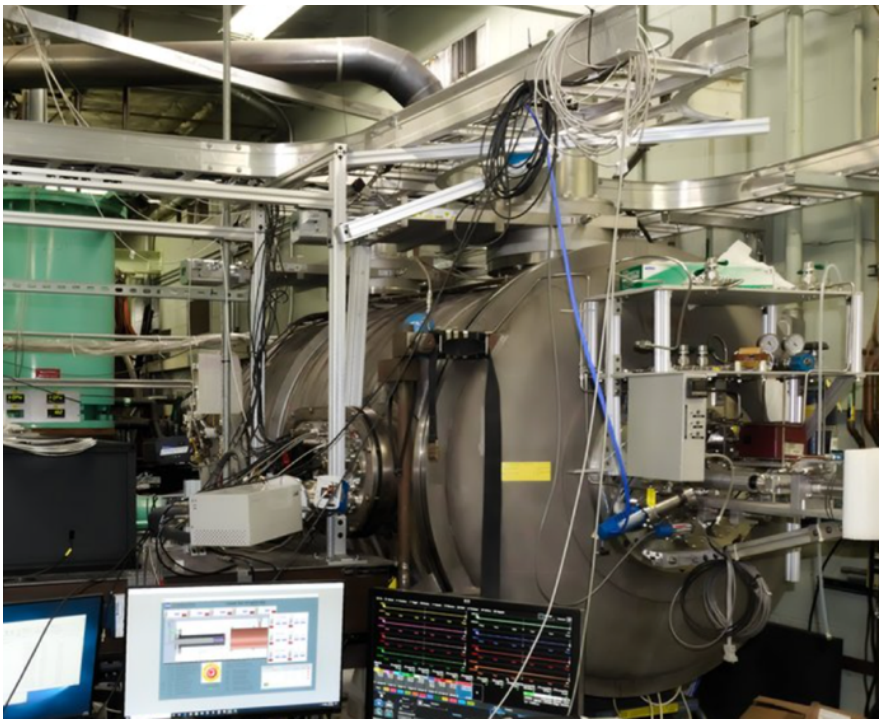

Figure 3.10: Cathode diagnostics facility at NASA JPL.

Harnessing and Data Acquisition. Figure 3.11 shows the power harnessing for the work performed at the NASA JPL cathode diagnostics vacuum chamber. The system used the following power supplies: a Sorensen DCS 50-60 (50-V, 60-A limit) for the anode; a Sorensen DLM 150-4 (150-V, 4-A limit) for the keeper; a Sorensen DLM 40-15 (40-V, 15-A limit) for the heater; and a Power Ten supply was used for the magnetic field simulator. The negative terminals of these three power supplies were connected to the cathode and the cathode was shorted to chamber ground. During testing at NASA JPL, some experiments involved induced current oscillations onto the anode using a Keysight 33600A arbitrary function generator (AFG), an AE Techron 7224 power amplifier, and a 6220-1B isolation transformer in line with the anode supply. The signals that were injected onto the anode are explored in Chapter 6.

An Optomux system (also known as Opto 22) was used to monitor the DC voltages and currents of the cathode operation in addition to chamber pressure, cathode temperatures, and gas flow rate. A PAC Control program interfaces with the Opto 22 boards to record the cathode performance data every second. The high speed anode and

keeper voltages with respect to ground were monitored using Pico Technology TA043 differential probes with selectable attenuation of 10X or 1000X and an upper bandwidth of 100 MHz. High speed discharge current was monitored with a 410 Pearson coil current monitors with bandwidth limits of 1 Hz and 20 MHz. High-speed data were captured on three GaGe Razor Express CompuScope CSE 1642 PCIe digitizers assembled into one computer. Table 3.6 gives the specifications of the CompuScope.

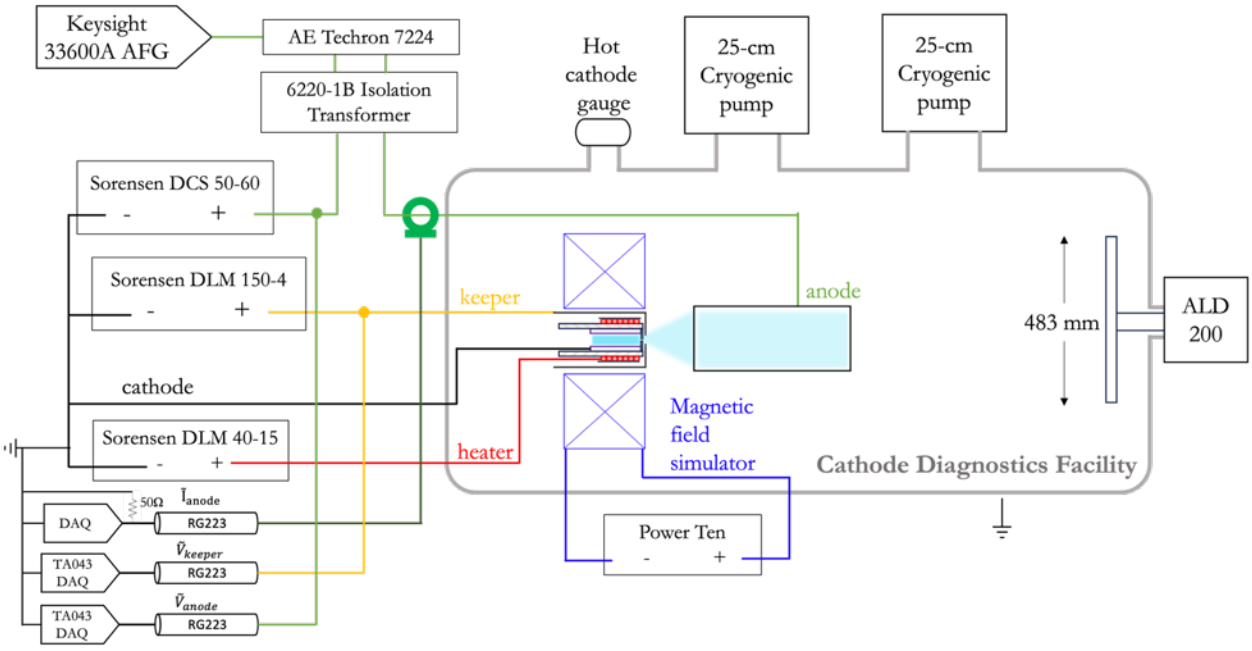

Figure 3.11: Power harnessing of the cathode diagnostic facility at NASA JPL.

Table 3.6: GaGe Oscar Express CompuScope CSE 1642 PCIe digitizer specifications.

Specification	CSE444
Maximum sample rate, per channel	200 MSa/s
Channel bandwidth	10 Hz to 65 MHz
Number of channels	4
Vertical resolution	16-bit
Voltage ranges	±100 mV, ±200 mV, ±500 mV, ±1 V, ± 2V, ±10 V, ±20 V, and ±50 V.
DC accuracy	±0.5%
Memory	4 GSa (8 GB)

3.5.1.4 Plasma Test Facility 1, U.S. Naval Research Laboratory.

Facility. Figure 3.12 shows the Plasma Test Facility 1 (PTF-1) at NRL. PTF-1 is a cylindrical vacuum chamber of 0.75-m-diameter and 1-m-length. It was outfitted with an Agilent Turbo-V and a CTI Cryo-Torr 400 cryopump for a combined ideal pumping speed of 6,950 L/s-air. A Lesker 392 series hot ionization gauge monitored the chamber pressure. PTF-1 achieved a base pressure in the high 10^{-8} Torr range.

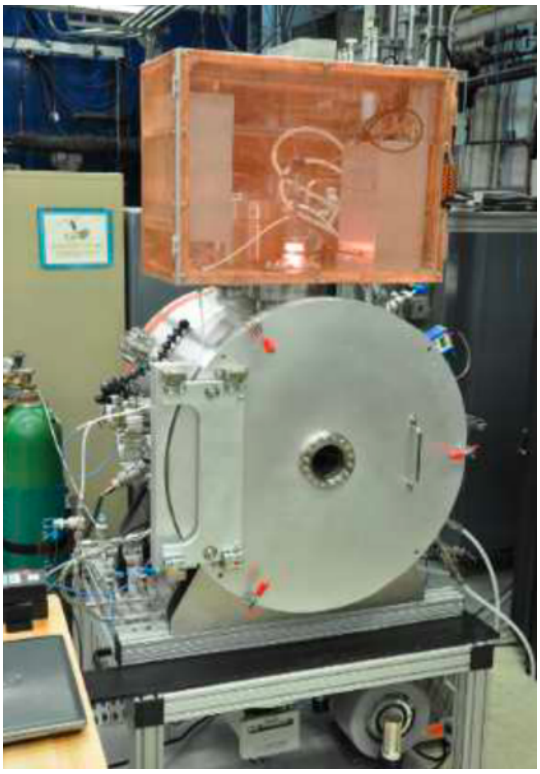

Figure 3.12: PTF-1 at NRL [88].

Harnessing and Data Acquisition. Figure 3.13 shows the power harnessing for PTF-1 at NRL. This setup used the following supplies: a Keysight N5772A 600V, 2.6A supply for the keeper; a Keysight N5769A 100 V, 15 A supply for the heater; a Keysight 1500 W supply for the magnetic field simulator; and a Sorensen 150 A supply for the anode. High-speed probe data was collected on a Tektronix MSO46 Scope. High-speed cathode performance was not monitored for the duration of this test.

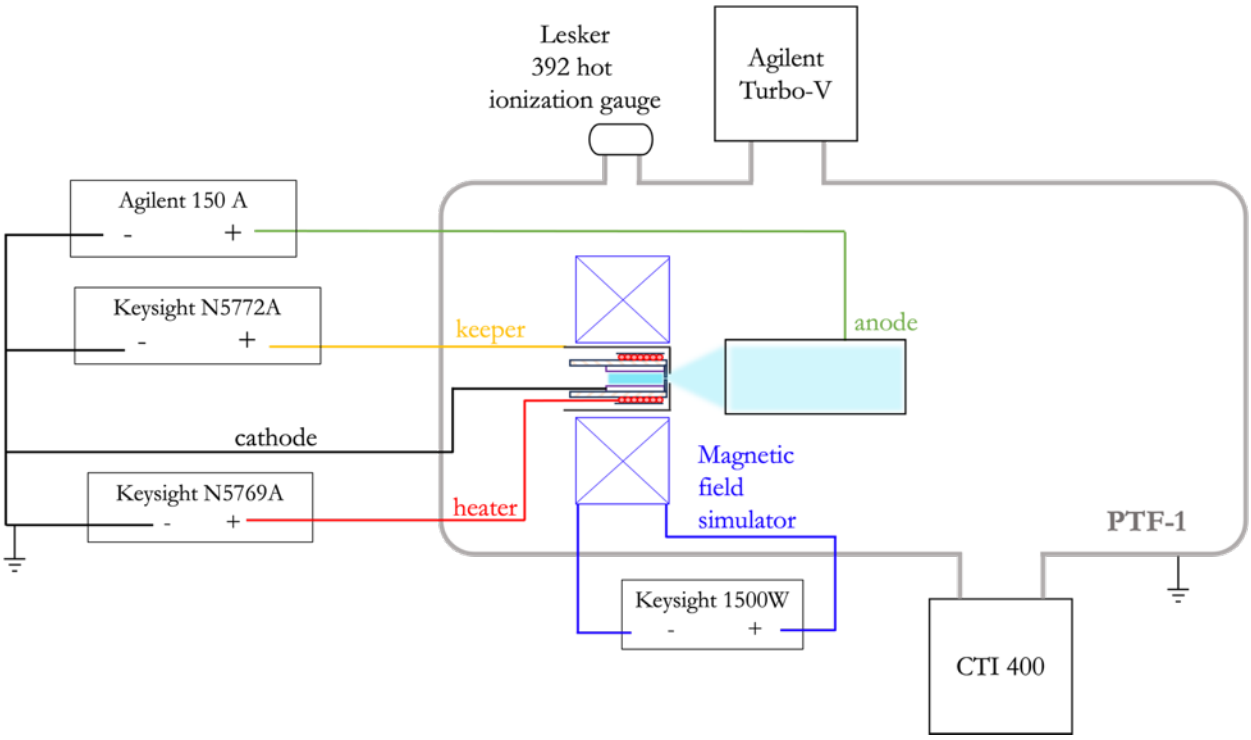

Figure 3.13: Power schematic of PTF-1 at NRL.

3.5.2 Summary of Chamber and Cathode Use

The work presented in this dissertation was performed in various vacuum chambers with unique power harnessing. The base pressures varied between high 10^{-8} Torr to 10^{-7} mid Torr, and the operational pressures varied depending on the pumping speed of the pumps installed on the chamber.

Further, this work utilized three flight-like hollow cathodes:

1. The second generation, 25-A class cathode developed for HERMeS with a barium oxide emitter. Proper conditioning of the cathode was performed prior to running any experiments with this cathode
2. A LaB_6 cathode with the same wetted surfaces as the cathode used for the HERMeS thruster.
3. The H6 hollow cathode with a LaB6 emitter.

Table 3.7 provides a summary of the dimensions and pumping speeds of the facilities used in this work.

Table 3.7: Summary of vacuum facilities and hollow cathodes used in this work.

Facility	Facility dimensions diameter, length [mm]	Ideal pumping speed, L/s-air	Cathode used	Emitter material
WMU, CEReS	[1.0, 1.5]	5,200	H6	LaB_6
NASA GRC, VF-1	[1.5, 4.5]	40,000	Mark II, HERMeS	BaO
NASA JPL, Cathode Facility	[1.0, 2.0]	6,000	HERMeS lab cathode	LaB_6
NRL, PTF-1	[0.8, 1.0]	6,950	H6	LaB_6

.

CHAPTER 4

Azimuthal Wave Onset Investigation

"What we find is that if you have a goal that is very, very far out, and you approach it in little steps, you start to get there faster. Your mind opens up to the possibilities."

Dr. Mae Jemison, Astronaut

4.1 Introduction

The goal of this chapter is to begin to address the first research question of this dissertation: what is the onset of the rotational instability with respect to the magnetic field strength? An iteration of the HERMeS cathode with a cylindrical anode and a magnetic field simulator that provided a magnetic field topography similar to the HERMeS thruster were utilized. The magnetic field, anode position, and mass flow rate were varied to investigate the onset of the rotational instability. High-speed ion saturation probes were azimuthally placed in front of the cathode to capture the azimuthally traveling ion population. Finally, the speed of the ion population was determined based on the time delay of the measured peak ion saturation current at each azimuthal probe.

4.2 Experiment Configuration

Figure 4.1 shows the general schematic of the hollow cathode, anode, and magnetic field simulator setup. The hollow cathode used in this experiment was the second generation, 25-A class cathode developed for HERMeS with a BaO emitter. The anode was constructed of four 50-mm-long, 254-mm-diameter cylinders constructed of molybdenum

sheets separated axially by 2 mm. The anode was segmented for a previous study to investigate the distribution of current along the length of the anode for varying cathode conditions [17], [156]. For the work in this dissertation, each anode segment was connected to a single power supply with a breakout box, effectively creating a single anode of 306-mm-length. The anode was mounted to a linear motion stage, allowing its axial position to be adjusted. This experiment utilized a magnetic field simulator placed upstream of the cathode exit that creates a similar centerline magnetic field profile and strength to HERMeS [15], [55], [57], [58], [157]. This experiment took place in the VF-1 chamber at NASA GRC where the base pressure was low 10^{-7} Torr with an operational pressure of 1.8×10^{-5} Torr-Xe for a cathode flow rate of 14.7 sccm.

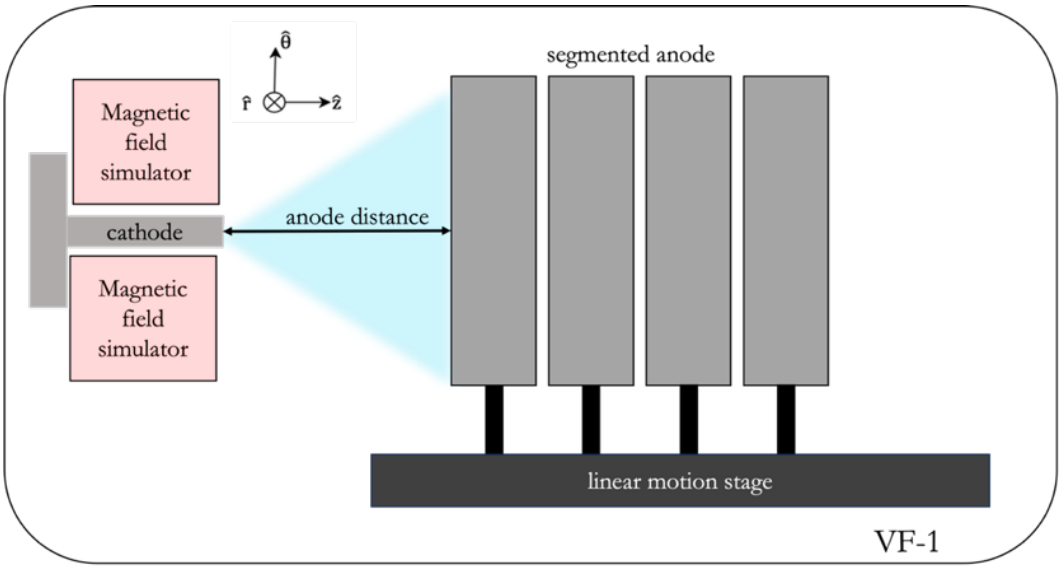

Figure 4.1: Schematic of the hollow cathode setup with upstream magnetic field simulator and segmented anode mounted on a linear motion stage.

Table 4.1 provides a summary of the cathode configurations for this experiment. The cathode was operated at 20.8 A and data were collected at the following conditions: two mass flow rates, 14.7 sccm and 25.0 sccm; varied centerline peak magnetic field strengths between 0 G and 325 G; and two anode separation distances, 68 mm and 120 mm. All magnetic field strengths provided in this chapter refer to the centerline peak

magnetic field strength. The anode separation distance is the length between the cathode exit orifice and the entrance to the anode.

Table 4.1: Summary of cathode operational parameters.

current, A	mass flow rate, sccm	magnetic field strength, G	anode distance, mm
20.8	14.7, 25.0	0-325	Position 1: 68 Position 2: 120

4.2.1 Azimuthal Probe Design

Figure 4.2 shows the orientation of the ion saturation probes downstream of the cathode exit and the axis convention. The origin of the reference frame was the center of the keeper orifice of the cathode. The probes were mounted azimuthally on an aluminum frame such that the arc angle between a single probe pair was 90°. The probe array was installed 20 mm downstream of the exit plane of the cathode. The electrode element of each probe was a tungsten wire protruding from telescoping alumina tubes such that only a small portion of the wire was exposed to the plasma. Figure 4.3 shows a picture of the setup installed in the VF-1 facility.

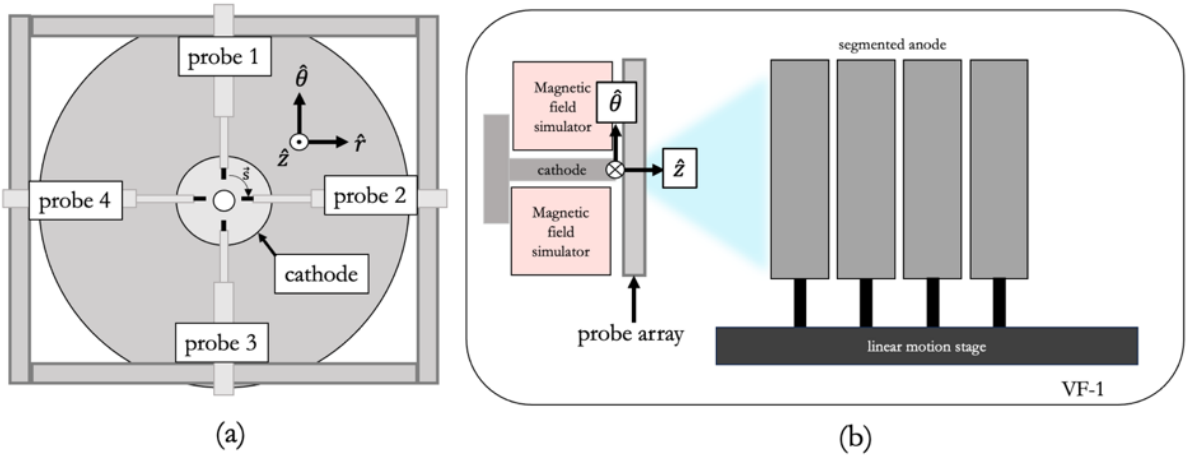

Figure 4.2: Schematic of the experimental setup. (a) ion saturation probe array and (b) probe array orientation in the setup between the cathode and anode.

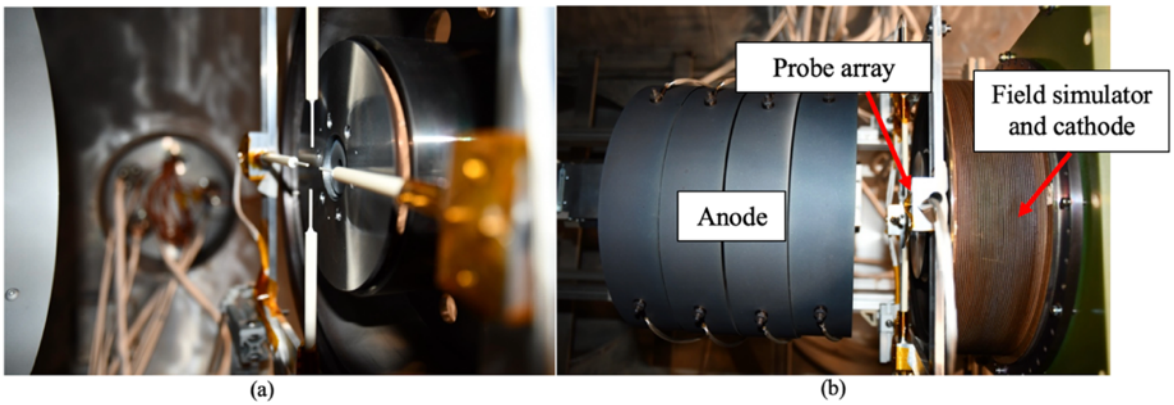

Figure 4.3: Installation of ion saturation probe array in cathode setup. (a) View of ion saturation probe array in front of the cathode exit and (b) placement of the array between the anode and cathode.

Figure 4.4 shows the electrical schematic of the ion saturation probe array. The probes were biased to -27 V using a series of 9-V batteries. The time-resolved ion saturation current was measured using the voltage drop across four 100-Ω shunt resistors and was collected using a Tektronix MSO58 oscilloscope. Each channel collected data at a sample rate of 3.125×10^8 samples per second with a sample window of 40 ms.

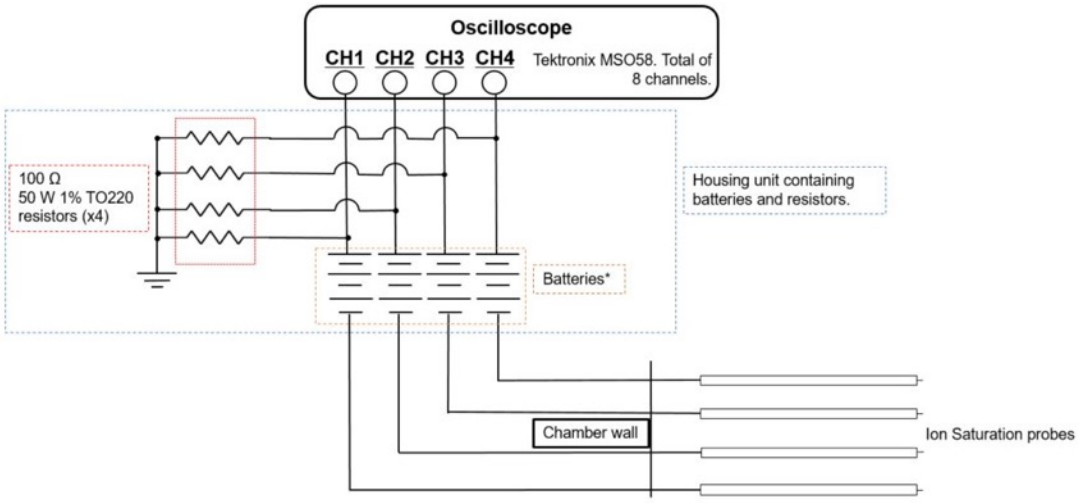

Figure 4.4: Electrical schematic for ion saturation probe measurement.

4.2.2 Limited Bandwidth with Shunt Resistors

Figure 4.5 shows an LT Spice simulation of the shunt resistor current collection mechanism for the work presented in this chapter. Approximately 20 ft of coax cabling

was used between the battery and the probe tip and from the resistor and the oscilloscope. This correlates to a transmission line delay of 20 ns for each line length (figure 4.5(a)). The LT Spice simulation shows an expected -3dB limit of 1 MHz. This gives an approximate Nyquist frequency of 500 kHz (figure 4.5(b)). Therefore, the analysis of these data presented in this chapter must be interpreted with the knowledge that signals oscillating at frequencies greater than 500 kHz are likely attenuated. Further, this bandwidth limit was not verified with the experimental setup and the true bandwidth could be potentially lower than the ideal LT Simulation.

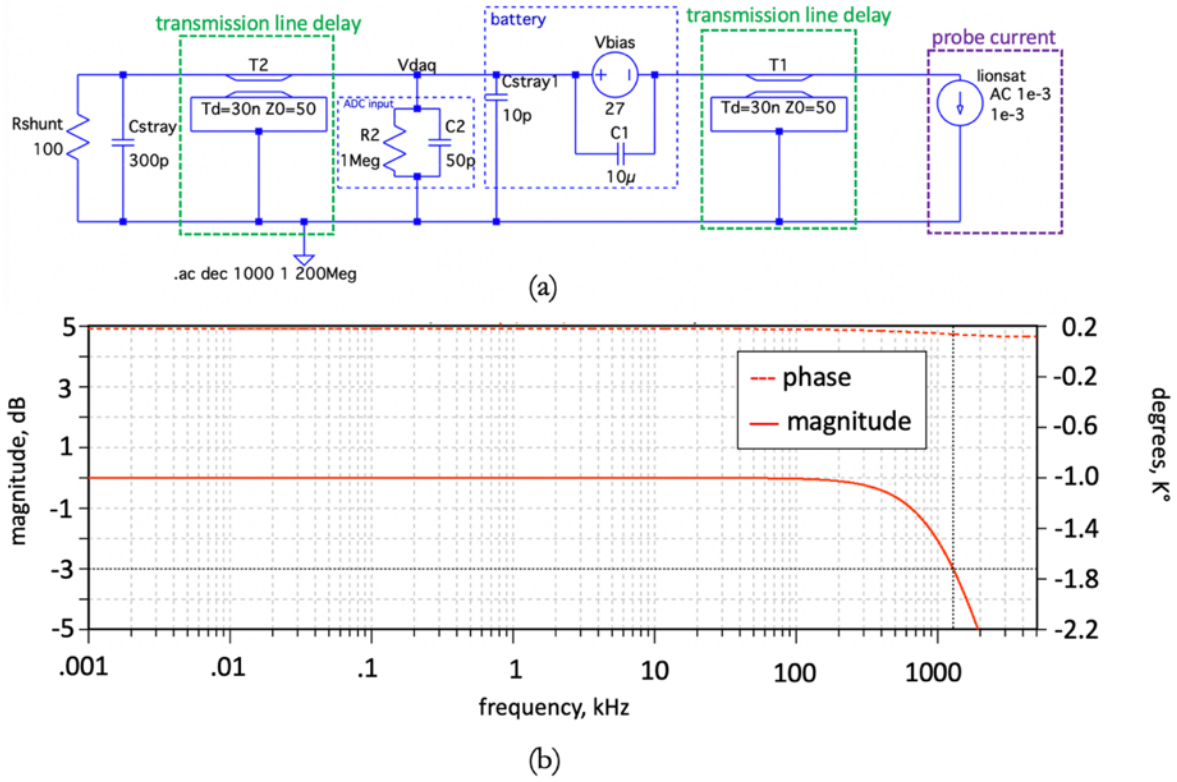

Figure 4.5: LT Spice simulation of probe current collection using an in-line resistor. (a) Circuit schematic of the shunt resistor with included expected transmission line delay and (b) the magnitude and phase showing the bandwidth limit of approximately 1 MHz.

4.3 Cathode Performance Measurements

Figure 4.6 shows the trend of discharge voltage, which is measured between the anode and cathode as shown in figure 3.9, and cathode-to-ground voltage with increasing magnetic field strengths. These trends can be separated into two regimes: above and below

50 G. The discharge voltage exhibits an initial transitory spike for both anode positions at the 14.7-sccm flow condition and for anode position 1 at the 25.0-sccm flow rate condition below 50 G. For anode position 2 at the 25.0-sccm flow rate condition, the discharge voltage decreases slightly before increasing for increasing magnetic field strengths. Above 50 G, the discharge voltage is positively correlated with magnetic field strength (figure 4.6(a)). The cathode-to-ground voltage exhibits similar behavior with an initial transitory spike decreasing in magnitude (closer to ground) with increasing magnetic field for all cathode operating conditions. Above 50 G, the magnitude of the cathode-to-ground voltage increases for increasing magnetic field strengths (figure 4.6(b)). Since the discharge current is held constant, the increasing discharge voltage and cathode-to-ground voltages for increasing magnetic field strength suggests the plasma resistivity is increasing. One explanation for this could be the confinement of electrons on magnetic field lines. As described in section 2.3.4.2, a strong magnetic field strength can confine the electron motion along the magnetic field lines, which restricts their motion to the anode surface. The diameter of the anode, 254 mm, is large enough that only some of magnetic field lines near the cathode exit impact the anode surface [125], [127]. This suggests the electrons must collide with other particles or be transported via turbulent mechanisms to reach the anode. This effect increases for increasing magnetic field strengths.

The rate of the increasing discharge voltage decreases for increasing magnetic field strengths; however, the discharge voltage does not appear to saturate for the magnetic field strengths tested. At the 14.7-sccm condition, the anode position affects the slope of the increasing anode voltage, with anode position 2 (120 mm separation between the cathode exit and the anode entrance) resulting in higher discharge voltages. The lower flow rate conditions and the farther anode position both result in greater cathode-to-ground voltages for magnetic field strengths above 50 G. This makes sense as the anode is placed farther downstream, less magnetic field lines impact the internal anode surface. Therefore, the plasma resistivity likely increases to achieve the DC current supply that

powers the anode. The discharge voltage at the 25.0-sccm conditions is lower than the 14.7-sccm conditions at equivalent magnetic field strengths This suggests that the mechanisms that heat the electrons and increases the plasma resistivity are damped by an increase in neutral pressure. Further, the anode position does not appear to affect the discharge voltage for increasing magnetic field strengths at the 25.0-sccm flow condition. It is possible that the heightened neutral density sufficiently increases the electron-neutral collision frequency which aids in the electron transport to the anode while the turbulent mechanisms are less impactful for the higher flow rate. This is explored further in section 4.5.1.

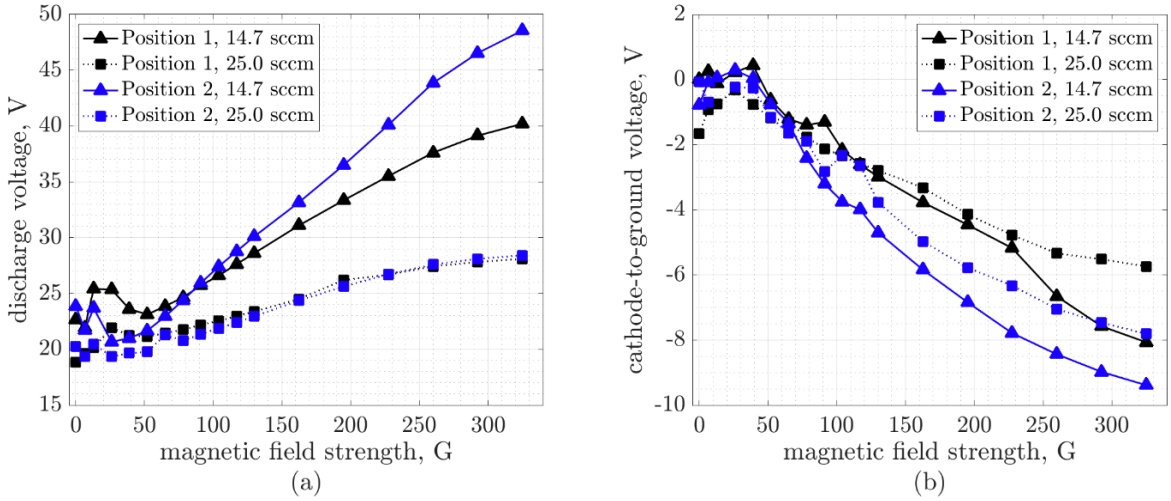

Figure 4.6: Time-averaged cathode performance metrics for increasing magnetic field strengths at both anode positions and flow conditions. (a) discharge voltage and (b) cathode-to-ground coupling voltages.

4.4 High-Speed Ion Saturation Data

Figure 4.7 shows the raw ion saturation current measured from all probes at the 14.7-sccm flow rate condition for three magnetic field conditions: without a magnetic field, with the applied magnetic field at 260 G (figure 4.7(b)), and with the magnetic field at 260 G in the reverse direction (figure 4.7(c)). Each probe signal is smoothed using a Savitsky-Golay filter for clarity and is shown with the raw data shown in the background

in grey. Without the applied magnetic field and at 14.7 sccm, the magnitude of the ion saturation current oscillations is approximately 1 mA. This peak-to-peak current increases with the application of the magnetic field at 260 G to greater than 3 mA. Further, the field excites the ion population to rotate counterclockwise about the axial direction ($\hat{z}$) as observed by a maximum in the measured ion current at each probe and indicated by arrows in figure 4.7(b) and figure 4.7(c). Notably, when the magnetic field direction is reversed (figure 4.7(c)), the rotating ion population also reverses direction (clockwise about $\hat{z}$), strongly suggesting this mode depends on the magnetic field direction.

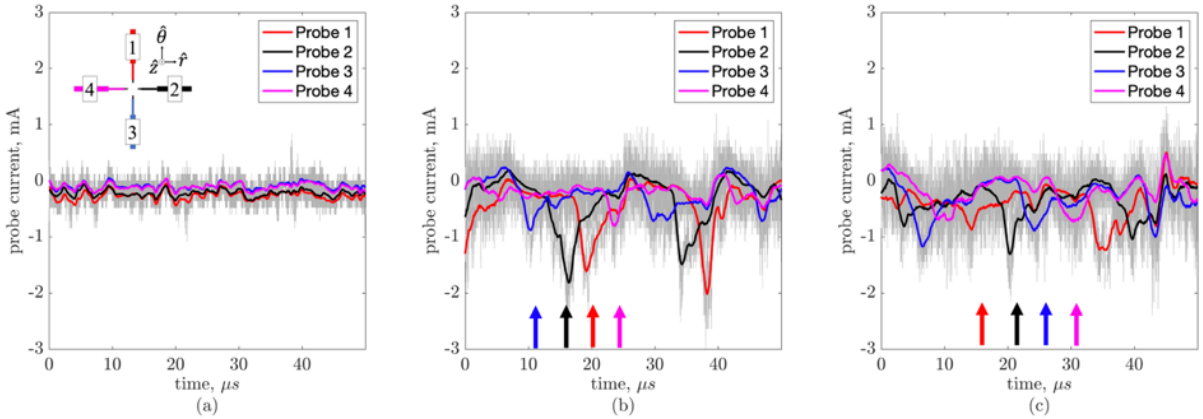

Figure 4.7: Raw time signal from each probe at the 14.7-sccm flow rate condition, and anode position 1 for magnetic field strengths of (a) 0 G, (b) 260 G, and (c) -260 G.

Figure 4.8 shows the evolution of the mean ion saturation current (figure 4.8(a)) and the peak-to-peak magnitude of the oscillations (figure 4.8(b)) in the ion saturation current measured at probe 1 for increasing magnetic field strengths. When the flow rate is 14.7 sccm, the mean ion saturation current generally saturates after 33 G for both anode positions; however, the magnitude of the ion saturation current anode at position 1 (68 mm separation between cathode exit and anode entrance) is greater than the magnitude at anode position 2 (120 mm separation). The difference in ion saturation current suggests that at the 14.7-sccm condition, the ion number density at the probe location is greater when the anode is closer to the cathode exit. Alternatively, the magnitude of the ion saturation current exhibits a consistent gradual increase for both anode positions with no apparent saturation for the 25.0-sccm flow rate condition. This behavior is similar to the

cathode performance metrics shown in figure 4.6 where the anode position did not affect the discharge voltage or the cathode-to-ground voltage at the 25.0-sccm condition. This is explored further in section 4.5.

The magnitude of the peak-to-peak ion current oscillations in the ion saturation current increases with increasing magnetic field strength above 33 G and appears to be independent of the flow rate and the anode position. Figure 4.7 shows that the azimuthal dynamic is the primary contributor to the peak-to-peak amplitude of the ion saturation current. Therefore, the increase in the magnitude of the ion saturation current oscillations shown in figure 4.8(b) suggests the azimuthal wave is less affected by the changes in anode position and mass flow rate.

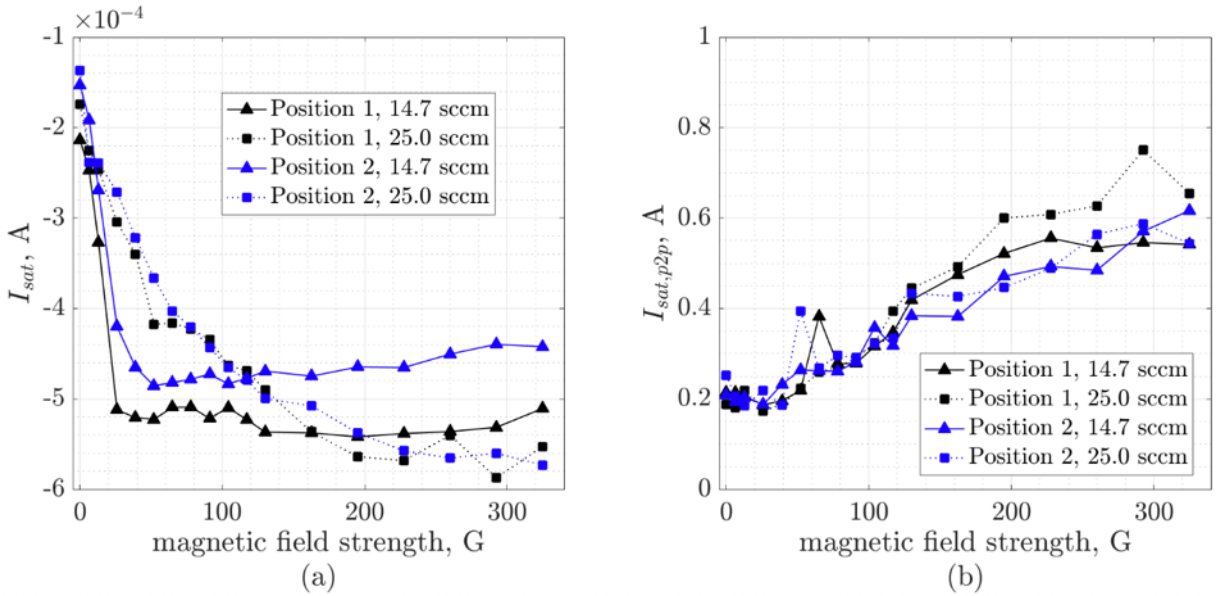

Figure 4.8: Effect of magnetic field strength on the ion saturation current from probe 2. (a) Mean ion saturation current and (b) magnitude of peak-to-peak ion saturation current.

4.4.1 Phase Offset Analysis

Figure 4.9 shows the raw data ion saturation current filtered with a Savitzky–Golay filter (figure 4.9 (a)), frequency spectra (figure 4.9(b)), and statistical dispersion from the Beall method outlined in section 3.4.2.5 (figure 4.9(c)) for probe 1 and probe 2 at anode position 1 and the 14.7-sccm flow rate condition and a magnetic field strength of 325 G. Since the

probes are oriented azimuthally, the wavenumber is corrected to mode number by $m = r * \kappa(\omega)$, where r is the radial position of the measurement with respect to the cathode centerline and $\kappa(\omega)$ is the wavenumber. The arc length between the probes limits the measurable wavenumber; therefore, the Beall plot is concatenated to show aliasing. The time delay between ion saturation current peaks in the two probe signals paired with the Fourier transform shows that this azimuthal wave exists at a frequency of 50 kHz and is dominant against all waveforms in the signals. The difference in the measured peak-to-peak ion saturation current between probe 1 and probe 2 is likely due to a difference in the probe surface areas as a result of imperfect probe construction. Further, the Beall analysis shows this wave exhibits an m=1 behavior (shown as a peak in S(ω,k) at 50 kHz and a mode number of 1).

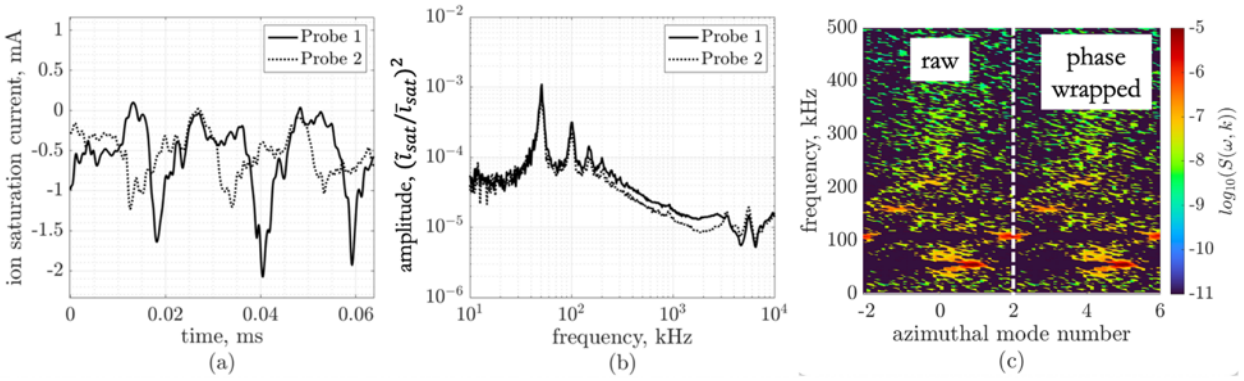

Figure 4.9: Frequency spectra analysis from probe 1 and probe 2 at the 325-G, 14.7-sccm, anode position 1 condition. (a) Raw current traces, (b) Fourier transform, and (c) statistical dispersion plot generated using the Beall method concatenated showing the m=1 behavior.

Figure 4.10 shows the Fourier spectra for probe 1 with the cathode operated at the 0-G and 325-G conditions and at both anode positions. For the 0-G cases (figure 4.10(a) and figure 4.10(c)), increasing the flow rate from 14.7 sccm to 25.0 sccm results in a decrease in the spectral power of the low frequency behavior (O(1-10 kHz)) and the high frequency peak (O(1,000 kHz)). The decrease in the high-frequency behavior is consistent with collisional neutral damping of high-frequency turbulence, such as IAT, at the higher mass flow rate condition. At anode position 2 and 0 G, the 14.7-sccm condition shows a

narrow-band peak at 2 kHz which is damped at 25.0 sccm. This behavior is consistent with characteristics of plume mode operation, described in section 2.3.4.1, as increasing the mass flow rate at a fixed discharge current reduces the $I_D/\dot{m}$ ratio. Higher $I_D/\dot{m}$ ratios typically lead to plume-mode oscillations, which could be linked to ionization instabilities.

For the 325-G conditions (figure 4.10(b) and figure 4.10(d)), increasing the flow results in an increase in the frequency of the narrow-band low frequency peak (O(50 kHz)) for anode position 1, but the frequency remains unchanged between the two flow rates for anode position 2. This frequency correlates with the large-scale oscillations captured in the time-resolved ion saturation probe current shown figure 4.7 at a similar operating condition where the magnetic field strength was at 260 G. As the anode is moved farther away, the divergence angle of the plasma can change, which could result in a change in the density near the probe measurement and could change the frequency of the rotational mode. For example, the dispersion relation of the azimuthal anti-drift instability is dependent upon the density via the diamagnetic drift (eq. (2.50)). The change in density gradient as a function of the increasing cathode-to-anode separation is explored in section 4.5. Furthermore, increasing the flow rate results in a lower spectral power of the high-frequency mode (O(3,500 kHz)) for anode position 2. The high-frequency mode is less affected by the increase in mass flow rate for anode position 1. Both the electric field changes and the number of magnetic field lines impacting the anode surface change when the anode position is increased (from anode position 1 to anode position 2). The reduction of number of magnetic field lines impacting the anode could result in enhanced turbulence to facilitate the electron transport across the magnetic field lines to the anode.

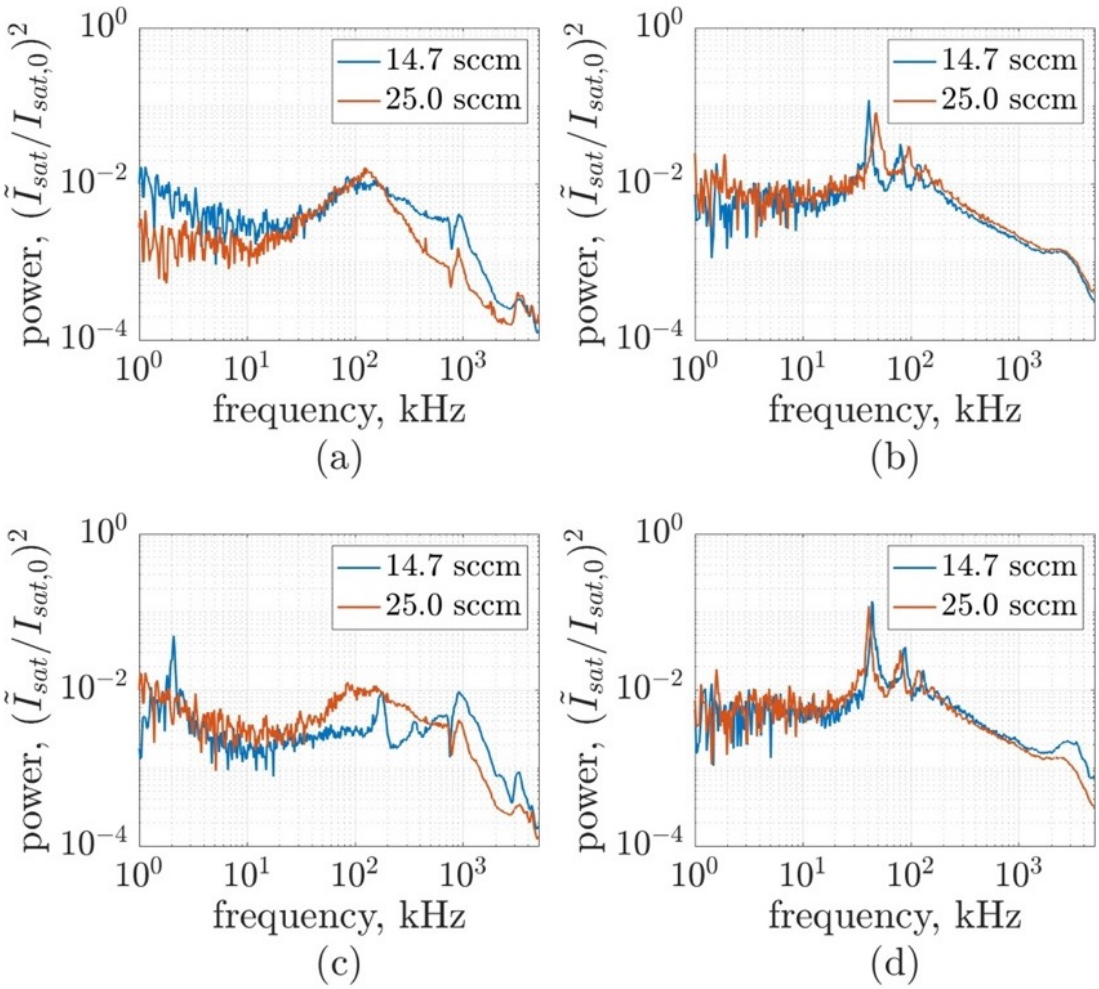

Figure 4.10: Fourier spectra of probe 1 at varying flow rates for (a) 0 G, anode position 1, (b) 325 G, position 1, (c) 0 G, position 2, and (d) 325 G, position 2.

Figure 4.11 shows the evolution of the frequency spectra for increasing magnetic field strengths. Figure 4.11 (a) shows the high-frequency domain up to 4,000 kHz and the low-frequency behavior is magnified to better display the growth of 50-kHz wave in figure 4.11 (b). The 50-kHz mode dominates the frequency domain at magnetic field strengths above 50 G, and the frequency of this mode increases with increasing magnetic field strengths. The frequency peak at 3,500 kHz grows in spectral power simultaneously with the increasing frequency of the azimuthal 50-kHz mode. Note that the signal is likely attenuated above 500 kHz due to the measurement technique used in this analysis. Thus, the amplitude of the high-frequency turbulence is likely higher than what was measured.

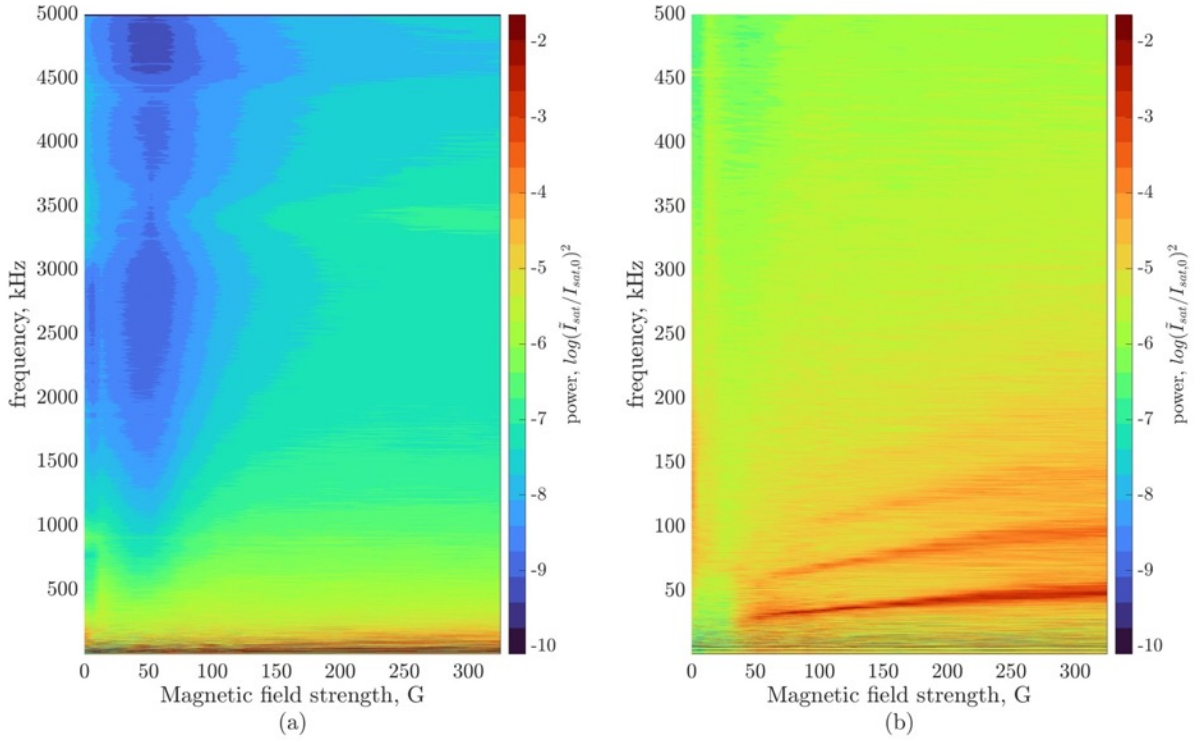

Figure 4.11: Frequency spectra for the position 2, 14.7-sccm flow rate condition across all magnetic field strengths.

Table 4.2 summarizes the characteristics of the low and high-frequency peaks observed in the probe 1 ion saturation current. The low-frequency peak without the magnetic field decreases in frequency and exhibits increased spectral bandwidth, as indicated by an increase in the full width at half maximum (FWHM), when the mass flow is increased. At the 25.0-sccm flow rate condition and anode position 1, the FWHM of this low-frequency peak is 167% larger than the 14.7-sccm flow rate condition at anode position 1. At anode position 2, the FWHM is 383% greater for the 25.0-sccm flow rate condition compared to the 14.7-sccm condition. This broadband growth with increasing flow rate suggests this mode has become more turbulent and that the instability is dependent on the position of the anode downstream. Further information regarding the axial and radial wave propagation combined with high-speed current fluctuations of the discharge is required to determine the source of the instability. Chapter 6 explores the propagation of this oscillation mode. Additionally, the high-frequency mode increased in power and spectral bandwidth with increasing anode separation distance with no magnetic

field, suggesting the wave energy grows with a larger cathode-to-anode coupling distance for this condition.

At 325 G, the FWHM of the low-frequency mode is less than 10 kHz at all conditions. The clear high-frequency peak is no longer measurable at the 25.0-sccm flow rate condition. It is possible the high-frequency mode is still present in the higher flow rate conditions but is masked by the low-frequency dynamics. Nonetheless, the high-frequency peak is not prominent compared to the 14.7-sccm flow rate condition; thus, a spectral power is not listed in table 4.2.

Table 4.2: Frequency, full-width half max, and power of instability modes measured at varying anode positions and cathode operating conditions.

Anode Position	Operating Condition	Low-frequency peak			High-frequency Peak		
		Frequency, kHz	FWHM, kHz	Power, $\left(\tilde{I}_{sat}/I_{sat,0}\right)^2$	Frequency, kHz	FWHM, kHz	Power, $\left(\tilde{I}_{sat}/I_{sat,0}\right)^2$
1	0 G, 14.7 sccm	170	45	6.7×10^{-3}	930	198	7.0×10^{-3}
	0 G, 25.0 sccm	120	120	15×10^{-3}	895	39	1.5×10^{-3}
2	0 G, 14.7 sccm	175	29	9.4×10^{-3}	895	202	8.8×10^{-3}
	0 G, 25.0 sccm	85	140	12×10^{-3}	905	143	3.5×10^{-3}
1	325 G, 14.7 sccm	50	4.5	1.0×10^{-1}	3414	151	1.8×10^{-3}
	325 G, 25.0 sccm	47	7.3	0.8×10^{-1}	-	-	-
2	325 G, 14.7 sccm	43	2.0	1.5×10^{-1}	3393	103	2.5×10^{-3}
	325 G, 25.0 sccm	40	3.0	1.4×10^{-1}	-	-	-

The data presented in table 4.2 are supported by the dispersion plots generated using the Beall analysis technique (figure 4.12 and figure 4.13). Figure 4.12 provides the azimuthal mode number of the high frequency modes. In the unmagnetized cases (figure 4.12 (a)-(d)), no azimuthal dispersion is measured as the probes show no azimuthal phase offset ($S(\omega, k)$ is centered about $m = 0$). For the magnetized cases at a flow rate of 14.7 sccm at both anode positions (figure 4.12(e)- figure 4.12(h)), the 3,500-kHz peak appears to exhibits some azimuthal dispersion. At the magnetized 25.0-sccm condition, the 3,500-kHz peak is damped, and therefore, it is difficult to determine clear azimuthal dispersion from the Beall analysis.

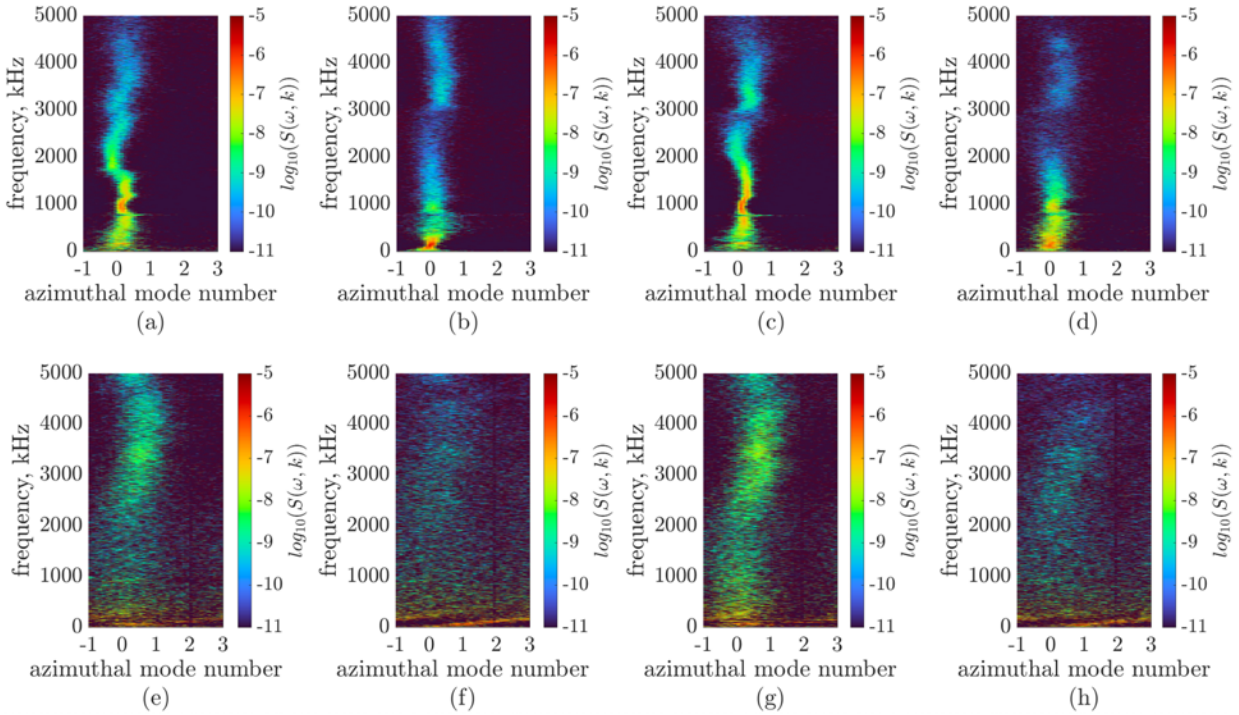

Figure 4.12: Dispersion plot showing azimuthal mode number for all cathode conditions and for frequencies up to 5,000 kHz. (a)-(d) 0 G and (e)-(h) 325 G (a) and (e): position 1, 14.7 sccm (b) and (f) position 1, 25.0 sccm (c) and (g) position 2, 14.7 sccm, and (d) and (h) position 2, 25.0 sccm.

Figure 4.13 shows the dispersion plots generated using the Beall technique focused on frequencies up to 500 kHz. Without the magnetic field, the low frequencies show no azimuthal dispersion. The absence of the magnetic field means the azimuthal drift due to the cross electric and magnetic fields is not excited. With the maximum magnetic field, the low-frequency peak is present for all cathode operating configurations and manifests as an $m = 1$ mode at the probe location. The frequency of the $m = 1$ mode varies for anode position and flow rate; however, the magnitude of the statistical dispersion remains relatively constant across all conditions.

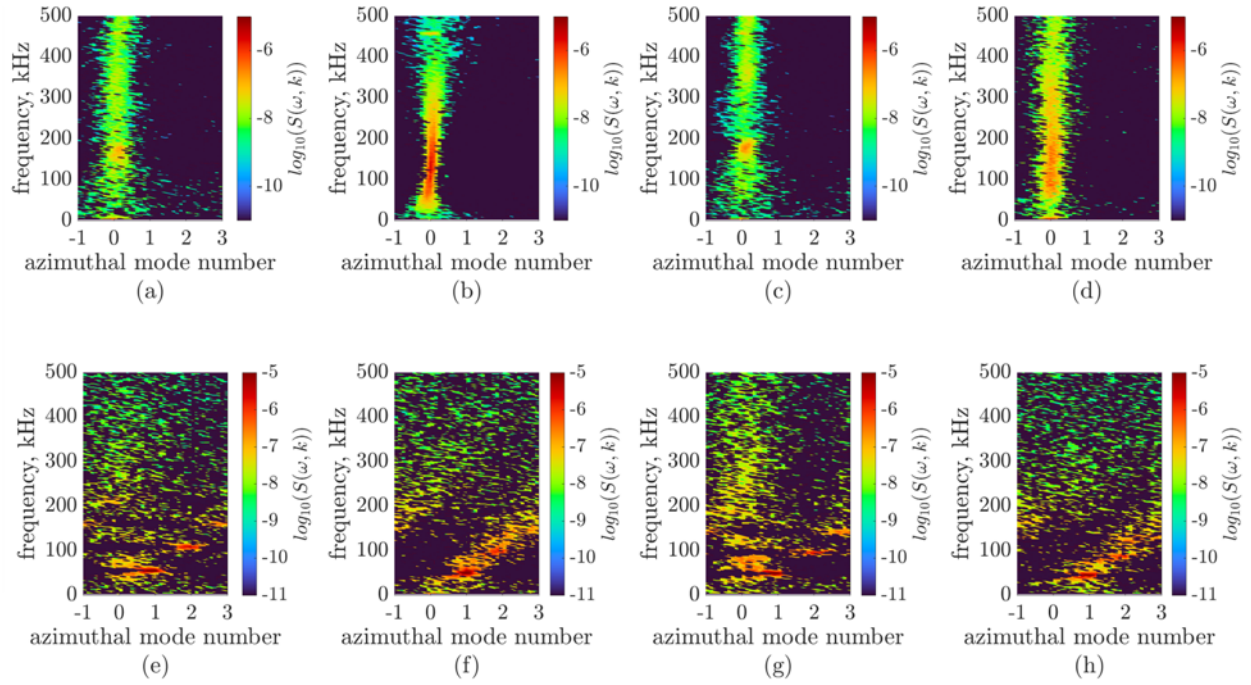

Figure 4.13: Dispersion plot showing azimuthal mode number for all cathode conditions and for frequencies up to 500 kHz. (a)-(d) 0 G and (e)-(h) 325 G (a) and (e): position 1, 14.7 sccm (b) and (f) position 1, 25.0 sccm (c) and (g) position 2, 14.7 sccm, and (d) and (h) position 2, 25.0 sccm.

4.4.2 Estimation of Wave Speed

The ion saturation current from the azimuthally placed probes can be used to determine the drift speed of the ion population, assuming the azimuthal oscillation remains as an m=1 mode. First, the time delay of the rotation is defined as:

$$\Delta t = \frac{\phi_{\text{off}}}{360}\frac{1}{f} \tag{4.1}$$

where ϕ_{off} is the phase offset of the probe measurements (ϕ_{off}=90°), and f is the frequency of the oscillation obtained from the Fourier spectra. The ion drift speed in the azimuthal direction can then be calculated as:

$$v_\theta = \frac{s}{\Delta t} \tag{4.2}$$

where s is the arc between a pair of probes in the diagnostic array.

Figure 4.14 shows the ion drift speed for increasing field strengths above 33 G where the azimuthal mode becomes dominant for all cathode conditions. The right y-axis

of figure 4.14 shows the correlated frequency peak value since v_θ correlates linearly with frequency. Between 65 G and 135 G, the drift speed is higher when the anode closer to the cathode exit (position 1). Additionally, the flow rate in this magnetic field regime does not appear to affect the speed of the azimuthal ion population. For magnetic field strengths above 150 G, both anode position and flow rate affect azimuthal drift speeds, with increased anode separation distance and higher flow rate leading to slower drift speeds.

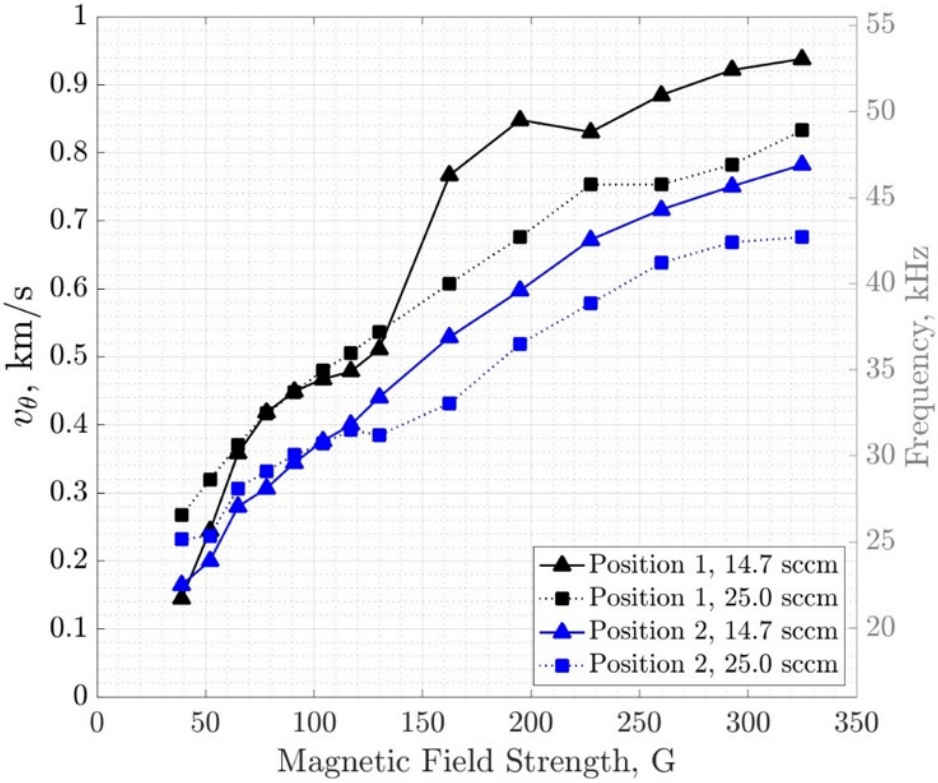

Figure 4.14: Ion population velocity for increasing magnetic field strengths of the low-frequency azimuthal mode.

4.5 Discussion

When the cathode is exposed to magnetic field strengths similar to those in the HET geometry, large-scale oscillations in the density of the downstream plasma are initiated, manifesting as peaks in the azimuthally placed probe current signals. The probe data show the frequency of the oscillation is around 50 kHz at the probe location and the dynamic

exhibits an $m = 1$ behavior. The frequency and spectral behavior of this mode is consistent with the azimuthal mode discussed in Chapter 2. This section explores the azimuthal behavior coupled with the cathode performance metrics.

4.5.1 Threshold for Magnetized Electrons

The magnetization condition in this experiment can be evaluated by using the techniques for determining particle magnetization, as defined in section 3.3.3. Using the anode diameter as the characteristic length (Larmor radius condition, eq. (2.46)) and approximating the total collision frequency as the Coulomb collision frequency (Hall parameter condition, eq. (2.47)), the ions remain unmagnetized for all magnetic fields tested. However, at the location of measurement the Larmor and Hall parameter magnetization conditions are both satisfied for the electrons above the peak centerline magnetic field of 65 G. Physically, this means for magnetic field strengths above 65 G, the electrons are confined around the magnetic field lines. The magnetic field lines near the cathode exit are primarily axial and the magnetic field lines that intersect with the keeper face do not impact the anode for the configuration used in this setup [125], [127]. Therefore, the electrons must collide with other particles or be transported via turbulent mechanisms to reach the anode and complete the plasma circuit. Mathematically, this process can be shown beginning with the electron momentum equation defined as [38]:

$$m_e n_e \frac{\mathrm{d}\vec{u}}{\mathrm{d}t} = q n_e\left(\vec{E} + \vec{u} \times \vec{B}\right) - \nabla p - m_e n_e \nu(\vec{u} - \vec{u}_0) \tag{4.3}$$

where $\nabla \mathrm{p}$ is the pressure tensor and ν is the total collision frequency. The steady-state electron momentum equation assuming the plasma is isothermal becomes:

$$0 = -q n_e\left(\vec{E} + \vec{u}_e \times \vec{B}\right) - qT\nabla n_e - m_e n_e\left((\vec{u}_e - \vec{u}_i)\nu_{\mathrm{ei}} + (\vec{u}_e - \vec{u}_n)\nu_{\mathrm{en}}\right) . \tag{4.4}$$

By assuming the electron velocity is significantly greater than the ion or neutral velocities, the x and y electron velocity components become:

$$u_x = -\mu_e E_x - D_e \frac{\partial n_e}{\partial x} \pm \mu_e u_y B \tag{4.5}$$

and

$$u_y = -\mu_e E_x - D_e \frac{\partial n_e}{\partial y} \mp \mu_e u_x B \tag{4.6}$$

where the mobility and diffusion coefficients are defined as:

$$\mu_e = \frac{q}{m_e \nu_e} \tag{4.7}$$

and

$$D_e = \frac{qT}{m_e \nu_e} \ . \tag{4.8}$$

Solving the series of equations for u_x and u_y gives:

$$u_y = \frac{1}{(1+\omega_{c,e}^2/\nu_e^2)} \left[-\mu_e E_y - \frac{D_e}{n_e}\frac{\partial n_e}{\partial y} - \frac{\omega_{c,e}^2}{\nu_e^2}\frac{E_x}{B} \pm \frac{\omega_{c,e}^2}{\nu_e^2}\frac{qT}{B}\frac{1}{n}\frac{\partial n_e}{\partial x} \right] \tag{4.9}$$

and

$$u_x = \frac{1}{(1+\omega_{c,e}^2/\nu_e^2)} \left[-\mu_e E_x - \frac{D_e}{n_e}\frac{\partial n_e}{\partial y} - \frac{\omega_{c,e}^2}{\nu_e^2}\frac{E_y}{B} \mp \frac{\omega_{c,e}^2}{\nu_e^2}\frac{qT}{B}\frac{1}{n_e}\frac{\partial n_e}{\partial y} \right] \tag{4.10}$$

where the last two terms account for the $\vec{E} \times \vec{B}$ and diamagnetic drifts, respectively. The first two coefficients are often referred to as the perpendicular mobility and diffusion coefficients:

$$\mu_\perp = \frac{\mu}{1+\omega_{c,e}^2/\nu_e^2} \tag{4.11}$$

and

$$D_\perp = \frac{D}{1+\omega_{c,e}^2/\nu_e^2} \tag{4.12}$$

where the ratio of $\omega_{c,e}^2/\nu_e^2$ is the Hall parameter, Ω. Eq.'s (4.11) and (4.12) show that an increase in the magnetic field strength causes a decrease the perpendicular mobility and diffusion, confining the electrons to the field lines. The perpendicular electron velocity is found by substituting eq.'s (4.11) and (4.12) into eq.'s (4.9) and (4.10):

$$\vec{u}_{e,\perp} = -\mu_\perp \vec{E} - D_\perp \frac{\nabla n_e}{n_e} + \frac{u_{E\times B} + u_d}{1+\nu_e^2/\omega_{c,e}^2} \tag{4.13}$$

where $u_{E\times B}$ is the $\vec{E}\times\vec{B}$ drift given by eq. (2.22) and u_d is the diamagnetic drift given by eq. (2.52). Similarly, the parallel electron velocity can be derived from the electron momentum equation resulting in:

$$\vec{u}_{e,||}=-\mu_{||}\vec{E}-D_{||}\frac{\nabla n}{n}\ . \tag{4.14}$$

The current density along centerline can be expressed as:

$$j_{e,||}=-n_e q u_{e,||}=\frac{n_e q^2}{m_e \nu_e}\left(\vec{E}+T_e\frac{\nabla n_e}{n_e}\right)\ . \tag{4.15}$$

Manipulating eq. (4.14) for electric field gives:

$$\vec{E}=-\nabla\phi=j_{e,||}\left(\frac{m_e\nu_e}{n_e q^2}\right)+T_e\frac{\nabla n_e}{n_e} \tag{4.16}$$

The first term on the right-hand side of eq. (4.16) is the parallel resistivity along the magnetic field lines and the second term accounts for variations in the electron temperature and density. Eq. (4.16) shows that an increase in the turbulent wave energy (increased ν_e) can contribute to the increased in anode potential. For example, the ion acoustic turbulence contributions to the anomalous collision frequency term can be defined from weak-turbulent theory [158]:

$$\nu_{\mathrm{an}}\propto\frac{\mathrm{W_k}}{nT_e}\omega_{\mathrm{pe}} \tag{4.17}$$

where $\mathrm{W_k}$ is the total wave energy density of the ion acoustic turbulence.

4.5.2 Estimation of Wave Energy

Wave energy is used to determine the contributions of turbulence to the increase in anode voltage. The spectral energy is approximated by summing the spectral power from the Fourier transform over a frequency regime,

$$\sum_{\Delta\omega}\left(\frac{\tilde{i}_{sat}}{\bar{i}_{sat,0}}\right)_{\omega}^{2} \tag{4.18}$$

where $\Delta\omega$ is the frequency domain of the targeted instability. Figure 4.15 shows the spectral energy of the waves in the low-frequency (100 Hz-250 kHz) and the high-frequency

(250 kHz-5,000 kHz) regimes. Note the difference in scale of the y-axis. Further, as noted in section 4.2.1, the bandwidth of the measurement technique is limited to approximately 500 kHz, which means signals above 500 kHz are likely attenuated. Therefore, since the altitude and phase of the high-frequency signals could be inaccurate, the magnitude of the wave energy should not be compared between the high-frequency domain and the low-frequency domain. However, the measurement technique is consistent between each operating condition; therefore, the wave energy is comparable across magnetic field strengths. The lower bound of the low-frequency regime is above any power-supply induced noise. The upper bound of the high-frequency regime is the bandwidth limit of the probe current collection circuitry. A vertical red line at 33 G marks the magnetic field strength in which the electrons approach magnetization. For field strengths below 33 G, both the low-frequency and high-frequency waves decrease in spectral power with increasing magnetic field. Once the electron magnetization threshold is passed, the energies of both waves generally increase with increasing magnetic field strengths. For field strengths greater than 135 G, the 25.0-sccm flow rate condition results in high spectral energies of the low-frequency regime at anode position 1 compared to anode position 2. Alternatively, the 14.7-sccm flow rate condition results in higher low-frequency spectral wave energy at anode position 2 (figure 4.15(a)).

In the high-frequency regime, the 14.7-sccm flow rate condition results in higher wave energy compared to the 25.0-sccm condition. The difference in wave energy between the flow rate conditions is more prominent at anode position 2 (figure 4.15(b)). This suggests that while the high-frequency turbulence is damped with increasing flow rate, the increase in anode separation increases the wave energy which manifests as an increase in the discharge voltage.

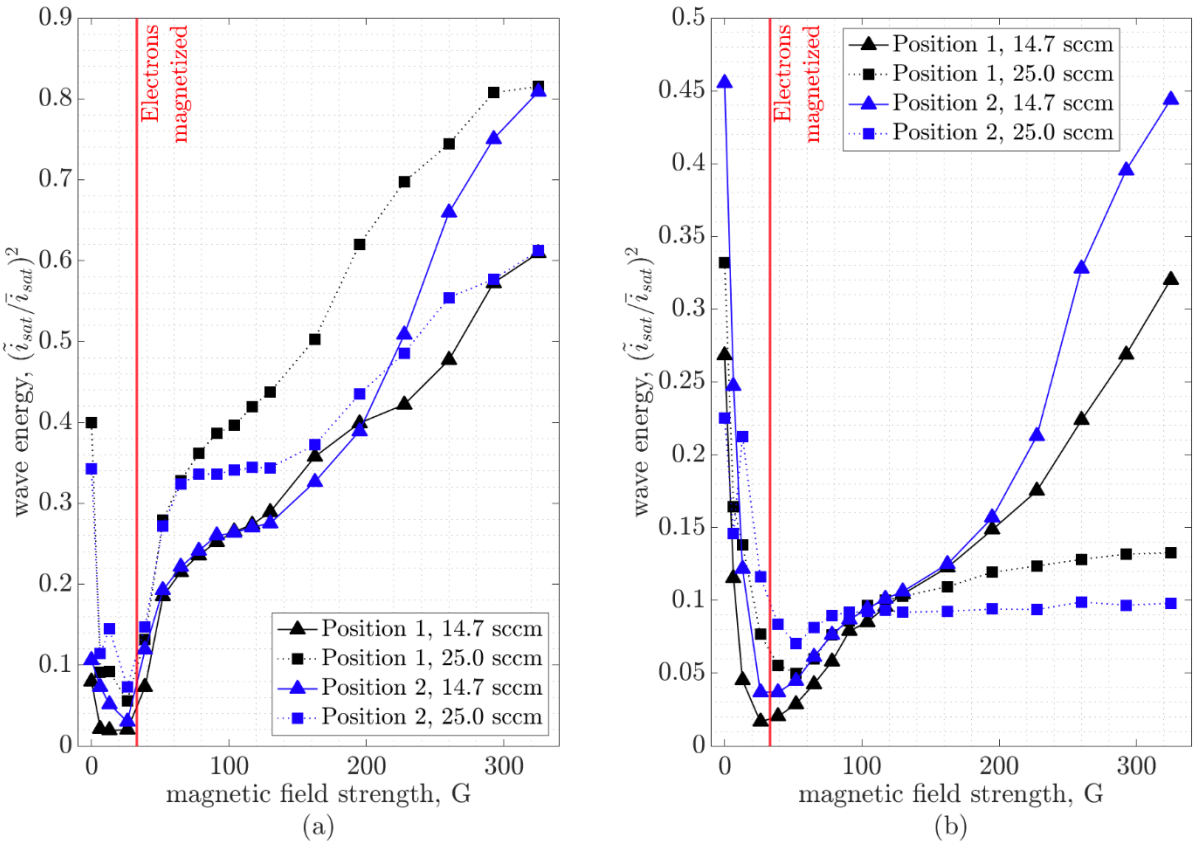

Figure 4.15: Energy of waves for increasing magnetic field strength for the frequency domains of (a) low-frequency domain and (b) high-frequency domain. A red vertical line marks the threshold for electron magnetization.

Figure 4.16 shows the statistical dispersion plots for position 1 at a flow rate of 14.7 sccm generated using the Beall method. As previously stated, the oscillations that are measured here do not propagate azimuthally without the magnetic field (figure 4.16 (a)). At 33 G, the high-frequency modes remain azimuthally dispersionless, but the low-frequency mode presents with some azimuthal dispersion. This azimuthal propagation is shown in figure 4.16 (b) as an increase in the statistical dispersion (S(ω,k) closer to m=1). Physically this means while the electrons remain unmagnetized at this magnetic field strength, the presence of the field begins to generate the azimuthal drift. Figure 4.15 (b) shows a minimum in the spectral wave energy at the 33-G condition, which is supported by low value for S(ω,k) above 400 kHz. At 135 G, the azimuthal mode is clearly defined

as an m=1 mode (figure 4.16 (c)). At 325 G, the azimuthal wave remains as an $m = 1$ and the harmonics appear in the dispersion.

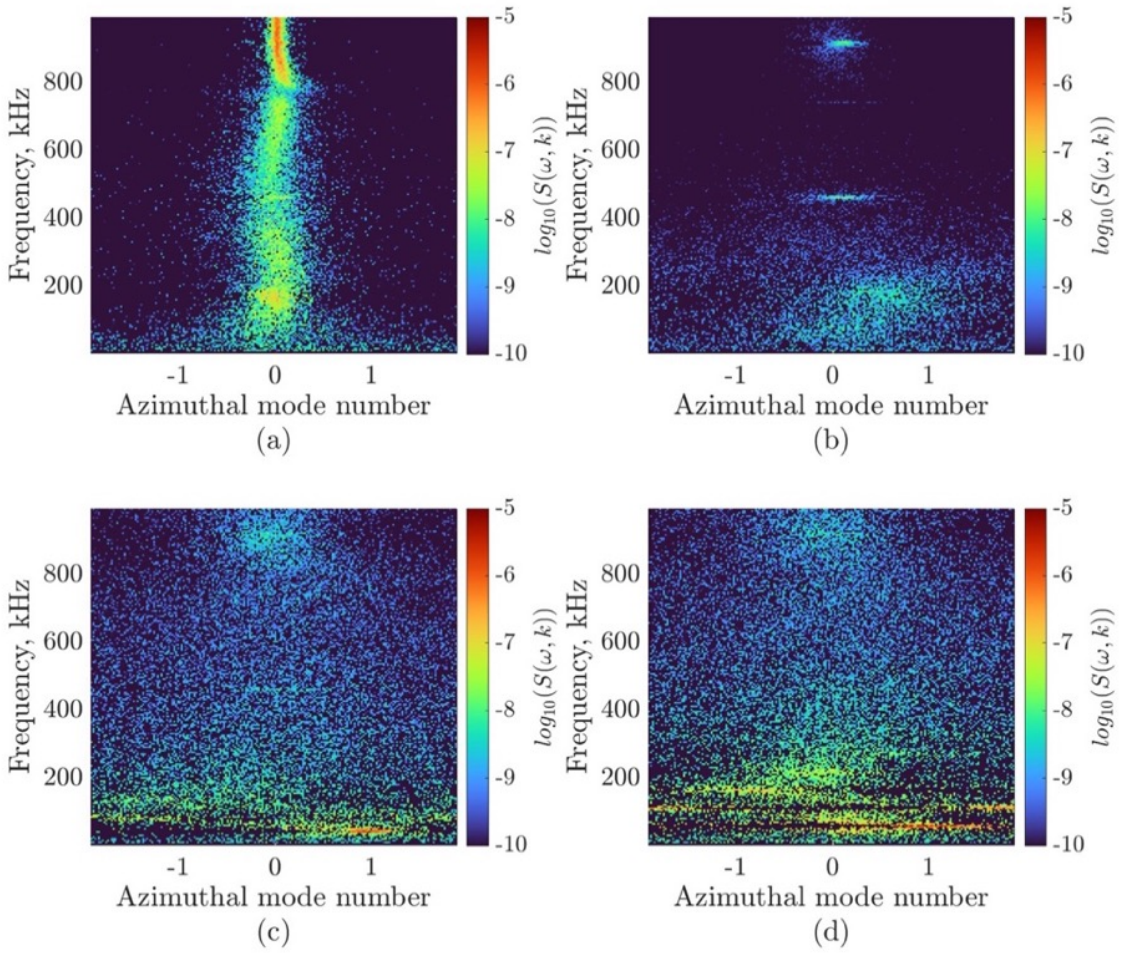

Figure 4.16: Azimuthal mode number of the position 1, 14.7-sccm flow rate condition showing the evolution of the azimuthal drift for increasing magnetic field strengths. (a) 0 G (b) 33 G (c) 135 G, and (d) 325 G.

4.5.3 Plasma Density as a Function of Anode Distance

Previous work with this setup provided neutral pressure measurements near the cathode exit using an ionization gauge and sense tube [127]. Those results show a consistent neutral density near the cathode exit for both anode position 1 and anode position 2 and for both flow rate conditions. However, one explanation for the difference in ion saturation current is a change in divergence angle of the cathode plume with increasing anode distance, as shown schematically in figure 4.17. A change in the cathode plasma divergence angle could

result in a change in the current density due to the change in the electric field profile as a result of changing the separation distance between cathode and anode (eq. (4.15)). Thus, for the same cathode geometry operating at equivalent discharge currents but with different anode separation distances, a larger divergence angle (smaller cathode exit-to-anode entrance separation distance) results in a smaller density gradient. Therefore, a higher magnitude of ion saturation current would be measured at the probe measurement location. Further, the current density is dependent on the anomalous collision frequency, which could be higher for the 14.7-sccm flow rate condition compared to the 25.0-sccm flow rate condition. This could be why the ion saturation current is consistent for increasing magnetic field strengths for the 25.0-sccm condition.

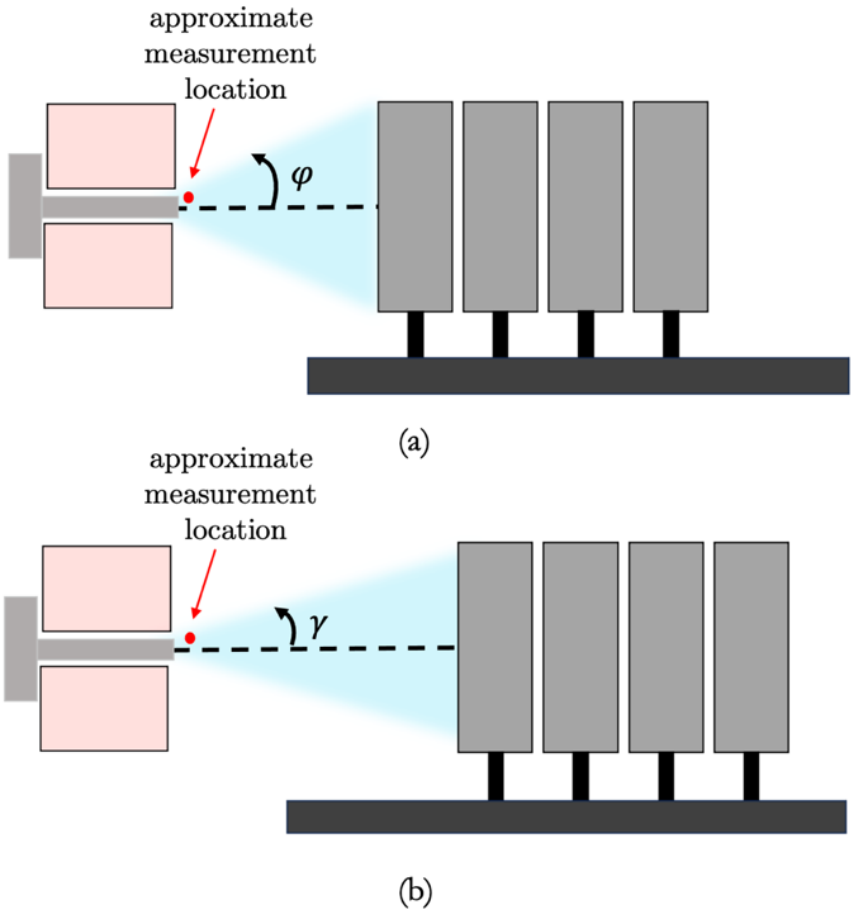

Figure 4.17: Difference in plasma divergence angle for (a) anode position 1 and (b) anode position 2.

4.6 Summary

This chapter explored the measurement of high-speed ion saturation current from azimuthally placed ion saturation probes. The rotational dynamic and high-frequency behavior appear to be affected by the location of the downstream anode, the strength of the magnetic field, and the mass flow rate to the cathode. When the cathode-to-anode coupling distance is increased (i.e. anode position 2), the magnetic flux to the anode is reduced, inhibiting the flow of electrons to the anode surface. An increase in discharge voltage for increasing field strengths was also observed, which could be a result of the increase in high-frequency wave energy, as shown in eq. (4.16).

Without the magnetic field and when the cylindrical anode was moved farther away from the cathode exit, the high-frequency mode grows in frequency and spectral bandwidth. The increase is observed at both flow rates; however, the frequencies and powers measured at the higher flow rate are less than what was measured at the lower flow rate. As the magnetic field is increased up, the low-frequency peak observed at approximately 50 kHz and its effect on the high-frequency behavior displays the following characteristics:

1. **Onset.** Once the electrons approach magnetization at the location of measurement (>33 G centerline peak) the azimuthal dynamic becomes dominant in the frequency spectra. The azimuthal dynamic can mask the peak of high-frequency modes in the Fourier spectra; however, the spectral wave energies show that an increase in spectral bandwidth occurs simultaneous with the growth of the azimuthal wave. It is possible that there exists a coupling between the azimuthal dynamic and the high-frequency behavior. Generally, lower flow rates and larger anode separation distances increase the spectral wave energy of the high-frequency modes. Further, as the magnetic field is increased, the discharge voltage and cathode-to-ground voltage increase while the probes shows an increase in the high-frequency power spectra for the plasma near the cathode

exit. This suggests the increase in the turbulent mechanisms could result in a change in the macro properties of the plasma (i.e. an increase in resistivity).

2. **Velocity.** Increasing the magnetic field results in an increase in the azimuthal drift speed. The azimuthal population is fastest when the anode is closer (anode position 1), and the flow rate is lower (14.7 sccm). Increasing the anode separation distance and increasing the flow rate both reduce the azimuthal ion drift speed, particularly above a magnetic field strength of 135 G. This strongly suggests the azimuthal wave exhibits an dependence on the electric field since the magnetic field topography does not change between cathode operating conditions.

CHAPTER 5

Independent Cathode Testing Compared to Full Thruster

"Big whorls have little whorls
Which feed on their velocity
And little whorls have lesser whorls,
And so on to viscosity."
- Lewis Fry Richardson

5.1 Introduction

This chapter addresses the second research objective of this dissertation: spatially mapping the turbulent and dynamic behavior of the HERMeS cathode operated independently of the HET. To achieve this, a parametric study of cathode oscillations was conducted using downstream diagnostics paired with cathode performance measurements. Various operational parameters were altered on independent cathode experiments including induced current oscillations onto the downstream anode, adjusted background pressure with cryogenic pumps, varied cathode flow rate, and varied magnetic field strength. This work utilized a LaB_6 version of the HERMeS cathode and a magnetic field simulator that creates a magnetic field topography similar to the HERMeS. The data collected from the independent cathode operation were directly compared to those gathered during a high-speed probing campaign of the HERMeS thruster at NASA's Jet Propulsion Laboratory (JPL).

5.2 Experimental Design

A recent high-speed probing campaign of the HERMeS thruster aimed to further validate models of the downstream plume by investigating the high-speed plume dynamics at various thruster throttle points [159]. Table 5.1 shows the throttle conditions that are herein referred to as thruster reference conditions (RC). RC 4 (outlined in the table below) is the primary nominal condition referenced in this work, particularly when compared to the independent cathode operation.

Table 5.1: Thruster reference conditions for induced oscillations.

RC	Thruster Condition	% B_{nom}
1	300 V, 20 A	75
2	300 V, 20 A	100
3	600 V, 20 A	75
4	600 V, 20 A	100
5	600 V, 20 A	125

Table 5.2 provides an overview of the cathode conditions used with varied magnetic field strength, induced oscillations onto the anode, varied operational pressure, and varied cathode flow rate. Each reference condition had a nominal cathode flow rate that is a percentage of the overall thruster flow rate. The independent cathode operation flow rate was matched to that nominal flow rate. When the cathode is operated without induced oscillations, the cathode flow rate was equivalent to the RC 4 flow rate.

Table 5.2: Independent cathode operation test conditions.

% B_{nom}	Induced oscillations	Number of Cryogenic pumps	Mass flow rate, % nom
[75,100,125]*	RC (1:5)	2	100
[0, 75, 87.5, 100]	None	2	100
100	None	1	100
100	None	2	94
100	None	1,2,3	100
100	None	2,3	67-100

*Magnetic field strength was matched at the equivalent RC from table 5.1.

5.3 Method for Inducing Oscillations

Independent cathode experiments are often operated at a constant DC discharge; however, while operated with the HET, the discharge current can oscillate with magnitudes on the order of the full DC current. The DC power supply used with independent cathode tests is often operated in current-controlled mode without injected current oscillations. This often results in a steady DC current on independent cathode configurations while full thruster tests often exhibit current oscillations on the order of the DC current. In this dissertation, oscillations were superimposed onto the anode signal in line with anode power supply. Figure 5.1 shows the schematic for the induced oscillations on the anode. The signal used to simulate the thruster discharge oscillations was generated by digitizing the high-speed discharge signal from a HERMeS RC (as summarized in table 5.1). The digitized thruster RC signal was digitized and loaded onto a Keysight 33600A function generator. The output of the Keysight was amplified using an AE Techron 7224 amplifier. The AC signal was injected into the discharge using a Solar Electronics Type 6220-1B 2:1 isolation transformer. Additionally, a 1Ω resistor was placed in series at the output of the AE Techron input. This setup was first introduced and used in ref. [160].

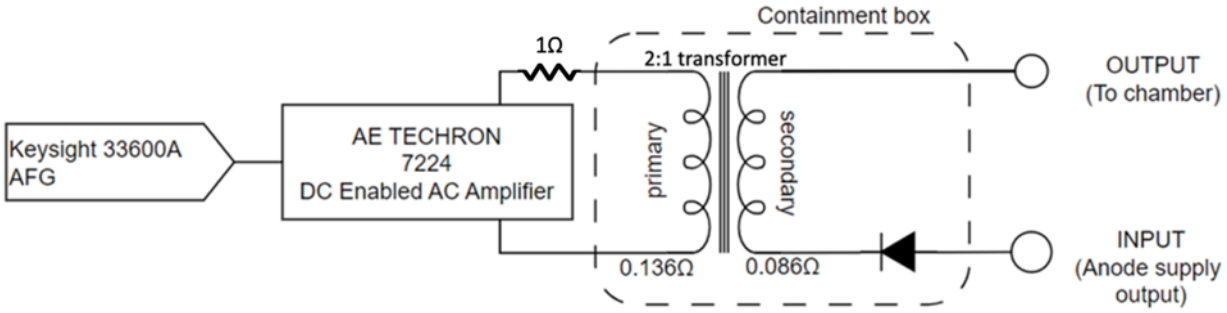

Figure 5.1: Schematic of the process for inducing oscillations onto the anode [160].

5.4 Facility and Cathode

The cathode emitter material used for this experiment was a LaB_6 tube with matched plasma-wetted surfaces to the HERMeS cathode. The cathode was concentrically mounted in a magnetic field simulator that creates a magnetic field topography similar to the HERMeS thruster such that the exit plane of the simulator was in-line with the keeper exit plane. A 254-mm-diameter cylindrical anode constructed of a thin molybdenum sheet was placed 64 mm downstream of the cathode keeper exit. Spatial high-speed ion saturation current was measured in the external cathode plume with a Langmuir probe held at a -57-V bias, sufficiently in the ion saturation regime. The next section details the probe configuration. The probe was injected into the cathode plume axially using a high speed Parker ML18-120M-N linear motion stage. The axial stage was mounted perpendicularly to a Parker ML18-150 linear motion stage to allow for adjustment of the radial position of the axial sweeps. Figure 5.2 shows the configuration of the cathode setup with the axially injected probe. The cathode, anode, magnetic field simulator and probe apparatus was mounted to an optical board for easy installation in the vacuum chamber. Figure 5.3 shows the experimental apparatus prior to full chamber installation and while the cathode was operated at RC 4.

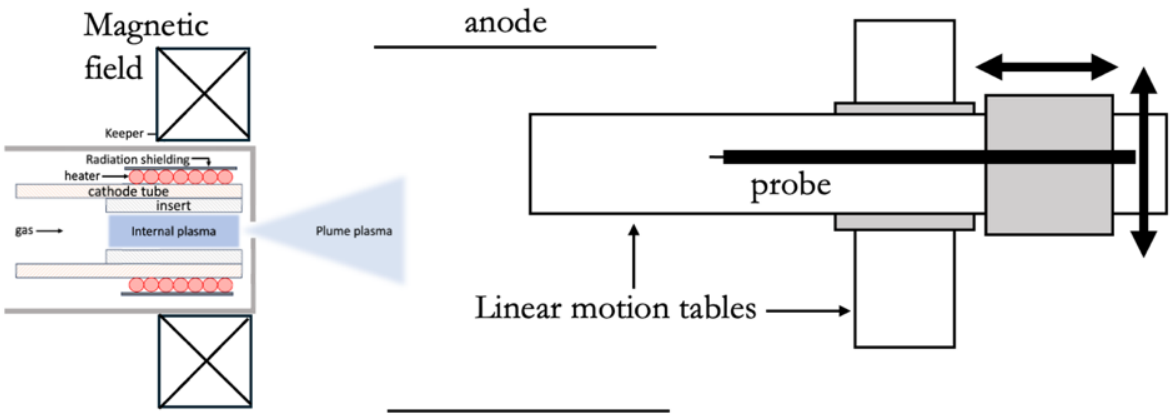

Figure 5.2: Schematic for axially injected wave probe.

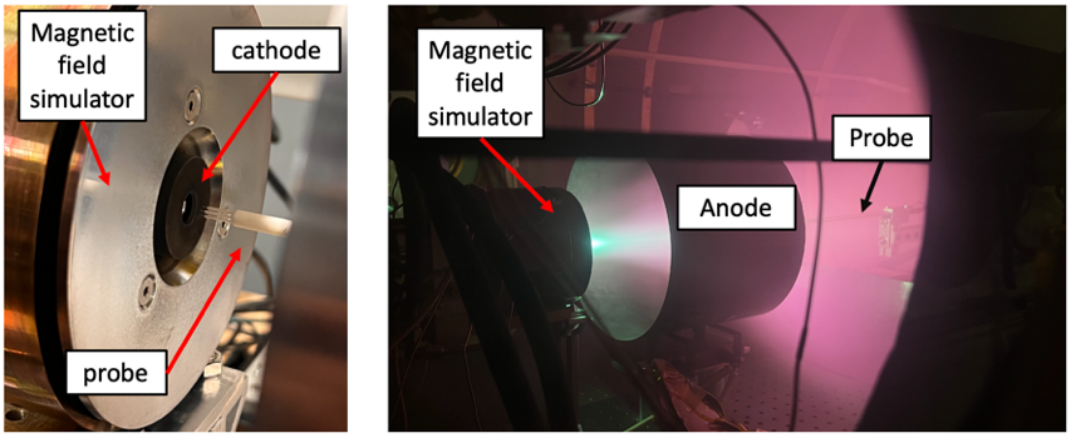

Figure 5.3: Experimental setup with magnetic field simulator, cathode, anode, and probe injection array.

This work was performed in a 1-m-diameter by 2-m-long vacuum facility at the NASA JPL, as described in section 3.5.1.3. Ultra-high purity xenon was used as the propellant. Three pumps were available on the cathode diagnostics chamber: two 25-cm-diamter cryogenic pumps and an AL200 Gifford-McMahon Cryocooler with a 48-cm-diameter cryogenic sail. These three pumps were used in three configurations (one 25-cm pump, two 25-cm pumps, and two 25-cm with the AL200). Table 5.3 provides the base pressure and the operational pressure for each cryogenic pump configuration at the nominal flow rate for RC 4.

Table 5.3: Background and operational pressures at thruster RC4 of JPL cathode facility chamber with various cryogenic pump configurations.

	Background Pressure [Torr	
	Base	Operational
25-cm (x1)	5×10^{-7}	2.3×10^{-4}
25-cm (x2)		1.3×10^{-4}
25-cm (x2) + AL200		9.5×10^{-5}

The data at the thruster RCs were collected in the Owens vacuum chamber, a 3-m diameter and 10-m-long cylindrical vacuum chamber with operational pressures less than 1.5×10^{-5} Torr.

5.4.1 Wave Probe

The primary diagnostic used in this work was a three-axis wave probe, designed to investigate the turbulence and dynamics in cathode plume. The wave probe was constructed of four 0.5-mm-diameter and 2-mm-length tungsten wires inserted into telescoped alumina ceramics and oriented to capture wave propagation along three axes: radial, azimuthal, and axial. Figure 5.4 shows the schematic of the wave probe. The downstream end of each tungsten wire was crimped to the center conductor of a coax cable. A stainless steel tube housed the large single-bore alumina tube and was shorted to the shield of the coax cable. The tube was grounded to chamber ground at the probe mount.

Figure 5.4: Wave probe configuration for three-axis wave propagation measurements

Each probe tip was biased to -57 V and the ion current was amplified using custom transimpedance amplifiers (TIAs) with selectable gain settings of 200 V/A, 1 kV/A, and

12 kV/A. The gain settings were selected depending on the region of measurement. The cable length from the probe tip to the amplifier was minimized such that the line resistance was less than 1 Ω and the cable capacitances were matched by ensuring consistent line lengths and cable types for all four conductors.

5.4.2 Optical Emission Spectroscopy

A single collection optic was aimed at the keeper face of the independent cathode setup with fiberoptic cables routed from the collection optic to a fiber feedthrough on the chamber wall. An additional fiberoptic cable connected to the feedthrough was routed to a Maya2000 Ocean Optics optical emission spectrometer (OES), which features a spectral range of 165 nm to 1100 nm. The OES was primarily used to capture the line ratios I_{823}/I_{828} and I_{460}/I_{828} . As described in section 3.4.3, these line ratios can provide electron temperature and ionization fraction, respectively, when paired with a collision radiative model (CRM). While the use of a full CRM is outside the scope of this dissertation, Konopliv et al. has provided a diagram with electron temperature with respect to line ratio and electron density [134]. The diagram is used in this work to approximate the electron temperature in the near-keeper region as a function of the varying cathode parameters.

5.4.3 Overview of DAQ Channel Distributions

High-speed data were captured on three GaGe Razor Express CompuScope CSE 1642 PCIe digitizers assembled into one computer for a total of twelve channels. More information regarding the DAQ can be found in section 3.5.1.3. Eight DAQ channels were used for this work, as outlined in table 5.4.

Table 5.4: CompuScope CSE DAQ channel configuration.

Channel	Purpose	Input configuration
1	Wave probe 1	TIA
2	Wave probe 2	TIA
3	Wave probe 3	TIA
4	Wave probe 4	TIA
5	Axial location of linear stage	Voltage output from motion stage
6	Anode current	410 Pearson coil
7	Anode voltage	TA043 differential probes
8	Keeper voltage	TA043 differential probes

5.4.4 High-Speed Dual Langmuir Probe

A high-speed dual Langmuir probe (HDLP) was used to capture the plasma parameters along a single radial slice. Figure 5.5 shows the electric schematic used for the HDLP. The probe was mounted to the same probe holder that was used for the wave probe. An SRS DS345 arbitrary function generator (AFG) provided the peak-to-peak voltage at a frequency of 200 Hz. A Krohn-Hite 7500 amplified the voltage from the AFG to sweep the HDLP from -40 V to 20 V. Three Keithley 6500 ½ digital multimeters (DMM) were used to capture the probe bias voltage, the active probe current, and the null probe current. The HDLP was rapidly swept into the plume with the linear motion stage at a single radial location. The 200 Hz sweep frequency provided an axial resolution of 4 mm for the plasma parameters along the injection.

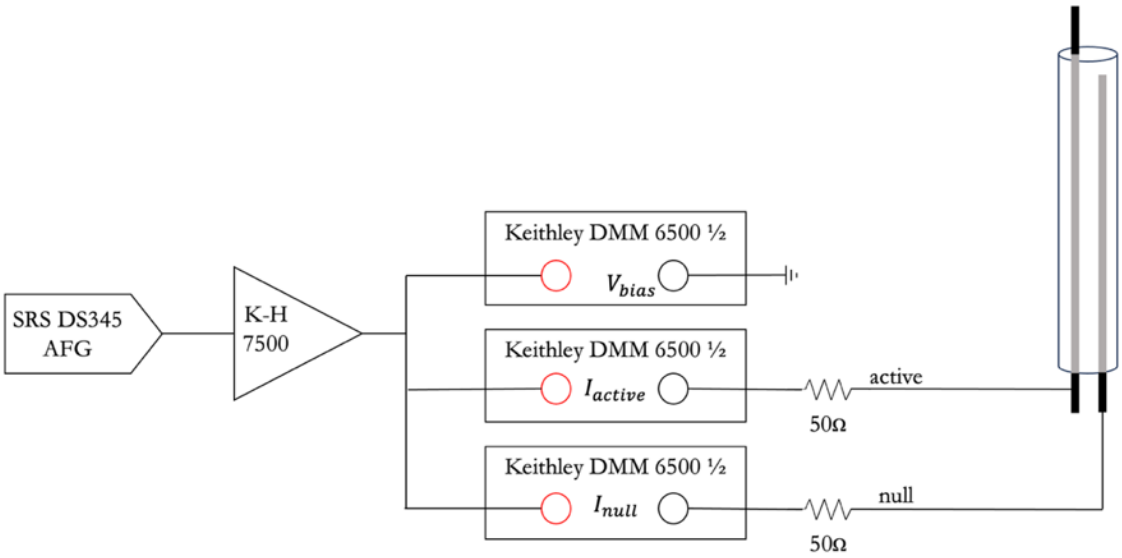

Figure 5.5: High-speed dual Langmuir probe configuration.

5.5 Thruster Reference Conditions

This section establishes the spatial spectral wave energies of the thruster RCs from a Fourier analysis of the relative fluctuations in the ion saturation current, $\tilde{i}_{sat}/\bar{i}_{sat}$, from the injected wave probe. The wave probe used for the thruster reference conditions was constructed in the same configuration for the independent cathode experiments. Figure 5.6 shows the HERMeS thruster operating in the JPL Owens facility with the probes used and the axis convention. The wave probe was injected in the axial ($\hat{z}$) direction using a High-speed Axial Reciprocating Probe (HARP) linear motion stage. A large high-speed ion saturation probe was paced in a fixed azimuthal position; however, the data from this probe are not reported in this dissertation.

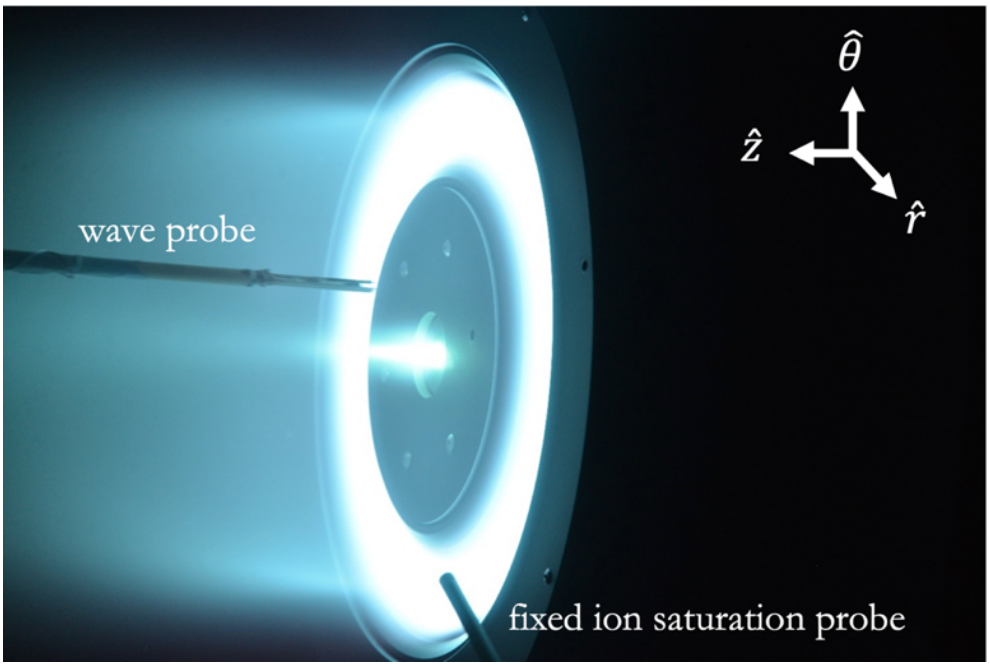

Figure 5.6: Operation of the HERMeS thruster in the JPL Owens facility. The axially injected wave probe, fixed position ion saturation probe, and axis convention are given.

In this section, the wave energy is estimated by first separating the Fourier spectra into two regions: a low-frequency band (100 Hz – 250 kHz), encompassing large-scale oscillations such as breathing mode and azimuthal drifts; and a high-frequency band (250 kHz – 14 MHz), capturing small-scale turbulence in the plume (e.g., ion acoustic turbulence and lower hybrid drift modes). An approximation of wave energy existent at the discrete frequencies can be made by integrating the power spectral density spectrum within the frequency bands. The low frequency limit of 100 Hz is above any power supply-produced noise and the high-frequency limit of 14 MHz is the upper bandwidth limit of the transimpedance amplifiers (TIA) used to capture the probe signal. The bandwidth of the TIAs were theoretically calculated using LT Spice and experimentally validated with the full probe setup ensuring the line lengths were consistent between bandwidth testing and the full thruster setup.

The position of the ion saturation probe throughout the injection was parsed for position to capture the Fourier spectra of the probe signals at a fixed axial location with an axial resolution of 2 mm. The spatial locations of ion saturation probe measurements

are herein normalized in the axial direction by the HERMeS channel length, L, and in the radial direction by the distance from cathode centerline to channel centerline on HERMeS, r_{cc}. z/L=r/r_{cc}=0 is the exit plane of the cathode on centerline. Figure 5.7 shows an example of the ratio of the ion saturation current fluctuations to the DC ion saturation current and the associated Fourier transform. The low-frequency and high-frequency domains are highlighted in the Fourier spectra. The Fourier spectra at this measurement location show that in the low-frequency domain, two modes are measured: a peak near 9 kHz which could be related to ionization instabilities and the dominant peak around 60 kHz with harmonics which is likely the azimuthal m=1 mode.

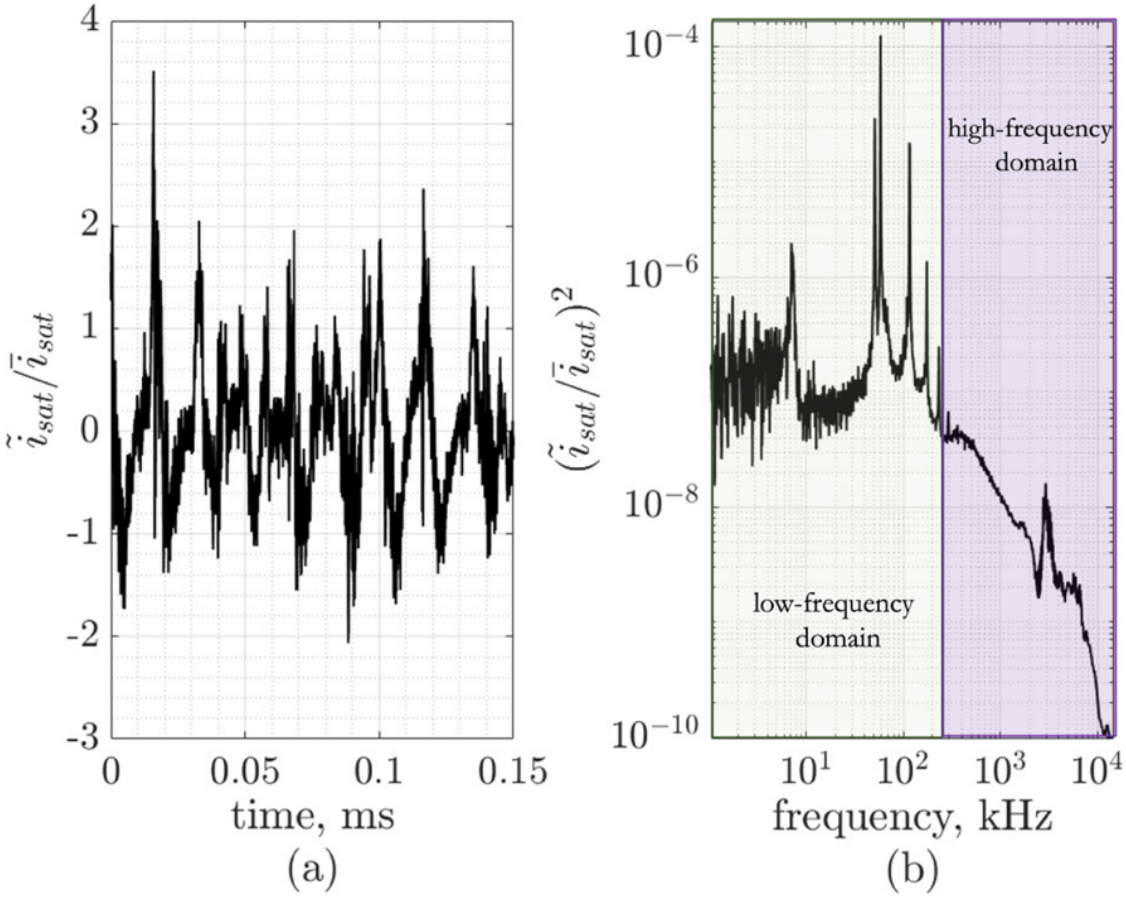

Figure 5.7: Example of ion saturation current fluctuations and Fourier transform from the lone cathode operation. (a) Raw ion saturation current fluctuations and (b) power spectral density from the Fourier transform with the low-frequency and high-frequency domains outlined.

5.5.1 Spatial Spectral Wave Energy Mapping of Thruster Reference Conditions

This section uses the "turbo" colormap to best outline the extremes; however, a colorblind-friendly version of these plots are included in appendix A.2. Figure 5.8 shows the spatial wave energy of the HERMeS thruster operating at RC 4. Thruster RC 4 is the only RC with wave probe measurements for $r/r_{cc}<0.17$. The change in TIA gain settings results in a step in the wave energy, as outlined in figure 5.8. In both frequency regimes, there are three regions of heightened wave energy near the exit plane of the thruster including near the outer pole, near the front pole close to the inner edge of the discharge channel, and at the outer edge of the cathode plume. The low-frequency regime wave energy plot also shows a coupling of low-frequency waves that bridges between the thruster beam and the cathode (figure 5.8(b)).

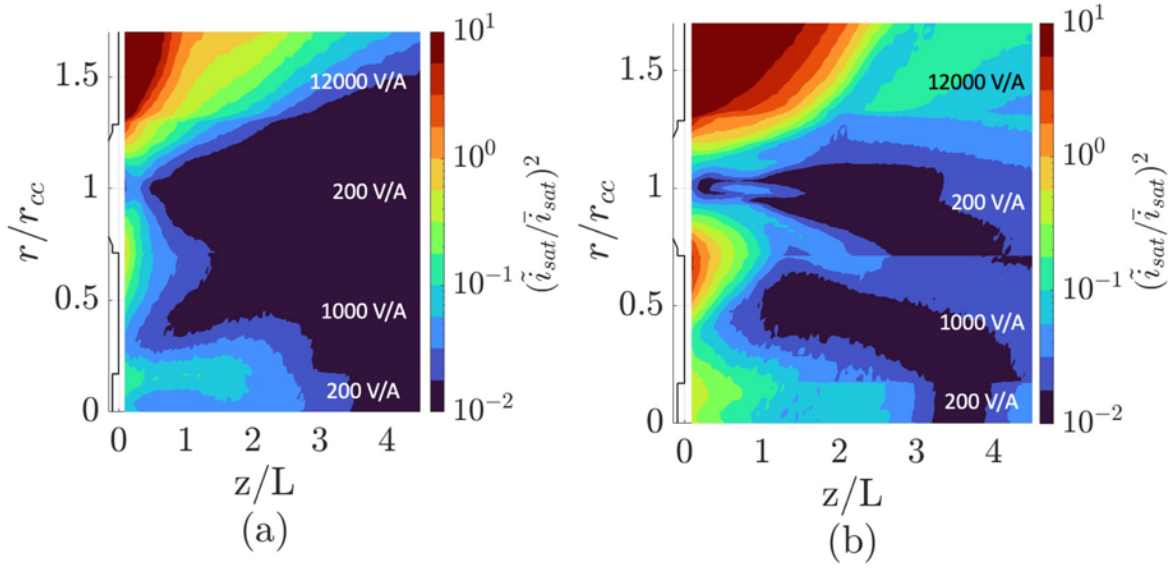

Figure 5.8: Spatial dependence of wave energy from thruster RC 4 for the (a) high-frequency band: 250 kHz-14 MHz and (b) low-frequency band: 100 Hz-250 kHz. The TIA gain settings are outlined for each section.

Figures 5.9 and 5.10 show the wave energy from the full HERMeS thruster testing of RC 1-5 in the high-frequency and low-frequency domains, respectively. The wave energy bordering the cathode discharge increases as the magnetic field increases for both the 300

V (RC 1-2, figures 5.9(a)-(b) and 5.10(a)-(b)) and 600 V (RC 3-5, figures 5.9(c)-(e) and 5.10(c)-(e)) discharge voltage thruster RCs. Note that near centerline wave energy data is only available for RC 4. There still appears to be an increase in spectral wave energy from RC 4 to RC 5 (100 % B_{nom} to 150 % B_{nom}). For example, the boundary of the heightened high-frequency wave energy region z/L=2 broadens from r/r_{cc}=0.25 at RC 4 to nearly r/r_{cc}=0.5 for RC 5. Further, the 600 V RCs results in higher wave energy in this region when compared to the 300 V RCs. Interestingly, the low-frequency wave energy that connects between the thruster beam and the cathode only appears in the 600 V conditions (figure 5.10 (c)-(e)). This region could be representative of the location in which the cathode beam couples to the cathode. The coupling in the 300 V conditions (RC 1-2) could be at lower spectral power when compared to the 600 V conditions (RC 4 and 5).

There also exists heightened high-frequency wave energy near the thruster beam (z/L=0 to z/L=0.5 and r/r_{cc}>0.4). This region does not appear to have a correlation with magnetic field strength or discharge voltage. For example, for the cases where the magnetic field is increased from 100 % B_{nom} to 150 % B_{nom}, the wave energy in this region appears to increase between RC 3 to RC 4 (600 V conditions), but decreases from RC 1 to RC 2 (300 V conditions). Further, RC 5 exhibited lower high-frequency wave energy near the thruster beam and close to the thruster exit ($z/L \cong 0$ and $r/r_{cc} \cong 0.6$) when compared to RC 4. This suggests there is not necessarily a link between the magnetic field strength and the growth of the high-frequency behavior in this region. It is possible that the high frequency wave energy in this region is related to the margins of stability of the thruster and therefore depend on the magnetic field, the discharge voltage, and the anode flow rate collectively. Nonetheless, this region is outside the scope of this dissertation as it appears to be more coupled to the thruster dynamics, particular in the beam near the channel exit, rather than the cathode plasma.

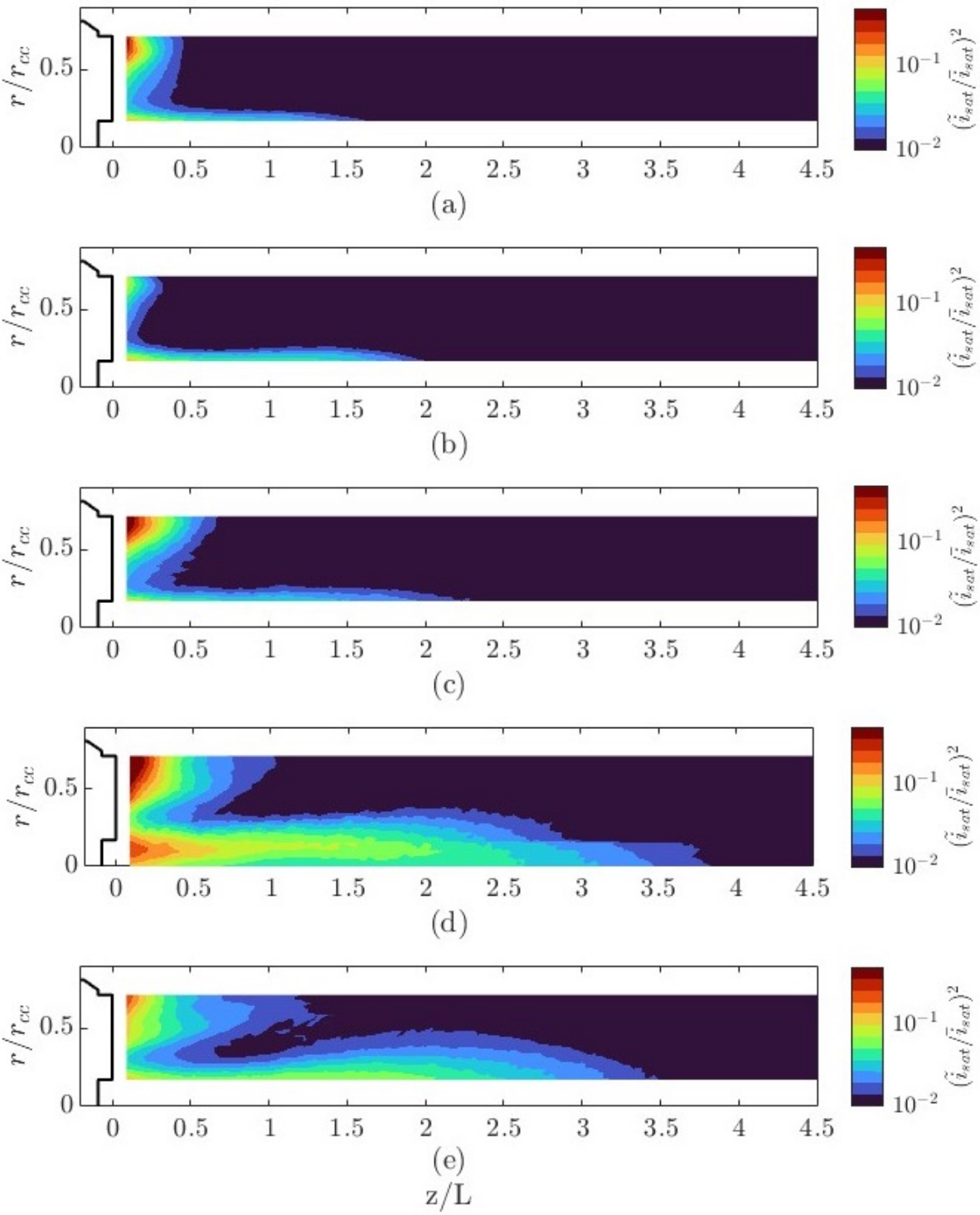

Figure 5.9: High-frequency wave energy diagrams for full thruster operation at RC 1-5 (a)-(e).

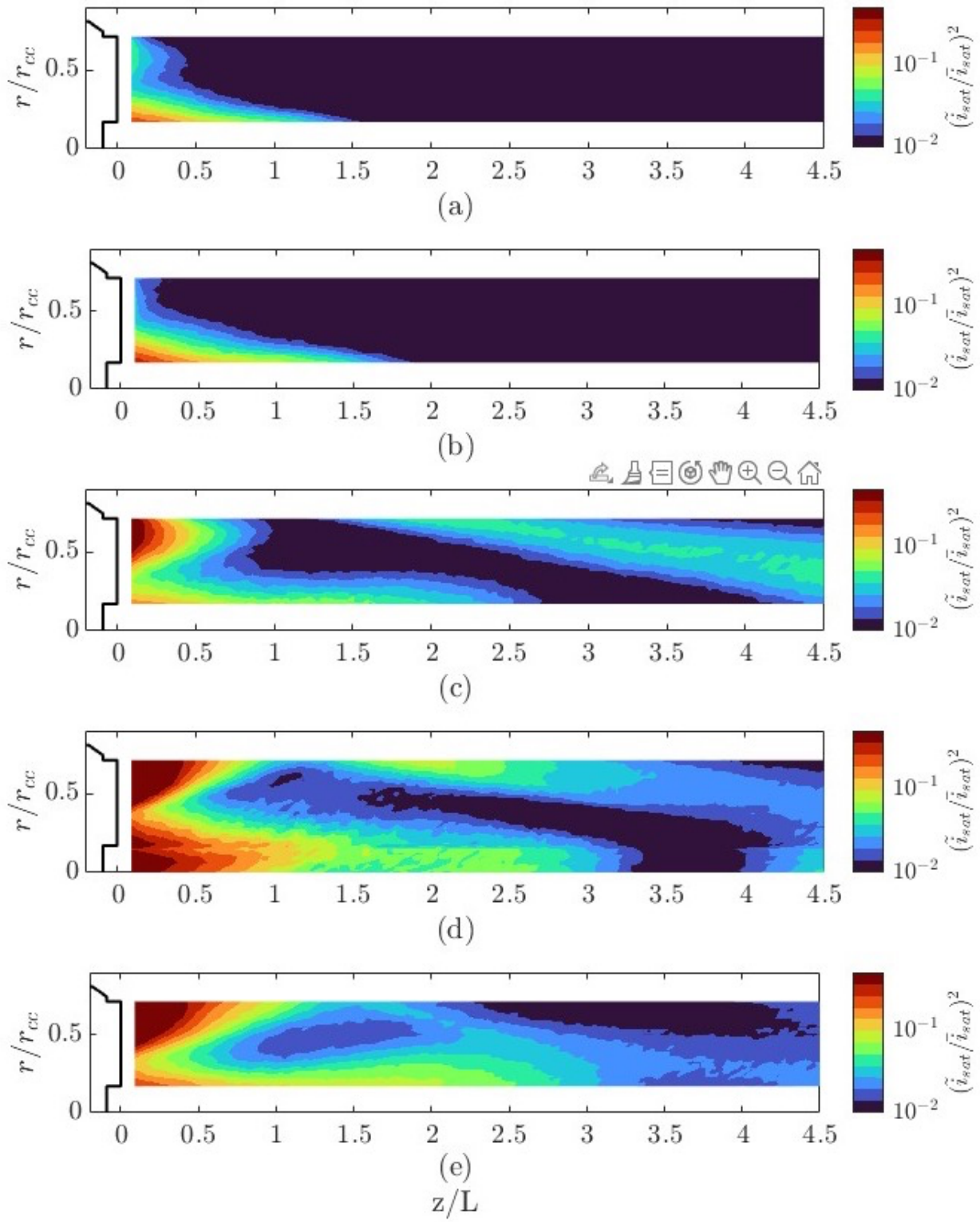

Figure 5.10: Low-frequency wave energy diagrams for full thruster operation at RC 1-5 (a)-(e).

5.6 Variation of Independent Cathode Operational Configurations

This section explores how induced oscillations, varied mass flow rate, and adjusted background pressure of the independent cathode configurations affect the frequency spectra. The section begins with an overview of the cathode and thruster RC performance for varying cathode operational modes. Next, the effects of changing background pressure, inducing anode oscillations, and varying mass flow rates on the spatial wave energy of the low-frequency and high-frequency domains are explored. Following, the line ratios from OES measurements near the keeper exit provide insight into the electron temperature in the region under the varying cathode operational parameters. Finally, the phase velocity of the low-frequency dynamic is analyzed using data from the wave probe.

5.6.1 Cathode Performance

Table 5.5 provides the cathode performance metrics for the lone cathode configurations without induced oscillations at the nominal flow rate for RC 4, (100% $\dot{m}_{nom}$). The magnitude of the peak-to-peak oscillations in the discharge current for all cathode cases without the induced oscillations remains below 5 A. The magnitude of the discharge current and discharge voltage oscillations are the greatest without the applied magnetic field. The application of the magnetic field appears to stabilize the plasma as the magnitude of the discharge current and discharge voltage oscillations decrease with increasing magnetic field. Increasing the background pressure does not change the magnitude of the discharge current oscillations, but the DC discharge voltage, magnitude of discharge voltage oscillations, and DC keeper voltage decrease at higher background pressures. Reducing the mass flow rate to 94% $\dot{m}_{nom}$ results in an increase of the discharge current and discharge voltage oscillations. The keeper oscillations remain relatively constant for all cathode configurations.

Table 5.5: Cathode performance metrics for the lone cathode operation without induced oscillations. Unless otherwise noted, the cathode condition is with both cryogenic pumps at the nominal flow rate condition for RC4.

Cathode Condition	$\mathbf{I_{D_{p2p}}, A}$	$\mathbf{\overline{V_D}, V}$	$\mathbf{V_{D_{p2p}}, V}$	$\mathbf{\overline{V_k}, V}$	$\mathbf{V_{k_{p2p}}, V}$
0% B_{nom}	4.07	18.1	19.7	3.86	2.21
75% B_{nom}	1.52	23.6	7.25	4.72	1.66
87.5% B_{nom}	1.69	25.8	7.84	4.84	2.10
100% B_{nom}	1.77	26.9	8.23	5.12	2.26
100% B_{nom}, 1 cryogenic pump	1.79	24.3	6.95	4.22	3.31
100% B_{nom}, 94% $\dot{m}_{nom}$	3.85	28.3	9.78	4.93	2.78

Figure 5.11 shows the effect of inducing oscillations digitized from thruster RC 4 (100% B_{nom} and 100% $\dot{m}_{nom}$) on the anode current, anode voltage, and keeper voltage of the independent cathode setup. The raw signals show that without induced oscillations, the cathode operation is generally quiescent with irregular, small-scale oscillations (figure 5.11(a), (c), and (e)). The induced anode current oscillations results in sinusoidal-like behavior in all signals (figure 5.11 (b), (d), and (f)). Further, while the DC value of the discharge current and discharge voltage remain relatively constant when the oscillations are induced on the anode signal, the DC floating keeper voltage decreases when oscillations are induced on the anode.

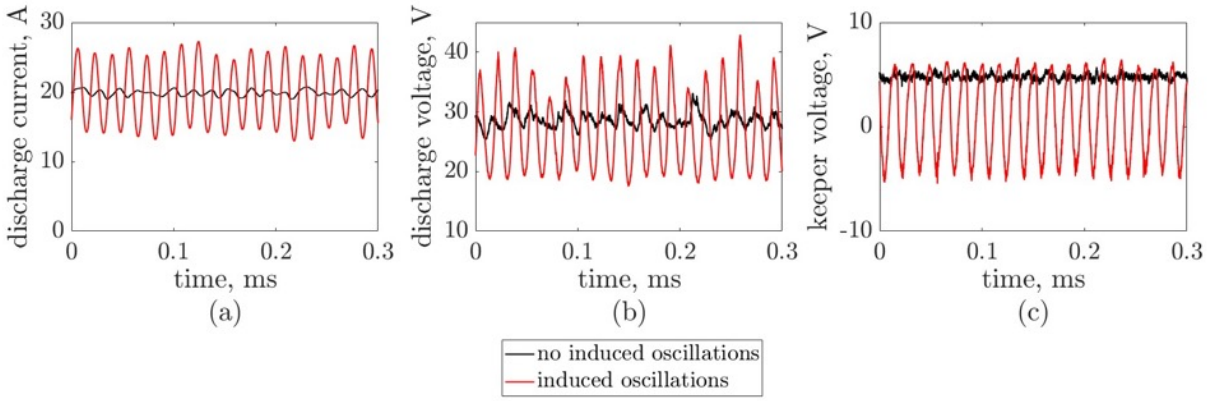

Figure 5.11: Raw signals of the independent cathode operation at the nominal magnetic field strength and the nominal flow rate condition for RC4.(a) anode current, (b) anode voltage, and (c) keeper voltage, without anode oscillations and with RC 4 induced oscillations injected onto the anode signal.

Table 5.6 presents the discharge current and discharge voltage characteristics for the cathode operating at each RC with induced oscillations compared to the matched thruster RC. With the applied oscillations, the magnitude of the peak-to-peak discharge current oscillations closely matches the equivalent thruster RC discharge current oscillation magnitude. The DC discharge voltage remains fairly constant between the induced and non-induced oscillation cases. The magnitude of the peak-to-peak discharge voltage increases when the oscillations are induced on the anode; however, the magnitude of the discharge voltage oscillations are still less than the thruster RC.

Table 5.6: Cathode discharge performance metrics from the discharge current signal for the thruster RCs 1-5. Data from full thruster operation listed as "HERMeS" and data from RC induced lone cathode operating listed as "CATH". The voltages are measured with respect to cathode.

Thruster RC	$\mathbf{I_{D_{p2p}}}$, **A**		$\mathbf{\overline{V_D}}$, **V**		$\mathbf{V_{D_{p2p}}}$, **V**	
	HERMeS	CATH	HERMeS	CATH	HERMeS	CATH
1	6.63	7.09	300	24.1	12.6	10.8
2	8.48	8.20	300	27.6	14.8	12.5
3	15.1	14.1	600	24.1	29.2	19.0
4	18.3	17.2	600	27.0	37.1	26.0
5	19.2	18.8	600	28.2	36.1	28.5

Table 5.7 presents the keeper voltage characteristics for the HERMeS thruster and the cathode operated with the associated RC induced oscillations. The DC keeper voltages on the independent cathode setup are larger for RC 1 and RC 2 (300 V conditions) compared to RCs 3-5 (600 V conditions); however, the peak-to-peak magnitude of the keeper oscillations are greater for RCs 3-5. This suggests the local plasma fluctuations near the keeper are larger for RC 3-5 compared to RC 1-2. Further, increasing the magnetic field also increases the magnitude of the keeper voltage oscillations. Increasing the magnetic field likely increases the temperature of the electrons as they become confined by the magnetic field, which could lead to an increase in the turbulence in the region.

The reported magnitude of keeper voltage oscillations for the HERMeS operation are large, but not necessarily linked to the local plasma fluctuations. Floating keeper voltages are captured on both the HERMeS setup and for each independent cathode configuration by turning the keeper supply off and monitoring the voltage in reference to cathode common. While the cathode was grounded on the independent cathode configurations, HERMeS was operated in the body-tied configuration where the cathode common was tied to the thruster body. Therefore, the external plasma is physically exposed to a large surface area that is oscillating (thruster body). This could lead to an erroneously large magnitude of voltage oscillations between the keeper and the cathode that does not necessarily correlate with local plasma behavior. However, the trends in the keeper DC voltage and the magnitude of the voltage oscillations on the independent cathode configurations, as mentioned above, are consistent with the HERMeS experiment. Nonetheless, the large-scale oscillations of the keeper voltage, particularly in different thruster operation conditions such as body-tied or floating, certainly merits further exploration. An investigation to local plasma fluctuations, particularly in the plasma potential, near the cathode exit on full thruster tests is necessary to determine the true plasma oscillations near the keeper.

Table 5.7: Cathode discharge performance metrics from the discharge current signal for the thruster RCs 1-5. Data from full thruster operation listed as "HERMeS" and data from RC induced lone cathode operating listed as "CATH". The voltages are measured with resp

Thruster RC	$\overline{V_k}$, V		$V_{k_{p2p}}$, V	
	HERMeS	CATH	HERMeS	CATH
1	5.58	4.22	13.20	4.39
2	5.93	4.70	13.20	4.42
3	1.55	2.67	42.00	8.61
4	-0.09	0.69	49.60	14.8
5	6.29	1.36	13.20	16.1

5.6.2 Spatial Wave Energy Mapping

This section explores the effect of adjusting the background pressure, inducing oscillations, and varying the flow rate on the high-frequency and low-frequency domains.

5.6.2.1 Effect of Background Pressure

Figures 5.12 and 5.13 show the spatial wave energy for thruster RC 4 (figures 5.12(a) and 5.13(a)) and the independent cathode configuration at $100\%\, B_{nom}$ and $100\%\, \dot{m}_{nom}$ for varying background pressures (figures 5.12(b)-(d) and 5.13(b)-(d)) in the high-frequency and low-frequency regimes, respectively. The high-frequency spatial wave energy maps identify two regions of heightened wave energy: off-centerline near the edge of the keeper and between $1 < z/L < 3$ near $r/r_{cc} \cong 0.5$. The region of heightened high-frequency wave energy on the boundary of the cathode plume for the independent cathode configurations remains fairly consistent in magnitude across all background pressure conditions; however, the region extends further downstream for the configuration with two cryogenic pumps (figure 5.12(c)). Directly outside of this region farther from centerline (near r/r_{cc}=0.5 and for $z/L < 1$), the wave energy decreases with increasing background pressures. This is consistent with neutral collisional damping of high-frequency turbulence. This region exhibits low high-frequency wave energy in the thruster RC (figure 5.12(a)) as the neutral density in this region of the thruster is on the order of the electron density [125].

The region near $1 < z/L < 3$ and $r/r_{cc} \cong 0.5$ is near the entrance to the downstream cylindrical anode, and this region consists of heightened high-frequency wave energy. The magnetic field confines electrons along the field lines, suggesting that turbulent mechanisms, manifesting as heightened high-frequency wave energy in figure 5.12(a), contribute to electron transport to the anode surface. This region is affected by the background pressure and will be addressed further in section 5.7.3.

The heightened low-frequency wave energy is primarily focused on the edge of the high-density region of the cathode plume with an off-centerline peak at approximately $r/r_{cc} = 0.1$. Notably, this region is likely the most significant region to replicate on

independent cathode operation tests. The region of heightened low-frequency wave energy near the cathode exit generally extends further downstream for the lone-cathode configurations (figure 5.13(b)-(d)) compared to the full thruster operation (figure 5.13(a)). This suggests that the low-frequency behavior is either damped or less dominant in the full thruster setup compared to the independent cathode setup. This effect is explored quantitatively further in section 5.7. Similar to the spatial high-frequency wave energy maps, the low-frequency wave energy extends further downstream for the operating condition with two cryogenic pumps (figure 5.13(c)).

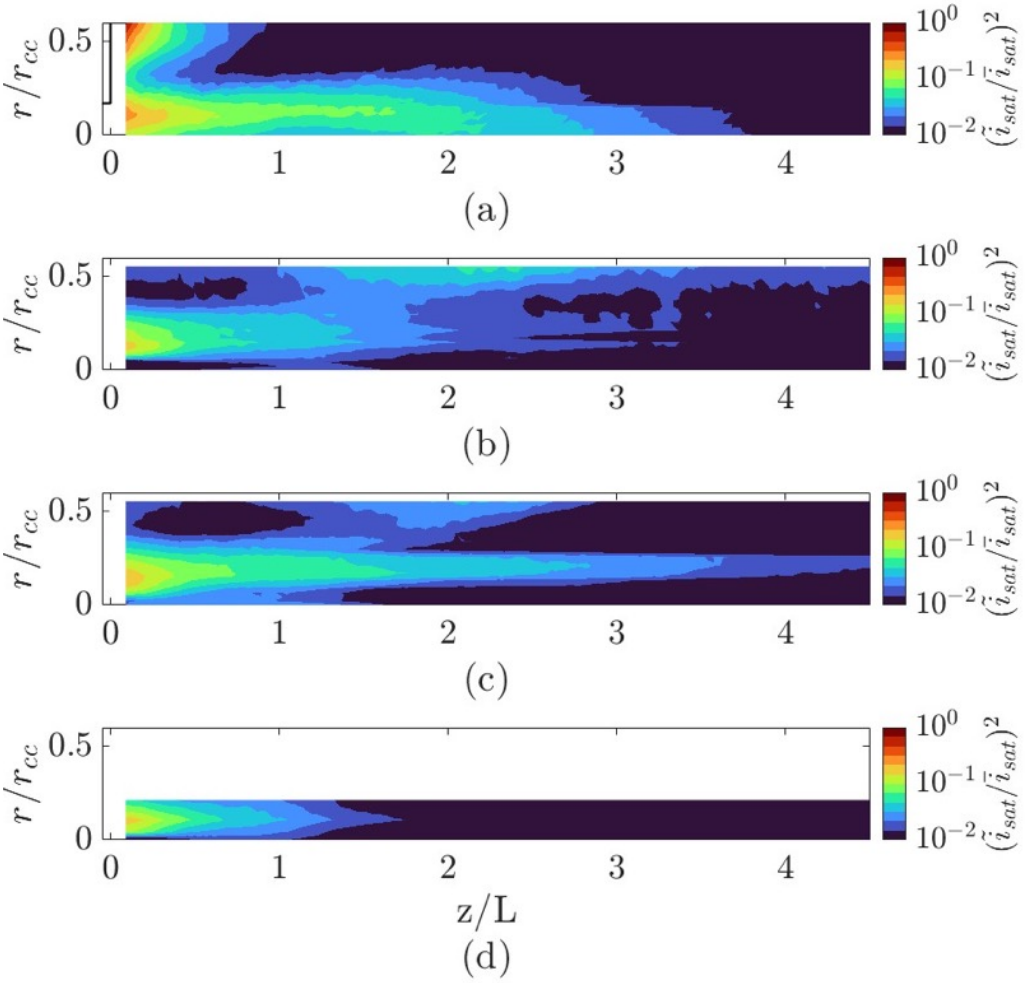

Figure 5.12: Spatial dependence of the high-frequency wave energy integrated from the power spectrum from 250 kHz to 14 MHz for (a) the RC 4 thruster + cathode configuration and the independent cathode operated at the nominal magnetic field strength with (b) three cryogenic pumps, (c) two cryogenic pumps, and (d) one cryogenic pump.

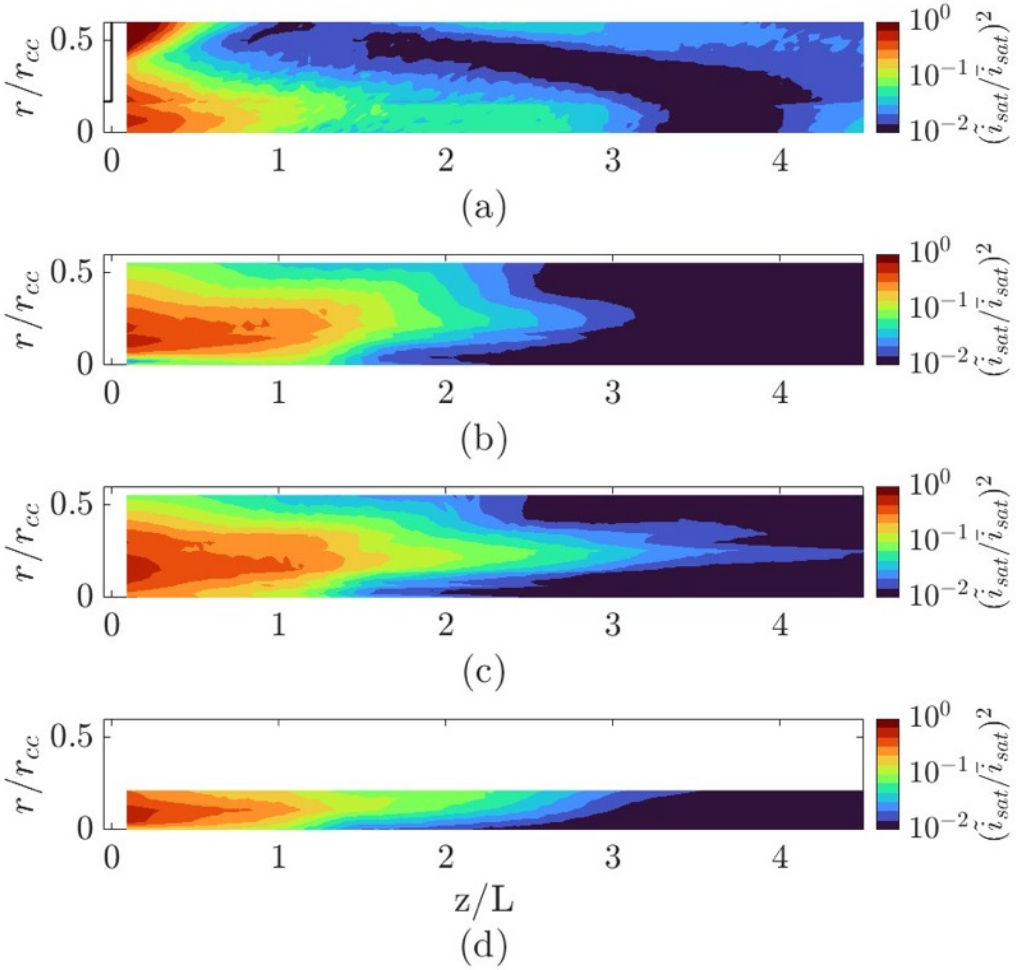

Figure 5.13: Spatial dependence of the low-frequency wave energy integrated from the power spectrum from 100 Hz to 250 kHz for (a) the RC 4 thruster + cathode configuration and the independent cathode operated at the nominal magnetic field strength with (b) three cryogenic pumps, (c) two cryogenic pumps, and (d) one cryogenic pump.

5.6.2.2 Effect of Induced Oscillations

Figures 5.14 and 5.15 show the spatial wave energy for thruster RC4 (figures 5.14(a) and 5.15(a)) and the independent cathode configurations at 100% B_{nom} and 100% $\dot{m}_{nom}$ without induced oscillations (figures 5.14(b) and 5.15(b)) and with induced RC4 oscillations (figures 5.14(c) and 5.15(c)). The high-frequency wave energy generally increases with the induced oscillations, except on the boundary of the cathode plasma where the high-frequency wave energy remains relatively constant with and without induced oscillations.

Inducing oscillations also results in higher low-frequency wave energies for $r/r_{cc} > 0.2$. However, it is unlikely that the region $r/r_{cc} > 0.2$ can be replicated on independent cathode configuration as this region is likely greatly impacted by the beam and less by the cathode plasma.

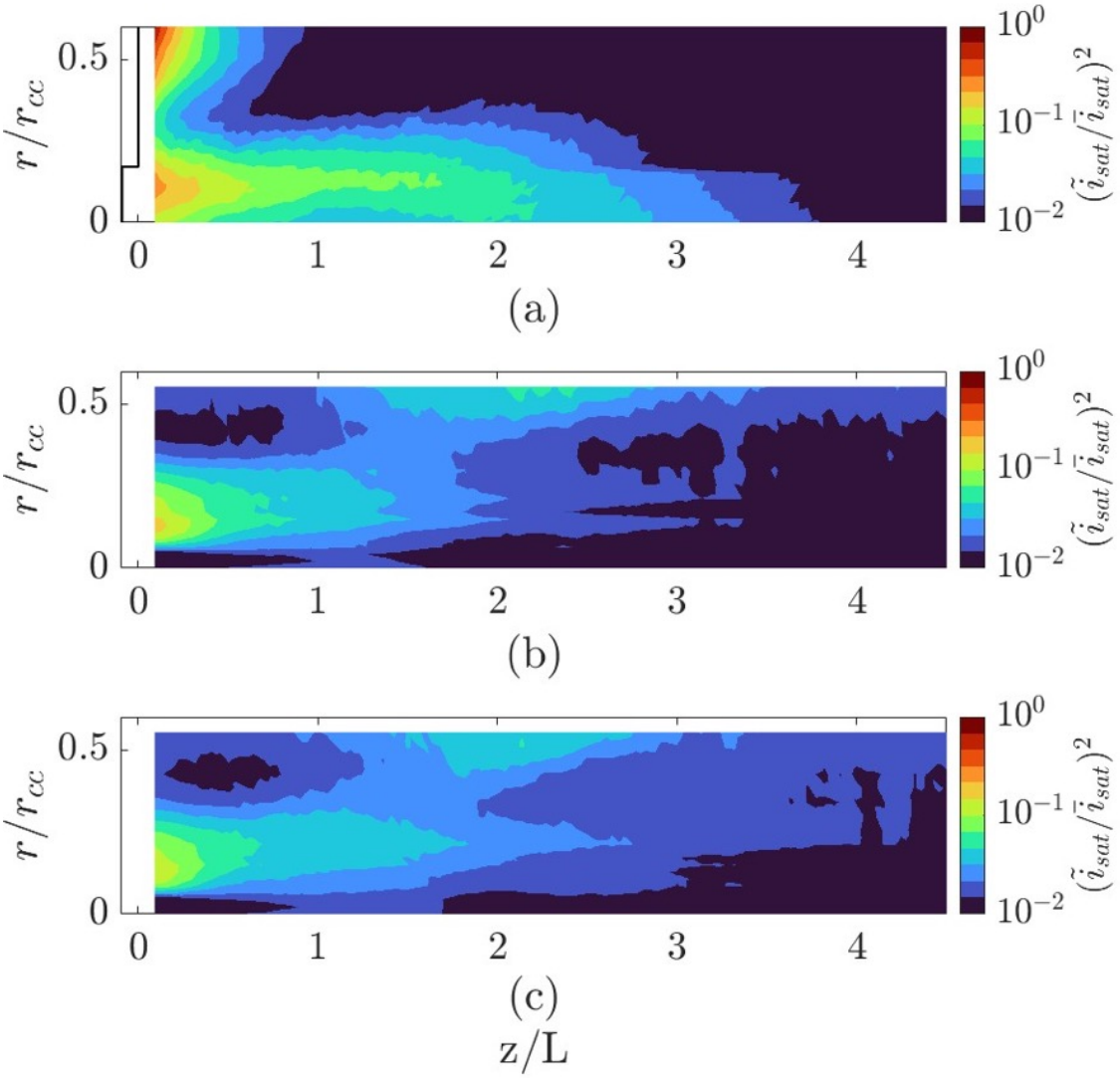

Figure 5.14: Spatial dependance of the high-frequency wave energy integrated from the power spectrum from 250 kHz to 14 MHz for (a) the RC 4 thruster + cathode configuration and the independent cathode operated at the nominal magnetic field strength and the nominal flow rate (b) without induced oscillations and (c) with induced oscillations.

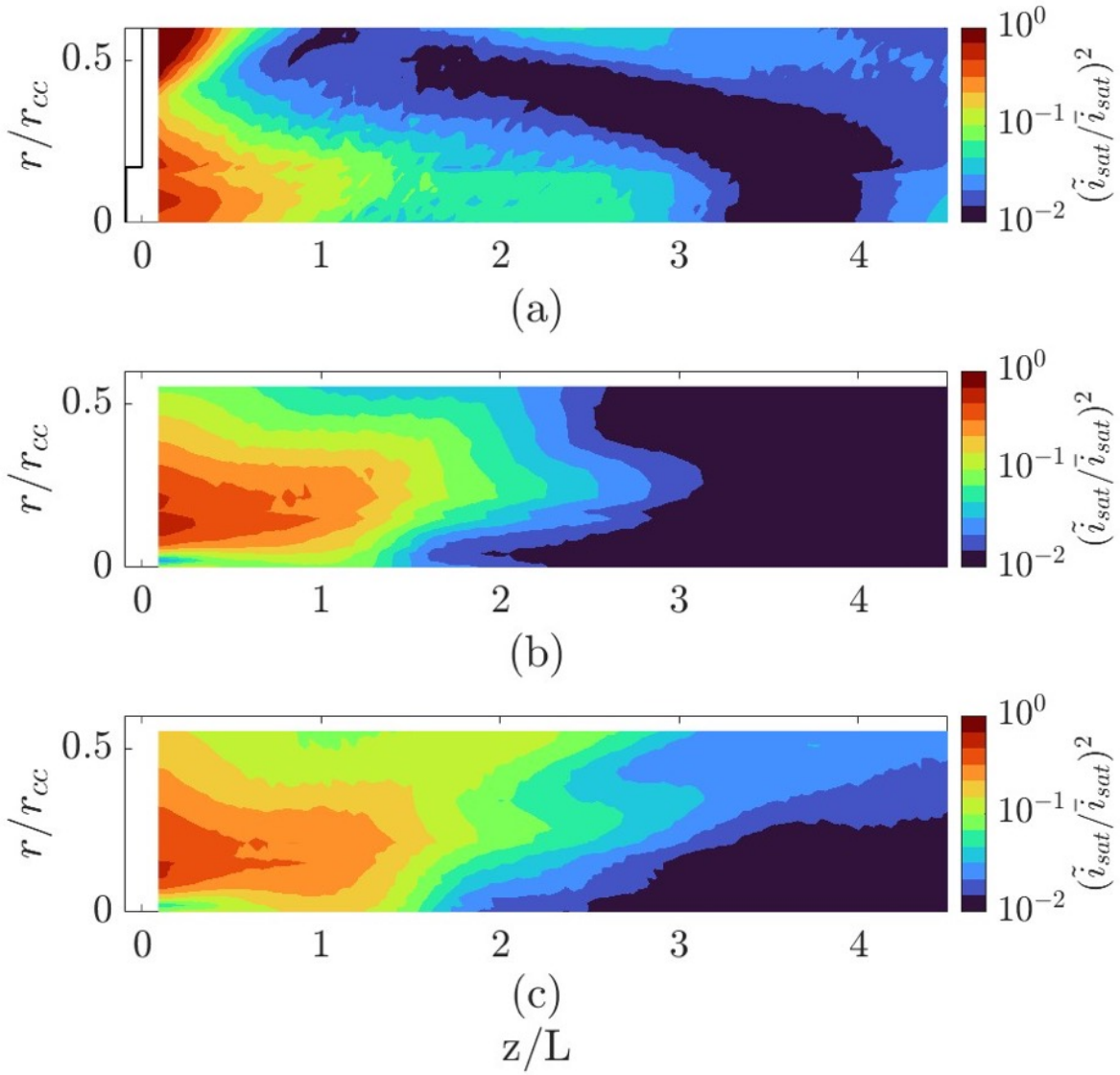

Figure 5.15: Spatial dependance of the low-frequency wave energy integrated from the power spectrum from 100 Hz to 250 kHz for (a) the RC 4 thruster + cathode configuration and the independent cathode operated at the nominal magnetic field strength and the nominal flow rate (b) without induced oscillations and (c) with induced oscillations.

Figure 5.16 shows the spatial dependance of the frequency of the dominant peak in the Fourier spectra for the thruster RC 4 in the low-frequency regime. The primary peak in this region around 60 kHz. Near the cathode exit, a lower frequency mode is present at around 50 kHz. Further, a 65-kHz peak is present bordering the cathode plume. Finally, a higher frequency (O(100 kHz)) peak appears downstream in the region where the

heightened low-frequency wave energy bridges between the thruster beam and centerline. This suggests this is a region of potential coupling between the cathode plasma and the thruster beam.

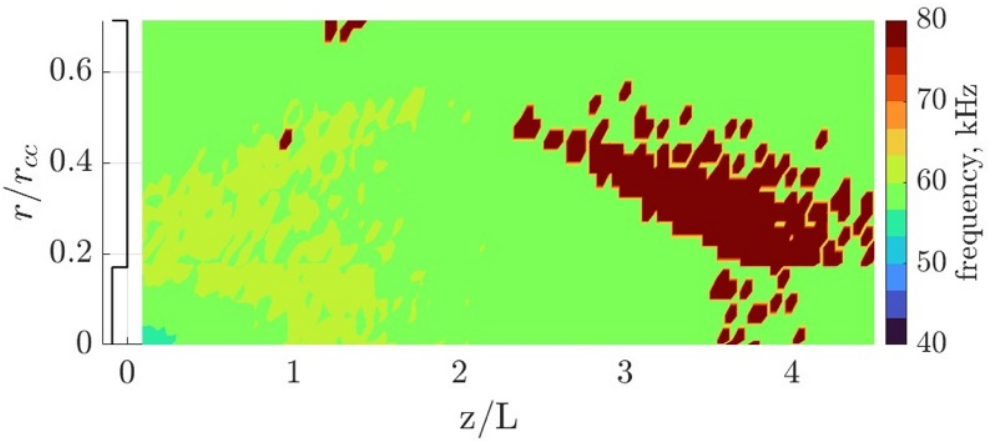

Figure 5.16: Spatial dependance of the dominant low-frequency peak for thruster RC 4.

Figure 5.17 shows the effect of the induced anode oscillations on the dominant, low-frequency peak from the Fourier spectra from the independent cathode configurations at 100% B_{nom} and 100% $\dot{m}_{nom}$ for RC 4. Without the induced oscillations, the low-frequency peak appears at approximately 60 kHz, except near the cathode exit for axial locations z/L < 2 where the low-frequency peak is closer to 50 kHz. The region where the 50 kHz peak is dominant is smaller for the higher base pressure (figure 5.17(b)). Inducing the anode oscillation drastically changes the distribution of the Fourier spectra peaks in this region. The 50-kHz peak extends further downstream and the 60 kHz peak increases to 65 kHz, matching the frequency peak of the thruster RC 4 (figure 5.16). The low-frequency peak is less affected by the introduction of the induced oscillations in the region along the steep density gradients of the cathode plasma and near the keeper exit. This suggests that while the induced oscillations aide in generating similar low frequency behavior downstream and closer to the anode boundary, the cathode plasma near the keeper exit is likely more driven by the internal cathode physics rather than the chamber pressure or induced anode current oscillations.

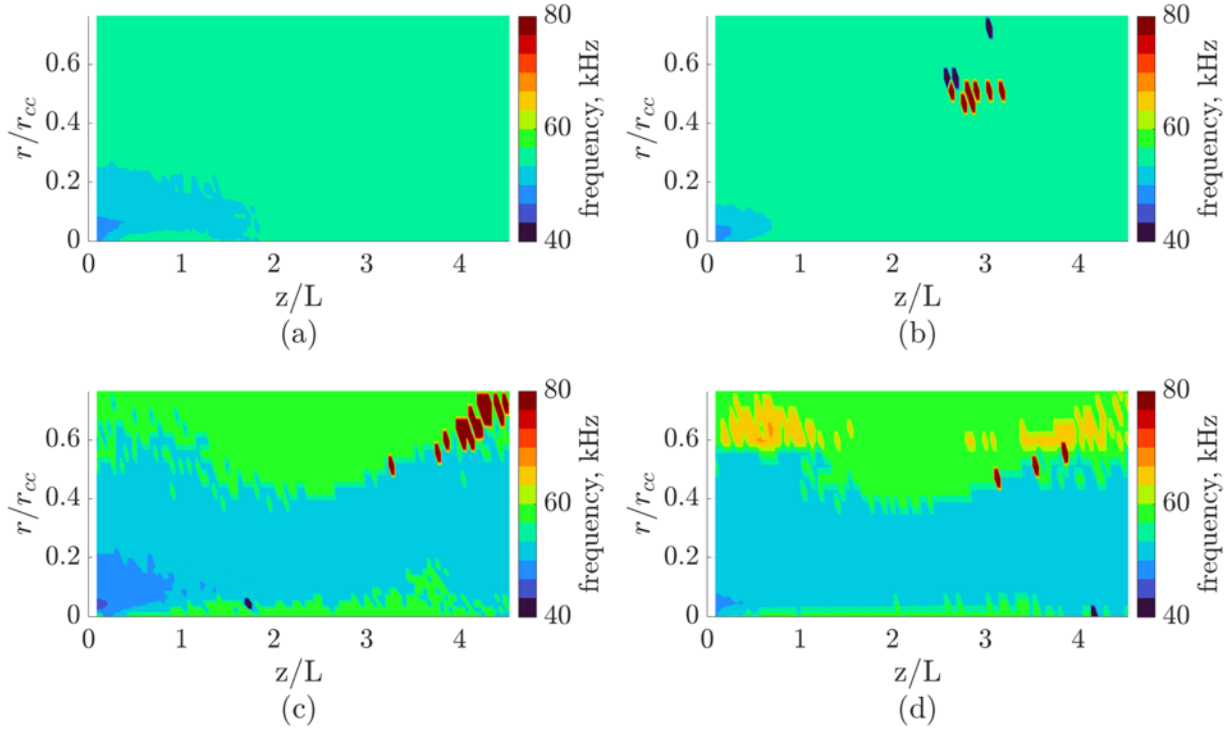

Figure 5.17: Spatial dependance of the dominant low-frequency peak for the lone cathode operation at the nominal magnetic field strength. (a)-(b) Without induced anode oscillations with three and two cryogenic pumps, respectively, and (c)-(d) with RC4 induced oscillations with three and two cryogenic pumps, respectively.

5.6.2.3 Effect of Varying Mass Flow Rate

Figures 5.18 and 5.19 show the spatial wave energy for thruster RC 4 (figures 5.18(a) and 5.19(a)) and the independent cathode configurations at 100% B_{nom} for three different flow rates (figures 5.18(b)-(d) and 5.19(b)-(d) without anode oscillations. Decreasing the mass flow rate results in heightened high-frequency and low-frequency wave energy in all areas of the plume. It is important to note that with a decrease in the mass flow rate, the background pressure in the chamber also decreases. Therefore, the increase in the high-frequency wave energy displayed in figure 5.18, which is possibly linked to an increase in the turbulence in the region, is also a function of the decreasing background pressure. Since adjusting the number of cryogenic pumps did not significantly affect high-frequency wave energy near the cathode centerline (figure 5.14), the increased high-frequency wave

energy near the centerline with decreasing mass flow rate is likely more related to flow rate rather than background pressure.

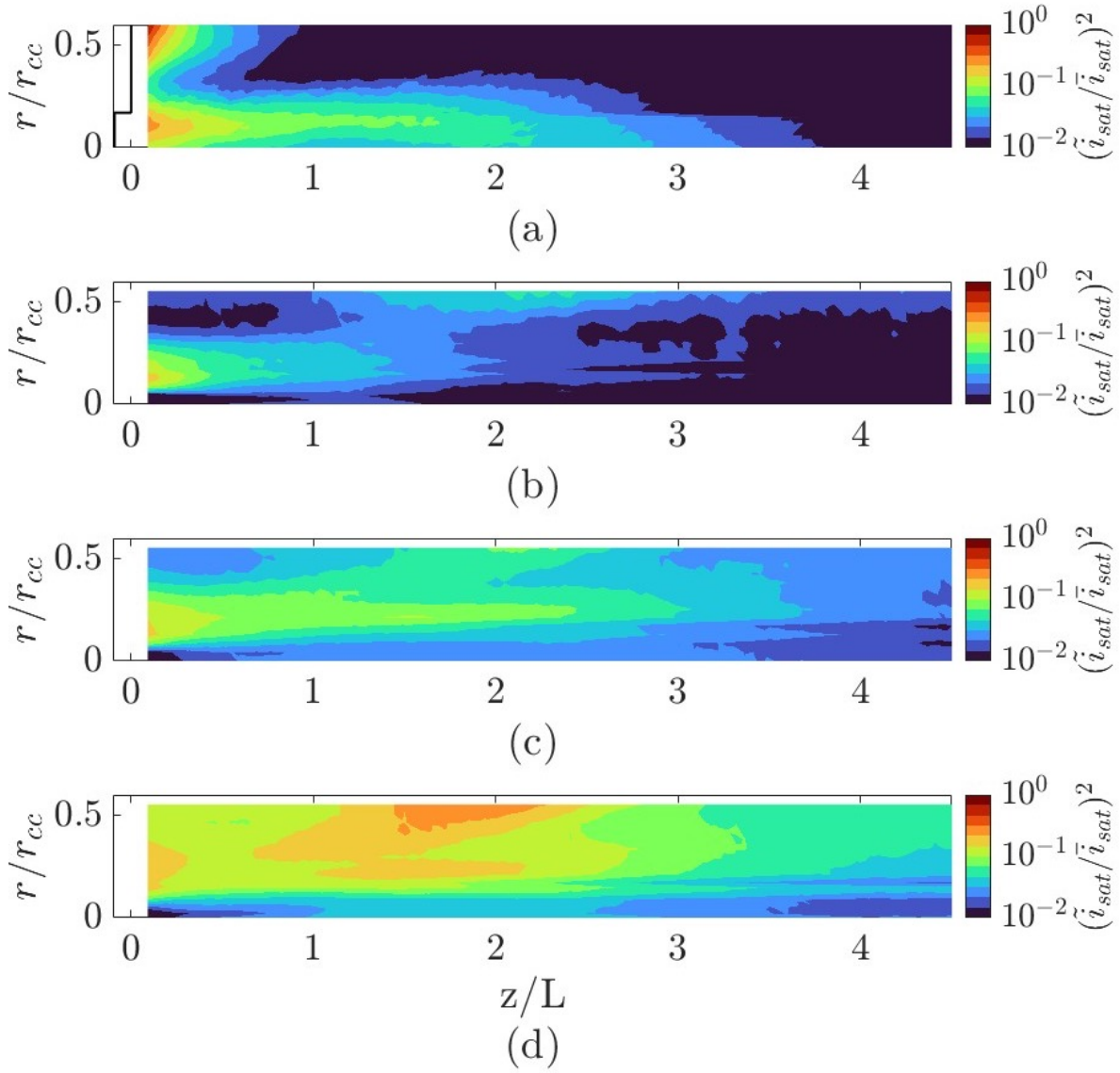

Figure 5.18: Spatial dependance of the high-frequency wave energy integrated from the power spectrum from 250 kHz to 14 MHz for (a) the RC4 thruster + cathode configuration and the independent cathode operated at the nominal magnetic field strength for (b) the nominal flow rate condition, (c) 83% of the nominal flow rate, and (d) 67% of the nominal flow rate.

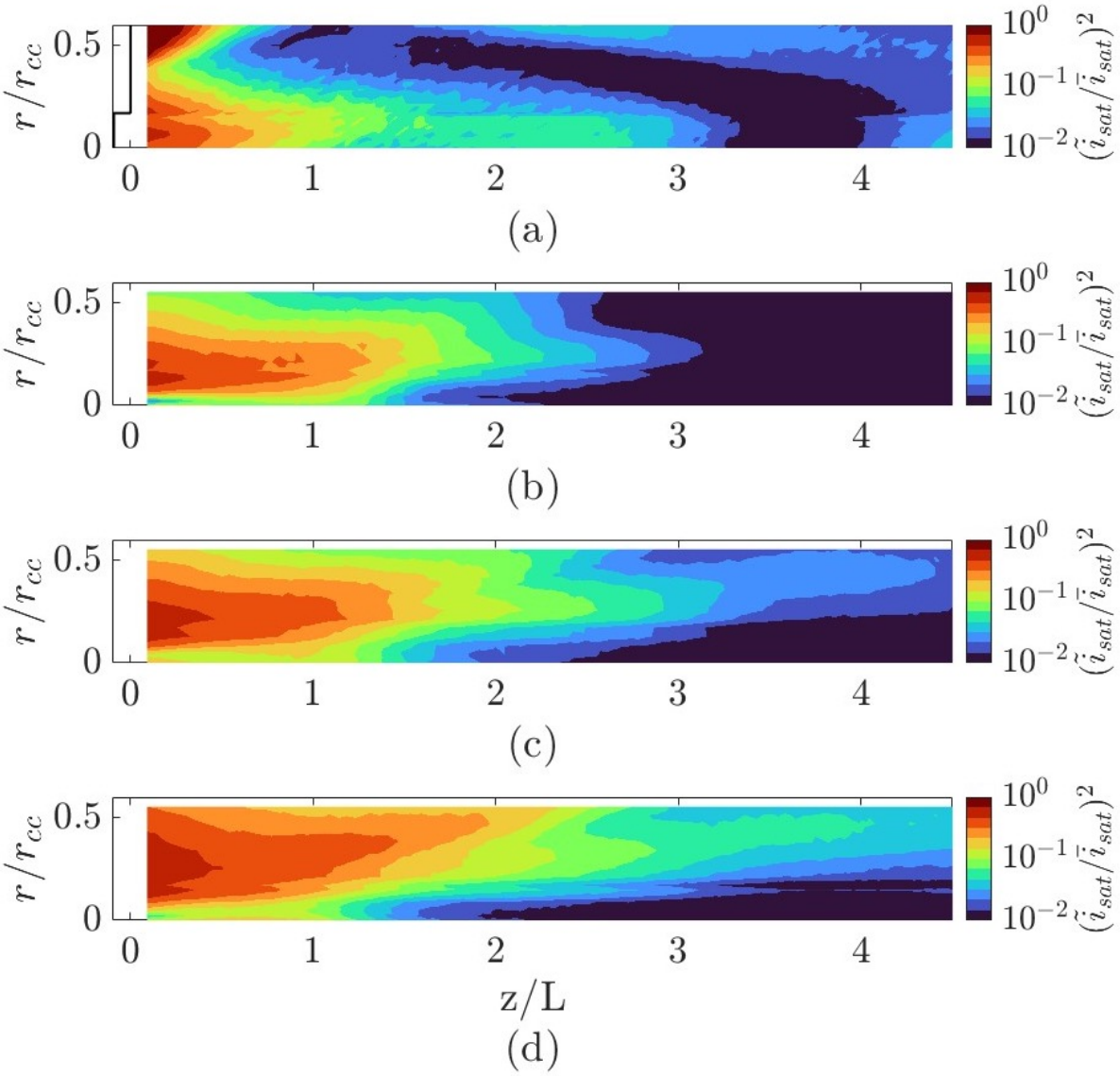

Figure 5.19: Spatial dependance of the low-frequency wave energy integrated from the power spectrum from 250 kHz to 14 MHz for (a) the RC4 thruster + cathode configuration and the independent cathode operated at the nominal magnetic field strength for (b) the nominal flow rate condition, (c) 83% of the nominal flow rate, and (d) 67% of the nominal flow rate.

Since the plasma along the steep density gradients from the cathode centerline is strongly influenced by the mass flow rate, sequentially lowering the flow rate could indicate which value produces a closer match to the thruster. Figure 5.20 shows the effect of varying the mass flow rate on the high-frequency wave energy of the independent cathode configuration compared to the thruster condition at $r/r_{cc} = 0.17$ with three

cryogenic pumps. Decreasing the mass flow rate increases the high-frequency wave energy between $r/r_{cc} = 0.5$ and $r/r_{cc} = 2.5$ for this radial sweep location. Outside of this boundary, the high-frequency wave energy is less affected by the change in mass flow rate. Figure 5.20 shows that the 83% $\dot{m}_{nom}$ condition appears to best mimic the cathode operation in the thruster. However, figure 5.18 shows an increase in the high-frequency wave energy throughout the measurement domain, which is greater than when the cathode is operated in the thruster. Lowering the mass flow rate appears to be the most effective way to mimic the cathode operation in the thruster based on the variables tested in this dissertation. However, adding external neutral flow to dampen the oscillations downstream and farther away from centerline through ion-neutral collisional damping could provide an even closer replication of the cathode behavior in the thruster.

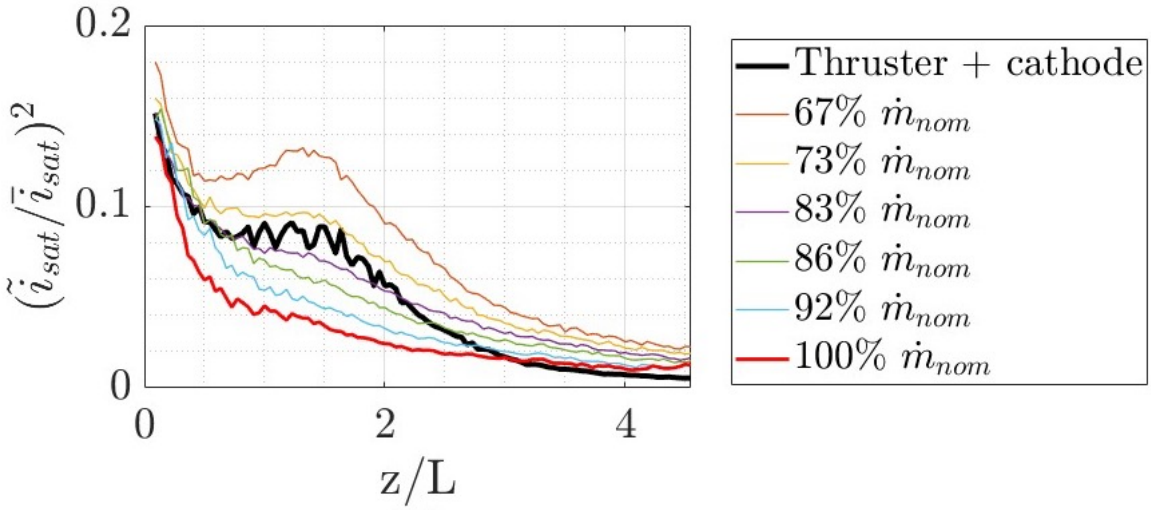

Figure 5.20: Wave energy for varying mass flow rate at $r/r_{cc} = 0.17$ without induced anode oscillations and three cryogenic pumps.

5.6.3 Optical Emission Spectroscopy Measurements

The optical emission spectroscopy (OES) measurements from this experiment were time-averaged. Konopliv et al. showed using high-speed OES that large fluctuations in the electron temperature have been measured in DC discharges [141]. Therefore, the measurements in this dissertation likely do not capture the momentarily warm electrons in the cathode plasma. Figure 5.21 shows the line ratios I_{823}/I_{828} and I_{460}/I_{828} from the

Maya2000 OES directed at the keeper face during the independent cathode configurations for varied mass flow rates at two background pressures and with and without induced thruster RC4 oscillations. The I_{823}/I_{828} ratio is consistently higher for the three-cryogenic-pump configuration versus the other pumping configurations, indicating a lower electron temperature at lower base pressures (less energy from collisions) near the keeper face (figure 5.21(a)) [141]. In contrast, the ionization rate (I_{460}/I_{828} ratio) is unaffected by background pressure. This indicates the ionization mechanisms near the keeper face are not significantly affected by variations in background pressure suggesting the local dynamics in the region dominate over neutral density effects. Direct calculation of the electron temperature and the ionization fraction from the line ratios used in this work require access to the full collision radiative model for xenon. This remains outside the scope of this dissertation and the author recommends further analysis of the time-averaged line ratio values with the full model to determine the plasma parameters.

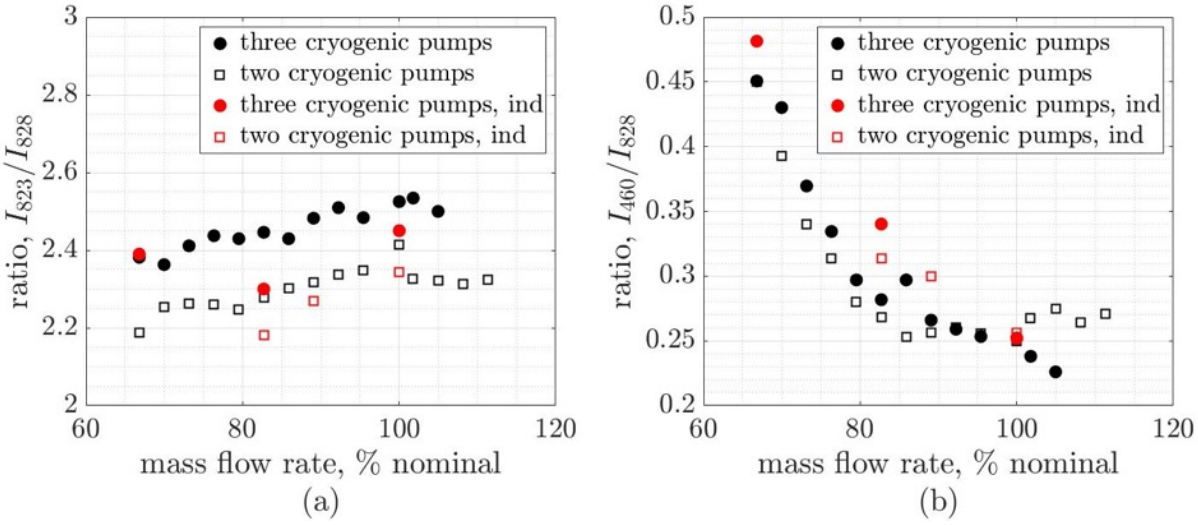

Figure 5.21: Line ratios for the independent cathode operation at the nominal magnetic field strength condition, varied mass flow rates, two background pressures, and with and without induces oscillations (RC4) focused on the keeper face. (a) I_{823}/I_{828} line ratio for determining density and temperature and (b) I_{460}/I_{828} for estimation of ionization fraction.

5.6.4 Low-Frequency Wave Phase Velocity

The Beall plots generated from the axial probe sweeps do not show significant dispersion in the high-frequency domain. The primary dispersion exists near the cathode exit in the low-frequency domain. Therefore, this section analyzes the wave dispersion of the low-frequency dynamic. The velocity components of the low frequency dynamic are found by locating the maximum wavenumber in the low-frequency domain for the radial and axial directions.

Figure 5.22 shows the direction of the low-frequency dynamic calculated from the Beall method for thruster condition RC 4 in the *r*-*z* plane (figure 5.22(a)) and for various cathode configurations (figure 5.22(b)-(f)). These data are for the two cryogenic pump configuration at the nominal magnetic field strength. For the thruster RC 4 condition, around $r/r_{cc} = 0.2$ near the inner front pole cover where the high-frequency and low-frequency wave energies are heightened, the velocity of the wave is primarily axial (figure 5.22(a)). However, in the lone cathode configurations, the wave has more of a radial component (figure 5.22(b)-(f)). Varying the cathode operational configuration does not appear to affect the direction of the low-frequency wave. While the energy of the low frequency wave can vary widely based on mass flow rate or background pressure, as described previously in this chapter, the direction of the wave appears to be generally consistent. This suggests that the mechanisms driving the low-frequency wave is likely tied to the electric field (anode location) and magnetic field (topography generated by the simulator) of the cathode setup.

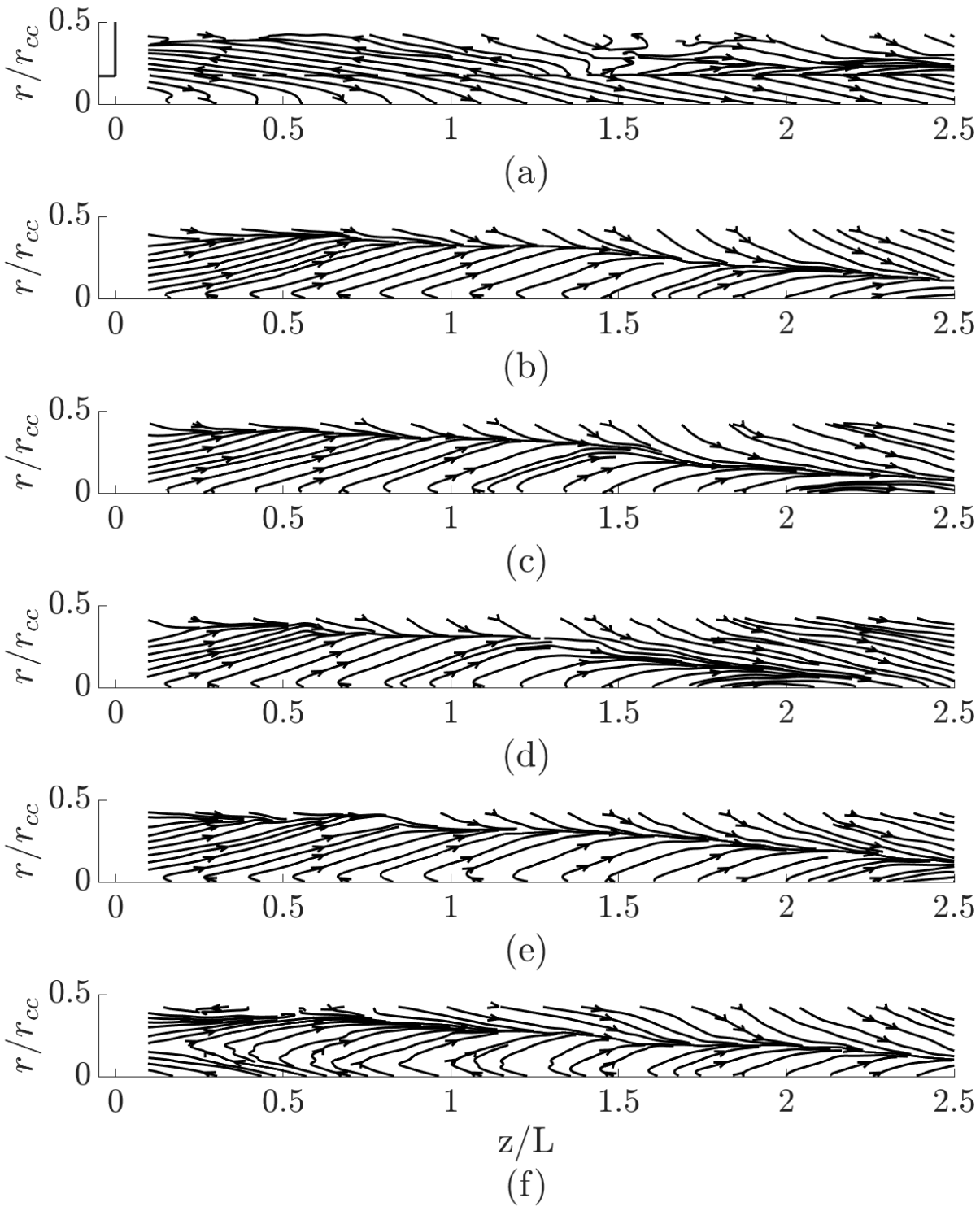

Figure 5.22: Low-frequency wave direction from Beall method.(a) Thruster and cathode. (b)-(e) Three cryogenic pumps independent cathode operation at the nominal magnetic field strength for (b) the nominal flow rate, (c) 83% of the nominal flow rate, (d) 67% of the nominal flow rate, and (e) the nominal flow rate with induced oscillations. (f)

Figure 5.23 shows the evolution of the phase speed of the low-frequency wave. The phase speed is calculated from the velocity components:

$$v_{ph} = \sqrt{v_z^2 + v_r^2} \tag{5.1}$$

where v_z and v_r are the axial and radial velocity components, respectively. Along centerline, the phase velocity of the low-frequency peak remains below 2 km/s for all cathode conditions and the thruster RC 4 for $z/L < 1.5$ (figure 5.23(a)). The phase velocity of the low-frequency peak increases farther away from centerline until $0.30 < r/r_{cc} < 0.43$ (figure 5.23(b)-(f)). At $r/r_{cc} = 0.43$, the higher background pressure appears to affect the phase speed closer to the cathode exit ((figure 5.23(f)).

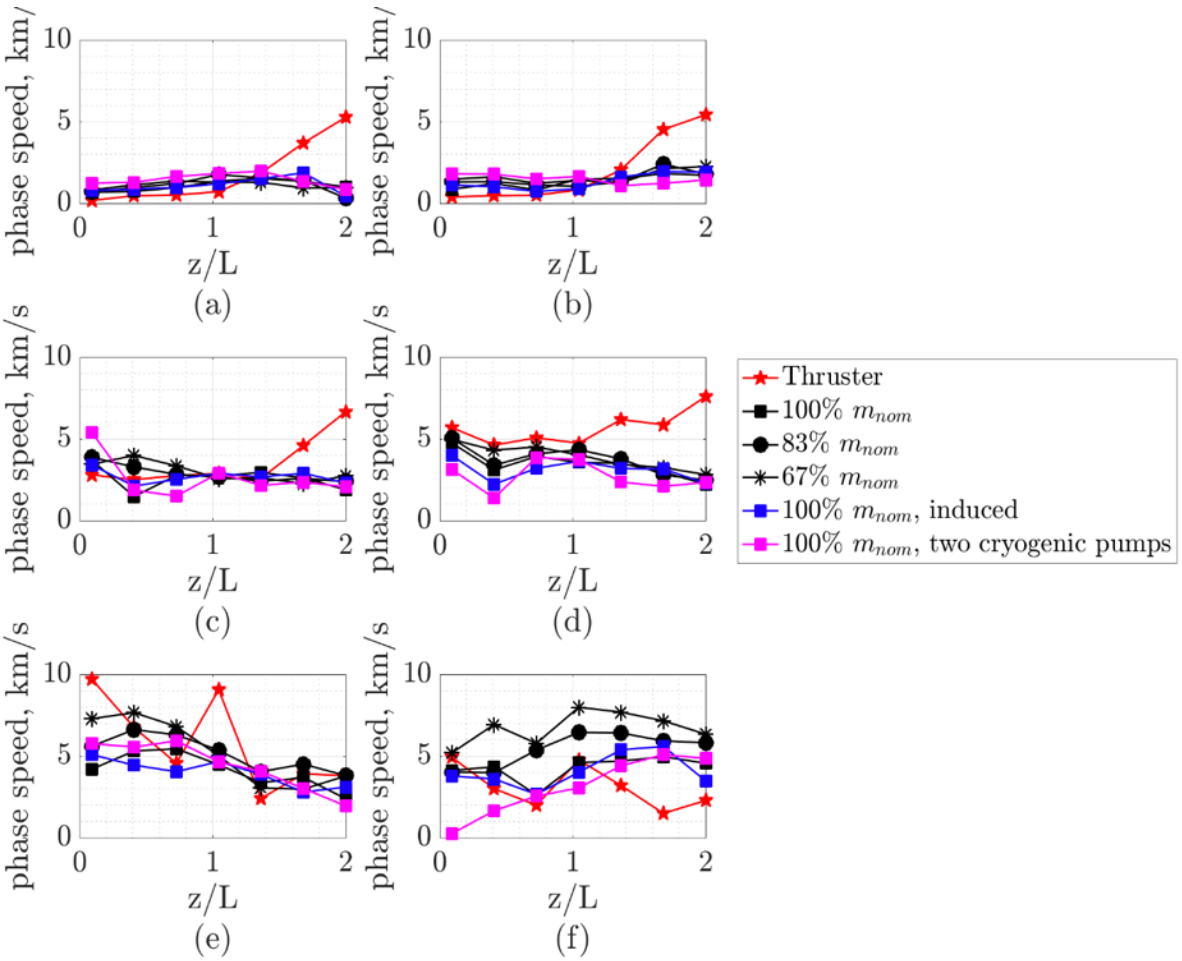

Figure 5.23: Low-frequency wave speed for the RC 4 thruster condition and various cathode operation configurations. (a)r/r_{cc}=0, (b) r/r_{cc}=0.04, (c) r/r_{cc}=0.11, (d) r/r_{cc}=0.17, (e) r/r_{cc}=0.30, and (f) r/r_{cc}=0.43. All independent cathode configurations are operated with three cryogenic pumps except otherwise noted.

5.7 Discussion

The wave energy plots in section 5.6.2 identified three regions of heightened wave energy in the independent cathode plume: (1) along the edge of the high-density cathode plasma region, (2) near z/L=0 farther away from centerline, and (3) near the entrance of the anode downstream. Figure 5.24 shows a schematic of the independent cathode setup highlighting the three regions. The wave energy in each region responds differently to variations in the cathode operational parameters.

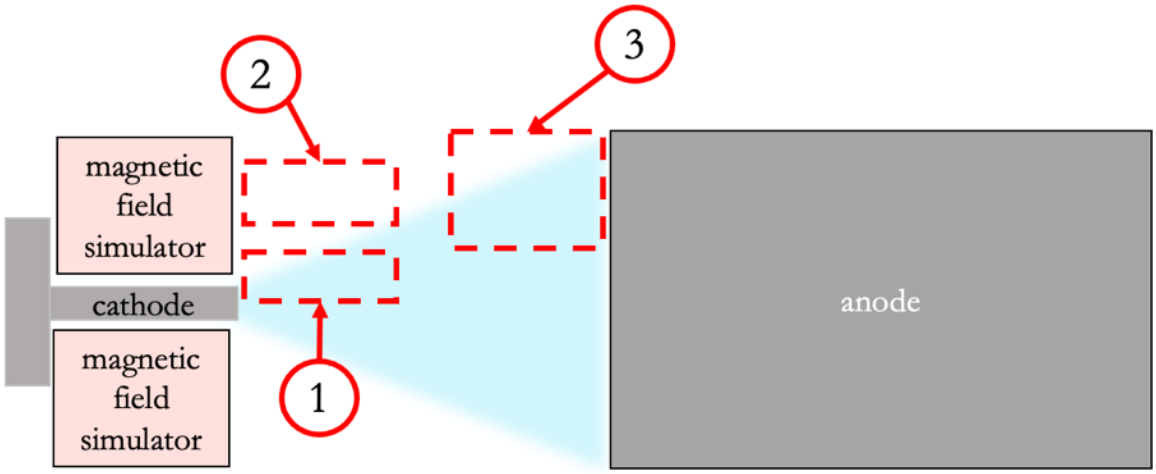

Figure 5.24: Regions of heightened wave energy in the independent cathode configuration.

5.7.1 Close to Centerline

Region 1 encompasses large density gradients and strong magnetic field strengths. Here, the electrons are strongly magnetized while the ions remain unmagnetized. The azimuthal ion wave is excited and dominant in this region; thus, the azimuthally rotating population of ions causes fluctuations in the local ion density. Figure 5.25 gives the high-frequency wave energy along the axial direction for the radial position r/r_{cc}=0.17. There appears to be no trend in the high-frequency wave energy with background pressure (figure 5.25(a)). This location is affected by the mass flow rate where the decreased mass flow more closely matched the thruster profile. However, it is worth noting that the local neutral pressure is a function of both the background pressure and the flow rate to the cathode. Further,

the neutral pressure near the cathode exit in the thruster is also subjected to the neutrals sourced by the anode flow and from the neutrals produced from charge exchange collisions in the beam. Therefore, the thruster high-frequency wave energy will be impacted as the presence of neutrals could dampen the turbulence in the region. The induced oscillations do not affect the high-frequency wave energy, except for the three cryogenic pumps, RC4 induced, and 67% $\dot{m}_{nom}$ operating condition, where the induced oscillations increase the wave energy.

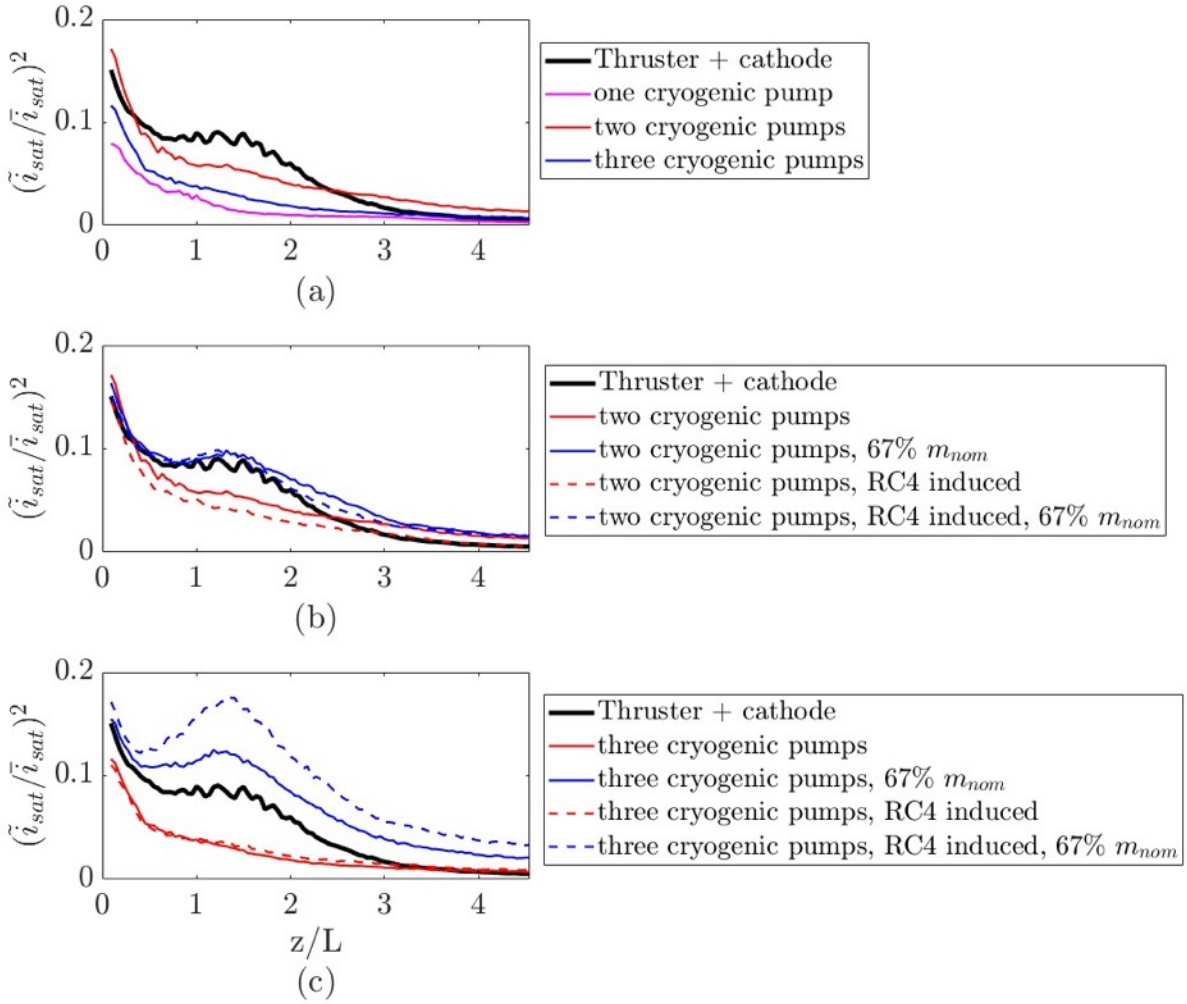

Figure 5.25: High-frequency wave energy for varying cathode parameters along r/r_{cc}=0.17. (a) varying background pressure. (b) varied mass flow rate and induced oscillations with two cryogenic pumps, and (c) varied mass flow rate and induced oscillations with three cryogenic pumps.

Figure 5.26 shows the wave energy at the radial sweep location of r/r_{cc}=0.13 for varying cathode parameters. Slightly closer to centerline, the high-frequency wave energy is less affected by the background pressure than at r/r_{cc}=0.17 (figure 5.26(a)). Lowering the flow rate increases the wave energy at this radial location closer to the thruster high-frequency wave energy and matches closely with the magnitude of the wave energy in the thruster at this radial location.

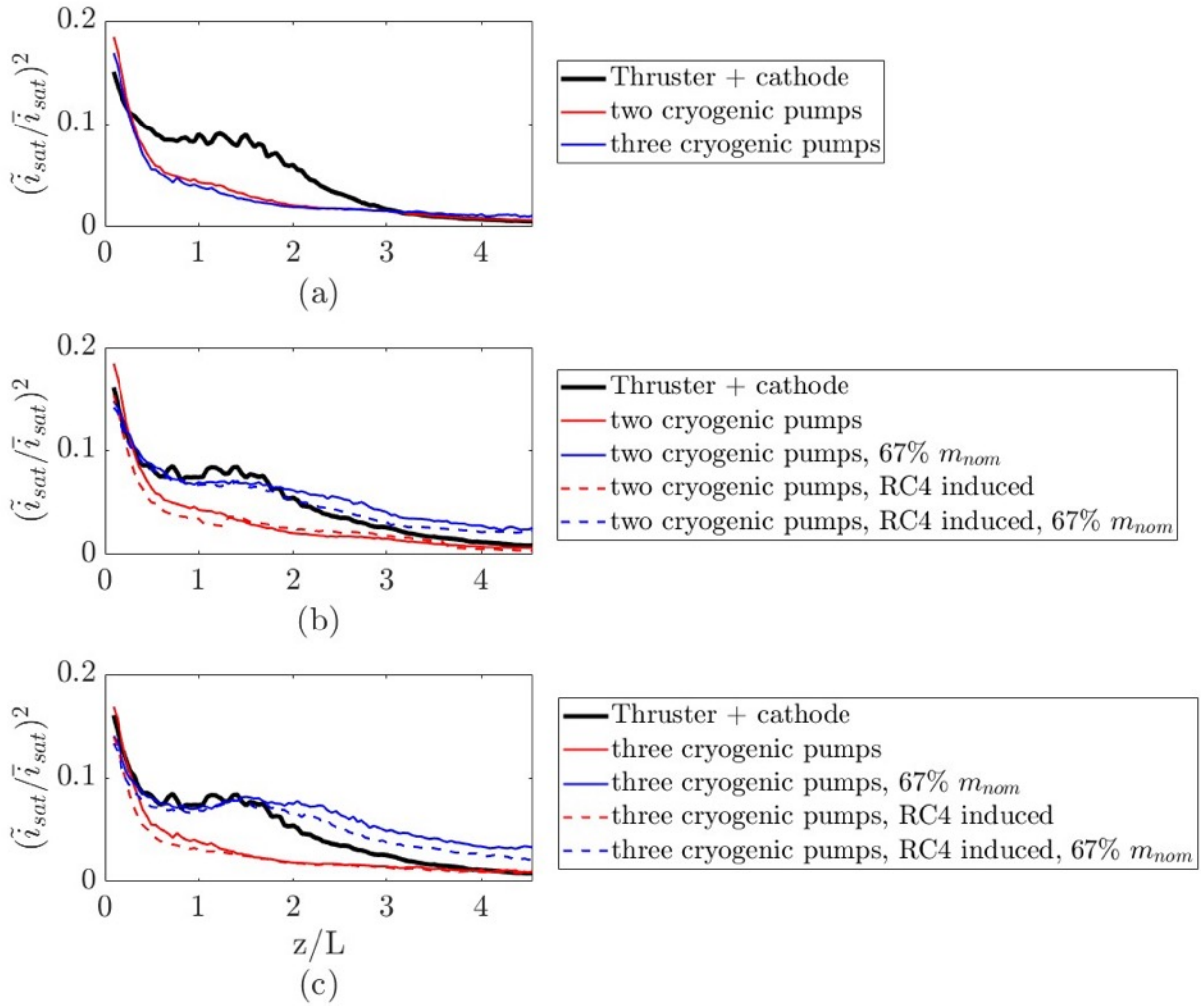

Figure 5.26: High-frequency wave energy for varying cathode parameters along r/r_{cc}=0.13. (a) varying background pressure. (b) varied mass flow rate and induced oscillations with two cryogenic pumps, and (c) varied mass flow rate and induced oscillations with three cryogenic pumps

Figure 5.27 shows the plasma properties along the radial sweep r/r_{cc}=0.17 for various cathode operational conditions captured with the HDLP. These results show the

magnetic field heats the electrons at this radial location, which is shown by warmer electrons measured by the HDLP for all magnetized cases compared to the unmagnetized cases (figure 5.27(a)). The electron density exhibits a peak density further downstream that subsequently decreases for the magnetized cases (figure 5.27 (b)). However, the electron number density increases continually for the case where the cathode was operated with induced oscillations. For axial locations $z/L < 1$, all three magnetized cases exhibit similar electron number densities. However, the lower mass flow rate condition results in the lowest electron number density, but higher electron temperatures for $z/L > 1$. The heightened electron temperature could be due to the large oscillations in ion density measured by the ion saturation probe at this flow rate. Alternatively, since the HDLP measurements were captured at 200 Hz, the cathode breathing mode and other high-frequency modes could be distorting the raw LP trace resulting in artificially high, or low, electron temperature.

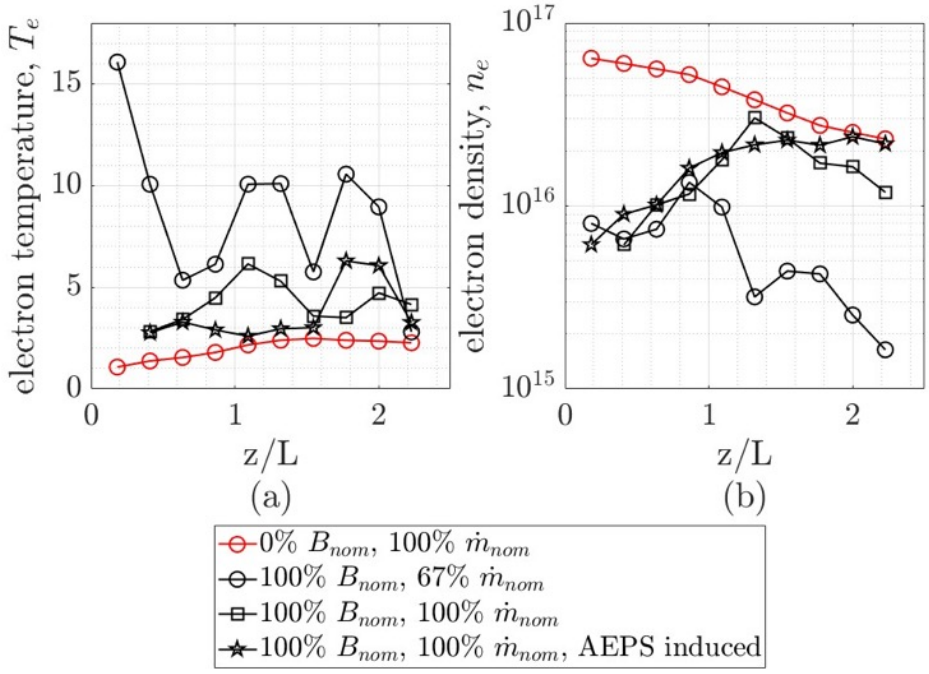

Figure 5.27: Plasma parameters along $r/r_{cc} = 0.17$. (a) electron temperature and (b) electron density. All conditions were tested with three cryogenic pumps.

The HDLP findings combined with the spatial dependence of the frequency of the low-frequency behavior (figure 5.17), further supports the idea that the induced

oscillations play a more significant role on the plasma regions outside of the near-keeper region (near the anode boundary and farther away from centerline near the cathode exit plane). The axial sweep for the HDLP measurements were taken along the edge of the jet shape created by the induced magnetic field.

5.7.2 Near the Cathode Exit Plane Far from Centerline

The wave energy in region 2 is mostly affected by the changes in background pressure. The plasma density in this region is low compared to other locations in the cathode plume. In the HET plume, this region has a high neutral density as well as heightened wave energy. Radially divergent beam ions have been measured in this region in the thruster, which combined with the steep magnetic field gradients of the magnetically shielded thrusters, likely breed the high-frequency turbulence measured in this region. Since this region is heavily influenced by the beam in the thruster, it is unlikely an accurate representation of this region is achievable on independent cathode configurations. Therefore, as previously mentioned, it is likely most important for independent cathode configurations to mimic the behavior of the cathode plasma in the thruster near centerline and along the steep density gradients.

5.7.3 Near the Anode Entrance

Figure 5.28 illustrates the effects of mass flow rate on the narrow-band, low-frequency peak at $r/r_{cc} = 0.17$ and $z/L = 1.4$ operating at two base pressures and without induced anode oscillations for 100% B_{nom} (figure 5.28(a)) and 75% B_{nom} (figure 5.28(b)). The nominal mass flow rate corresponds to RC 4 for figure 5.28(a) and RC 3 for figure 5.28(b). Figure 5.28 also shows the low-frequency peak for the equivalent thruster RC at the nominal flow rate. The flow rate was not varied for the HERMeS thruster test, therefore, only the nominal flow rate condition is shown. Decreasing the mass flow rate correlates with an increase in the frequency peak of the azimuthal mode. The frequency of the

azimuthal mode is higher when the cathode is operated at higher background pressures for all flow rates and both background pressures.

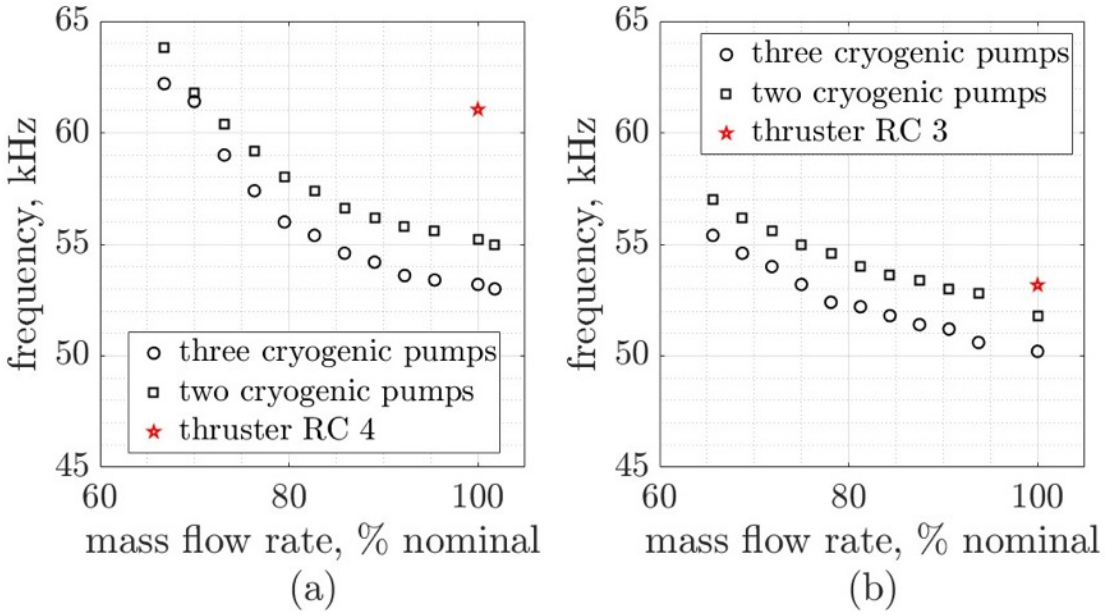

Figure 5.28: Frequency peak of azimuthally travelling wave at $r/r_{cc} = 0.17$ and z/L=1.4 with increasing flow rates with and without a third cryogenic pump. (a) 100% B_{nom} (RC 4) and (b) 75% B_{nom} (RC 3).

Figure 5.29 shows the wave energy for the high-frequency domain (figure 5.29(a)-(b)) and the low-frequency domain (figure 5.29(c)-(d)) at $r/r_{cc} = 0.17$ and $z/L = 1.4$ under two operational pressures and without induced anode oscillations for 100% B_{nom} (figure 5.29(a) and figure 5.29(c)) and 75% B_{nom} (figure 5.29(b) and figure 5.29(d)). Similar to figure 5.28, figure 5.29 shows the high-frequency and low-frequency wave energies for the equivalent thruster RC. The high-frequency wave energy increases for decreasing flow rates, which matches the trend of increasing low-frequency peak. While the frequency peak in the low-frequency domain is affected by the mass flow rate, the energy of the low-frequency mode does not show a consistent trend for decreasing flow rates or changing operational pressure under either the 100% B_{nom} or 75% B_{nom} conditions. Therefore, the increase in the low-frequency peak paired with increase in the high-frequency wave energy suggests the plasma in this regions becomes more turbulent for decreasing mass flow rate.

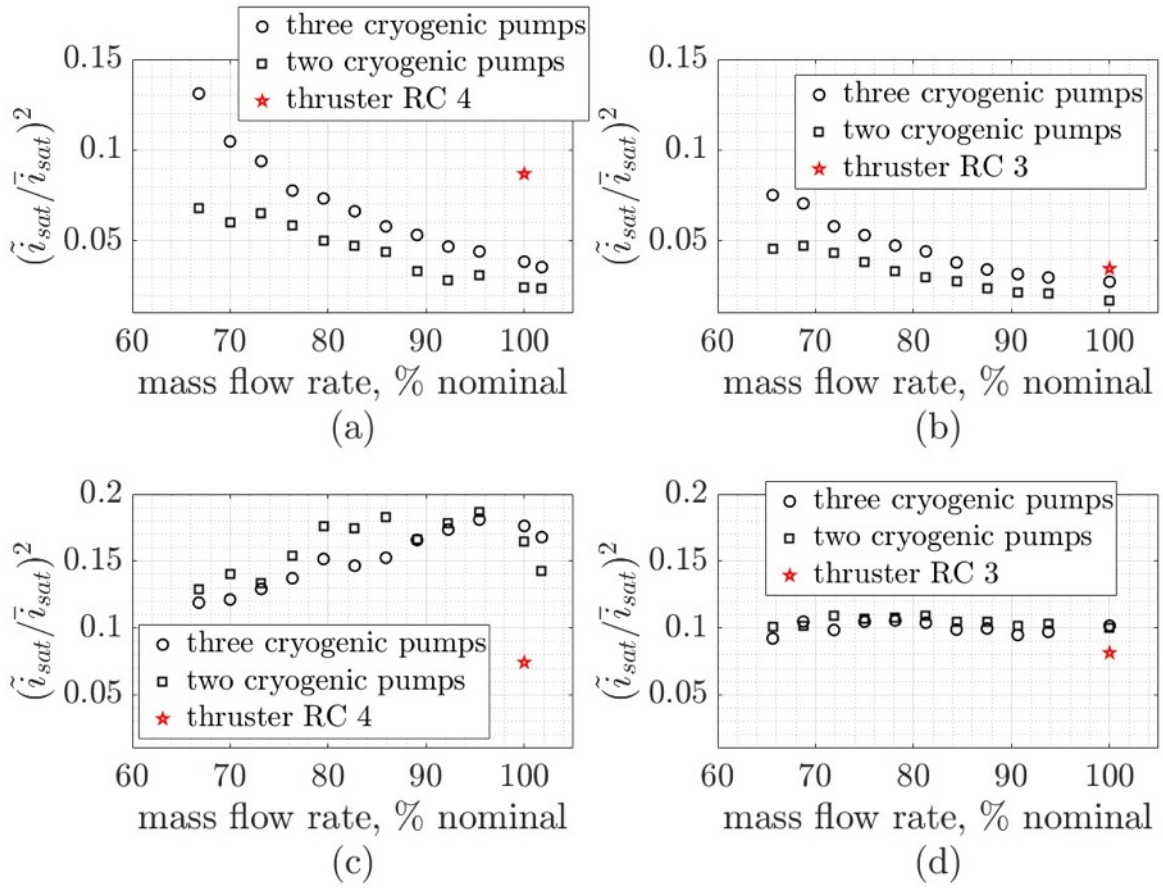

Figure 5.29: Wave energies for increasing flow rates and with and without a third cryogenic pump at $r/r_{cc} = 0.17$ and $z/L = 1.4$ (a) High-frequency domain, 100% B_{nom}, (b) high-frequency domain, 75% B_{nom}, (c) low-frequency domain, 100% B_{nom}, and (d) low-frequency domain, 75% B_{nom}, .

In the thruster, the wave energy in region 3 could be lower as a result of high neutral density from charge exchange collisions and recombination. However, measurements of the neutral profile in this region are needed to compare. Therefore, a higher background pressure on independent cathode tests can better mimic the high-frequency behavior in the thruster specifically in region 3.

5.8 Summary

This chapter explored the effect of inducing oscillations, adjusting background pressure, varying mass flow rate, and varying magnetic field strengths on the low-frequency dynamics and high-frequency dynamics of independent cathode operation and how those

results compare to full thruster operation. The primary findings of this chapter from the two frequency regimes are as follows.

1. **Low-frequency dynamic.** The primary low-frequency dynamic in the partially magnetized hollow cathode plume is the azimuthal ion dynamic as shown in Chapter 4. The wave energy of low-frequency dynamic is generally unaffected by the changes in background pressure; however, the frequency downstream is slightly higher for higher background pressures. Inducing anode oscillations and varying the mass flow rate both significantly change both the wave energy and the frequency of the dynamic. Inducing oscillations on the anode create a boundary in the plasma where the low-frequency peak matches the thruster frequency. Decreasing the mass flow rate greatly increases the wave energy of the low-frequency dynamic throughout the plume and the frequency of this mode also increases.
2. **High-frequency turbulence.** The formation of high-frequency (>250 kHz) turbulence in the cathode plume occurs in three distinct regions: (1) along the large density gradient near the cathode exit, (2) near the cathode exit plane, but farther away radially, and (3) near the entrance to the anode.
    1. The large gradients in density and magnetic field along the edges of the high-density plasma induce the high-frequency turbulence in region 1. The mass flow rate is the primary cathode parameter that contributes to heightened wave energy in this region with lower flow rates increasing the wave energy. Lower background pressures also increase the wave energy, although this has less of an effect compared to varying the mass flow rate. This suggests that the turbulence in this region is primarily driven by the cathode plasma.
    2. The high-frequency turbulence farther from centerline, but near $z/L = 0$, is affected by the background pressure. During the thruster operation, this

region shows reduced high-frequency turbulence due to the elevated neutral density. Significantly, this suggests higher background pressures can provide a more thruster-like cathode plume.

3. The magnetic field lines that the cathode is exposed to in the centrally-mounted position confine the electrons along the field lines, as mentioned in previous chapters. This chapter shows the presence of high-frequency turbulence in the region near the anode entrance. This turbulence manifests to transport the electrons to the anode surface. This region of high-frequency turbulence is not captured in the thruster measurements perhaps due to heightened neutral pressure. The heightened neutral density could be from the anode neutral flow or from charge exchange collisions from the beam. Modelling results, such as from Hall2De, or neutral pressure measurements in this region to determine the neutral pressure is needed. Further, if the local neutral pressure is heightened, it is likely impossible to mimic the local neutral pressure in the independent cathode configurations by merely adjusting the number of pumps used in the setup. Adjusting background pressure by varying the vacuum pumping speeds affects the global neutral population rather than the local neutral pressure. Therefore, additional flow mechanisms, such as neutral flow injections near the cathode exit on independent tests, might be necessary to mimic the thruster neutral profile.

CHAPTER 6

Neutral Species Investigation

"There's no such thing as the unknown-only things temporarily hidden, temporarily not understood"

James T. Kirk

6.1 Introduction

This chapter investigates the final research objective: examining waves in the hollow cathode plume with different neutral species. The cathode was tested in two different vacuum chambers, operated in HET-like magnetic field simulators, and featured a downstream cylindrical anode. Cathode performance metrics, including discharge current and voltage and floating keeper voltage, were evaluated. Additionally, a three-axis wave probe was used to study wave propagation in the hollow cathode operated with xenon, krypton, and argon.

6.2 Experimental Design

This work was performed at the Aerospace Laboratory for Plasma Experiments (ALPE) at Western Michigan University (WMU) and the Plasma Test Facility at the U.S. Naval Research Laboratory (NRL). This section provides an outline of the experimental design for each facility. An outline of the chamber configurations is given in section 3.5.

6.2.1 Hollow Cathode Configuration

The hollow cathode used in this experiment was the LaB_6 cathode designed for the H6 thruster [161]. The H6 is a 6-kW class HET developed in collaboration between the University of Michigan, the NASA Jet Propulsion Laboratory, and the Air Force Research Laboratory [162], [163]. This section outlines the cathode, anode, and magnetic field configurations for the two facilities. Vacuum chamber information for both facilities, including cryogenic pumps and power availability, is given in section 3.5.1.

6.2.1.1 Aerospace Laboratory for Plasma Experiments

The experiment in ALPE used the coils of an HET to generate the magnetic field [11]. A 66.5-mm-diameter and 203.2-mm-long copper anode was placed downstream of the cathode exit plane. The anode was cooled with copper water lines welded along the assembly that were electrically isolated from the vacuum chamber with short nylon tubing. High-speed anode current was measured using a 410 Pearson coil. The DC anode current was monitored on the power supply. Two Micsig DP10013 high-voltage probes were used to capture the high-speed voltage between the anode and ground and between the keeper and ground. The cathode was shorted to ground.

Table 6.1 gives the test matrix used for this work. The cathode was operated at a constant DC discharge current of 20 A with a DC supply in current controlled mode, various mass flow rates, and magnetic field strengths ranging from 0% B_{max} to 100% B_{max}. In addition to the flow rates selected, the keeper-to-anode distance was also adjusted between 31.8 mm and 63.5 mm. Anode positions are not listed in the text matrix below. Thermocouple measurements at the cathode base and the anode monitored the thermal equilibrium of the system which dictated the time between measurements.

Table 6.1: Experimental test matrix for work performed at ALPE with the H6 cathode and magnetic field coils.

Neutral Species	Field Strength, % B_{max}	Flow Rate, sccm
Kr	0	[8.7, 10.0, 10.75]
	28	[7.9, 9.5, 10.75]
	50	[7.9, 8.7, 9.5, 10.75]
	100	[9.5, 10.75]
Xe	0	[7.0, 8.0]
	9	[6.0, 7.0, 8.0]
	28	[6.0, 7.0, 8.0]
	50	[5.0, 6.0, 7.0, 8.0]
	100	[7.0, 8.0]

Table 6.2 compares the mass flow rates of krypton and xenon used in ALPE, along with their corresponding base pressures. All krypton flow rates resulted in a lower base pressure compared to xenon operation. Two flow rates (0.59 mg/s and 0.67 mg/s) were selected to match between xenon and krypton. Chapter 5 demonstrated that variations in mass flow rate significantly influence small-scale turbulence and large-scale dynamics, while base pressure has minimal impact. Therefore, the difference in base pressure between xenon and krypton is unlikely to affect the interpretation of the probe measurements.

Table 6.2: Mass flow rate comparison for xenon and krypton cathode operation in ALPE.

Neutral Species	Flow rate, sccm	Flow Rate, mg/s	Base Pressure, Torr
Kr	7.9	0.49	7.55×10^{-5}
	8.7	0.54	7.99×10^{-5}
	9.5	0.59	8.36×10^{-5}
	10.75	0.67	8.81×10^{-5}
Xe	6	0.59	9.10×10^{-5}
	7	0.69	1.45×10^{-4}
	8	0.79	1.90×10^{-4}

6.2.1.2 U.S. Naval Research Laboratory

The H6 cathode was inserted into a magnetic field simulator developed at the U.S. Naval Research Laboratory that creates a magnetic field topography similar to an HET. Although the magnetic field simulator differed from the one used in ALPE, the topography and strength of the magnetic field remained consistent between the two setups. The downstream cylindrical anode was a stainless-steel mesh, which allowed for a visual inspection of the plasma plume inside the anode. The anode was placed immediately downstream of the cathode such that the cathode-to-anode gap was negligible. The cathode was operated at a 20 A with a constant flow rate of 37 sccm of argon, 1.10 mg/s, with a base operational pressure of 4.3×10^{-4} Torr.

6.2.2 Diagnostic Methods

6.2.2.1 Wave Probe

A wave probe was employed to interrogate the propagation of waves in the cathode plume. Figure 6.1 shows the full probe (figure 6.1(a)), a close up on the probe tip (figure 6.1(b)), and the schematic for the probes including the numeric order of the probes (figure 6.1(c)). The probe electrodes were inserted into four single bore alumina tubes housed in a quad-bore alumina tube to align the probe tips. Each probe was constructed of 0.635-mm-diameter tungsten rods protruding the single bore alumina by 5 mm. Three of the probes protrude the quad bore alumina at the same distance (probe 2-4) and one is inset (probe 1) allowing for radial, axial, and azimuthal measurements of the fluctuation in the ion saturation current.

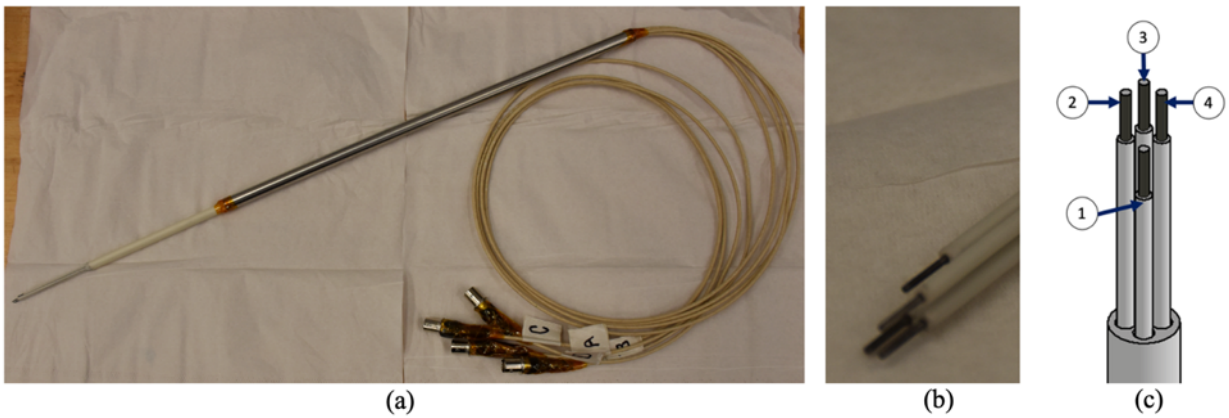

Figure 6.1: Ion saturation probe array for wave measurements. full view of the probe, (b) probe tip and (c) schematic order of probes.

ALPE Wave Probe Orientation. The probes were biased to -57 V using a series of AAA batteries and the current was collected using a transimpedance amplifier (TIA) with selectable gains of 200x and 1000x. The output of each TIA was connected to a channel on a 16-bit GaGe PCIe oscilloscope. The wave probe was inserted between the anode and cathode with all probe tips perpendicular to cathode centerline.

NRL Wave Probe Orientation. The probes were biased to -27 V using a series of 9 batteries and high-speed ion saturation current was collect using a shunt resistor and a 12-bit scope Tektronix MSO46 scope. A linear motion stage injected the wave probe axially toward the cathode concentric with the anode.

The since the anode-to-cathode gap used at NRL was negligible, the probe needed to be inserted axially. Conversely, the anode-to-cathode gap was adjusted in the experiment in ALPE, which allowed for radial insertion of the probe. Figure 6.2 shows the injection orientation of the two probes at NRL (figure 6.2(a)) and ALPE (figure 6.2(b)). Both configurations allow for three-axis wave measurements. All probe measurement distances are referenced to the center of the field simulator exit plane (0mm, 0mm).

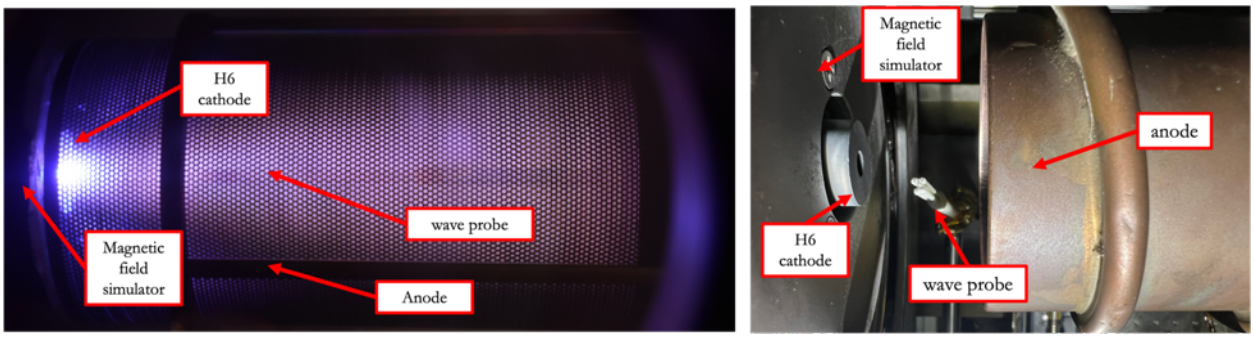

Figure 6.2: H6 cathode experimental setup and probe configuration for ALPE and NRL. (a) Cathode operation at NRL showing axially inject probe inside the perforated anode and (b) the probe location between the anode and cathode for experiments at ALPE.

6.2.2.2 Optical Emission Spectroscopy

Figure 6.3 shows the schematic of the optical emission spectroscopy (OES) setup used in ALPE. The experiment at NRL did not utilize an OES. The optical lens tube houses two collimating lenses: an uncoated LA1708 with a focal length of 203.2 mm (L1), and an uncoated LA1134 lens with a focal length of 59.8 mm (L2). A fiber optic coupler was mounted at the base of the lens tube. A 200 µm fiber optic cable with a 0.22 numerical aperture connected the lens tube with the fiber feedthrough. An SMA-SMA fiber patch cable connected to the OES outside of the chamber. A FLAME-S-RAD Ocean Optics spectrometer was used with a wavelength range of 200-850 nm and a resolution of 1.34 nm. The OES connected to the chamber computer via serial, and the OES measurements were recorded with the Ocean View software.

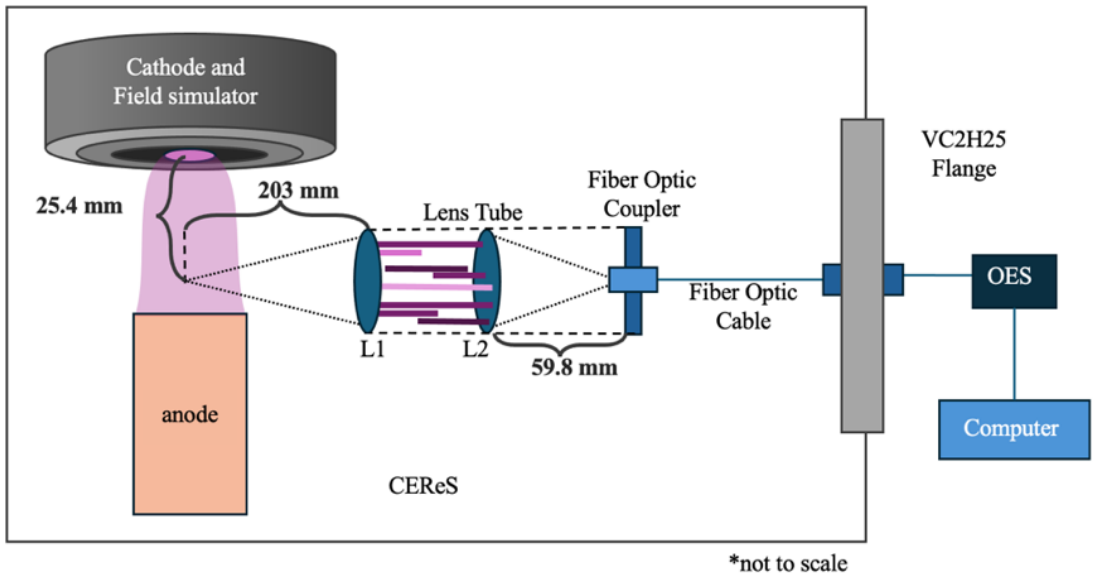

Figure 6.3: OES schematic for downstream investigation with H6 cathode and 63.5 mm cylindrical anode.

6.3 Neutral Species Analysis

This section begins with an analysis of cathode performance metrics between cathode operation on xenon, krypton, and argon. Next, visual changes in the plume are correlated with optical emission spectroscopy measurements. Finally, the energy and propagation of waves in the plume for krypton, xenon, and argon are presented.

6.3.1 Cathode Performance Metrics

Figure 6.4 presents passive cathode performance measurements of magnitudes in current oscillations and keeper voltage oscillations, labeled as anode current, A_{p2p}, and keeper voltage, V_{p2p}, respectively, for the cathode operating on xenon at increasing anode separation distance. Generally, decreasing the mass flow rate increases the magnitude of peak-to-peak oscillations of the anode current and keeper voltage. As the cathode is starved for neutrals, ionization oscillations begin to rise. For farther anode positions and lower flow rates, the ionization instabilities become unrecoverable, and the cathode begins to visibly flicker. The $28\%\,B_{max}$ condition is unique in that for all anode separation distances and all flow rates, the cathode is stable (figure 6.4(c) and (h)). At this condition

the magnitude of the peak-to-peak oscillations in the anode current remain below 5 A, and the magnitude of the oscillations in the keeper floating voltage remain below 2.5 V.

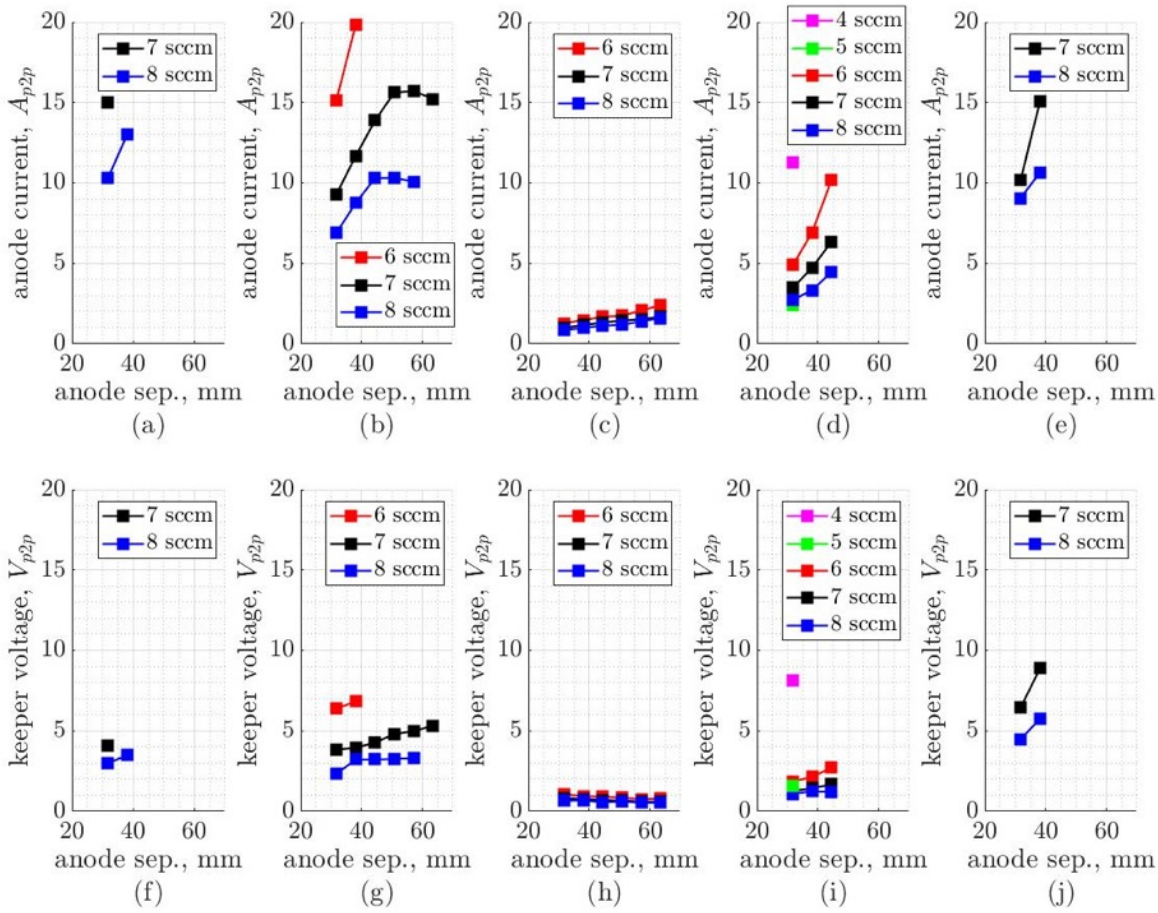

Figure 6.4: Passive cathode performance metrics for increasing anode separation for xenon. (a)-(e) peak-to-peak magnitude of discharge current oscillations and (f)-(j) peak-to-peak magnitude of floating keeper oscillations for magnetic field strengths B = [0%, 9%, 28%, 100%] B_{max}, respectively.

Figure 6.5 shows the cathode performance measurements for krypton. The behavior is similar to xenon in that the decreasing flow rate increases the magnitude of the peak-to-peak oscillations in both the keeper voltage and anode current for all cases except the $28\%B_{max}$, where all anode positions and cathode flow rates result in stable operation with minimal oscillation magnitude in the keeper and anode signals (figure 6.5(c) and (h)). At the $100\%\,B_{max}$ condition, the cathode is only stable at one anode position and one flow rate, thus only one data point was captured (figure 6.5 (e) and (i)).

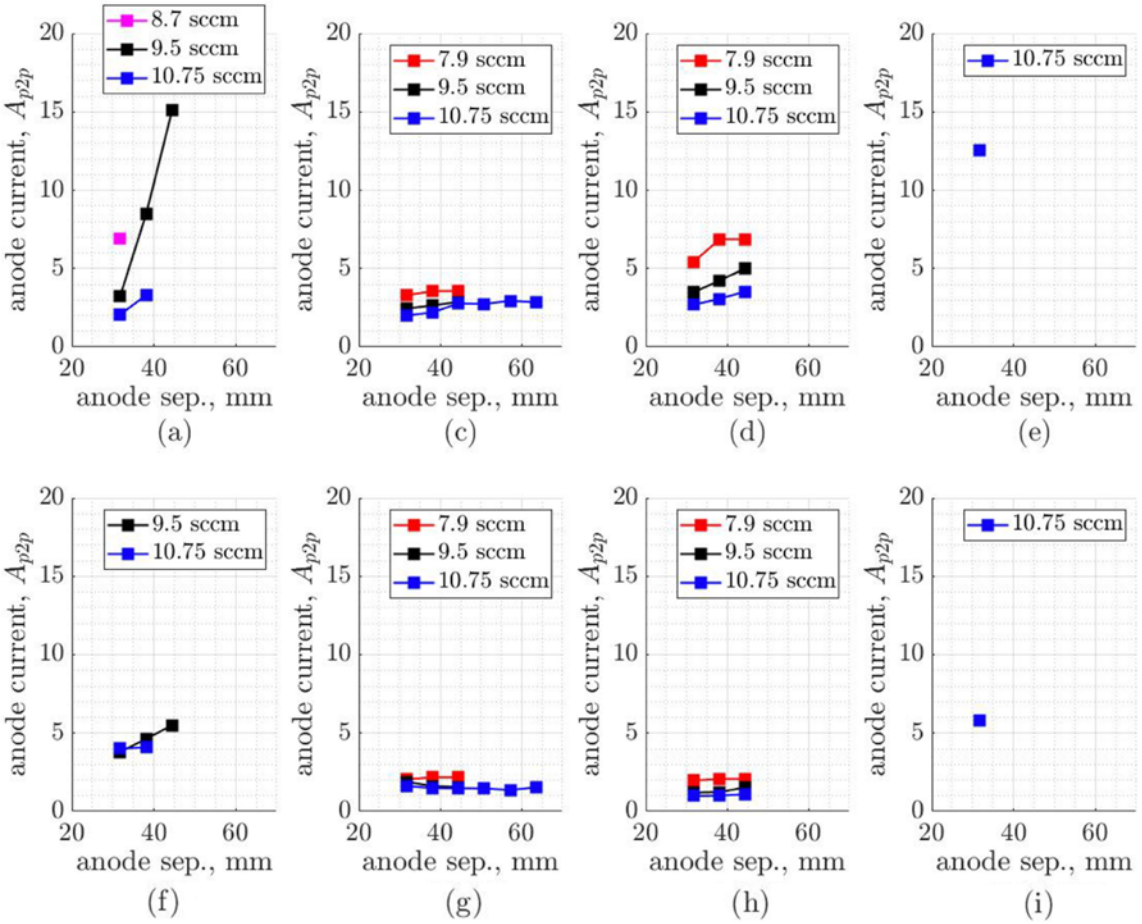

Figure 6.5: Passive cathode performance metrics for increasing anode separation for krypton. (a)-(e) peak-to-peak magnitude of discharge current oscillations and (f)-(j) peak-to-peak magnitude of floating keeper oscillations for magnetic field strengths B = [0%, 9%, 28%, 100%] B_{max}, respectively.

Notably, the magnitude of the anode current oscillations for xenon are larger when compared to krypton operation at a near-equivalent magnitude of keeper voltage oscillations. Table 6.3 shows this phenomenon at the 0% B_{max} condition. This suggests that at a higher magnitude of oscillations in the discharge current for krypton operation, which would occur with at lower mass flow rates, the magnitude of oscillations in the keeper voltage will be greater for krypton than for xenon. At the lower flow rate condition for krypton (7.9 sccm-Kr), the cathode visually flickers. Additionally, at equivalent flow rates (in mg/s), the magnitude of the peak-to-peak discharge oscillations and keeper

oscillations are much less than for xenon. This suggests that without a magnetic field, a high sccm flow is required to stabilize the krypton discharge.

Table 6.3: Difference in the magnitude of peak-to-peak anode current at near-equivalent magnitude of keeper peak-to-peak voltage for the 0% B_{max} condition.

	Flow rate, sccm	Flow rate, mg/s	$I_{D,p2p}$, A	$V_{k,p2p}$, V
Xenon	7	0.69	15	4.1
Krypton	9.5	0.59	3.2	3.8
Krypton	10.75	0.67	2.1	1.3

6.3.2 Visual Plume Changes and Optical Emission Spectroscopy

This section pairs visual changes in the plume with optical emission spectroscopy measurements to evaluate trends in the electron density, temperature, and ionization fraction. First, figure 6.6 shows the H6 cathode operated at NRL on argon for increasing magnetic field strengths. The perforated anode used at NRL allows for clear visualization of the cathode divergence throughout the plume and how the plume evolved for increasing magnetic field strengths. The application of the magnetic field drastically changes the shape of the external plasma of the cathode. As magnetic field increases from 0% B_{max}, the high-density region outside of the cathode exit changes shape from a ball (figure 6.6(a)) to a cone (figure 6.6(b)). The cone reshapes into a high-density plasma ball when the magnetic field strength is further increased, but the "jet"-like form remains downstream (figure 6.6(c)). The visual light intensity of the plasma also increases with increasing field strengths suggesting a growth in the ion population.

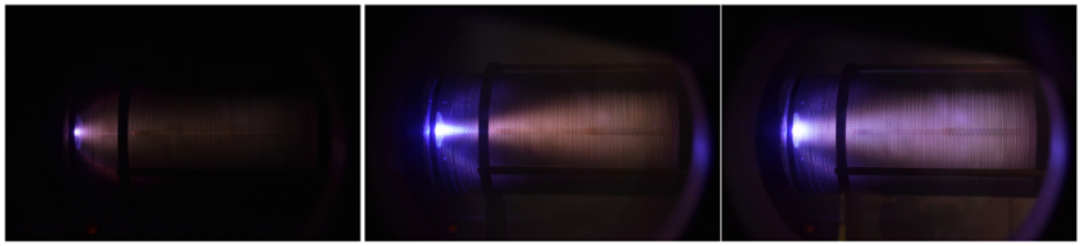

Figure 6.6: Visual change in cathode plume with increasing magnetic field. (a) $0\%B_{max}$ (b) $10\%B_{max}$, and (c) $100\%B_{max}$. The camera settings were consistent between the three images.

The OES spectra provides a quantitative plume analysis, complementing the qualitative insights from visual inspections. In general, xenon and krypton ions emit light in the ultraviolet and visible spectra while the neutrals generally emit in the infrared spectra. However, there exists overlap between the ion and neutral emission for krypton and xenon as shown in table 6.4. The prominent ion and neutral lines used in this chapter are described below and are derived from work performed in references [95], [97], [141].

Table 6.4: General range of strong lines of emission for xenon and krypton emission.

	Ions nm	Neutrals nm
Xenon	97-610	828-3507
Krypton	84-1022	116-1816

Figure 6.7 shows the OES spectra from the experiment in ALPE for the $50\%\,B_{max}$ field strength condition comparing xenon and krypton at a keeper-to-anode separation distance of 31.8 mm. A spectrometer integration time of 20 ms was used for the xenon traces and 10 ms for the krypton traces. For xenon, (Figure 6.7(a)-(d)), the lower flow rate (5 sccm) emit light at a higher intensity at the wavelengths associated with ion emission within the visible spectra compared to higher flow rate conditions. It is likely the 5-sccm condition is approaching the plume mode transition where ions are generated through macro-oscillations such as ionization instabilities or through small scale turbulent mechanisms, such as ion acoustic turbulence. This heightened ion population regime is

not observed during krypton operation suggesting the instability transition occurs at slightly lower flow rates for krypton than what were tested.

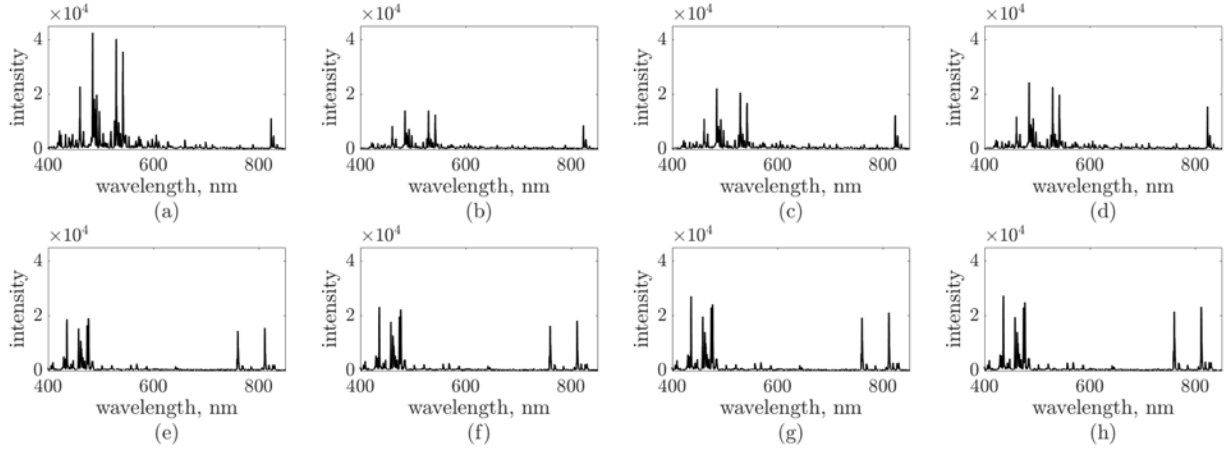

Figure 6.7: OES spectra with the magnetic field strength at 50% B_{max} for (a)-(d) xenon for [5, 6, 7, 8] sccm respectively and for (e)-(h) krypton for [7.9, 8.7, 9.5, and 10.75] sccm respectively.

Figure 6.8 shows the line intensity ratios for I_{823}/I_{828} and $I_{460}/I_{828}$for increasing magnetic field strengths and varying anode position. As stated in previous chapters, the I_{823}/I_{828} can be used to determine electron temperature using methods described by Konopliv et al. with an estimation of the plasma density in this region on the on the order of $1{\times}10^{17}\mathrm{m}^{-3}$ [141]. As the intensity of the magnetic field is increased, the density likely changes; however, $1{\times}10^{17}\mathrm{m}^{-3}$ is an estimate used for all conditions. The I_{823}/I_{828} ratio decreases for increasing magnetic field strengths correlating to increasing electron temperatures. This makes sense as the electrons travel along the magnetic field lines and gain energy with increasing magnetic field strength. Using the diagram relating temperature and $\mathtt{I_{823}/I_{828}}$ developed by Konopliv et al, the electron temperature in this work varies between approximately 4 eV for the unmagnetized cases and 7 eV for the full magnetic field cases [141]. For the 7-sccm and 8-sccm flow conditions (Figure 6.8(c) and (e)) and at the 28% B_{max} condition, the electron temperature is lower (as indicated by a higher I_{823}/I_{828} ratio, assuming a constant plasma density) than the preceding and succeeding magnetic field conditions. At this condition, the ionization fraction is high (as

indicated by a higher I_{460}/I_{828} line ratio) (Figure 6.8(b),(d), and (f)). This suggests the ionization fraction is higher for these cases.

The anode position appears to have little effect on the plasma parameters (as observed as a consistent I_{823}/I_{828} line ratio) at all magnetic field strengths at the OES measurement location (Figure 6.8(a),(c) and (e)). However, with the anode farther downstream the plasma density could be lower as neutrals are able to diffuse away rather than being trapped in the anode when the anode is closer to the cathode exit. This difference in plasma density would result in a different electron temperature. The anode position also does appear to affect the ionization fraction as the I_{460}/I_{828} line ratio is also consistent for all separation distances, except at the 28% B_{max} condition (figure 6.8(b),(d) and (f)).

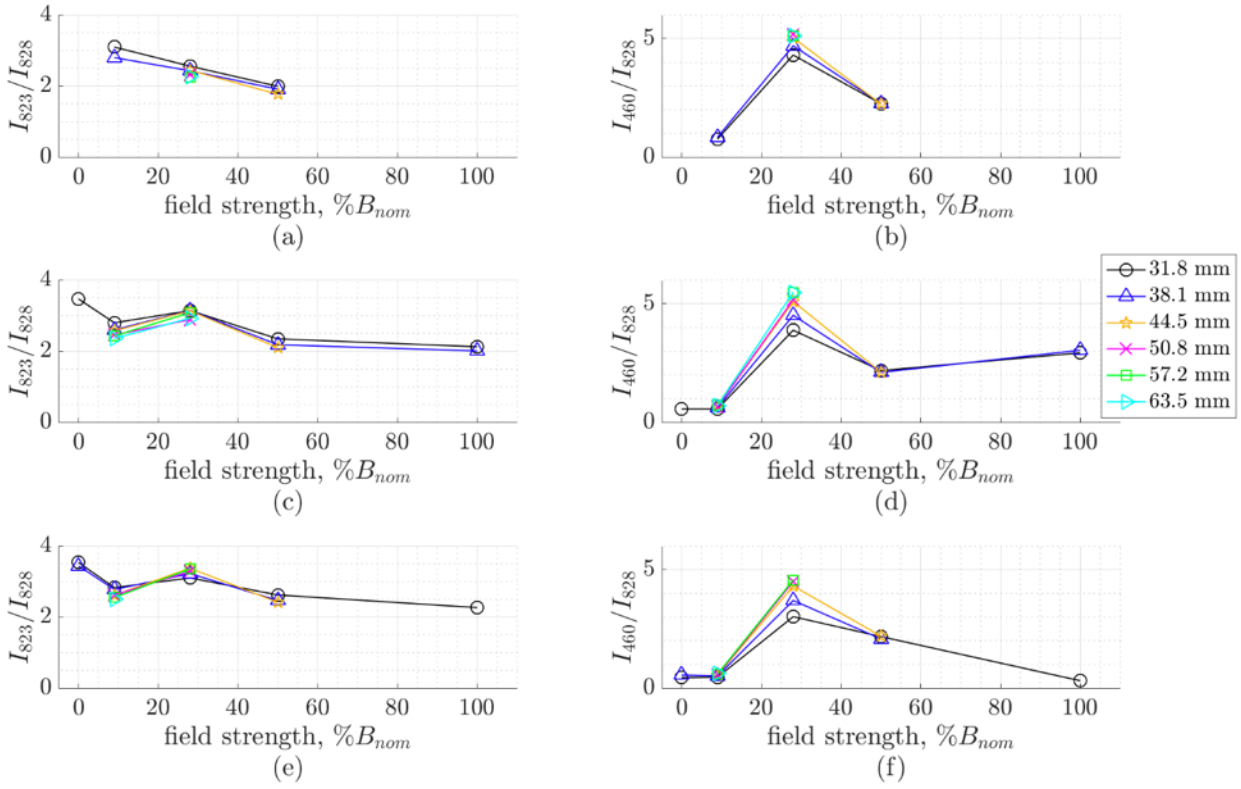

Figure 6.8: I_{823}/I_{828} and I_{460}/I_{828} line intensity ratios for xenon. (a)-(b) 6 sccm, (c)-(d) 7 sccm, and (e)-(f) 8sccm.

Figure 6.9 shows images of the cathode operating in ALPE on xenon at 7 sccm and a keeper-to-anode separation distance of 31.8 mm for increasing magnetic field strengths

with Fourier transforms of the anode signals. While the power supply was set to current controlled mode, the current collected at the anode can still oscillate about the set DC setpoint. Therefore, this section explores the Fourier spectra for both the anode current from the Pearson coil measurement and the Fourier transform of the anode voltage from the high voltage probe measurement between anode and ground. The Fourier spectra from anode voltage is likely more representative of the cathode performance as the voltage is able to float. Note that the cathode was shorted to ground for the duration of the experiment. At the 0% B_{max} condition (Figure 6.9(a)), the cathode appears to be operating in stable spot mode. This is supported by the expected low electron temperature, low values for magnitude of the anode current and keeper voltage peak-to-peak oscillations, and a low ionization fraction (small I_{460}/I_{828} ratio). At 28% B_{max} (Figure 6.9(b)), the plasma is collimated into a jet form where there appears to be substantially lower plasma densities radially away from this cylindrical structure. At this condition, the ionization fraction (I_{460}/I_{828} ratio) is higher suggesting a large number density of ions, but relatively colder electron temperature. Thus, the mechanisms generating the ions at this condition are likely not related to processes in which the electron drift feeds the instability. Further, the magnitude of the peak-to-peak oscillations in the keeper voltage is also low for the 9% B_{max} and 28% B_{max} conditions. Thus, it is likely that these ions are not returning to the cathode surfaces which would lead to erosion. Further, the Fourier transform of the anode current (figure 6.9(d)) and the anode voltage (figure 6.9(e)) at this condition shows lower power low-frequency behavior when compared to the magnetic field at 0% B_{max} or 50% B_{max}. At 50% $\mathrm{B_{max}}$ (Figure 6.9(c)), the plasma column visually expands radially, the magnitude of the peak-to-peak oscillations of the keeper voltage, anode voltage, and anode current increase, and the ionization fraction (I_{460}/I_{828} ratio) decreases. The increase in the magnitude of oscillations in the cathode performance metrics also manifests as an increase in the Fourier spectral power, particularly in the low-frequency domain, when

the magnetic field strength is at 50% B_{max} compared to the 28% B_{max} condition (figure 6.9(d-e)).

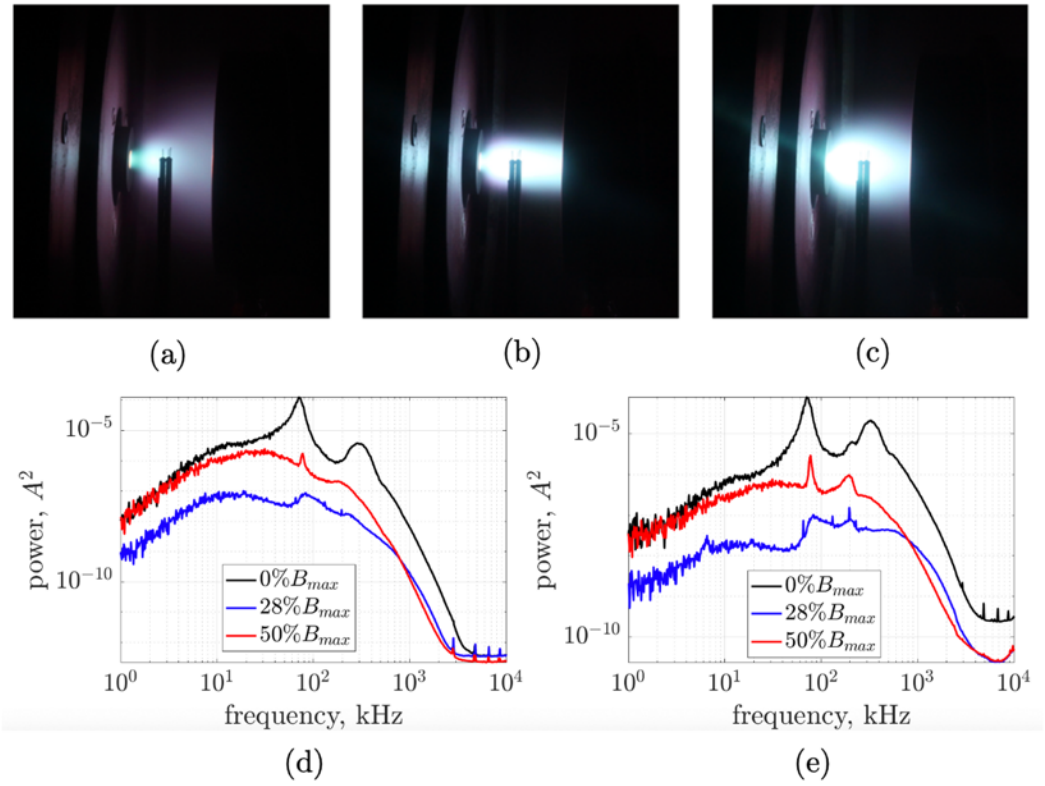

Figure 6.9: Photos and Fourier transform of the anode signal for cathode operation on xenon at 7 sccm and a keeper-to-anode separation of 31.8 mm for (a) 0% B_{max}, (b) 28% B_{max}, (c) 50% B_{max}, (d) Fourier transform of anode current and (e) Fourier transform of anode voltage.

Figure 6.10 shows photos of the cathode operating on krypton at 9.5 sccm for increasing magnetic field strengths and the Fourier spectra of the anode current and voltage. A similar visual trend to xenon is observed with the krypton images: in spot mode at 0% B_{max} (Figure 6.10(a)) and a cylindrical column form with the application of the magnetic field at 28% B_{max} (Figure 6.10(b)). The visual widening of the plasma is observed at the 50% B_{max} condition (Figure 6.10(c)); although, the expansion appears less pronounced compared to xenon under the same condition. The power Fourier spectra of the anode current and voltage show the magnetic field has less of an impact on the behavior of the plasma for this cathode operating condition. However, the application of the magnetic field does appear to slightly decrease the power of the high-frequency

behavior shown in the Fourier spectra of the anode voltage. Nonetheless, the power of the Fourier spectra of the anode voltage is less for the krypton cases compared to the xenon cases. This suggests that the 9.5-sccm flow rate condition for the cathode operating on krypton is possibly more stable than the 7-sccm flow rate condition for the cathode operating on xenon at the magnetic field strengths presented in these figures.

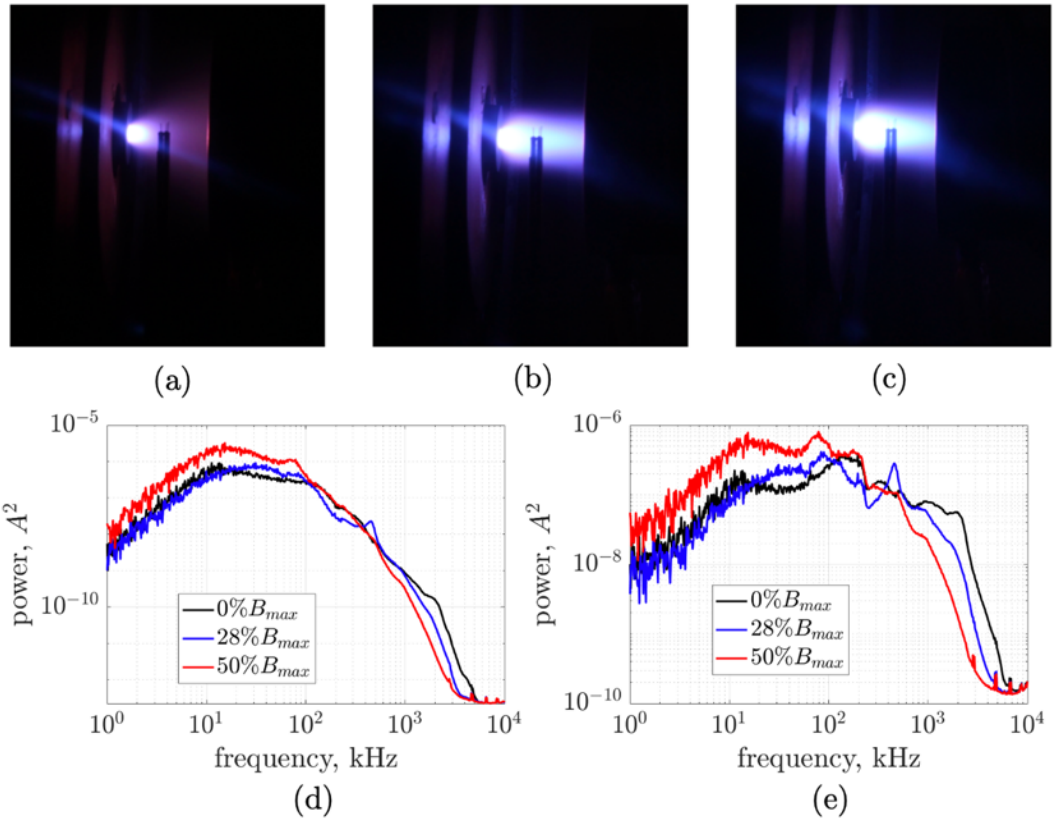

Figure 6.10: Photos and Fourier transforms of the anode signal for cathode operation on krypton at 9.5 sccm and a keeper-to-anode separation of 31.8 mm. (a) 0% B_{max}, (b) 28% B_{max}, (c) 50% B_{max}, (d) Fourier transform of the anode current and (e) Fourier transform of the anode voltage.

6.3.3 Wave Energies

Figures 6.11 and 6.12 present the low-frequency and high-frequency wave energies for increasing magnetic field strengths beginning at 28% B_{max} (once the electrons are magnetized and the azimuthal dynamic appears) for the cathode operated on xenon and krypton, respectively. The low-frequency domain spans frequencies between 100 Hz (above power supply noise) and 250 kHz while the high-frequency domain ranges between 250

kHz and 14 MHz (bandwidth of the TIAs). Probe 2 from the wave probe is used as the input signal for the Fourier transform. The wave energy is approximated by integrating within each corresponding frequency range. Increasing the magnetic field strength beyond 28% B_{max} increases the low frequency and high-frequency wave energies for both xenon and krypton. The low-frequency wave energy for krypton is less than that for xenon at the 50% B_{max} condition. One explanation for the lower wave energy in this regime could be the lower mass of krypton low-frequency wave energy captures the azimuthal dynamic, which is dependent on the mass of the ion. Alternatively, at the 100% B_{max} condition at equivalent mg/s mass flow rates, the low frequency wave energies are equivalent for xenon and krypton.

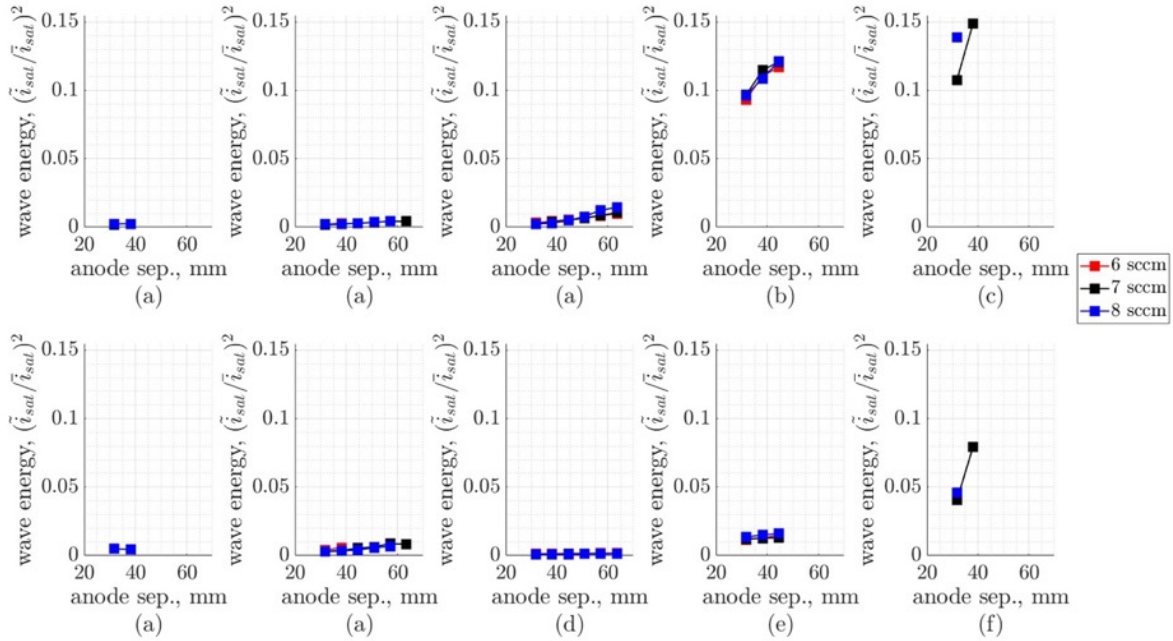

Figure 6.11: Wave energies from the integral under the Fourier transform for cathode operation on xenon for increasing anode separation distances.(a)-(d) Low-frequency band (100 Hz to 250 kHz) and (e)-(h) high-frequency band (250 kHz-14 MHz). (a) and (e)0% B_{max}, (b) and (f) 28% B_{max}, (c) and (g) 50% B_{max}, and (d) and (h) 100% B_{max}.

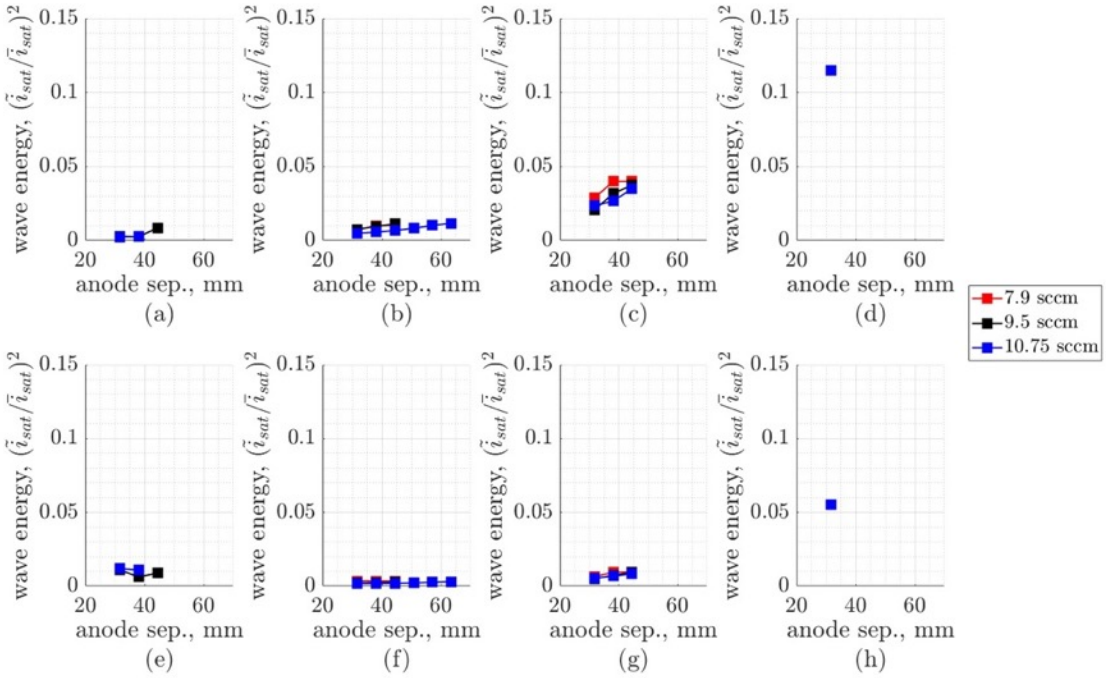

Figure 6.12: Wave energies from the integral under the Fourier transform for cathode operation on krypton for increasing anode separation distances.(a)-(d) Low-frequency band (100 Hz to 250 kHz) and (e)-(h) high-frequency band (250 kHz-14 MHz). (a) and (e)0% B_{max}, (b) and (f) 28% B_{max}, (c) and (g) 50% B_{max}, and (d) and (h) 100% B_{max}.

Figure 6.13 shows the low-frequency and high-frequency wave energy as the magnetic field is increased for argon. While the same cathode was used and the probe locations and magnetic field topographies were similar between the argon tests at NRL and the krypton and xenon tests at ALPE, the tests performed at NRL were with a different anode configuration in a different facility. Therefore, the results might not be there could be slightly different behavior due to the change in facility. Nonetheless, the low-frequency wave energy begins to increase beyond 40% B_{max} and saturates at around 80% B_{max}. At 100% B_{max}, the low-frequency wave energy for argon is similar to the low-frequency wave energy of xenon and krypton. The high-frequency wave energy decreases for increasing magnetic field strengths up to 40% B_{max} where it reaches a minimum. Then, for increasing magnetic field strengths, the high-frequency wave energy increases, similar to xenon and krypton.

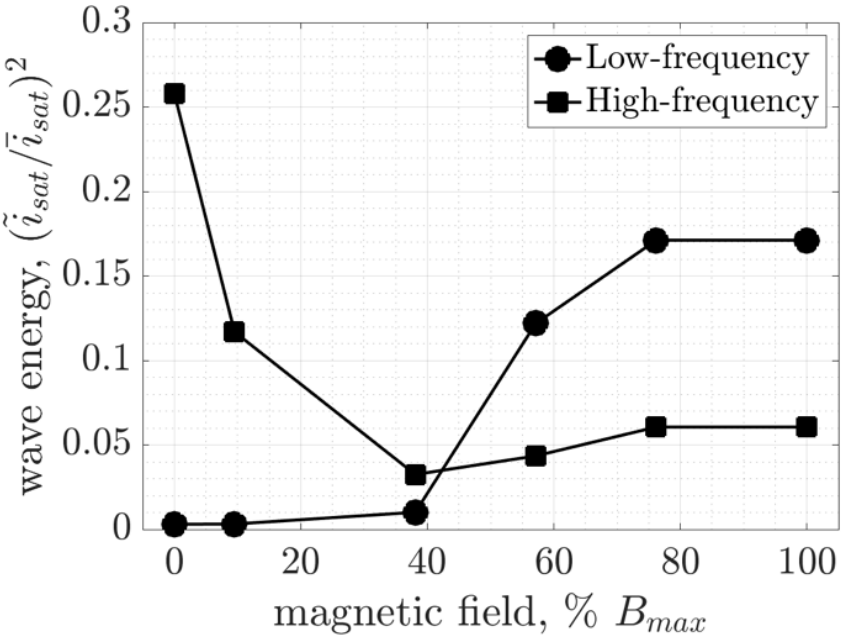

Figure 6.13: Low-frequency and high-frequency wave energy for increasing magnetic field strength of the cathode operated on argon.

6.3.4 Azimuthal Mode

The characteristics of the azimuthally drifting ion population near the cathode exit were first described in Chapter 3 and discussed at length in Chapter 4 with xenon. This section observed the azimuthal wave onset as a function of magnetic field strength for xenon, krypton, and argon. Figure 6.14 shows the Fourier spectra for xenon, krypton, and argon for increasing magnetic field strengths. The xenon and krypton flow rates shown in figure 6.14 were chosen because the cathode was operational at all magnetic field strengths and the mass flow rate is equivalent (mg/s). Once the magnetic field reaches $50\%B_{max}$, the rotational mode dominants the Fourier spectra in cathode operation with xenon, krypton, and argon. The rotation mode is shown in the Fourier transform as a narrowband peak at frequencies typically below 150 kHz. When the cathode is operated on argon without a magnetic field, there exists high-frequency oscillations in the low-MHz range that dominate the Fourier space. The magnetic field stabilizes the argon plasma and the high-frequency spectral power decreases.

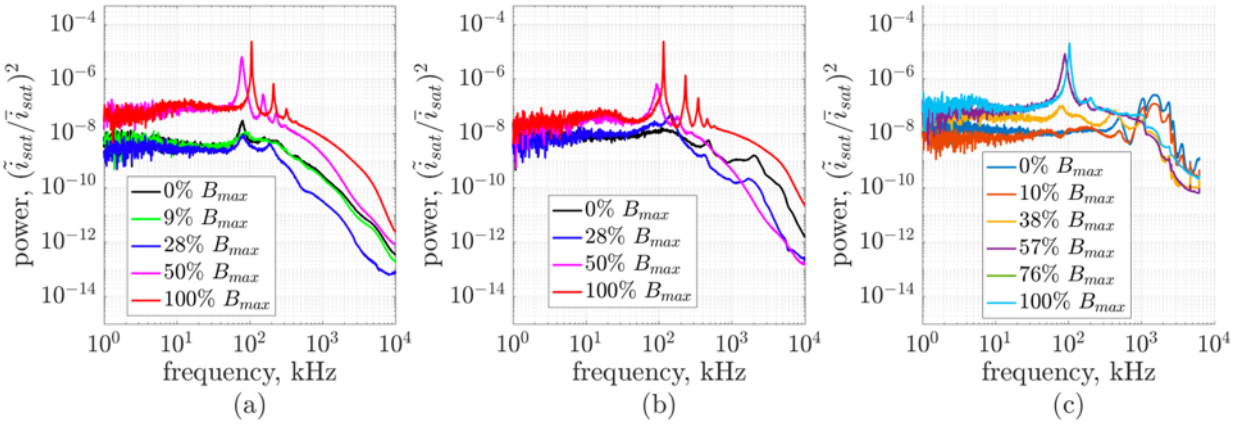

Figure 6.14: Fourier spectra from probe 2 for increasing magnetic field strengths. (a) Xenon, 7 sccm, (b) krypton, 10.75 sccm, and (c) argon, 37 sccm.

Figure 6.15 shows the appearance of the low-frequency dynamic measured by probe 2 in the wave probe for various axial locations at a radial distance 6.35 mm from centerline in the cathode plume for argon operation at NRL. The wave appears at approximately 28% B_{max} and dominates the frequency spectra above 40% B_{max}. Figure 6.15 shows the oscillation is consistent in frequency at each measurement location, while the intensity of the wave (magnitude of the power spectrum) at the 6.35-mm radial location is greatest 10-mm downstream.

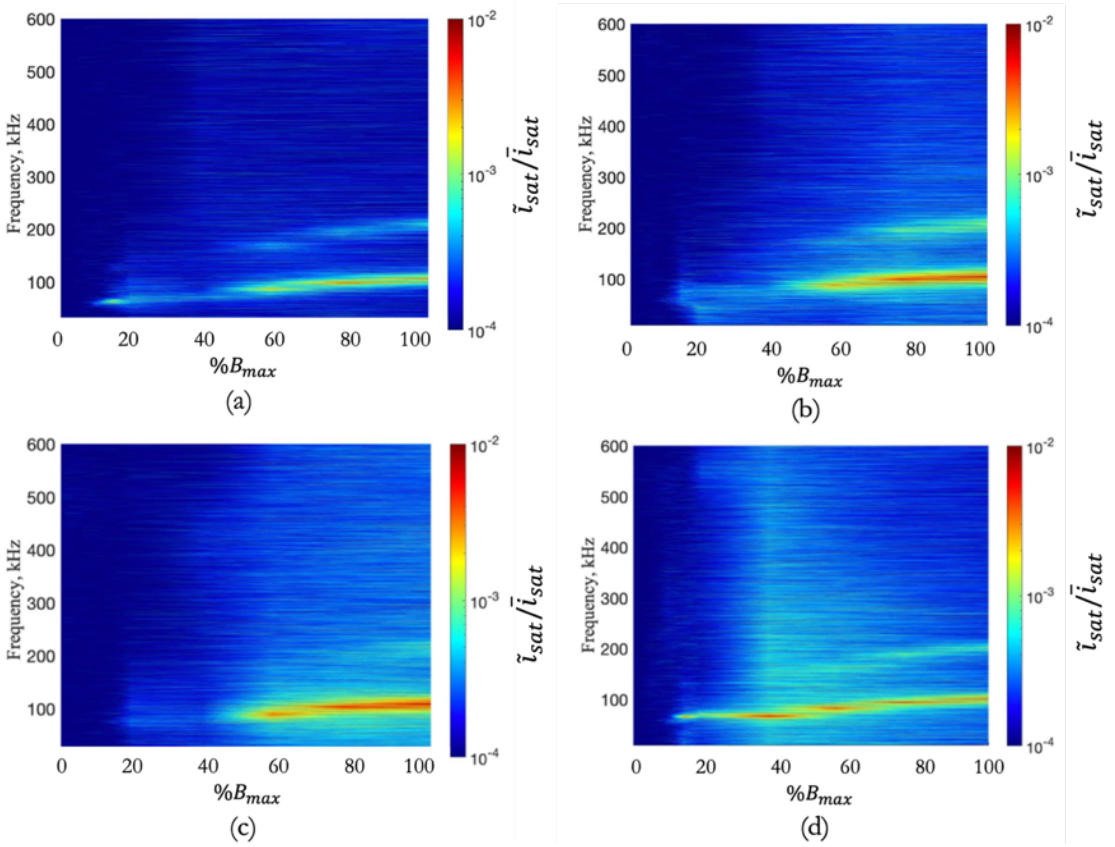

Figure 6.15: Fourier transforms for different probe positions of cathode operation on argon from the NRL experiment. (a) (r,z)=(6.35 mm, 40 mm), (b) (r,z)=(6.35 mm, 20 mm), (c) (r,z)=(6.35 mm, 10 mm), and (d) (r,z)=(0 mm, 5 mm).

Figure 6.16 shows the statistical azimuthal dispersion calculated from the Beall method at a radial position 6.35 mm from centerline at three axial locations for the cathode operated on argon at 100% B_{max}. The azimuthal mode which occurs at 100 kHz is an m=1 with harmonics at all locations. As with the Fourier transform, the intensity of the dispersion increases closer to the cathode exit.

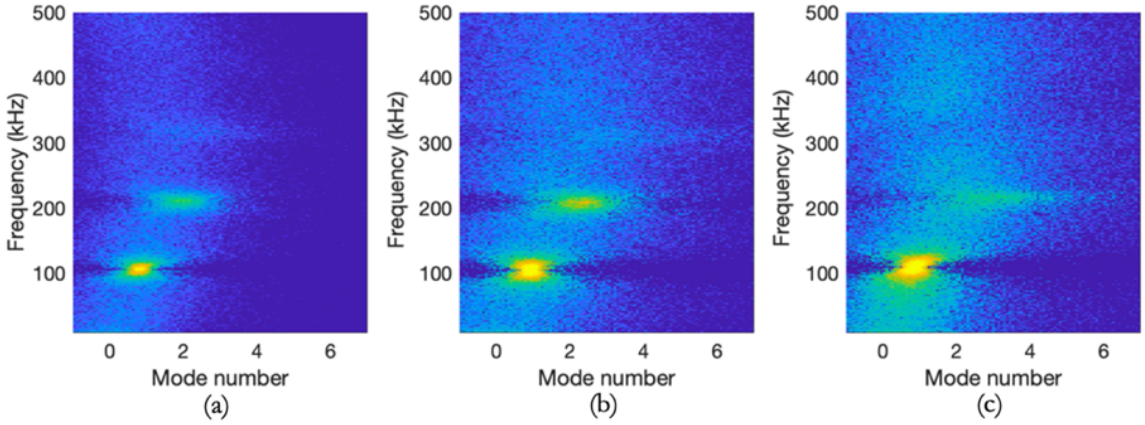

Figure 6.16: Low frequency wave mode number for the H6 cathode operated on argon at NRL. Axial locations: (a) 40 mm, (b) 20 mm, and (c) 5 mm from the magnetic field simulator exit.

Figures 6.17 and 6.18 show the mode number and axial velocity of the azimuthal mode for increasing magnetic field strengths beyond 28% B_{max} and increasing anode-to-cathode separation distances for xenon and krypton, respectively. At the 28% B_{max} condition, the excitation of the m=1 mode occurs only for larger anode separation distances for xenon and is dependent on the flow rate (figure 6.17(b)). This suggests the wave is dependent on the plasma potential (anode voltage increases for increases anode separation distances). Alternatively, the m=1 mode is not fully excited the krypton at the 28% B_{max} condition, which is shown as an m=0 mode for all krypton flow rates and anode separation distances (figure 6.18(b)). At and above 50% B_{max}, the azimuthal mode is excited for both xenon and krypton shown as an $m \approx 1$ mode (figure 6.17(c)-(d) and figure 6.18(c)-(d)).

Once the azimuthal mode is fully excited, characterized by the presence of the m=1 mode, an axial velocity is measured in both krypton and xenon cases figure 6.17(g)-(h) and figure 6.18(g)-(h)). This is in support of the literature, which suggests this mode is helical in nature. The axial velocities measured are low, however, at approximately 200 m/s. The axial speeds are greater for krypton, which could be due to the lighter mass of krypton.

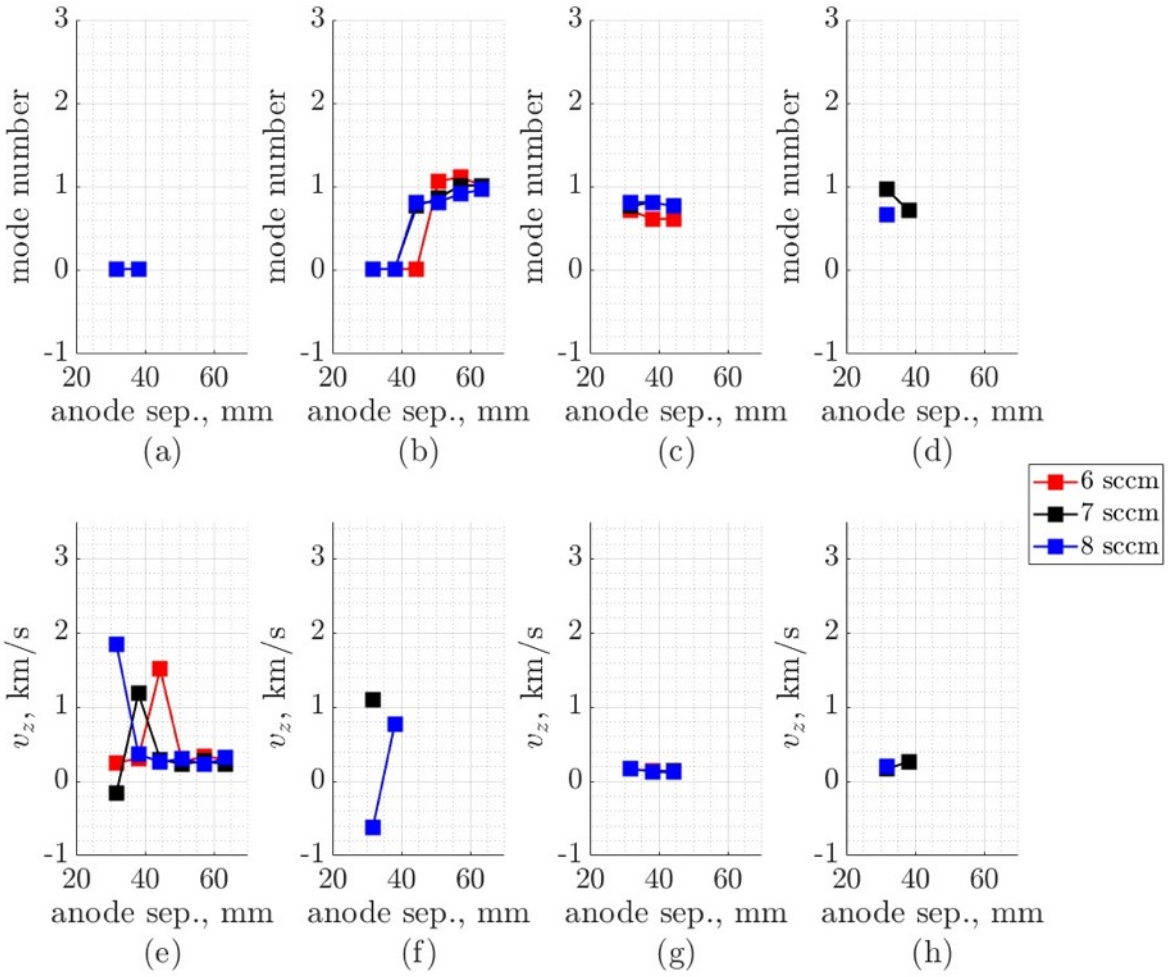

Figure 6.17: Mode number, (a)-(d), and axial velocity, (e)-(h), of the low-frequency dynamic for xenon. (a) and (e) 0% B_{max}, (b) and (f) 28% B_{max}, (c) and (g) 50% B_{max}, and (d) and (h) 100% B_{max}.

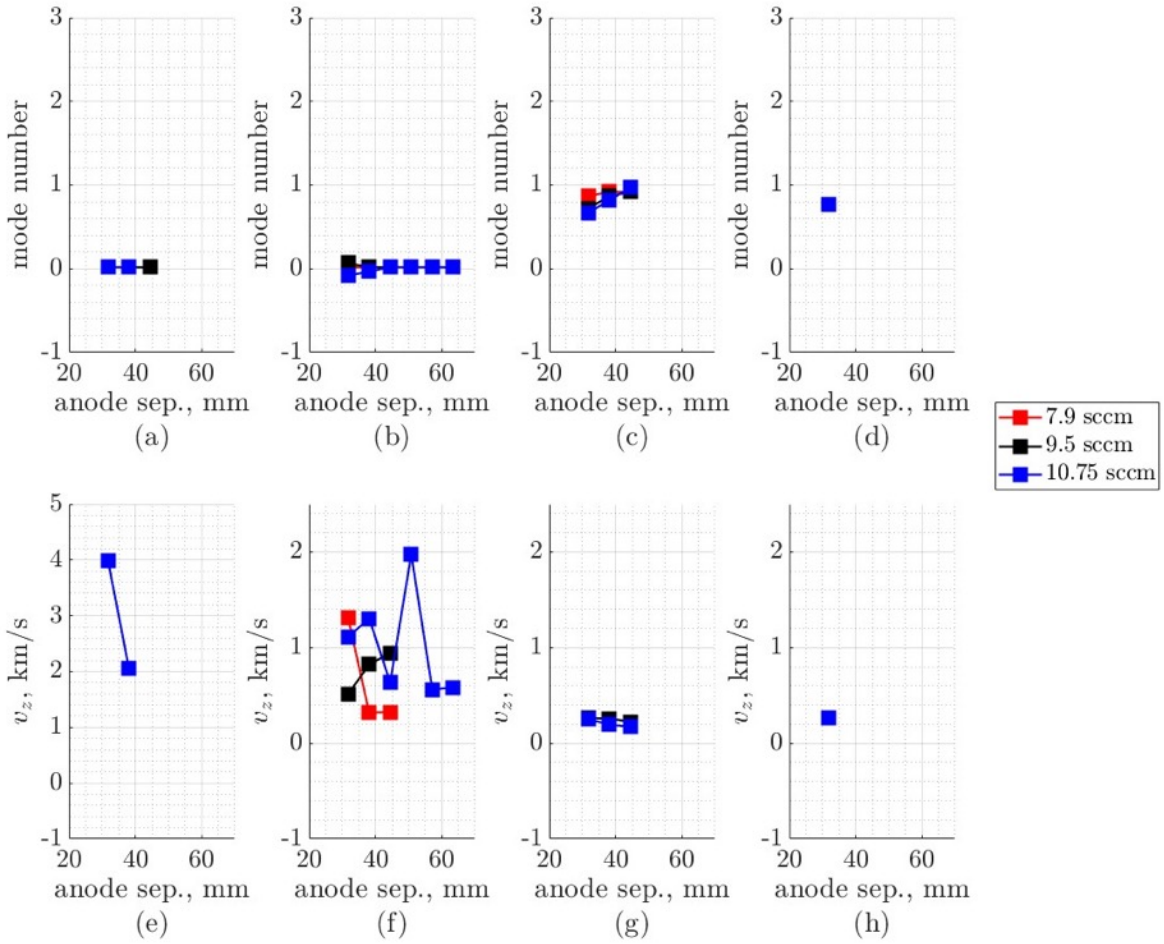

Figure 6.18: Mode number, (a)-(d), and axial velocity, (e)-(h), of the low-frequency dynamic for krypton. (a) and (e) 0% B_{max}, (b) and (f) 28% B_{max}, (c) and (g) 50% B_{max}, and (d) and (h) 100% B_{max}.

6.4 Summary

This chapter addresses the final research objective of this dissertation: to assess the changes in cathode performance and the azimuthal dynamics induced by the magnetic field with different ideal gas propellants. The mass flow rate, magnetic field strength, and anode-to-cathode distance were adjusted to observe the difference in the performance as well as the onset and wave properties of the azimuthal mode. The primary findings of this chapter are as follows:

1. **Cathode Performance.** Without the magnetic field, the magnitude of oscillations in the cathode performance metrics (anode current, anode voltage, and keeper voltage) are large. As the magnetic field strength is increased, a minimum in the magnitude of oscillations is observed around the magnetization condition for the electrons. At the magnetization condition, the electrons in the plasma are confined along the primarily axial magnetic field lines and the plasma appears to form a single column. For magnetic field strengths above the magnetization condition, the magnitude of oscillations in the cathode performance metrics begin to increase, and the plume visually widens in the radial direction.
2. **Azimuthal Mode Onset.** The onset of the azimuthal oscillation occurs at slightly different magnetic fields between xenon, krypton, and argon ($B_{onset,Xe} < B_{onset,Kr} < B_{onset,Ar}$). Once the dynamics is excited, the high-frequency and low-frequency wave energies are at a minimum. Beyond 50% B_{max}, the azimuthal dynamic is excited for all gases. Significantly, once the electrons are magnetized, the anode position does not greatly affect the wave properties of the azimuthal dynamic for the anode positions tested (wave energy and axial velocity). This suggests that for lone-cathode experiments with smaller anodes, the position does not greatly affect the behavior near the cathode exit. Further, the azimuthal oscillation is an m=1 mode for all regions in the cathode that were investigated.
3. **Wave Energy and Velocity.** Xenon operation results in the highest wave energy in the low-frequency regime, which includes the azimuthal dynamic, for magnetic field strengths less than the full HET-level. This might be attributed to the higher atomic mass and lower first ionization of xenon, which results in greater electron-ion collisions and energy transfer within the plasma. Krypton and argon follow in decreasing order of wave energy; however, the speed of the wave is higher in the axial direction for krypton compared to xenon. Once at the HET-level magnetic field strengths, the wave energies of the low-frequency dynamic are

equivalent for the xenon, krypton, and argon operation. This suggests the wave saturates at some magnetic field strength.

CHAPTER 7

Conclusions and Future Work

"We are not at the end but at the beginning of a new physics. But whatever we find, there will always be new horizons continually awaiting us."

~ Michio Kaku

7.1 Summary of Work

Hollow cathodes are a critical component of the Hall Effect Thruster (HET). Advancements in magnetic shielding has nearly eliminated the life-limiting channel erosion by redirecting the ions away from the channel walls through manipulation of the magnetic field lines. Studies with magnetically shielded HETs have identified new erosion patterns on the inner front pole cover, which protects the inner magnetic coil of the HET. These erosion patterns appeared over longer timescales compared to the channel erosion of unshielded HETs; however, understanding these patterns is critical to mitigate any life-limiting risks of the HET. Predictive models can provide a representation of the HET behavior during the lifetime of the thruster; however, experimental verification is required to ensure the accuracy of the models. Lifetime experimental testing of HETs consists of both full thruster testing, which can be expensive and time-intensive, and independent component testing. It is imperative that the independent testing of hollow cathodes is conducted in such a way that best mimics the thruster environment. In the HET, centrally mounted hollow cathodes experience magnetic fields sufficiently strong to magnetize electrons, while ions remain unmagnetized, which can generate a large disparity in the

local electron and ion velocity profiles. These effects combined with steep density gradients and non-Maxwellian electron distributions promote plasma instabilities that can significantly impact cathode lifespan. Therefore, component testing of hollow cathodes often involves the use of a magnetic field simulator to generate a magnetic field topography similar to an HET and a downstream cylindrical anode. This dissertation explored the dynamic and turbulent behavior of independent cathodes operation with varying operational parameters. The results were compared with operation of a full HET to aid in the refinement of the models.

Chapter 1 outlined the dissertation and introduced the research objectives. Chapter 2 reviewed the current solar electric propulsion landscape with a focus on HETs, including the instabilities observed in hollow cathode plumes. Chapter 3 reviews independent cathode operations reported in the literature, the diagnostic tools used to study plasmas, and the facilities utilized in this dissertation work. The findings of this dissertation began in Chapter 4, which examined the onset of the azimuthal ion instability. Chapter 5 compared the dynamics and turbulence of independent cathode operation under varying parameters to cathode operation within the HET. Chapter 6 investigated cathode instabilities in partially magnetized plumes for operation with xenon, krypton, and argon. This final chapter summarizes the major findings of this dissertation, provides recommendations for independent cathode configurations, and gives direction for future work.

7.1.1 Onset of Large-Scale Azimuthal Instability

The ion population that rotates in the azimuthal direction near the cathode exit grows with increasing magnetic field strengths. At HET-level magnetic field strengths, the azimuthal mode dominates the frequency spectra near the cathode. Further, increasing the strength of the magnetic field damps the high-frequency modes observed in unmagnetized cathodes. The prominence of the azimuthal mode and the damping of the high-frequency behavior suggests that HET cathodes do not exhibit plume-mode

oscillations at the flow rates used for nominal operation. Additionally, the frequency and energy of the azimuthal dynamic is affected by the downstream anode position, which underscores the importance of understanding the difference in plasma behavior between independent cathode tests and full thruster operation.

7.1.2 Spatial Instability Mapping of the Turbulent and Dynamic Behavior of the HERMeS Cathode Operated Independently of the HET

A comprehensive spatial investigation of the waves in the cathode plume was performed. Variations in the independent cathode operation included: induced anode oscillations, background pressure, mass flow rate, and magnetic field strength. Data were collecting using a suite of high-speed electrostatic diagnostics and time-averaged optical emission spectroscopy. Additionally, high-speed monitoring of the cathode performance, including floating keeper voltage, discharge voltage, and discharge current, was conducted.

This dissertation shows that independent cathode operation is sensitive to changing experimental parameters. Certain parameters, however, affect different aspects of the cathode behavior. For example, independent cathode testing is traditionally performed with a DC current discharge. Inducing HET-like oscillations onto the anode current produced cathode discharge current oscillations similar to the thruster with the magnitude of the discharge voltage and floating keeper voltage oscillations growing to better match what is observed in HET operation. Further, inducing oscillations affected the frequency behavior in the independent cathode plume. The induced oscillations affected primarily the regions of lower density where the low-frequency oscillations in the independent setups matched the frequency observed in the thruster. However, the higher density regions of the plasma were less affected by the induced oscillations. Further, the induced oscillations did not significantly impact the high-frequency wave energy downstream of the cathode.

The one exception to this was observed for conditions with low flow rate and low background pressure.

The three regions of high-frequency wave energies identified include: (1) along the steep density gradient from centerline, (2) near the exit plane of the cathode farther from centerline, and (3) near the anode entrance. All regions are affected by the variation of different cathode operational parameters. Background pressure most significantly impacted regions 2 and 3, with higher base pressures resulting in lower high-frequency wave energy. In these regions, it is likely that the high-frequency waves are damped through collisional processes due to the increased neutral densities at higher background pressures. For the full HET operation, the equivalent regions for cathode-only operation regions 2 and 3, as shown in figure 5.24, on independent cathode tests exhibit low wave energy. This is likely due to the high local neutral densities due to charge exchange collisions from the beam and escaping neutrals from the anode flow. Significantly, this suggests that independent cathode tests operated at higher base pressures could be more representative of thruster operation in these regions.

The high-frequency wave energy in region 1 is complex. The energy in this region is primarily affected by changes in mass flow rate, with lower flow rates resulting in an increase in the local wave energy. Additionally, the azimuthal velocity of the ion species increases as the flow rate decreases. This suggests a possible coupling between the low-frequency wave and the high-frequency behavior, where the rise in azimuthal ion drift speeds may drive the observed increase in high-frequency wave energy due to the large-scale fluctuations in the ion density. Background pressure was not observed to have a consistent effect on the wave energy of region 1 at the nominal flow rates. At the lowest background pressure, 9.5×10^{-4} Torr, the heightened wave energy in regions 2 and 3 appear to couple with the heightened wave energy in region 1, which shifts the spatial profile of the region 1 heightened wave energy closer to centerline, as described in section 5.7. At a background pressure of 1.4×10^{-4} Torr, a common background pressure used in independent

cathode testing (section 3.3.2), the wave energy in region 1 best matches that observed during operation with an HET. At an increased background pressure of 2.3×10^{-4} Torr, the background neutrals begin to damp the high-frequency oscillations in region 1, reducing the wave energy. Thus, to match the high-frequency wave energy profile in region 1 between independent cathode experiments and full thruster testing, it is best to operate around 1×10^{-4} Torr at lower flow rates.

Of all the variable cathode parameters used in this work, decreasing the mass flow rate most affects the wave energy in the cathode plume in both the low-frequency and high-frequency domains. Nonetheless, at lower flow rates, the low-frequency and high-frequency wave energies throughout the entire measurement domain increase beyond the levels observed in the HET.

7.1.3 Partially magnetized cathode behavior with alternative noble propellants

Xenon has historically been the preferred propellant for HETs due to its relatively high atomic mass and low first ionization energy. However, the cost of xenon is perpetually tied to the geopolitical landscape, which has sparked interest in alternative propellants for HET operation. Among family of noble gases, krypton and argon have both been heavily researched as alternatives for xenon. For the flow rates selected in this dissertation, that the magnitude of anode oscillations and the wave energies were comparable for krypton and argon without a magnetic field. The magnetic field introduces stability into the plume (indicated by a decrease in the magnitude of oscillations in the discharge current and ion density oscillations measured by the high-speed ion saturation probe) as the electron magnetization condition is reached. As the magnetic field strength is further increased, the electrons are confined along the magnetic field lines. In the cathode plume, the magnetic field lines are primarily axial, which confines the plasma into a cylindrical-like plasma beam. As the degree of magnetization increases, the azimuthal wave is excited,

which instigates an azimuthally travelling ion population about the plasma column. This population causes a radial expansion of the cathode plume, which can be visually observed as an increase in the divergence of the plasma plume, and the gradients in density paired with the large-scale oscillations in plasma density breed high-frequency turbulence in the region.

Importantly, while the onset of the azimuthal wave is tied to the magnetization of electrons, this dissertation also linked the mass of the propellent to the excitation of the m=1 mode ($B_{excitation,Xe}<B_{excitation,Kr}<B_{excitation,Ar}$). Therefore, the excitation of the azimuthal wave begins with the magnetization of the electrons (not dependent on ion mass) and the speed of the azimuthal ion population is dependent on the mass of the neutral particle. Nonetheless, the transition from the electron magnetization condition and the excitation of the azimuthal m=1 mode occurs between 28%-50% of the nominal HET-level magnetic field strength. Once at full HET-level magnetic fields, the wave energy of the m=1 mode is equivalent for all three gases tested.

7.2 Conclusions

The major contributions of this work include the following:

1. The onset and excitation of the azimuthal ion mode with increasing magnetic field strengths for xenon, krypton, and argon was characterized. This instability is first instigated by the magnetization of the electrons and the excitation of the wave is unique for each noble gas.
2. The energy of the azimuthal mode saturates at HET-level magnetic fields and is equivalent for xenon, krypton, and argon.
3. A minimum in the magnitude of oscillations for cathode performance metrics and ion density occurs at the electron magnetization condition.
4. Independent cathode operation exhibits three unique regions of heightened wave energy which are affected by different cathode operational parameters.

5. While no independent cathode configuration can ideally match the thruster environment, particularly farther away from centerline, the following steps can be made to ensure the operation is close as possible:
    a. Induced oscillations can provide similar cathode performance metrics to the thruster operation without drastically changing the plume characteristics.
    b. Higher background pressures are satisfactory in mimicking the thruster dynamic and turbulent environment, though a lower flow rate at these pressures could achieve an even closer match to thruster conditions.

7.3 Future Work

The work presented in this dissertation has provided a quantitative investigation of the spatial wave energy of the hollow cathode plume when exposed to HET-like magnetic fields, a downstream anode, and HET-like discharge current oscillations. The following experiments could support this body of work:

1. **Analysis of the azimuthal wave at higher discharge currents with alternative propellants.** This work focused on the 20-A cathode operation regime. Advancements in the power available onboard spacecraft has led to operating HETs at high current densities, providing higher thrust. The difference in the characteristics of the azimuthal wave for 20-A cathode operation suggest a larger impact at higher currents as the density of the plasma increases. If the azimuthal wave is coupled to the generation of high-frequency turbulence, then the region with the large density gradients will exhibit heightened high-frequency wave energy with increasing discharge currents.
2. **Operation with externally injected neutral flow at lower base pressures.** This work showed that adjusting the background pressure does not necessarily result in a similar dynamic and turbulent profile between independent cathode configurations and the full thruster experiments. Adjusting the global pressure affects the near cathode region as well as the downstream plume; therefore,

manipulation of the local neutral pressure near the cathode keeper while maintaining a low background pressure could produce a closer match. Externally injected neutral gas is known to improve cathode stability at high currents due to the neutral collisional damping. If the cathode is operated at lower background pressures ($<1 \text{ X } 10^{-4}$ Torr), the turbulent wave energy growth in regions 2 and 3 could be damped with the injection of neutrals while potentially maintaining the high-frequency wave energy in region 1.

3. **Unique anode configurations.** Anode configurations for independent cathode testing usually takes the form of a cylinder or a planar surface. However, while the cathode plasma does couple to the effective anode downstream in the HET, a large population of electrons must travel from the cathode exit upstream to the discharge channel of the HET. An anode placed upstream of the cathode exit in an independent cathode configuration could redirect some of the electron population upstream, which would affect the propagation and growth of the instability modes.
4. **Keeper oscillations on full thruster tests.** This work identified large-scale floating keeper oscillations when the cathode was operated with the full thruster. In this configuration, the cathode was tied to the thruster body (body-tied). It is unclear from this work if the large magnitude keeper voltage oscillations is linked to the local plasma behavior or if the oscillations are due to the presence of a large oscillating thruster body. Further measurements in this region of the full thruster setup, including plasma potential oscillations from high-speed emissive probes, could provide insight into the true plasma oscillation behavior. Additionally, it is worth investigating alternative thruster power harnessing configurations, such as grounded cathode, to determine if the electrical configuration could affect the measurement.

References

[1] W. Gerstenmaier, "Progress in Defining the Deep Space Gateway and Transport Plan," *NASA Advisory Council Human Exploration and Operations Committee Meeting*, 2017.

[2] J. Crusan *et al.*, "NASA's Gateway: An Update on Progress and Plans for Extending Human Presence to Cislunar Space," in *IEEE Aerospace Conference Proceedings*, 2019. doi: 10.1109/AERO.2019.8741561.

[3] NASA, "Deep Space 1 Launch." [Online]. Available: https://www.jpl.nasa.gov/news/press_kits/ds1launch.pdf

[4] D. Lev, R. M. Myers, K. M. Lemmer, J. Kolbeck, H. Koizumi, and K. Polzin, "The technological and commercial expansion of electric propulsion," *Acta Astronaut*, vol. 159, pp. 213–227, 2019, doi: 10.1016/j.actaastro.2019.03.058.

[5] P. Lord *et al.*, "Psyche: Journey to a Metal World," *IEEE Aerospace Conference Proceedings*, vol. 2014, pp. 1–11, 2017, doi: 10.1109/AERO.2017.7943771.

[6] J. C. McDowell, "The Low Earth Orbit Satellite Population and Impacts of the SpaceX Starlink Constellation," *Astrophys J Lett*, vol. 892, no. 2, p. L36, 2020, doi: 10.3847/2041-8213/ab8016.

[7] M. Runnels, "On Launching Environmental Law Into Orbit in the Age of Satellite Constellations," *Journal of Air Law and Commerce*, vol. 88, no. 1, pp. 181–207, 2023.

[8] S. Fuller, E. Lehnhardt, C. Zaid, and K. Halloran, "Gateway program status and overview," *Journal of Space Safety Engineering*, vol. 9, no. 4, pp. 625–628, 2022, doi: 10.1016/j.jsse.2022.07.008.

[9] D. M. Goebel, K. Jameson, I. Katz, and I. G. Mikellides, "Energetic Ion Production and Keeper Erosion in Hollow Cathode Discharges," in *29th International Electric Propulsion Conference*, 2005.

[10] I. G. Mikellides, A. Lopez Ortega, D. M. Goebel, and G. Becatti, "Dynamics of a hollow cathode discharge in the frequency range of 1-500 kHz," *Plasma Sources Sci Technol*, vol. 29, no. 3, 2020, doi: 10.1088/1361-6595/ab69e4.

[11] B. A. Jorns and R. R. Hofer, "Plasma oscillations in a 6-kW magnetically shielded Hall thruster," *Phys Plasmas*, vol. 21, no. 5, pp. 1–19, 2014, doi: 10.1063/1.4879819.

[12] B. A. Jorns *et al.*, "Mechanisms for pole piece erosion in a 6-kW magnetically-shielded hall thruster," *52nd AIAA/SAE/ASEE Joint Propulsion Conference, 2016*, pp. 1–21, 2016, doi: 10.2514/6.2016-4839.

[13] W. Huang and H. Kamhawi, "Counterstreaming ions at the inner pole of a magnetically shielded Hall thruster," *J Appl Phys*, vol. 129, no. 4, 2021, doi: 10.1063/5.0029428.

[14] W. Huang, H. Kamhawi, and D. A. Herman, "Evidence of counter-streaming ions near the inner pole of the HERMeS hall thruster," in *AIAA Propulsion and Energy Forum and Exposition, 2019*, 2019. doi: 10.2514/6.2019-3897.

[15] J. D. Frieman *et al.*, "Completion of the long duration wear test of the NASA HERMeS hall thruster," in *AIAA Propulsion and Energy Forum and Exposition, 2019*, 2019. doi: 10.2514/6.2019-3895.

[16] A. L. Ortega, I. G. Mikellides, V. H. Chaplin, W. Huang, and J. D. Frieman, "Anomalous ion heating and pole erosion in the 12.5-kw hall effect rocket with magnetic shielding (hermes)," in *AIAA Propulsion and Energy 2020 Forum*, 2020, pp. 1–23. doi: 10.2514/6.2020-3620.

[17] S. J. Hall *et al.*, "The Effect of a Hall Thruster-like Magnetic Field on Operation of a 25-A class Hollow Cathode," in *36th International Electric Propulsion Conference*, 2019.

[18] A. Lopez Ortega and I. G. Mikellides, "The importance of the cathode plume and its interactions with the ion beam in numerical simulations of Hall thrusters," *Phys Plasmas*, vol. 23, no. 4, 2016, doi: 10.1063/1.4947554.

[19] I. G. Mikellides and A. Lopez Ortega, "Growth of the lower hybrid drift instability in the plume of a magnetically shielded Hall thruster," *J Appl Phys*, vol. 129, no. 19, 2021, doi: 10.1063/5.0048706.

[20] A. L. Ortega, B. A. Jorns, and I. G. Mikellides, "Hollow Cathode Simulations with a First-Principles Model of Ion-Acoustic Anomalous Resistivity," *J Propuls Power*, vol. 34, no. 4, pp. 1026–1038, Feb. 2018, doi: 10.2514/1.b36782.

[21] B. A. Jorns, I. G. Mikellides, and D. M. Goebel, "Ion acoustic turbulence in a 100-A LaB6 hollow cathode," *Phys Rev E Stat Nonlin Soft Matter Phys*, vol. 90, no. 6, 2014, doi: 10.1103/PhysRevE.90.063106.

[22] B. A. Jorns, S. E. Cusson, Z. Brown, and E. Dale, "Non-classical electron transport in the cathode plume of a Hall effect thruster," *Phys Plasmas*, vol. 27, no. 2, 2020, doi: 10.1063/1.5130680.

[23] G.-C. Potrivitu and S. Xu, "Evidence of the ionization instability and ion acoustic turbulence correlation in sub-ampere hollow cathodes," *Journal of Electric Propulsion*, vol. 1, no. 1, pp. 1–22, 2022, doi: 10.1007/s44205-022-00005-y.

[24] M. P. Georgin, "Ionization Instability of the Hollow Cathode Plume," 2020.

[25] A. P. Scott and D. M. Goebel, "Hollow cathode discharge instability onset in electric thrusters," *J Appl Phys*, vol. 135, no. 12, 2024, doi: 10.1063/5.0188988.

[26] J. E. Polk *et al.*, "Characterization of hollow cathode performance and thermal behavior," in *42nd AIAA/ASME/SAE/ASEE Joint Propulsion Conference & Exhibit*, 2006, p. AIAA 2006-5150. doi: doi:10.2514/6.2006-5150.

[27] M. P. Georgin, B. A. Jorns, and A. D. Gallimore, "Dependence of Low Frequency Waves on Magnetic Field Strength in Hollow Cathode Plume," in *36th International Electric Propulsion Conference*, 2019.

[28] R. R. Hofer, L. K. Johnson, D. M. Goebel, and R. E. Wirz, "Effects of internally mounted cathodes on Hall thruster plume properties," *IEEE Transactions on Plasma Science*, vol. 36, no. 5 PART 1, pp. 2004–2014, 2008, doi: 10.1109/TPS.2008.2000962.

[29] A. Lopez Ortega and I. G. Mikellides, "The importance of the cathode plume and its interactions with the ion beam in numerical simulations of Hall thrusters," *Phys Plasmas*, vol. 23, no. 4, 2016, doi: 10.1063/1.4947554.

[30] M. P. Georgin, B. A. Jorns, and A. D. Gallimore, "An Experimental and Theoretical Study of Hollow Cathode Plume Mode Oscillations," in *35th International Electric Propulsion Conference*, 2017. [Online]. Available: https://iepc2017.org/sites/default/files/speaker-papers/an_experimental_and_theoretical_study_of_hollow_cathode_plume_mode_oscillations.pdf

[31] C. Chhavi and M. L. R. Walker, "Review of non-conventional Hall effect thrusters," *Journal of Electric Propulsion*, vol. 3, no. 1, 2024, doi: 10.1007/s44205-024-00073-2.

[32] A. Cuthbertson, "Elon Musk now controls two thirds of all active satellites," *Independent*, 2024.

[33] C. E. Fruneck, S. J. Hall, J. D. Sommerville, J. M. Makela, K. J. Terhune, and L. B. King, "Qualification of the Aurora Low-Power Hall-Effect Thruster Part I: Environments and Performance," in *38th International ELectric Propulsion Conference*, Toulouse, France, 2024, pp. 1–16.

[34] J. Szabo *et al.*, "A commercial one newton hall effect thruster for high power in-space missions," *47th AIAA/ASME/SAE/ASEE Joint Propulsion Conference and Exhibit 2011*, no. August, pp. 1–11, 2011, doi: 10.2514/6.2011-6152.

[35] O. S. T. Inc., "Download Slides," 2024. [Online]. Available: https://orbionspace.com/

[36] D. Y. Oh and P. Neuman, "A year of firsts for electric propulsion," 2023.

[37] R. G. Jahn and F. A. Lyman, "Physics of Electric Propulsion," *J Appl Mech*, vol. 36, no. 3, p. 655, 1969, doi: 10.1115/1.3564751.

[38] D. M. Goebel and I. Katz, *Fundamentals of Electric Propulsion: Ion and Hall Thrusters*. 2008. doi: 10.1109/9780471746218.ch2.

[39] G. Sutton and O. Biblarz, *Rocket Propulsion Elements*, vol. 8. Wiley, 2011.

[40] M. Baird, "Investigating newly discovered oscillation modes in magnetically shielded Hall effect thrusters utilizing high speed diagnostics," 2020.

[41] SpaceX, "Falcon Heavy." [Online]. Available: https://www.spacex.com/vehicles/falcon-heavy/

[42] NYC Mayor's Office of Climate and Sustainability, "NYC is building a clean, resilient, and affordable energy system," NYC.gov. [Online]. Available: https://www1.nyc.gov/site/sustainability/our-programs/energy.page

[43] P. M. Bellan, *Fundamentals of Plasma Physics*, vol. 49, no. 2. 2007. doi: 10.1088/0741-3335/49/2/b01.

[44] F. F. Chen, *Erratum to: Introduction to Plasma Physics and Controlled Fusion*. 2018. doi: 10.1007/978-3-319-22309-4_11.

[45] W. Huang, R. Shastry, G. C. Soulas, and H. Kamhawi, "Farfield Plume Measurement and Analysis on the NASA-300M and NASA-300MS," in *33rd International Electric Propulsion Conference*, 2013. [Online]. Available: http://www.sti.nasa.gov

[46] A. Tomori, "Plasma Dispersion Relation and Instabilities in Electron Velocity Distribution Function," *WDS'14 Proceedings of Contributed Papers*, pp. 298–303, 2014.

[47] R. C. Davidson and N. T. Gladd, "Anomalous transport properties associated with the lower-hybrid-drift instability," *Physics of Fluids*, vol. 18, no. 10, pp. 1327–1335, 1975, doi: 10.1063/1.861021.

[48] S. Janhunen, A. Smolyakov, O. Chapurin, D. Sydorenko, I. Kaganovich, and Y. Raitses, "Nonlinear structures and anomalous transport in partially magnetized e × B plasmas," *Phys Plasmas*, vol. 25, no. 1, 2018, doi: 10.1063/1.5001206.

[49] I. G. Mikellides, I. Katz, D. M. Goebel, and K. K. Jameson, "Evidence of nonclassical plasma transport in hollow cathodes for electric propulsion," *J Appl Phys*, vol. 101, no. 6, 2007, doi: 10.1063/1.2710763.

[50] V. H. Chaplin *et al.*, "Extended Life Qualification of the Magnetically Shielded Miniature (MaSMi) Hall Thruster," in *37th Annual Small Satellite Conference*, 2023, pp. SSC23-VI-01 Extended.

[51] I. G. Mikellides, I. Katz, R. R. Hofer, and D. M. Goebel, "Magnetic shielding of walls from the unmagnetized ion beam in a Hall thruster," *Appl Phys Lett*, vol. 102, no. 2, 2013, doi: 10.1063/1.4776192.

[52] L. L. Su *et al.*, "Operation and Performance of a Magnetically Shielded Hall Thruster at Ultrahigh Current Densities on Xenon and Krypton," in *AIAA Propulsion and Energy Forum*, 2023, pp. 1–32. doi: 10.2514/6.2023-0842.

[53] S. Cusson, B. Jorns, and A. Gallimore, "Impact of Neutral Density on the Magnetic Shielding of Hall Thrusters," in *Proceedings of the 36th International Electric Propulsion Conference, University of Vienna, Austria*, 2019, p. IEPC-2019-276.

[54] I. G. Mikellides, I. Katz, R. R. Hofer, and D. M. Goebel, "Magnetic shielding of a laboratory Hall thruster. I. Theory and validation," *J Appl Phys*, vol. 115, no. 4, 2014, doi: 10.1063/1.4862313.

[55] J. D. Frieman *et al.*, "Long Duration Wear Test of the NASA HERMeS Hall Thruster," in *54th Joint Propulsion Conference*, 2018. doi: 10.2514/6.2018-4645.c1.

[56] A. Lopez Ortega, I. G. Mikellides, and D. M. Goebel, "Numerical Simulations for Life Assessments of the BaO and LaB6 Cathode Options in the Hall Effect Rocket with Magnetic Shielding (HERMeS)," in *35th International Electric Propulsion Conference*, 2017.

[57] W. Huang, H. Kamhawi, and T. Haag, "Plasma Oscillation Characterization of NASA's HERMeS Hall Thruster via High Speed Imaging," in *52nd Joint Propulsion Conference*, 2016.

[58] W. Huang, G. J. Williams, P. Y. Peterson, H. Kamhawi, J. H. Gilland, and D. A. Herman, "Plasma Plume Characterization of the HERMeS during a 1722-hr Wear Test Campaign," *35th International Electric Propulsion Conference*, pp. 1–16, 2017, [Online]. Available: http://erps.spacegrant.org/IEPC_2017/IEPC_2017_307.pdf%0Ahttps://iepc2017.org/sites/default/files/speaker-papers/2017iepc_tdu_wt_probes_v11.pdf

[59] I. G. Mikellides, P. Guerrero, A. Lopez Ortega, and J. E. Polk, "Spot-to-plume Mode Transition Investigations in the HERMeS Hollow Cathode Discharge Using Coupled 2-D Axisymmetric Plasma-Thermal Simulations," in *Propulsion and Energy Forum*, 2018. doi: 10.2514/6.2018-4722.

[60] J. E. Polk, R. B. Lobbia, A. Barriault, P. Guerrero, I. G. Mikellides, and A. Lopez Ortega, "Inner Front Pole Cover Erosion in the 12.5 kW HERMeS Hall Thruster Over a Range of Operating Conditions," in *35th International Electric Propulsion Conference*, 2017. [Online]. Available: http://erps.spacegrant.org/IEPC_2017/IEPC_2017_409.pdf%0Ahttps://iepc2017.org/sites/default/files/speaker-papers/iepc2017sla_measurements_final_0.pdf

[61] European Commission, "Rare Gases (Krypton, Neon, Xenon): Impact assessment for supply security," *Science for Policy Brief*, 2022.

[62] L. L. Su, "Performance of a Magnetically Shielded Hall Thruster Operating on Krypton at High Powers," University of Michigan, 2023. [Online]. Available: https://www.ncbi.nlm.nih.gov/books/NBK558907/

[63] "How rare-gas supply adapted to Russia's war," *The Economist*, pp. 1–6, 2023.

[64] M. S. Mcdonald, "Electron Transport in Hall Thrusters by," University of Michigan, 2012.

[65] A. Shabshelowitz, A. D. Gallimore, and P. Y. Peterson, "Performance of a helicon Hall thruster operating with xenon, argon, and nitrogen," *J Propuls Power*, vol. 30, no. 3, pp. 664–671, 2014, doi: 10.2514/1.B35041.

[66] A. J. Eckhaus, A. J. Rocha, A. M. Saladino, and B. A. Jorns, "Student-led Design, Construction, and Testing of a PermanentMagnet Hall Thruster on Argon Propellant," in *AIAA SciTech Forum and Exposition, 2024*, 2024, pp. 1–19. doi: 10.2514/6.2024-1955.

[67] G. C. Potrivitu and S. Xu, "Phenomenological plasma model for open-end emitter with orificed keeper hollow cathodes," *Acta Astronaut*, vol. 191, pp. 293–316, 2022, doi: 10.1016/j.actaastro.2021.11.005.

[68] E. T. Dale and B. A. Jorns, "Experimental characterization of Hall thruster breathing mode dynamics," *J Appl Phys*, vol. 130, no. 13, 2021, doi: 10.1063/5.0046048.

[69] Z. R. Taillefer, J. J. Blandino, and J. Szabo, "Characterization of a barium oxide cathode operating on xenon and iodine propellants," *J Propuls Power*, vol. 36, no. 4, pp. 575–585, 2020, doi: 10.2514/1.b37315.

[70] G. P. Thomas, "Argon (Ar) - Discovery, Occurrence, Production, Properties and Applications of Argon." [Online]. Available: https://www.azom.com/article.aspx?ArticleID=7906#:~:text=Argon is industrially extracted from,of argon as an impurity.

[71] L. L. Su *et al.*, "Operation and Performance of a Magnetically Shielded Hall Thruster at Ultrahigh Current Densities," pp. 1–32, 2023, doi: 10.2514/6.2023-0842.

[72] G. C. Potrivitu, R. Joussot, and S. Mazouffre, "Anode position influence on discharge modes of a LaB6 cathode in diode configuration," *Vacuum*, vol. 151, pp. 122–132, 2018, doi: 10.1016/j.vacuum.2018.02.010.

[73] D. M. Goebel, G. Becatti, I. G. Mikellides, and A. Lopez Ortega, "Plasma hollow cathodes," *J Appl Phys*, vol. 130, no. 5, 2021, doi: 10.1063/5.0051228.

[74] A. Ghazari *et al.*, "Intense cyclic heating effects on thermo-fracture and thermal shock of solid tungsten and open-cell tungsten foam," *Journal of Nuclear Materials*, vol. 565, p. 153730, 2022, doi: 10.1016/j.jnucmat.2022.153730.

[75] J. E. Polk, I. G. Mikellides, A. M. Capece, and I. Katz, "Barium depletion in hollow cathode emitters," *J Appl Phys*, vol. 119, no. 2, 2016, doi: 10.1063/1.4938489.

[76] E. Y. Wu and B. Li, "The Schottky emission effect: A critical examination of a century-old model," *J Appl Phys*, vol. 132, no. 2, 2022, doi: 10.1063/5.0087909.

[77] R. R. Hofer, D. M. Goebel, and R. M. Watkins, "Compact LaB6 Hollow Cathode for a 6 kW Laboratory Hall Thruster," in *54th JANNAF Propulsion Meeting*, 2007. doi: 10.1063/1.3474921.

[78] M. Coletti and S. B. Gabriel, "A model for barium oxide depletion from hollow cathode inserts," *IEEE Transactions on Plasma Science*, vol. 37, no. 1, pp. 58–66, 2009, doi: 10.1109/TPS.2008.2006898.

[79] J. E. Polk, I. G. Mikellides, A. M. Capece, and I. Katz, "Barium depletion in hollow cathode emitters," *J Appl Phys*, vol. 119, no. 2, Jan. 2016, doi: 10.1063/1.4938489.

[80] T. G. Gray, T. W. Haag, T. R. Sarver-Verhey, and S. J. Hall, "Effects of Environmental Exposure on Barium Oxide Cathode Operation," in *37th International Electric Propulsion Conference*, Boston, MA, 2022, pp. 1–10.

[81] B. Rubin and J. D. Williams, "Hollow cathode conditioning and discharge initiation," *J Appl Phys*, vol. 104, no. 5, 2008, doi: 10.1063/1.2973690.

[82] D. M. Goebel and R. M. Watkins, "Compact lanthanum hexaboride hollow cathode," *Review of Scientific Instruments*, vol. 81, no. 8, 2010, doi: 10.1063/1.3474921.

[83] D. Pedrini, R. Albertoni, F. Paganucci, and M. Andrenucci, "Modeling of LaB6 hollow cathode performance and lifetime," *Acta Astronaut*, vol. 106, pp. 170–178, 2015, doi: 10.1016/j.actaastro.2014.10.033.

[84] M. M. Mooney, M. Baird, and K. Lemmer, "Featherweight Heaterless Hollow Cathode Characterization," in *36th International Electric Propulsion Conference*, 2019, pp. 1–9.

[85] V. Vekselman, Ya. E. Krasik, S. Gleizer, V. Tz. Gurovich, A. Warshavsky, and L. Rabinovich, "Characterization of a Heaterless Hollow Cathode," *J Propuls Power*, vol. 29, no. 2, pp. 475–486, 2013, doi: 10.2514/1.B34628.

[86] D. R. Lev, D. Mikitchuk, and L. Appel, "Development of a Low Current Heaterless Hollow Cathode for Hall Thrusters," in *34th International Electric Propulsion Conference*, 2015.

[87] L. P. Rand, "A Calcium Aluminate Electride Hollow Cathode," Colorado State University, 2014. [Online]. Available: https://minerva-access.unimelb.edu.au/handle/11343/56627%0Ahttp://www.academia.edu/download/39541120/performance_culture.doc

[88] M. S. Mcdonald and N. R. S. Caruso, "Ignition and Early Operating Characteristics of a Low- Current C12A7 Hollow Cathode," in *35th International Electric Propulsion Conference*, 2017.

[89] F. Paschen, "Ueber die zum Funkenübergang in Luft, Wasserstoff und Kohlensäure bei verschiedenen Drucken erforderliche Potentialdifferenz (On the potential difference required for spark initiation in air. hydrogen, and carbon dioxide at different pressures)," *Ann Phys*, vol. 273, no. 5, pp. 69–75, 1889.

[90] R. K. Ham, "An Experimental investigation of heaterless hollow cathode ignition," 2019. [Online]. Available: https://minerva-access.unimelb.edu.au/handle/11343/56627%0Ahttp://www.academia.edu/download/39541120/performance_culture.doc

[91] G. Becatti, R. W. Conversano, and D. M. Goebel, "Demonstration of 25,000 ignitions on a proto-flight compact heaterless lanthanum hexaboride hollow

cathode," *Acta Astronaut*, vol. 178, no. September 2020, pp. 181–191, 2021, doi: 10.1016/j.actaastro.2020.09.013.

[92] R. R. Hofer, L. K. Johnson, D. M. Goebel, and R. E. Wirz, "Effects of internally mounted cathodes on Hall thruster plume properties," *IEEE Transactions on Plasma Science*, vol. 36, no. 5 PART 1, pp. 2004–2014, 2008, doi: 10.1109/TPS.2008.2000962.

[93] V. K. Rawlin and E. V. Pawlik, "A mercury plasma-bridge neutralizer," *J Spacecr Rockets*, vol. 5, no. 7, pp. 814–820, 1968, doi: 10.2514/3.29363.

[94] M. P. Georgin, M. Byrne, B. A. Jorns, and A. Gallimore, "Passive High-speed Imaging of Ion Acoustic Turbulence in a Hollow Cathode," in *53rd AIAA/SAE/ASEE Joint Propulsion Conference*, 2017, pp. 1–12. doi: 10.2514/6.2017-4973.

[95] G. F. Karabadzhak, Y. H. Chiu, and R. A. Dressler, "Passive optical diagnostic of Xe propelled Hall thrusters. II. Collisional-radiative model," *J Appl Phys*, vol. 99, no. 11, 2006, doi: 10.1063/1.2195019.

[96] V. H. Chaplin, L. K. Johnson, R. B. Lobbia, M. F. Konopliv, T. Simka, and R. E. Wirz, "Insights from Collisional-Radiative Models of Neutral and Singly Ionized Xenon in Hall Thrusters," *J Propuls Power*, vol. 38, no. 5, pp. 866–879, 2022, doi: 10.2514/1.B38676.

[97] X. M. Zhu *et al.*, "A xenon collisional-radiative model applicable to electric propulsion devices: III. Determination of the ionization fraction in low-temperature xenon plasma by using ionic and atomic 6p lines," *Plasma Sources Sci Technol*, vol. 32, no. 9, 2023, doi: 10.1088/1361-6595/acfb37.

[98] D. M. Goebel, K. K. Jameson, I. Katz, and I. G. Mikellides, "Potential fluctuations and energetic ion production in hollow cathode discharges," *Phys Plasmas*, vol. 14, no. 10, 2007, doi: 10.1063/1.2784460.

[99] T. Meng, Z. Ning, and D. Yu, "Triggering of ionization oscillations in hollow cathode discharge by keeper electrode," *Phys Plasmas*, vol. 093510, no. September, 2019, doi: 10.1063/1.5116830.

[100] I. G. Mikellides, I. Katz, D. M. Goebel, and J. E. Polk, "Theoretical Model of a Hollow Cathode Plasma for the Assessment of Insert and Keeper Lifetimes," in *41st AIAA/ASME/SAE/ASEE Joint Propulsion Conference and Exhibit*, 2005.

[101] B. A. Jorns, S. E. Cusson, Z. Brown, and E. Dale, "Non-classical electron transport in the cathode plume of a Hall effect thruster," *Phys Plasmas*, vol. 27, no. 2, 2020, doi: 10.1063/1.5130680.

[102] G. Becatti, F. Burgalassi, F. Paganucci, M. Zuin, and D. M. Goebel, "Resistive MHD modes in hollow cathodes external plasma," *Plasma Sources Sci Technol*, vol. 31, no. 1, 2022, doi: 10.1088/1361-6595/ac43c4.

[103] G. Becatti and D. M. Goebel, "Investigation of plasma instabilities in the plume of high current hollow cathodes and their relation to the cathode life," in *38th International Electric Propulsion conference*, Toulouse, France, 2024, pp. 1–13.

[104] A. L. Verdon, I. H. Cairns, D. B. Melrose, and P. A. Robinson, "Properties of lower hybrid waves," *Proceedings of the International Astronomical Union*, vol. 4, no. 257, pp. 569–573, 2008, doi: 10.1017/S1743921309029871.

[105] J. P. Boeuf, "Tutorial: Physics and modeling of Hall thrusters," *J Appl Phys*, vol. 121, no. 1, 2017, doi: 10.1063/1.4972269.

[106] S. Cao *et al.*, "Modeling on plasma energy balance and transfer in a hollow cathode," *J Phys D Appl Phys*, vol. 52, no. 28, 2019, doi: 10.1088/1361-6463/ab197e.

[107] A. L. Ortega, I. Katz, I. G. Mikellides, and D. M. Goebel, "Self-Consistent Model of a High-Power Hall Thruster Plume," *IEEE Transactions on Plasma Science*, vol. 43, no. 9, pp. 2875–2886, 2015, doi: 10.1109/TPS.2015.2446411.

[108] T. A. Marks, "Modeling Anomalous Electron Transport in a Fluid Hall Thruster Code," University of Michigan, 2023.

[109] B. Jorns, "Predictive, data-driven model for the anomalous electron collision frequency in a Hall effect thruster," *Plasma Sources Sci Technol*, vol. 27, no. 10, 2018, doi: 10.1088/1361-6595/aae472.

[110] T. A. Marks and B. A. Jorns, "Challenges with the self-consistent implementation of closure models for anomalous electron transport in fluid simulations of Hall thrusters," *Plasma Sources Sci Technol*, vol. 32, no. 4, 2023, doi: 10.1088/1361-6595/accd18.

[111] I. G. Mikellides and A. Lopez Ortega, "Challenges in the development and verification of first-principles models in Hall-effect thruster simulations that are based on anomalous resistivity and generalized Ohm's law," *Plasma Sources Sci Technol*, vol. 28, no. 1, 2019, doi: 10.1088/1361-6595/aae63b.

[112] H. C. Dragnea, A. Lopez Ortega, H. Kamhawi, and I. D. Boyd, "Simulation of a hall effect thruster using krypton propellant," *J Propuls Power*, vol. 36, no. 3, pp. 335–345, 2020, doi: 10.2514/1.B37499.

[113] M. R. Nakles, W. A. Hargus, J. J. Delgado, and R. L. Corey, "A Performance Comparison of Xenon and Krypton," in *32nd International Electric Propulsion Conference*, 2011.

[114] C. J. Wordingham, P.-Y. Taunay, and E. Choueiri, "A Critical Review of Orificed Hollow Cathode Modeling: 0D Models," in *Propulsion and Energy Forum*, 2017. doi: 10.2514/6.2017-4888.

[115] J. E. Polk *et al.*, "Characterization of hollow cathode performance and thermal behavior," *Collection of Technical Papers - AIAA/ASME/SAE/ASEE 42nd Joint Propulsion Conference*, vol. 10, no. July 2006, pp. 7911–7929, 2006, doi: 10.2514/6.2006-5150.

[116] D. R. Lev, I. G. Mikellides, D. Pedrini, D. M. Goebel, B. A. Jorns, and M. S. McDonald, "Recent progress in research and development of hollow cathodes for

electric propulsion," *Rev Mod Plasma Phys*, vol. 3, no. 1, p. 6, 2019, doi: 10.1007/s41614-019-0026-0.

[117] R. R. Hofer *et al.*, "Completing the Development of the 12.5 kW Hall Effect Rocket with Magnetic Shielding (HERMeS)," *36th International Electric Propulsion Conference*, p. IEPC-2019-193, 2019.

[118] S. J. Hall, T. R. Sarver-Verhey, J. D. Frieman, H. Kamhawi, and J. L. Myers, "Preparation for hollow cathode testing for the advanced electric propulsion system at nasa glenn research center," in *2018 Joint Propulsion Conference*, 2018, pp. 1–11. doi: 10.2514/6.2018-4425.

[119] G. Becatti, R. W. Conversano, and D. M. Goebel, "Demonstration of 25,000 ignitions on a proto-flight compact heaterless lanthanum hexaboride hollow cathode," *Acta Astronaut*, vol. 178, no. July 2020, pp. 181–191, 2021, doi: 10.1016/j.actaastro.2020.09.013.

[120] G. Becatti, D. M. Goebel, J. E. Polk, and P. Guerrero, "Life evaluation of a lanthanum hexaboride hollow cathode for high-power hall thruster," *J Propuls Power*, vol. 34, no. 4, pp. 893–900, 2018, doi: 10.2514/1.B36659.

[121] R. W. Conversano, R. B. Lobbia, T. V. Kerber, K. C. Tilley, D. M. Goebel, and S. W. Reilly, "Performance characterization of a low-power magnetically shielded Hall thruster with an internally-mounted hollow cathode," *Plasma Sources Sci Technol*, vol. 28, no. 10, 2019, doi: 10.1088/1361-6595/ab47de.

[122] D. Pedrini, R. Albertoni, F. Paganucci, and M. Andrenucci, "Modeling of LaB6 hollow cathode performance and lifetime," *Acta Astronaut*, vol. 106, pp. 170–178, 2015, doi: 10.1016/j.actaastro.2014.10.033.

[123] T. R. Sarver-Verhey, "Destructive Cathode Evaluation of a Xenon Hollow Cathode After a 28,000 Hour Life Test," in *34th Joint Propulsion Conference and Exhibit*, 1998.

[124] K. K. Jameson, D. M. Goebel, and R. M. Watkins, "Hollow Cathode and Thruster Discharge Chamber Plasma Measurements," *Proceedings of the International Electric Propulsion Conference*, pp. 1–16, 2005.

[125] S. J. Hall *et al.*, "The Effect of Anode Position on Operation of a 25-A class Hollow Cathode," *36th International Electric Propulsion Conference*, p. IEPC-2019-300, 2019, [Online]. Available: https://ntrs.nasa.gov/search.jsp?R=20190032078

[126] G. C. Potrivitu, S. Mazouffre, L. Grimaud, and R. Joussot, "Anode geometry influence on LaB6 cathode discharge characteristics," *Phys Plasmas*, vol. 26, no. 11, 2019, doi: 10.1063/1.5115834.

[127] S. J. Hall, T. G. Gray, J. T. Yim, M. Choi, T. R. Sarver-Verhey, and H. Kamhawi, "The effect of facility background pressure on hollow cathode operation," *J Appl Phys*, vol. 130, no. 11, 2021, doi: 10.1063/5.0061045.

[128] M. M. Mooney and K. M. Lemmer, "Wave characterization of a hollow cathode plume in a HET- like magnetic field," in *37th International Electric Propulsion Conference*, Boston, MA, 2022, pp. 1–8.

[129] M. M. Mooney, G. E. Klang, and K. M. Lemmer, "Analysis of Stability Regime for Hollow Cathode on Noble Gas Propellants," in *38th International Electric Propulsion Conference*, Toulouse, France, 2024, pp. 1–9.

[130] M. M. Mooney, K. M. Lemmer, and R. B. Lobbia, "Effect of Induced Hall Thruster Discharge Current Oscillations on External Cathode Plume Ion Population," in *38th International Electric Propulsion Conference*, Toulouse, France, 2024, pp. 1–10.

[131] H. M. MOTT-SMITH, "the Theory of Collectors in Gaseous Discharges," *Physics Review Letters*, vol. 28, no. 4, pp. 99–132, 1961, doi: 10.1016/b978-1-4831-9909-2.50013-8.

[132] R. B. Lobbia and A. D. Gallimore, "High-speed dual Langmuir probe," *Review of Scientific Instruments*, vol. 81, no. 7, Jul. 2010, doi: 10.1063/1.3455201.

[133] J. P. Sheehan, Y. Raitses, N. Hershkowitz, and M. McDonald, "Recommended practice for use of emissive probes in electric propulsion testing," *J Propuls Power*, vol. 33, no. 3, pp. 614–637, 2017, doi: 10.2514/1.B35697.

[134] M. F. Konopliv, R. E. Wirz, L. Angeles, and L. K. Johnson, "Ion-Neutral Density and Electron Temperature Phasing in the Hall Thruster Breathing Mode," in *38th International Electric Propulsion Conference*, Toulouse, France, 2024, pp. 1–16.

[135] C. C. Farnell, J. D. Williams, and C. C. Farnell, "Comparison of hollow cathode discharge plasma configurations," *Plasma Sources Sci Technol*, vol. 20, no. 2, 2011, doi: 10.1088/0963-0252/20/2/025006.

[136] J. E. Polk, C. M. Marrese-Reading, B. Thornber, L. Dang, L. K. Johnson, and I. Katz, "Scanning optical pyrometer for measuring temperatures in hollow cathodes," *Review of Scientific Instruments*, vol. 78, no. 9, 2007, doi: 10.1063/1.2774828.

[137] G. Becatti, D. Pedrini, B. Kasoji, F. Paganucci, and M. Andrenucci, "Triple Langmuir probes measurements of LaB6 hollow cathodes plume," *Front Phys*, vol. 7, no. MAR, pp. 1–11, 2019, doi: 10.3389/fphy.2019.00027.

[138] G. C. Miars, G. L. Delzanno, B. E. Gilchrist, O. Leon, and F. Lucco Castello, "Ion Emission from a Positively Biased Hollow Cathode Plasma," *IEEE Transactions on Plasma Science*, vol. 48, no. 8, pp. 2693–2705, 2020, doi: 10.1109/TPS.2020.3004553.

[139] J. D. Frieman, J. A. Walker, M. L. R. Walker, V. Khayms, and D. Q. King, "Electrical Facility Effects on Hall Thruster Cathode Coupling: Performance and Plume Properties," *J Propuls Power*, vol. 32, no. 1, pp. 251–264, Aug. 2015, doi: 10.2514/1.b35683.

[140] J. Polk, D. Goebel, R. Watkins, K. Jameson, and L. Yoneshige, "Characterization of Hollow Cathode Performance and Thermal Behavior," in *42nd Joint Propulsion Conference*, American Institute of Aeronautics and Astronautics (AIAA), Dec. 2012. doi: 10.2514/6.2006-5150.

[141] M. F. Konopliv and R. E. Wirz, "Time-resolved electron temperature of a low power Hall thruster," no. January, pp. 1–13, 2024.

[142] M. F. Konopliv, R. E. Wirz, and L. K. Johnson, "Cathode Species Contributions to Hall Thruster Plume Dynamics," in *38th Internatioal Electric Propulsion conference*, Toulouse, France, 2024, pp. 1–14.

[143] G. J. Williams, T. B. Smith, M. T. Domonkos, K. J. Shand, A. D. Gallimore, and R. P. Drake, "Ions Emitted from Hollow Cathodes," in *AIAA 35th Joint Propulsion Conference*, 1999.

[144] Y. Dancheva, P. Coniglio, D. Pagano, A. Garde, and F. Scortecci, "Laser-induced fluorescence detection of the 4d4D7/2 →5p4P◦ 5/2 transition of Kr II in a hollow cathode discharge," 2023, [Online]. Available: http://arxiv.org/abs/2311.02479

[145] J. L. S. Betancourt *et al.*, "Thomson scattering measurements in the krypton plume of a lanthanum hexaboride hollow cathode in a large vacuum test facility," *J Appl Phys*, vol. 135, no. 8, 2024, doi: 10.1063/5.0180251.

[146] S. Tsikata, K. Hara, and S. Mazouffre, "Characterization of hollow cathode plasma turbulence using coherent Thomson scattering," *J Appl Phys*, vol. 130, no. 24, 2021, doi: 10.1063/5.0071650.

[147] R. B. Lobbia, "A Time-resolved Investigation of the Hall Thruster Breathing Mode," *University of Michigan*, pp. 96–146, 2010.

[148] R. Lobbia and B. Beal, "Recommended Practice for Use of Langmuir Probes in Electric Propulsion Testing," *J Propuls Power*, vol. 33, no. 3, pp. 614–637, Nov. 2016, doi: 10.2514/1.b35697.

[149] J. Williams, J. Williams, and N. F. Avenue, "A simple , inexpensive Langmuir Probe Experiment ∗ Contact Information," 2014.

[150] F. Chen, "Langmuir Probe Diagnostics," 2003.

[151] R. B. Lobbia and A. D. Gallimore, "Temporal limits of a rapidly swept Langmuir probe," *Phys Plasmas*, vol. 17, no. 7, 2010, doi: 10.1063/1.3449588.

[152] J. M. Beall, Y. C. Kim, and E. J. Powers, "Estimation of wavenumber and frequency spectra using fixed probe pairs," *J Appl Phys*, vol. 53, no. 6, pp. 3933–3940, 1982, doi: 10.1063/1.331279.

[153] M. P. Georgin, B. A. Jorns, and A. D. Gallimore, "An Experimental and Theoretical Study of Hollow Cathode Plume Mode Oscillations," in *35th International Electric Propulsion Conference*, 2017.

[154] M. P. Georgin, "Ionization Instability of the Hollow Cathode Plume," 2020.

[155] M. P. Georgin, B. A. Jorns, and A. D. Gallimore, "Dependence of Low Frequency Waves on Magnetic Field Strength in Hollow Cathode Plume," in *36th International Electric Propulsion Conference*, 2019.

[156] S. J. Hall *et al.*, "The Effect of Anode Position on Operation of a 25-A class Hollow Cathode," *36th International Electric Propulsion Conference*, p. IEPC-2019-300, 2019.

[157] R. R. Hofer *et al.*, "Development Status of the 12.5 kW Hall Effect Rocket with Magnetic Shielding (HERMeS)," in *35th International Electric Propulsion Conference*, 2017, p. IEPC-2017-231. doi: IEPC-2017-231.

[158] R. Z. Sagdeev and A. A. Galeev, *Nonlinear plasma theory*. 1969.

[159] R. B. Lobbia, S. Arestie, J. Simmonds, and M. M. Mooney, "AEPS Near-Field Turbulent Plasma Plume Measurements," in *2025 AIAA SciTech*, Orlando, Florida, 2025, pp. 1–23.

[160] J. E. Polk and R. B. Lobbia, "The Effect of Time-Varying Currents on Hollow Cathode Operation," in *37th International Electric Propulsion Conference*, Boston, MA, 2022. doi: 10.2514/6.2006-5153.

[161] R. R. Hofer, D. M. Goebel, and R. M. Watkins, "Compact LaB6 Hollow Cathode for a 6 kW Laboratory Hall Thruster," in *54th JANNAF Propulsion Meeting*, 2007. doi: 10.1063/1.3474921.

[162] B. A. Jorns and R. R. Hofer, "Plasma oscillations in a 6-kW magnetically shielded Hall thruster," *Phys Plasmas*, vol. 21, no. 5, pp. 1–19, 2014, doi: 10.1063/1.4879819.

[163] A. Lopez Ortega and I. G. Mikellides, "The importance of the cathode plume and its interactions with the ion beam in numerical simulations of Hall thrusters," *Phys Plasmas*, vol. 23, no. 4, 2016, doi: 10.1063/1.4947554.

Appendix A: Effect of Probe Separation Distance on the Beall Analysis Technique

An experiment utilizing two-electrode wave probes mounted to a rotary stage was performed to observe this variance. Figure A.1.1 provides a picture of the setup with an associated schematic showing the axis convention. The probes were oriented perpendicular to centerline and rotated about the $\hat{r}$ direction. At 90° rotation, the upstream probe, probe 1, was closer to the cathode exit. Data were collected at 10-A and 15-A DC discharge currents and at 8-sccm and 10-sccm flow rates. The magnetic field strengths reported below are in reference to the magnitude of the field at the exit plane of the upstream solenoid. The solenoid exit is in-plane with the cathode keeper orifice. The field strength varied between 0 G and 133 G.

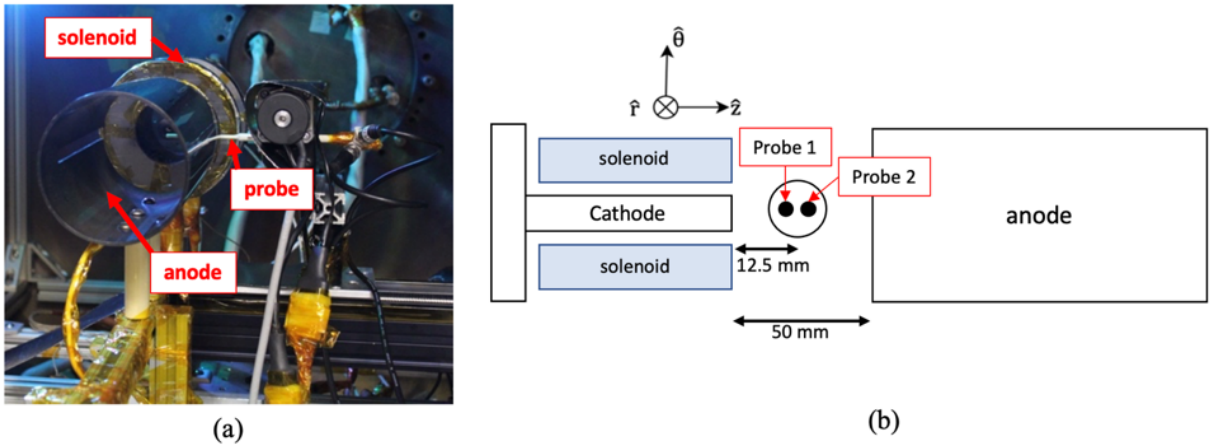

A.1.1: Cathode configuration to determine the effects of probe separation on wave probe analysis.(a) Orientation of the cathode-anode placement and probe mounted on the rotary stage and (b) probe orientation at 90° rotation.

The AC component of the current was collected using a combination of 2877 Pearson current monitor and an OPA847 OPAMP for a combined amplification of 1000X. Bench testing of this setup showed a -3dB bandwidth limit of 17 MHz for the AC measurement. The DC component was collected separately via a differential voltage measurement across an in-line 100 Ω resistor. The AC measurement was captured on a CSE4444 GaGe computer scope and the DC measurement was collected on a TI-6440 data acquisition (DAQ) system. Both were triggered externally using a function generator for

simultaneous measurements. The variance in the measured ion current between the two probes can be shown as the percent difference in the DC current:

$$\% \, diff = \frac{abs(\bar{I}_1 - \bar{I}_2)}{\frac{(\bar{I}_1 + \bar{I}_2)}{2}} \tag{7.1}$$

where $\bar{I}_{1,2}$ are the collected DC current from probe 1 and 2, respectively.

Figure A.1.2 shows that probe 1 begins to shield probe 2 along the rotation of the probe about the r axis, resulting in the greatest percent difference in measured current at the 90° rotation orientation. This effect was more prominent in the 1-mm separation configuration, where the percent difference was nearly 20% greater at the 90° rotation orientation compared to the 3-mm separation.

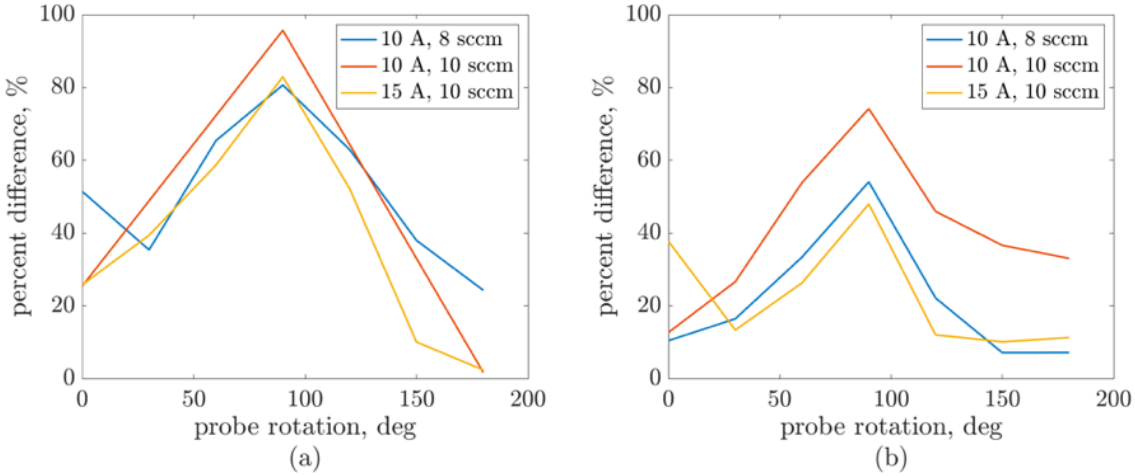

Figure A.1.2: Percent difference in measured DC probe current along the rotation about the r axis without the magnetic field. (a) 1-mm separation and (b) 3-mm separation.

Figure A.1.3 shows the percent difference in the measured ion saturation current between probes 1 and 2 as a function of cathode and solenoid operating conditions for the 1-mm and 3-mm separation distances for 0° and 90° rotation orientations. When the probes were aligned along the azimuthal direction, rotation condition 0° (figure A.1.3 (a) and (b)), the percent difference was approximately 5-15% less for 3-mm separation condition when compared with the 1-mm separation condition. In other words, the DC measurement of probes 1 and 2 were more similar at 3-mm separation than at 1-mm separation. While there is no clear correlation between magnetic field strength and percent

difference of ion saturation current measured by the two probes at the 1-mm separation condition for azimuthally-aligned probes (figure A.1.3 (a)), increasing the magnetic field strength for the 3-mm probe separation at 0° (figure A.1.3 (b)) resulted in an increasing difference in measured saturation current such that it nearly matched the 1-mm probe measurement for the equivalent cathode condition. When the probes were aligned axially, 90°, (Figure A.1.3 (b) and (c)), the 1-mm probe separation condition showed a 20% increase in the percent difference when compared with the 3-mm separation condition. Increasing the magnetic field when the probes were aligned axially resulted in a clear decrease in the percent difference of the measured ion saturation current for both separation distances.

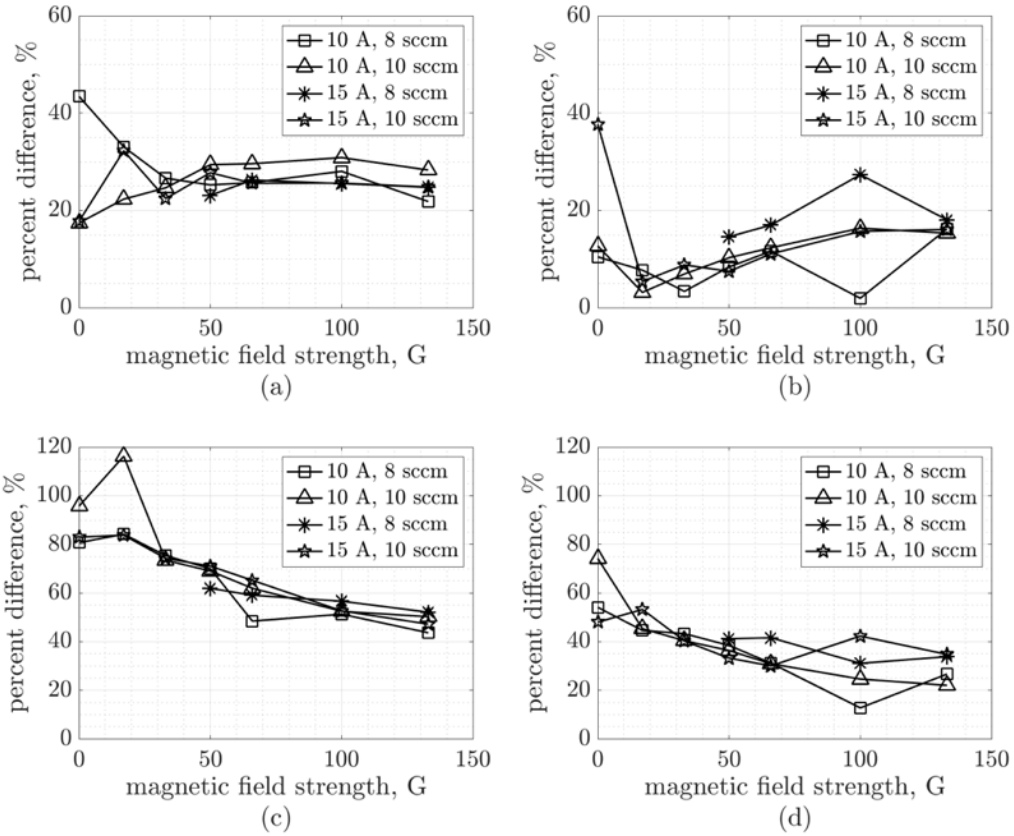

Figure A.1.3: Percent difference in measured ion saturation current between the two probe configurations. (a) 0°, 1-mm probe separation, (b) 0°, 3-mm probe separation, (c) 90°, 1-mm probe separation, and (d) 90°, 3-mm probe separation.

Figures A.1.4-A.1.7 show the dispersion plots generated by the Beall method from the probe signals at the 10-A, 8-sccm condition. The z-scale of these plots is the statical representation of the dispersion, $S(\omega, k)$, and has arbitrary units. Figures A.1.4 and A.1.5 show the statistical dispersion up to 10 MHz and both have been concatenated to show wavenumbers between $\pm 2000\ m^{-1}$. Figures A.1.6 and A.1.7 display the same data but focuses on the low-frequency behavior (up to 250 kHz).

When the probes were azimuthally aligned ($0°$ probe orientation) for the unmagnetized cases (figures A.1.4-A.1.7 (a)-(d)), both separation distances showed no dispersion in the high-frequency domain ($S(\omega, k)$ was centered around k = 0). Figures A.1.4 and A.1.5 showed that there was some dispersion above 6 MHz, particularly for the 1-mm probe separation condition; however, it was unclear if this was an artifact of the analysis technique or a true plasma behavior. For the 133-G condition (figures A.1.4 and A.1.5 (e)-(h)), as the probe was rotated about the r axis, the 1-mm separation dispersion differs significantly from the 3-mm separation condition measurement. It was clear in the 3-mm separation condition that there exits longitudinal dispersion ($S(\omega, k)$ slopes to the right) for the 100-kHz peak. However, the dispersion was less clear for the 1-mm separation condition. The 1-mm probe showed some curving around 1 MHz while the dispersion for the 3-mm separation was linear. The maximum slope in both dispersion plots for the 100-kHz peak was between $60°$ and $90°$; however, waves that exist at this frequency typically propagate purely in the axial direction ($90°$ in this experiment). It is possible that the probes were slightly misaligned, and therefore, the true axial measurement was somewhere between $60°$ and $90°$. Alternatively, the propagation of the wave could depend on the location of the anode which would shift the primary propagation direction slightly off the axial axis ($\hat{z}$ direction). Further studies with adjustment of axial location are needed.

In the low-frequency regime (figures A.1.6-A.1.7 (e)-(h)), the unmagnetized cases for the 1-mm separation showed no waves with dispersion while the 3-mm separation exhibited some global phenomena (k=0). In the azimuthal direction (figures A.1.6 (e) and

A.1.7 (e)), the rotational mode was measured at 60 kHz. Converting the wavenumber to mode number, using $\mathsf{m} = \mathsf{k} \times \mathsf{r}$, where r was the distance from centerline along the r-axis of the measurement (6.35 mm), shows that the rotational mode measured is consistent the $\mathsf{m} = 1$ mode described in section 2.3.4.3.

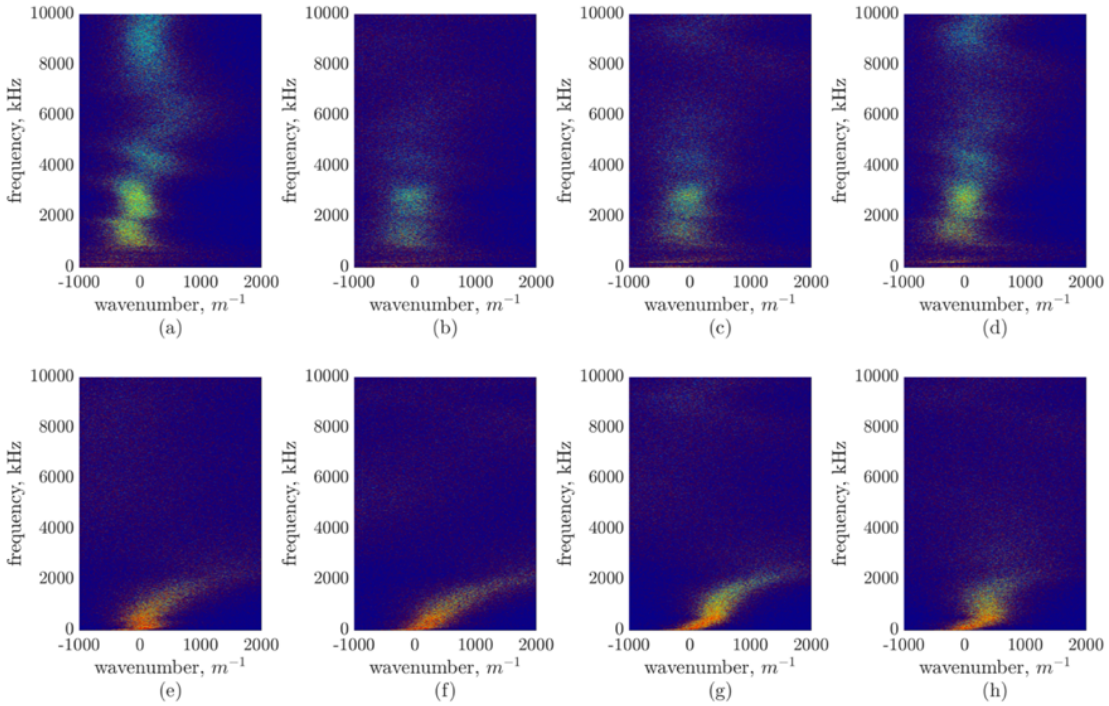

Figure A.1.4: Statistical dispersion plots for the 1-mm probe separation at the 10-A, 8-sccm condition for frequencies up to 10 MHz. (a) – (d) 0°, 30°, 60°, and 90° probe orientations for the 0-G condition. (e) – (h) 0°, 30°, 60°, and 90° probe orientations for the 133-G condition.

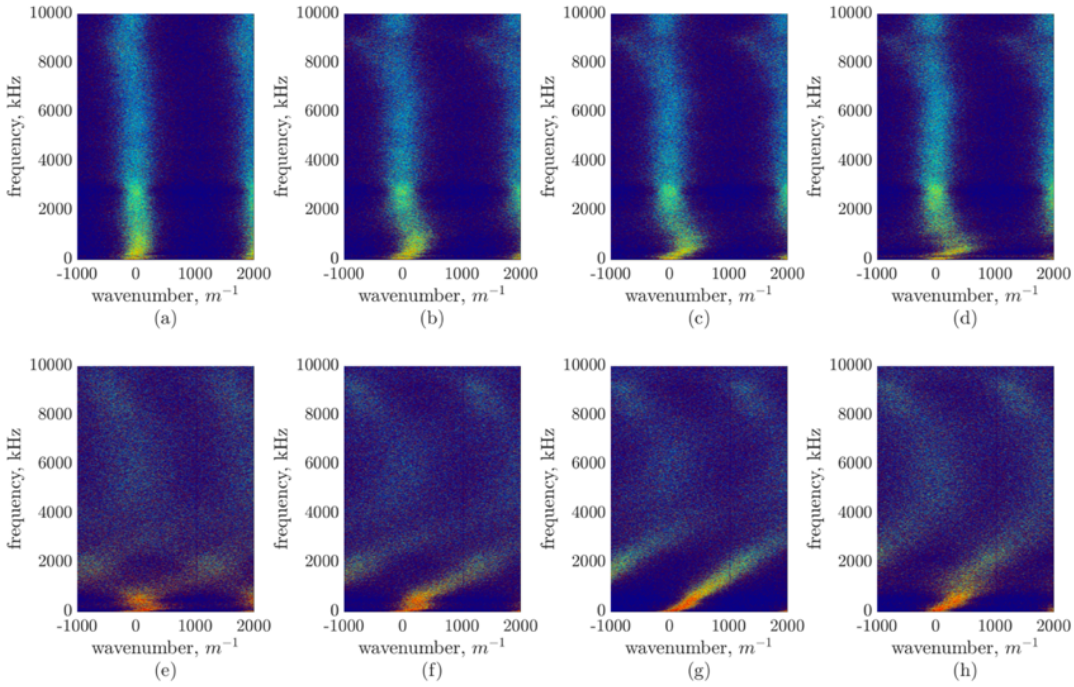

Figure A.1.5: Statistical dispersion plots for the 3-mm probe separation at the 10-A, 8-sccm condition for frequencies up to 10 MHz. (a) – (d) 0°, 30°, 60°, and 90° probe orientations for the 0-G condition. (e) – (h) 0°, 30°, 60°, and 90° probe orientations for the 133-G condition.

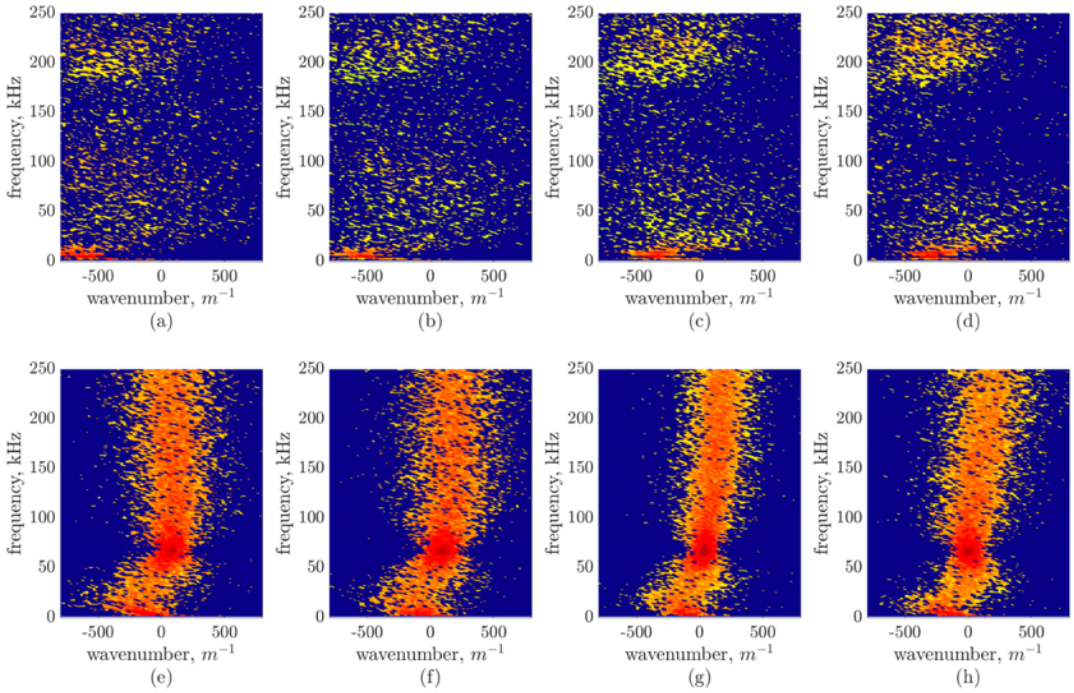

Figure A.1.6: Statistical dispersion plots for the 1-mm probe separation at the 10-A, 8-sccm condition for frequencies up to 250 kHz. (a) – (d) 0°, 30°, 60°, and 90° probe orientations for the 0-G condition. (e) – (h) 0°, 30°, 60°, and 90° probe orientations for the 133-G condition.

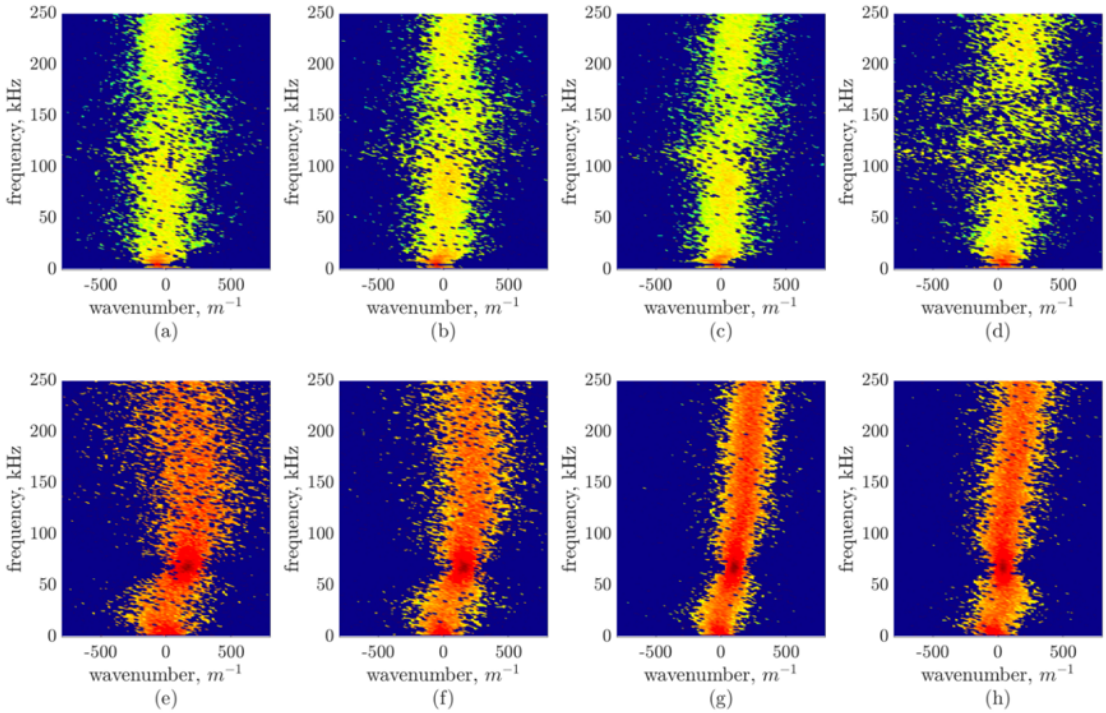

Figure A.1.7: Statistical dispersion plots for the 3-mm probe separation at the 10-A, 8-sccm condition for frequencies up to 250 kHz. (a) – (d) 0°, 30°, 60°, and 90° probe

orientations for the 0-G condition. (e) – (h) 0°, 30°, 60°, and 90° probe orientations for the 13-G condition.

In summary, when the ion saturation probes were closer together (1-mm versus 3-mm separation), the upstream probe shielded the downstream probe, resulting in a large percent difference in the measured ion current. The dispersion plots generated from these data suggest that the shielding effects, whether due to sheath interactions, flowing plasma effects, or other mechanisms, skew the Beall plots, directly impacting the analysis of the ion dynamics and turbulence. It is evident that care must be used in constructing invasive probes with the intent of measuring wave propagation. Wave probes with smaller surface areas can reduce this effect. As such, the probes configured for the work in this dissertation have much smaller radii compared to the above study.

Appendix B: Colorblind-Friendly Surface Plots

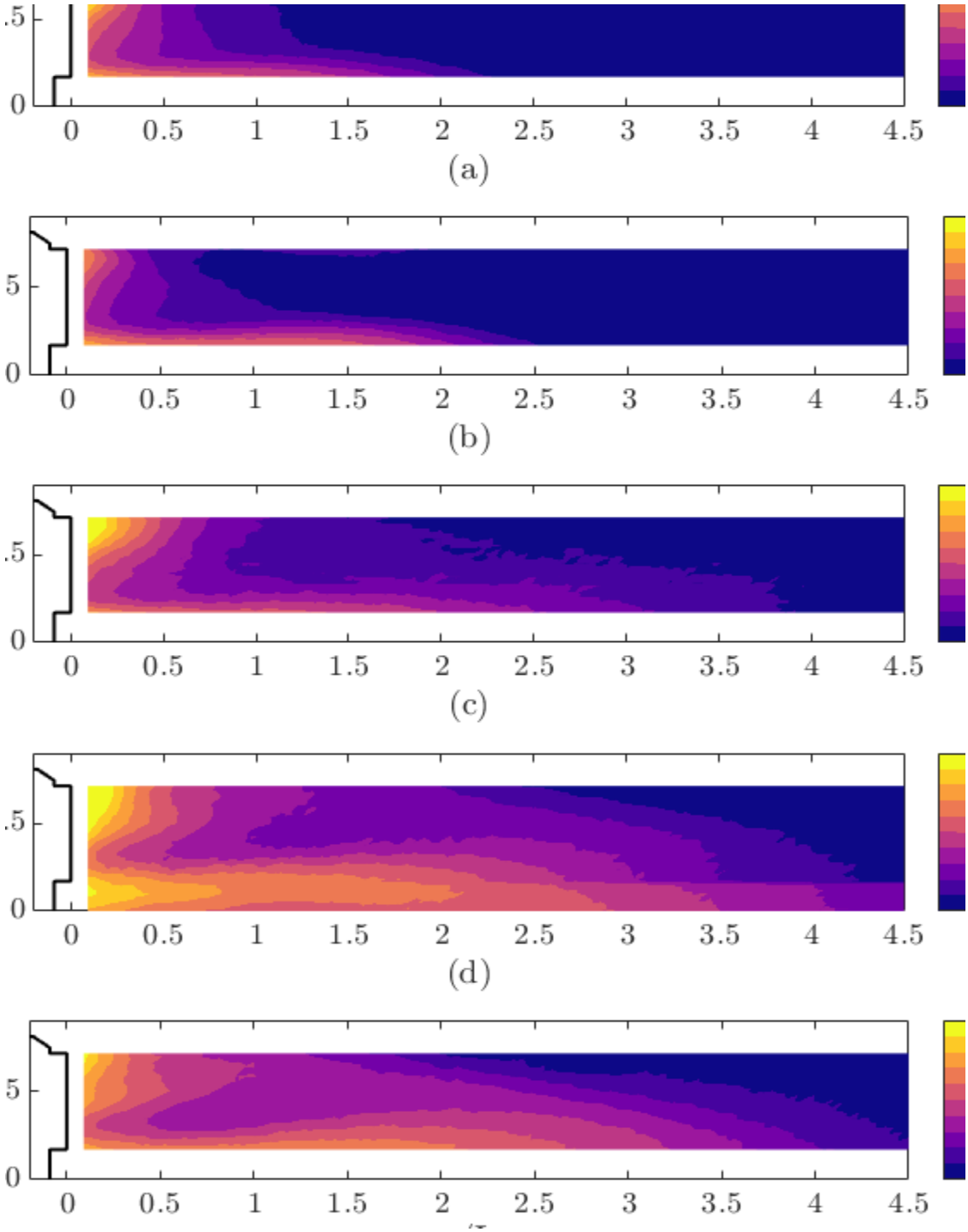

Figure A.2.8: Colorblind-friendly version of figure 5.7.

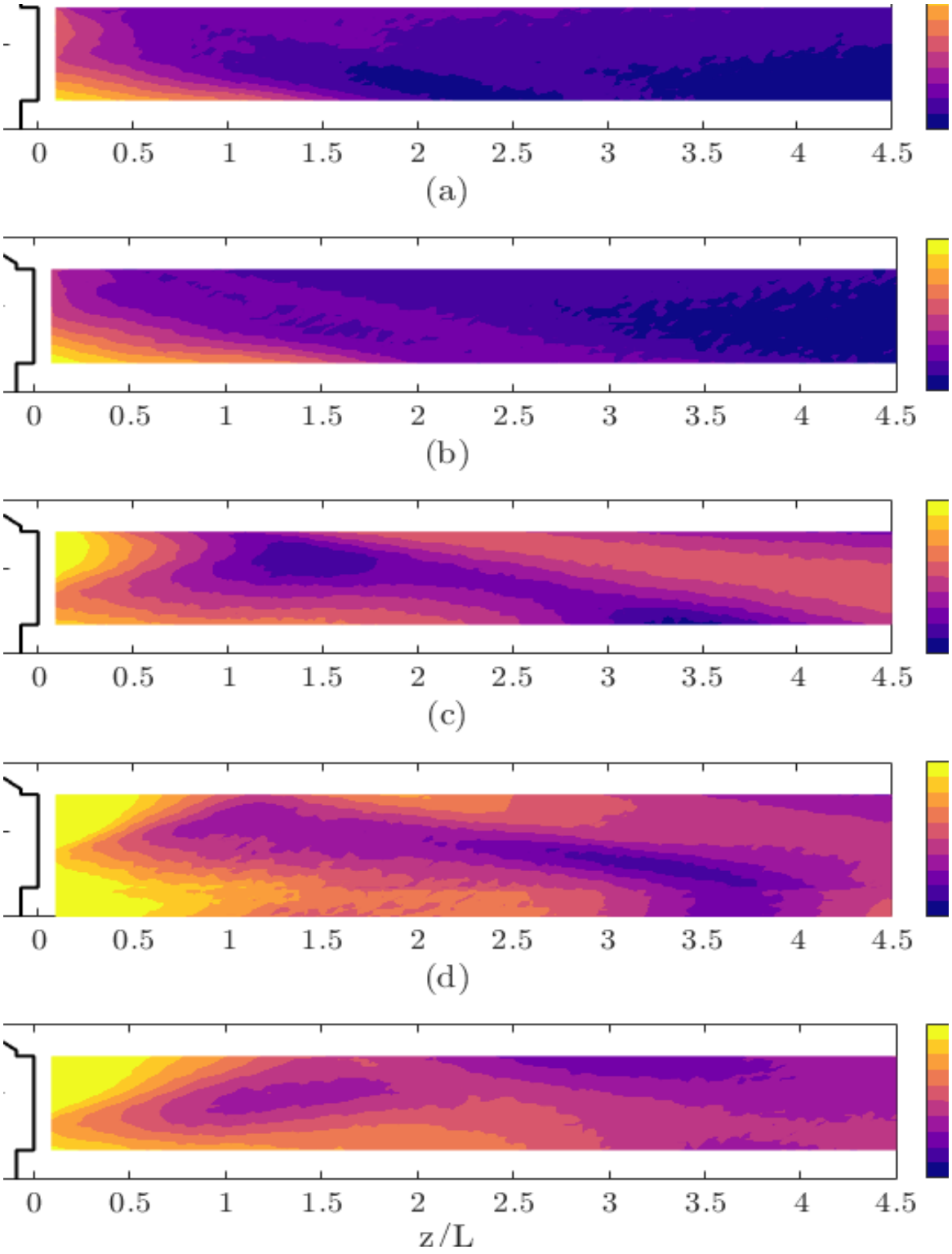

Figure A.2.9: Colorblind-friendly version of figure 5.8.

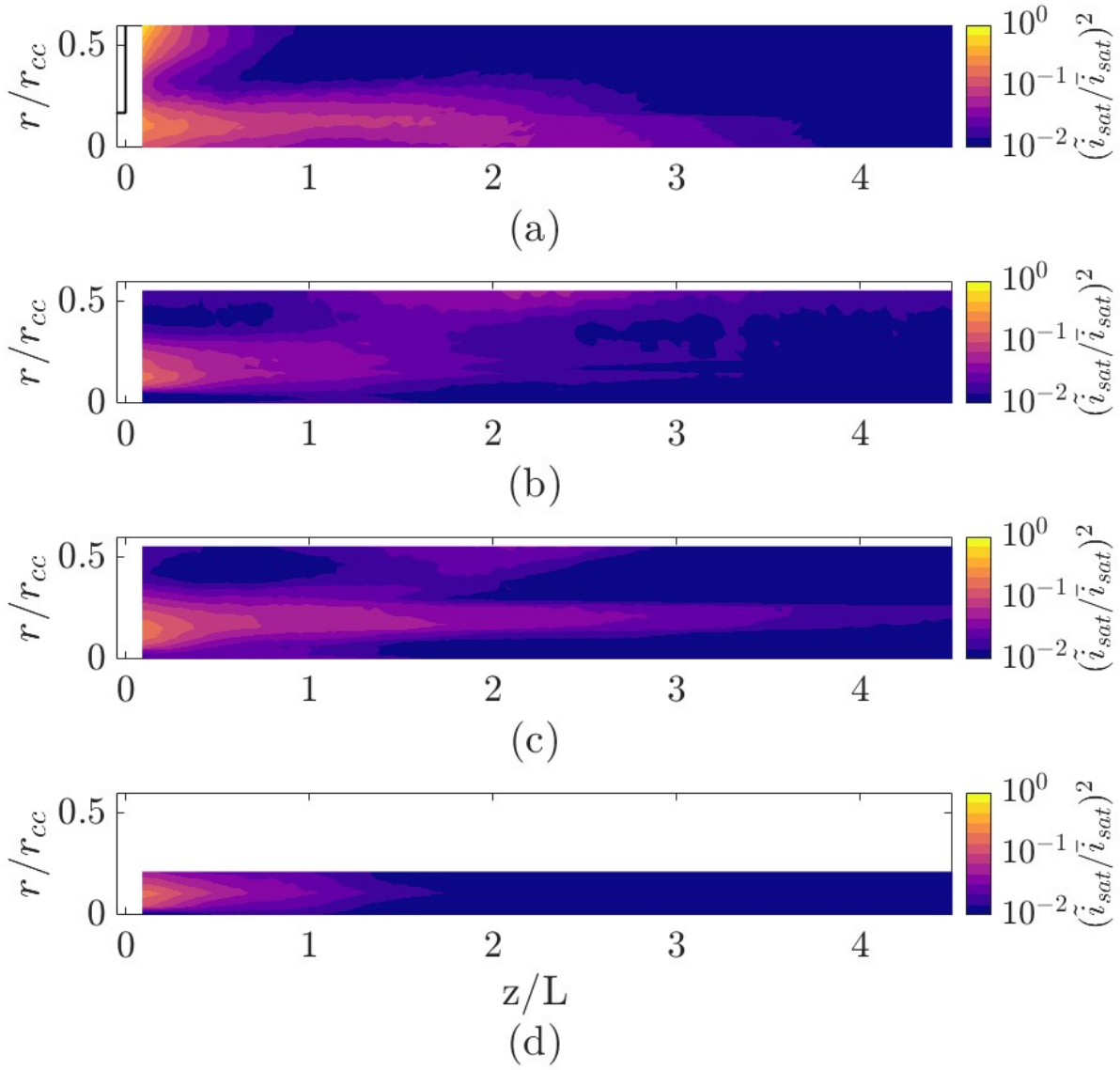

Figure A.2.10: Colorblind-friendly version of figure 5.10

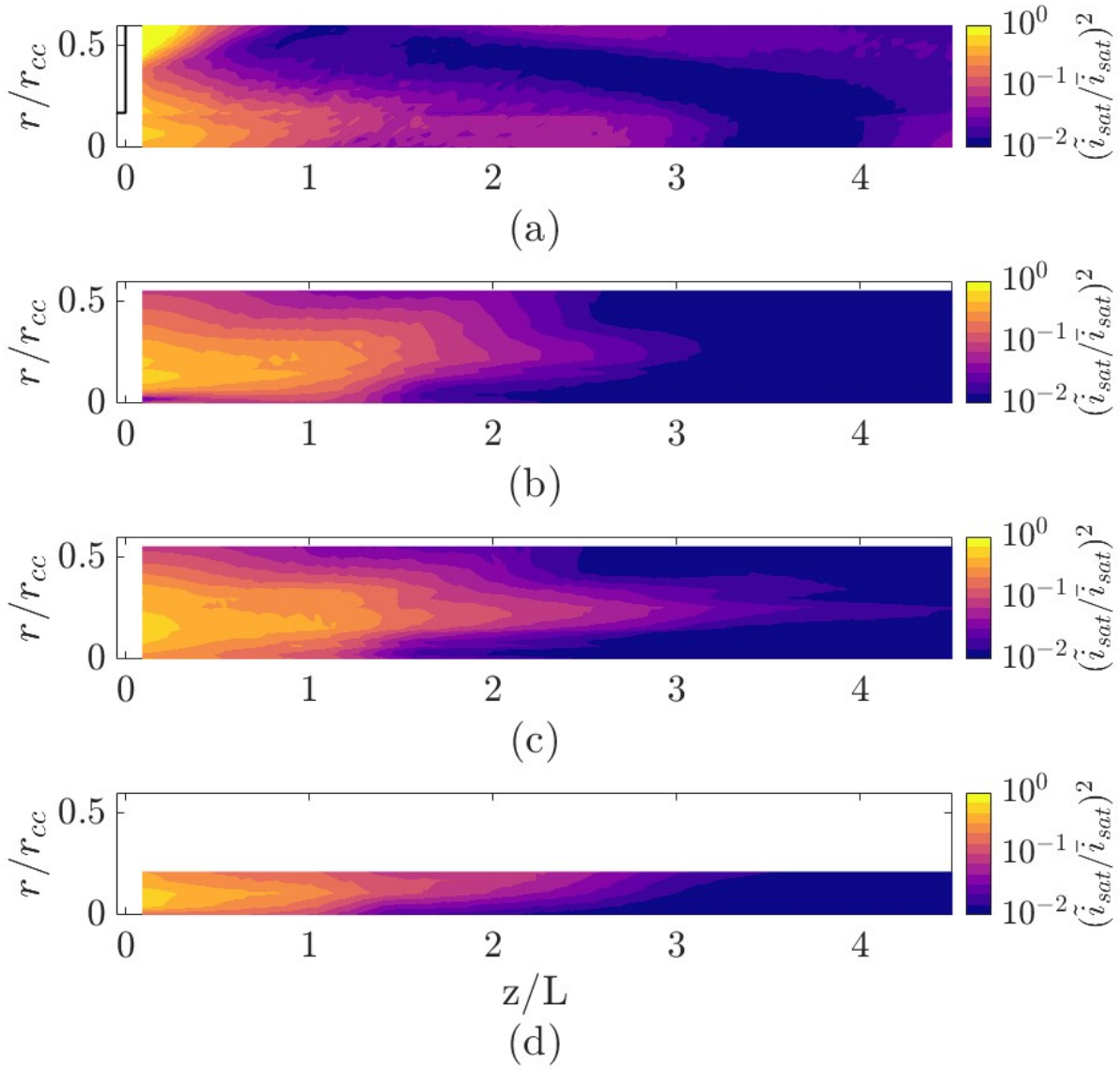

Figure A.2.11: Colorblind-friendly version of figure 5.11

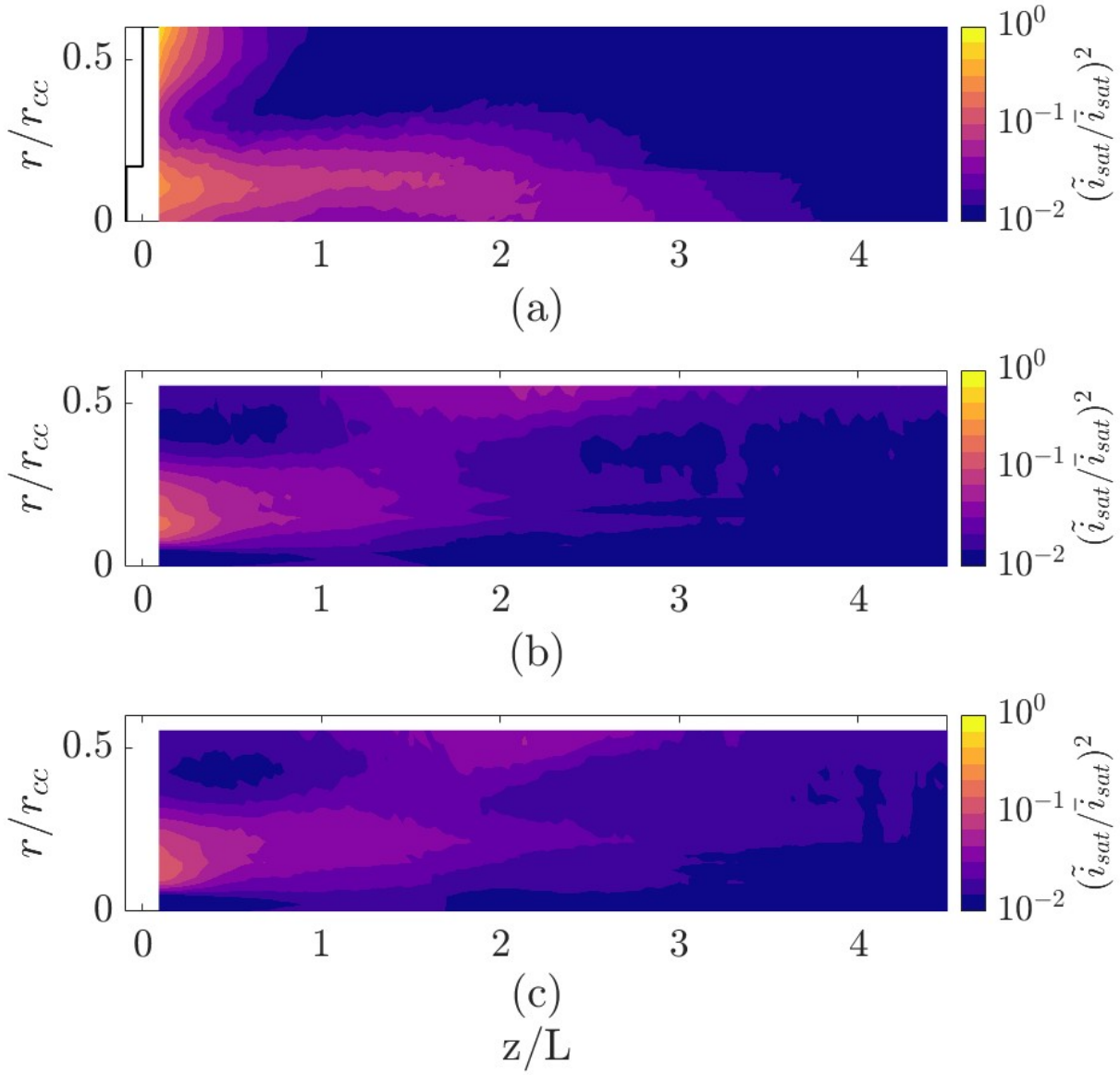

Figure A.2.12: Colorblind-friendly version of figure 5.12.

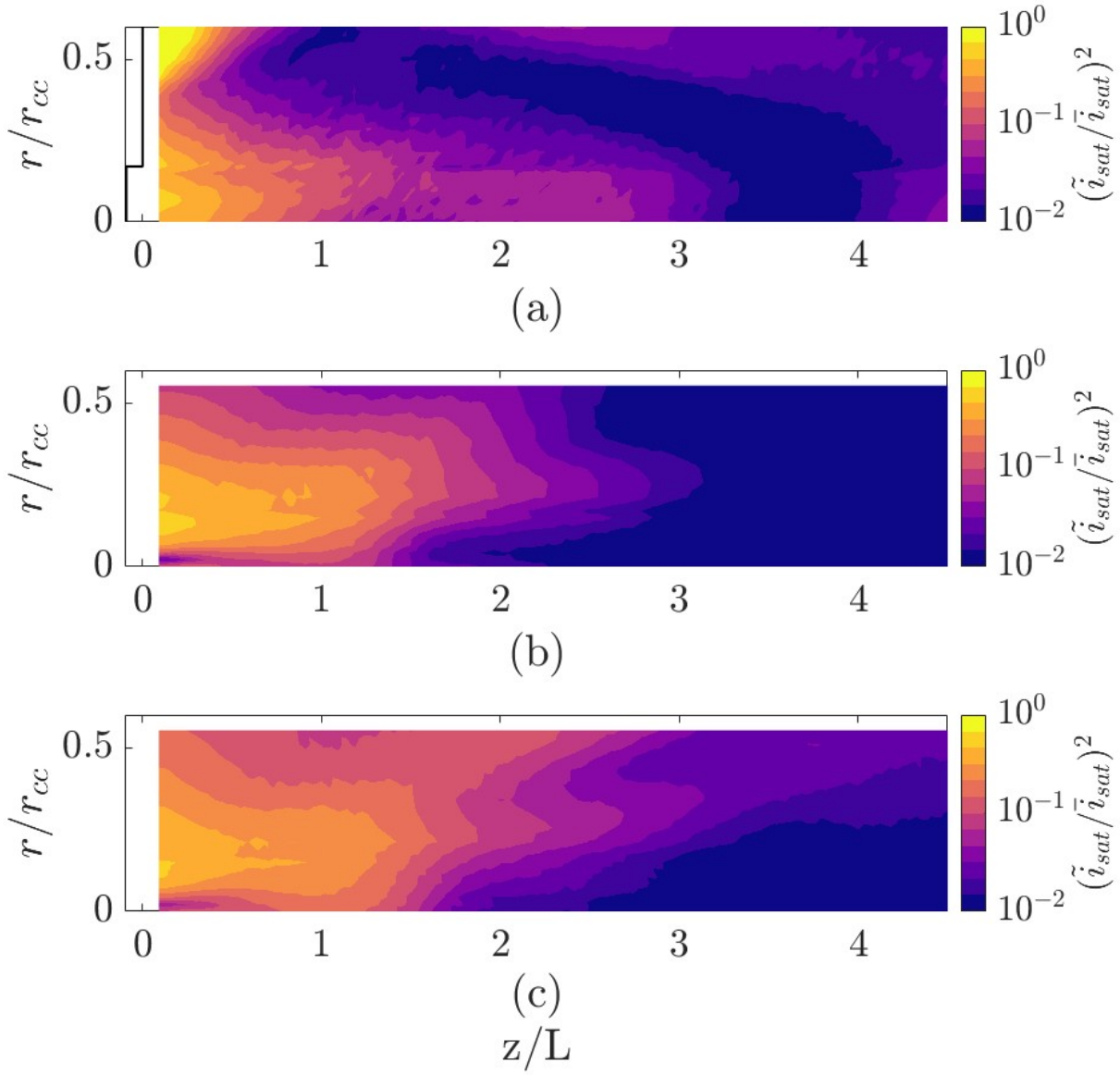

Figure A.2.13: Colorblind-friendly version of figure 5.13.

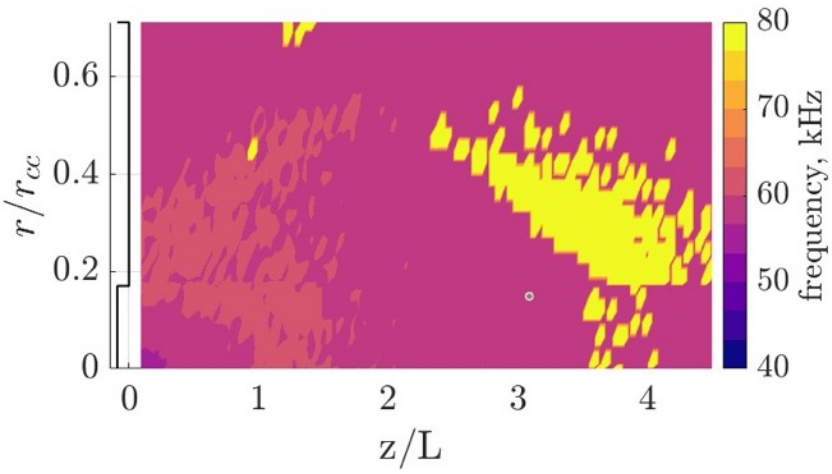

Figure A.2.14 Colorblind-friendly version of figure 5.14.

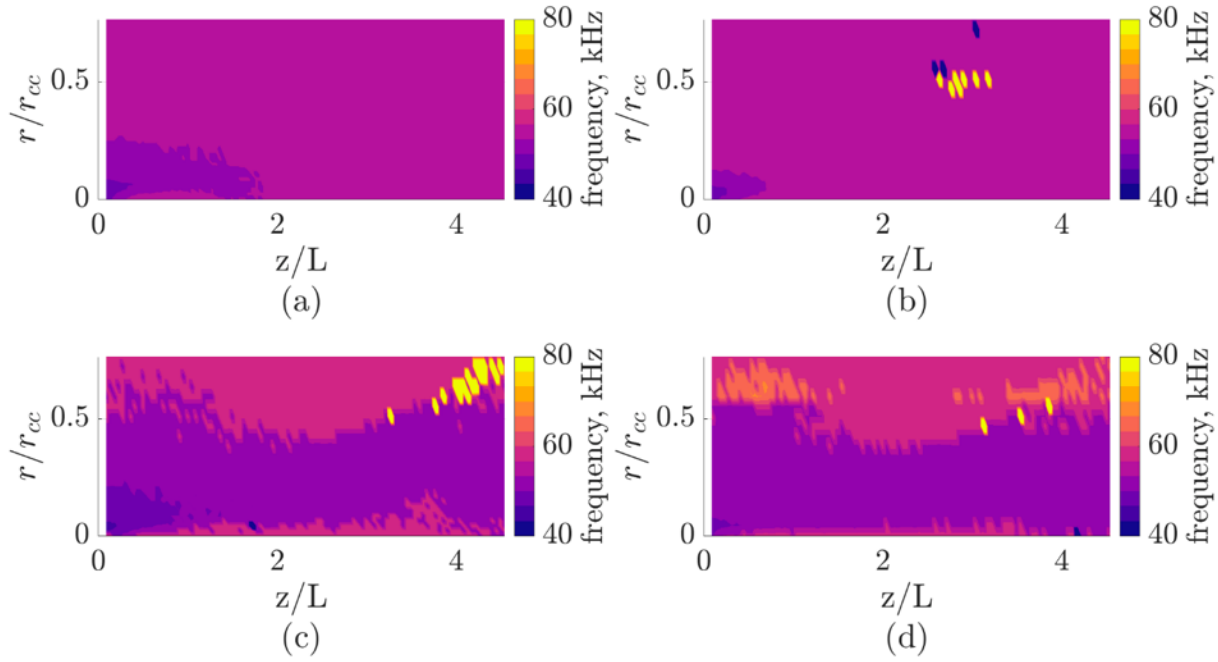

Figure A.2.15: Colorblind-friendly version of figure 5.15.

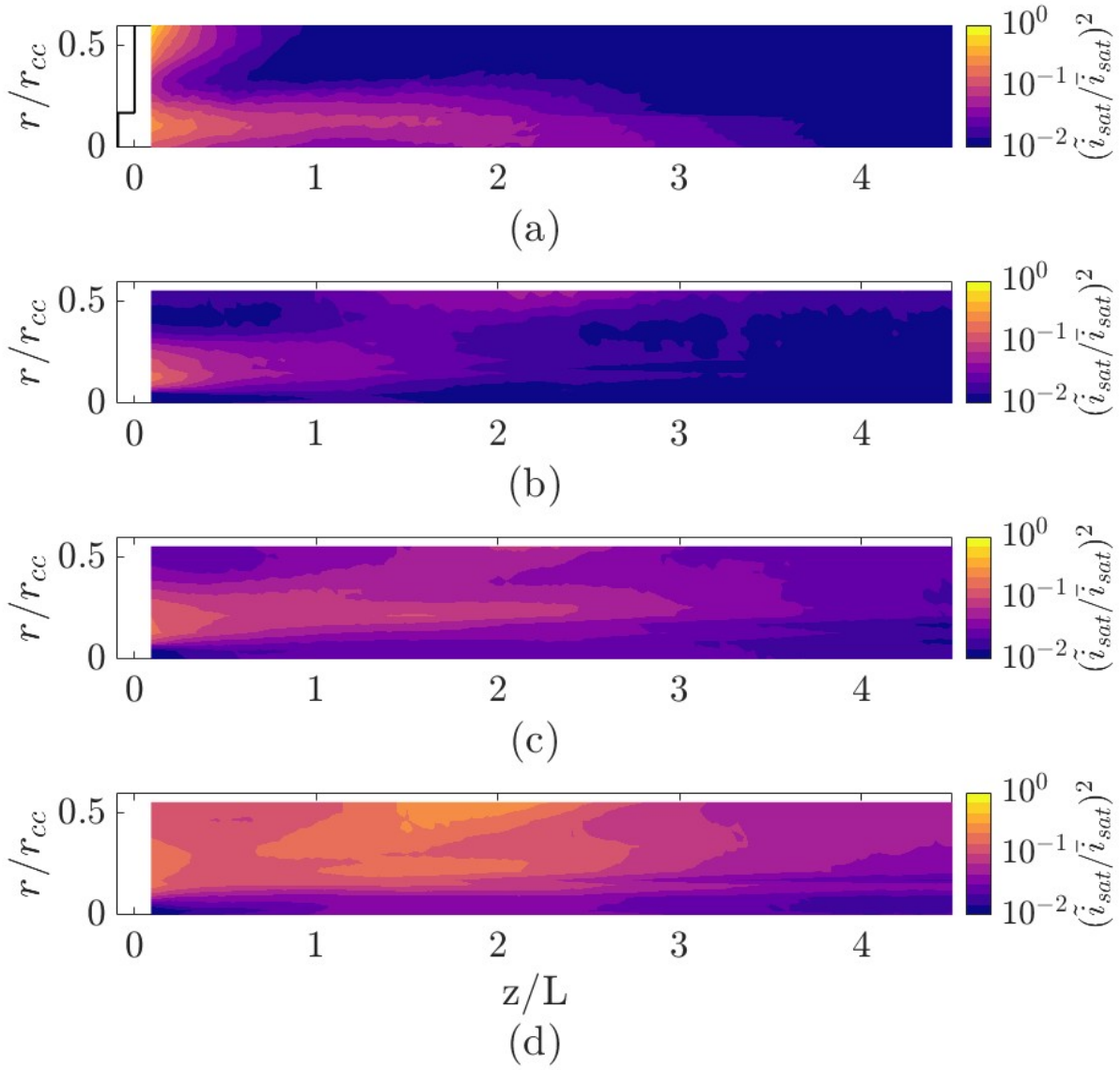

Figure A.2.16: Colorblind-friendly version of figure 5.16

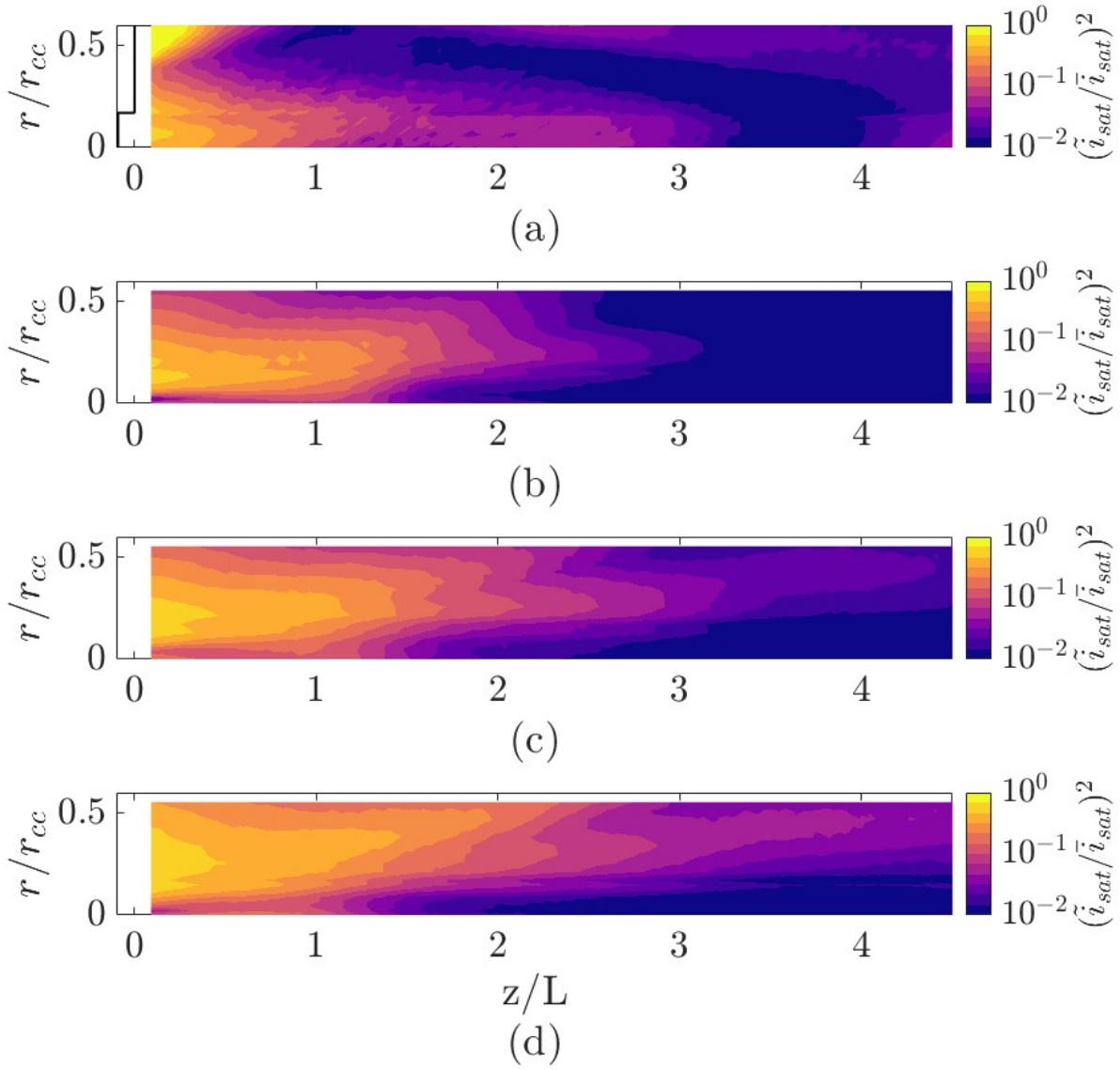

Figure A.2.17: Colorblind-friendly version of figure 5.17.